

Experimental Demonstration of Superradiant Amplification of Ultra-Short Laser Pulses in a Plasma

Dissertation der Fakultät für Physik
der Ludwigs-Maximilian-Universität München

vorgelegt von
Matthias Dreher
aus Singen (Hohentwiel)

München, den 14. Dezember 2004

1. Gutachter: Prof. Dr. Dieter Habs
2. Gutachter: Prof. Dr. Klaus Witte

Tag der mündlichen Prüfung: 3. Februar 2005

Abstract

The present work for the first time demonstrates superradiant amplification (SRA) of ultra-short laser pulses in a plasma [1]. The novel amplification scheme has the potential to create multi-PW, two-cycle light pulses thus surpassing the limits of current laser technology. At intensities of 10^{15} W/cm^2 - 10^{18} W/cm^2 , a short signal pulse of 20 - 40 fs duration is directly amplified in a plasma by a counter-propagating, picosecond-long, blue-shifted pump pulse. In the interaction region, the plasma electrons get trapped in the ponderomotive potential formed by the interference pattern of the two pulses. The electrons start oscillating along the propagation axis and are quickly arranged to a transient density grating. The grating reflects a part of the pump pulse coherently back into the signal pulse. The ongoing oscillations of the electrons destroy the grating again, which leads to a further shortening of the signal pulse.

In the framework of this thesis, the complete experiment including the diagnostics has been set up at the MPI für Quantenoptik using the Advanced Ti:Sapphire Laser (ATLAS) as a source for the pump and signal pulses. Each of the pulses is focused from opposite directions into a hydrogen gas jet, which is quickly ionized by the pedestal of the pump pulse. The generation of the short frequency-shifted signal pulse synchronized to the ATLAS pump pulse proved to be rather difficult. Several schemes were too sensitive to short-time variations of the surrounding temperature and shot-to-shot energy fluctuations of the ATLAS pulses. Therefore, pump and signal pulses of equal central wavelengths were used in the first series of measurements. Numerical simulations had shown that the initial signal pulse launches the generation of a detuned new pulse by stimulated Raman backscattering, which is first amplified by Raman amplification and later by SRA.

The signal pulse was generated from a small fraction split off from the ATLAS pulse. Spectral broadening in an Argon-filled hollow fiber allowed the further compression 23 fs. In first experiments, these unshifted signal input pulses were significantly amplified in energy and verified the generation of a new pulse at the Raman Stokes line showing up in its spectrum. Evidence for the transition from Raman amplification to SRA was concluded from the spectral broadening around the Stokes line when the duration of the pump pulse and hence the amplification length was increased. The fully established SRA regime was anticipated for longer pump pulses. However, these pulses were strongly backscattered by stimulated Brillouin scattering concealing the amplified signal and frustrating further improvements. The Brillouin scattering was resonantly excited by the undetuned laser pulses.

In the second approach, SRA was observed using the original scheme with a red-shifted signal pulse. The spectrum was shifted by suppressing short-wavelength components after the hollow fiber. This measure also increased the duration to 80 fs. In the plasma, this pulse was amplified 20 times in energy to about 1 mJ and surpassed the intensity threshold for SRA, which manifested in the doubling of the spectral bandwidth and the breakup of the signal pulse into a train of three equidistant 28-fs pulses. The latter finding is a direct consequence of the ongoing oscillations of the electrons in the ponderomotive potential in case of a long signal pulse entailing alternately amplification and attenuation. The observed pulse durations and distances agree with the theoretical predictions. Particle-in-Cell simulations of the experiments reproduce these findings. Single sub-10-fs pulses and higher amplification are anticipated for shorter and stronger input signal pulses with a higher contrast.

Amplification slightly improved the near- and far-field patterns of the signal pulse proving that the pulse is spatially filtered by the higher on-axis amplification.

Kurzfassung

In der vorliegenden Arbeit wurde die superradiante Verstärkung (engl.: superradiant amplification, SRA) ultrakurzer Laserimpulser in einem Plasma erstmals verwirklicht [1]. Das neuartige Verstärkungsprinzip hat das Potenzial Multi-PW Laserimpulse mit einer Dauer von zwei Lichtzyklen zu erzeugen, was jenseits der Möglichkeiten heutiger Lasertechnik liegt. Bei Intensitäten von 10^{15} W/cm^2 - 10^{18} W/cm^2 wird ein kurzer Signalimpuls von 20 - 40 fs in einem Plasma direkt durch einen gegenläufigen langen, blauverschobenen Pumpimpuls verstärkt. Im Wechselwirkungsbereich werden die Plasmaelektronen im ponderomotorischen Potenzial eingefangen, das vom Interferenzmuster der beiden Impulse gebildet wird. Die Elektronen schwingen im Potenzial entlang der Propagationsachse der Impulse und werden rasch zu einem kurzlebigen Dichtegitter angeordnet. Das Gitter reflektiert einen Teil des Pumpimpulses kohärent zurück in den Signalimpuls. Die fortschreitende Oszillation der Elektronen zerstört das Gitter wieder, wodurch der Signalimpuls weiter verkürzt wird.

Im Rahmen dieser Doktorarbeit wurde das gesamte Experiment einschließlich der Diagnostik am MPI für Quantenoptik aufgebaut. Als Quelle für die Pump- und Signalimpulse diente der Advanced Ti:Sapphire Laser (ATLAS). Die Impulse werden aus entgegengesetzten Richtungen in einen Wasserstoff-Gasstrom fokussiert, der von der Vorderflanke des Pumpimpulses ionisiert wird. Einen frequenzverschobenen Eingangs-Signalimpuls herzustellen, der mit dem Pumpimpuls zeitlich synchronisiert ist, erwies sich als schwierig. Mehrere Anordnungen waren zu empfindlich gegenüber Schwankungen der Umgebungstemperatur und der Energie der ATLAS-Impulse. Für die ersten Messungen wurden Pump- und Signalimpulse mit der gleichen Wellenlänge benutzt. Numerische Simulationen ergaben, dass der Eingangs-Signalimpuls in diesem Fall die Erzeugung eines neuen, frequenzverstimmten Impulses durch Ramanstreuung anregt, der zunächst im Raman- und später im SRA-Regime verstärkt wird.

Zur Erzeugung des Signalpulses wurde ein kleiner Teil des ATLAS Impulses abgetrennt, in einer Argon gefüllten Hohlleiter spektral verbreitert und anschließend auf 23 fs komprimiert. Erste Experimente zeigten eine deutliche Energieverstärkung und bestätigten die Erzeugung eines neuen Impulses anhand der Raman-Stokes Linie im Spektrum des Ausgangsimpuls. Der Übergang in das SRA Regime deutete sich an durch eine spektrale Verbreiterung um die Stokes-Linie, wenn die Pumpimpulse und damit die Verstärkungslänge verlängert wurden. Jedoch verhinderte das plötzlich Einsetzen von Brillouinstreuung bei noch längeren Pumpimpulsen, dass sich SRA beobachten ließ. Die Brillouinstreuung wurde resonant von den Pump- und Signalimpulsen angeregt und überdeckte das verstärkte Signal.

SRA konnte mit dem ursprünglichen SRA Schema gezeigt werden, das einen rotverschobener Eingangs-Signalimpuls benutzt. Das Spektrum wurde verschoben, indem die kurzwelligen Anteile weggefiltert wurden, was gleichzeitig die Dauer auf 80 fs erhöhte. Der Impuls wurde im Plasma 20fach auf etwa 1 mJ verstärkt. SRA zeigte sich durch die Verdopplung der spektralen Bandbreite und das Aufbrechen des Signalimpulses in drei 28 fs Impulse mit gleichem Abstand. Dies ist eine Folge der fortdauernden Schwingungen der Elektronen im ponderomotorischen Potenzial, die zu einem periodischen Wechsel von Verstärkung und Abschwächung des Signalimpulses führen. Die beobachteten Impulsdauern entsprechen den theoretisch vorhergesagten Werten. Numerische Simulationen der Experimente bestätigen die Erklärung. Einzelne Impulse von weniger als 10 fs Dauer könnten erreicht werden, indem kürzere, stärkere Eingangsimpulse mit einem besseren zeitlichen Kontrast benutzt werden.

Die Verstärkung verbesserte die Nah- und Fernfelder des Signalimpulses, was zeigt, dass die höhere Verstärkung im Zentrum zu einer räumlichen Filterung führt.

Contents

1	Introduction: The Quest for Ever Shorter Light Pulses and Higher Intensities	1
2	Superradiant Amplification: Theoretical Background	7
2.1	Laser Plasma Interaction	7
2.1.1	Laser-Electron Interaction	8
2.1.2	The Propagation of Light in a Plasma	9
2.1.3	Collective Effects in a Plasma	9
2.1.4	Stimulated Raman and Brillouin Scattering	10
2.2	Amplification of Laser Pulses in a Plasma	12
2.3	Mechanism of Superradiant Amplification	13
2.3.1	Ponderomotive Potential of the Counter-propagating Laser Pulses	13
2.3.2	A Single Electron in the Ponderomotive Potential	15
2.3.3	Threshold Condition for SRA	15
2.3.4	Electron Trapping, Oscillation and Bunching	16
2.3.5	Signal Shortening and Optimal Frequency Detuning	20
2.3.6	Amplification by Coherent Emission from Bunched Electrons	20
2.3.7	Remark on the Carrier Envelope Stability	22
2.3.8	Scaling Laws for Intensity, Duration, and Energy	23
2.3.9	Analogy to Free-Electron Lasers	24
2.4	Numerical Particle-In-Cell Simulations	27
2.4.1	Particle-In-Cell codes	27
2.4.2	Numerical Study of SRA	28
2.5	Raman Amplification versus SRA	30
2.5.1	Amplification by Stimulated Raman Backward Scattering	30
2.5.2	Raman Amplification in the Pump Depletion Regime	31
2.5.3	Distinction between SRA and Raman Amplification	32
2.6	Detection of SRA	34
3	Experiment	37
3.1	Implementation	37
3.2	The ATLAS System	39
3.3	Generation of the Input Signal Pulse	41
3.3.1	Non-Collinear Optical Parametric Amplification of a Whitelight Spectrum	42
3.3.2	One Common Oscillator with a Broad Spectrum	45
3.3.3	Two-Color-Oscillator	45
3.3.4	Electronically Coupled Oscillators	46

3.4	Signal-Pulse Generation with the Hollow-Fiber Technique	47
3.4.1	Self-Phase Modulation (SPM) at High Intensities	47
3.4.2	Pulse Propagation as Fiber Mode	49
3.4.3	Spectral Broadening by SPM in the Gas-Filled Hollow Fiber	51
3.5	Implementation of the Short-Pulse Generation	53
3.5.1	Setup	53
3.5.2	The Resulting Short Input Signal Pulse	56
3.5.3	Red-Shifting of the Central Wavelength by Filtering	57
3.6	Setup and Alignment of the Amplification Experiment	60
3.6.1	Target Chamber	60
3.6.2	Precise Alignment of the Focusing Parabolas	63
3.6.3	Diagnostics to Assure the Spatio-Temporal Overlap	63
3.6.4	The Single-Shot Autocorrelator	65
4	Results with an Unshifted Signal Pulse and Discussion	69
4.1	Energy Amplification	69
4.2	Analysis of the Spectra	71
4.3	Autocorrelation and Streak Measurements	72
4.4	Density Dependence of the Amplification	73
4.5	Further Detailed Analysis of the Amplified Spectra	74
4.5.1	Chirped Input Pulses	74
4.5.2	Dependence of the Amplified Spectrum on the Delay	75
4.5.3	Dependence of the Amplified Spectrum on the Backing Pressure	75
4.6	Stimulated Brillouin Scattering for Longer Pump Pulses	78
5	Observation of SRA for a Red-Shifted Signal Input Pulse	81
5.1	Improvements of the Experimental Setup	81
5.2	Energy Amplification to the mJ Level	82
5.3	Spectral Broadening of the Amplified Pulse	84
5.4	Autocorrelation Measurement	86
5.4.1	Origin of the Pulse Breakup	87
5.4.2	Numerical Simulation of the Pulse Breakup in the SRA Regime	89
5.5	SRA at Different Densities	90
5.5.1	Autocorrelation Measurements	90
5.5.2	Energy Dependence on Density	93
5.6	Spatial Profiles of the Amplified Pulse	95
5.6.1	Near- and Far-Field Patterns	95
5.6.2	Using Near-Field Profiles as Overlap Diagnostics	96
6	Summary, Conclusions, and Outlook	99
6.1	Summary of the Present Measurements	99
6.2	Future Studies of SRA	100
6.3	Outlook: Amplification of Divergent Beams	100

A	Density Calibration	105
A.1	Measurement Techniques	105
A.2	Calibration Measurements	106
B	Propagation of the Pump Pulse through the Plasma	109
B.1	Nonlinear Plasma Phenomena Affecting the Pump Pulse	109
B.2	Pre-experiment to Check Pump Pulse Propagation	110
C	Analytic Solution of the Amplification in Divergent Beams	113
D	Publications	117
	Bibliography	129
	Danksagung	141

1 Introduction: The Quest for Ever Shorter Light Pulses and Higher Intensities

Laser, firstly demonstrated in 1960 [2], have increased the power and intensity of light beams dramatically due to their significantly improved spatio-temporal coherence. They opened up new fields in science and technology, like non-linear optics [3], high-precision metrology [4], high-resolution spectroscopy [4], manipulation of atoms and molecules [4] including laser cooling, quantum computing and coherent control [5]. They also found their way into more traditional areas such as in material processing and medicine improving and replacing there conventional methods as well as leading to completely new processes and treatments.

The peak powers of pulsed laser systems rose quickly in the 1960s with the invention of Q-switching [6] and mode-locking [7] allowing to concentrate the energy into ever shorter pulses (Fig. 1.1). The resulting higher peak intensities were used to investigate nonlinear ionization processes in strong electric fields [8, 9, 10, 11], create laser-produced plasma, including the research on inertial confinement fusion [12], and building new light sources such as X-ray lasers [13].

From the late 1960s on, the laser peak powers stagnated for almost 20 years, because it was not possible to amplify pulses shorter than a few hundred picoseconds to the Terawatt power level without causing damage to the optical components. Phase shifts originating from the the intensity dependent refractive index of the optics and varying over the laser profile were identified as the limiting phenomena. Subsequent small-scale self-focusing lead to the loss of the focusing quality and when too severe, to damage in the laser system. The invention of chirped pulse amplification (CPA) in 1985 [16] solved this problem making the amplification of femtosecond pulses possible. The pulses are stretched before the amplification by a factor $10^3 - 10^4$ by adding a linear chirp thus increasing the duration to several hundred ps as before. At low powers, the pulses are amplified to high energies and finally recompressed by a system of opposite dispersion removing the chirp. This technique lead to a rapid increase in the pulse powers up to the the petawatt level in 1996 [17, 18]. Furthermore, compact terawatt systems became available also to small institutes and universities such as the ATLAS system at the MPI für Quantenoptik [19].

New fields of physics became accessible [17, 20], in particular the relativistic plasma physics. When the electrons oscillate in the laser field with a velocity close to the speed of light, their effective mass increases and the ponderomotive force becomes huge, too. Non-linear effects appear like self-focusing of laser beams [21] leading to enormous current in excess of 100 kA and magnetic fields of 100 kT. Particles are effectively accelerated by the electrostatic wake fields reaching TV/m behind the laser pulse [22, 23, 24, 25]. As a consequence also ions are accelerated [26]. States of matter are produced as they exist inside the sun [27] and new X-ray laser schemes were implemented [28]. Other applications not only need the high laser intensities but also depend on shortest pulse durations [29], in particular high-harmonic generation

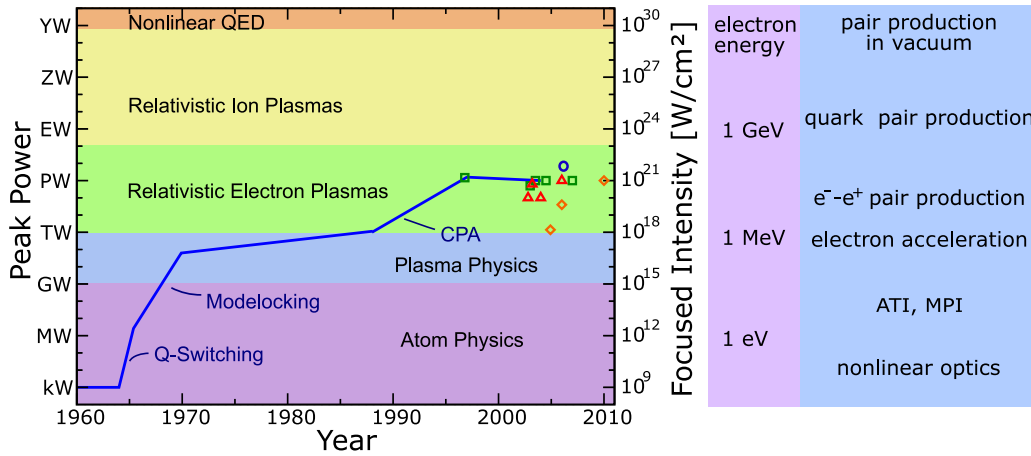


Figure 1.1: Evolution of the peak power of pulsed laser and the focused intensities and physical regimes that become accessible. The intensities are given for a focal spot size of $100 \mu\text{m}^2$ corresponding to a diameter of about $11 \mu\text{m}$. Nowadays Ti:sapphire laser pulses can be focused to $10 \mu\text{m}^2$, yielding ten times higher intensities. The symbols represent a selection of high power laser systems already commissioned or planned: Nd:glass based systems (green squares) with pulse durations of 350 - 600 fs; Ti:Sapphire based systems with pulse durations of 25 - 40 fs (red triangles); planned sub-10 fs systems based on optical parametric CPA (orange diamonds) [14]. Recently, an intensity of $10^{22} \text{W}/\text{cm}^2$ has been reported for the first time (blue circle), which was achieved by tighter focusing of a Ti:Sapphire laser pulse [15]. The right plot gives the kinetic energy of the electrons in the laser fields and the observed and expected physical phenomena at the corresponding intensities.

[30], which is the base of attosecond pulse generation [31, 32, 33].

For even higher intensities, the average kinetic energy of the electrons in the laser field is sufficient to create pairs of e^+e^- and later mesons when the electrons collide with the ions. Completely new types of plasmas can be generated and studied in laboratories. Finally at intensities above $10^{29} \text{W}/\text{cm}^2$, quantum electrodynamics predicts the polarization of the vacuum leading to e^+e^- pair production in vacuum [34, 35]. There are already theoretical proposals how to achieve these enormous intensities [36, 37].

Hence numerous applications are waiting for laser pulses much more powerful than those available today. However, the peak powers stagnate again since they have reached the PW-level. Efforts to surpass this barrier with current laser technology face two serious problems: (a) The optical components are large and expensive. The gratings needed for the recompression measure about 1m^2 and have almost reached the manufacturing limits. To solve this problem, one ambitious approach assembles several gratings to a larger array [38, 39]. (b) So far the amplification of the most powerful laser pulses is based on induced emission. The laser materials either allow for largest pulse powers and low repetition rate (Nd:glass) or shortest durations at higher repetition rate (Ti:Sapphire). New materials are needed that combine these features and allow for shorter pulses and higher energies at high repetition rate.

An alternative to the amplification in laser crystals is non-collinear optical parametric amplification in nonlinear crystals. Combined with CPA, this technique is denoted OPCPA [40]. Longer pulses around 100 fs could already be amplified to more than 100 TW using a Nd:glass laser as a pump. More interesting is the amplification of short pulses, where bandwidths ex-

ceeding 200 nm allow for sub-10-fs pulses [41, 42]. Originally limited to μJ , the mJ-level has been reached recently [43] and plans for even larger systems exist [14]. Such pulses cannot be compressed by gratings, because their reflectivity is not sufficiently flat over the broad pulse spectrum. New compression schemes have still to be developed.

It is yet open, whether OPCPA or conventional CPA is more favorable for the generation of ultra-powerful light pulses. Both techniques face serious challenges, in particular the compression becomes more and more difficult. This raises again the question, whether amplification of ultra-short powerful pulses is possible without stretching and recompression.

In 1998 G. Shvets has published a theoretical work [44], in which he proposed a plasma based amplifier solving the above problems. It is not only able to directly amplify such pulses the high powers but has even more an intrinsic mechanism to shorten their duration further. Although not yet used, a plasma is a natural choice as an amplifier medium for ultra-high pulse powers, because it can sustain almost arbitrarily high electric field strengths without suffering from damage. Furthermore, the considered light pulses are such short that crucial non-linearities set in only in the relativistic regime. For pulses in the visible, this allows for intensities on the order of 10^{18} W/cm^2 and durations of 5 fs resulting in a tremendous fluence of several kJ/cm^2 . Such pulses can carry powers of up to 10 PW on a cross section of merely 1 mm^2 , much smaller than in conventional amplifiers. Furthermore, the intrinsic pulse shortening is a major advantage compared to CPA lasers, where pulse duration usually increases due to gain narrowing during the amplification and imperfect compression.

The scheme is depicted in Fig. 1.2. The short input signal pulse is amplified in a plasma by a counter-propagating long pump pulse of several ps duration. The energy transfer from the pump to the signal pulse is mediated by the plasma electrons. The ponderomotive forces of the interfering laser pulses arrange them to a density grating reflecting a fraction of the pump coherently into the signal pulse, similar to Bragg reflection. Due to the transient nature of the grating, the reflection stops after a short time leading to a further pulse shortening.

Shortly after SRA, a second plasma amplifier was proposed by Malkin [45]. It is similar to SRA but works at lower pump and signal intensities and higher plasma densities, where collective plasma oscillations excited by the ponderomotive forces dominate the electron dynamics. This so called backward Raman amplifier also exhibits pulse shortening if the pump pulse is completely backscattered. The scheme is described in greater detail in section 2.5.

The advantages of plasma based amplifiers are apparent. There is no need for stretching and recompression apart from the laser system delivering the long pump pulses. The pulse shortening mechanism allows rather long input pulses, which are easier to generate. The amplifier is very compact: Plasma lengths of a few mm for SRA and several cm for Raman amplification are sufficient to achieve a gain of 1000.

On the other hand, SRA and Raman amplification are still unknown techniques, proposed only theoretically. Furthermore, it is uncertain how plasma instabilities may affect the amplification and the pulse propagation. Therefore, first studies have to aim at proof-of-principle experiments. Most groups working in this field opted for Raman amplification, because the required intensities are lower and easier to achieve and the scheme is more familiar from the already known Raman instability in plasmas.

The goal of this work was the first experimental demonstration of SRA. We chose to study SRA, because larger knowledge was available from a previous theoretical work [46]. Second, SRA produces shorter pulses than Raman amplification. This allows to head for pulses that

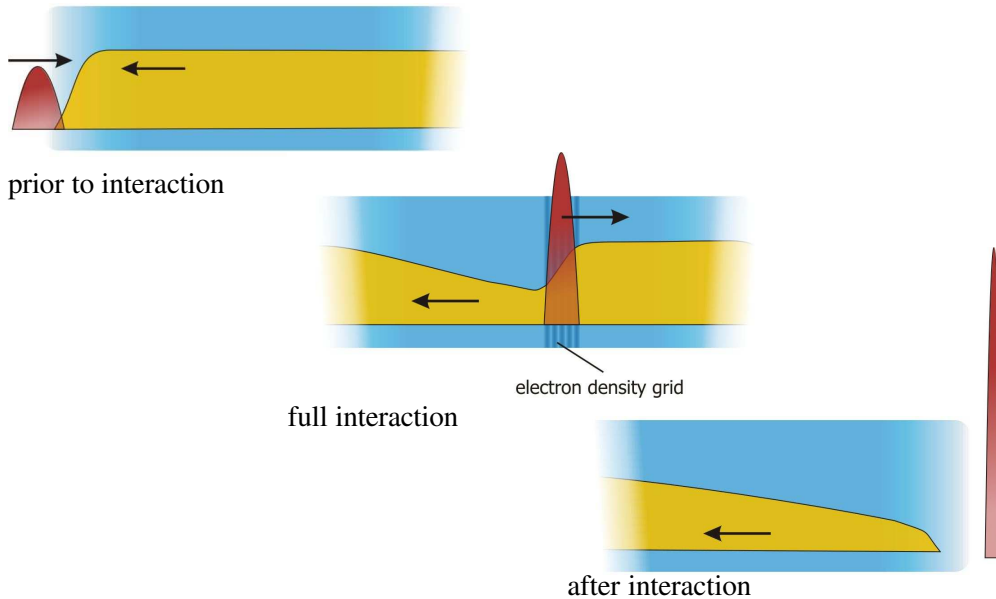


Figure 1.2: Superradiant amplification in a plasma: The short signal pulse of 20 - 40 fs (red) and the ps-long, counter-propagating pump pulse (yellow) meet at intensities of 10^{15} - 10^{16} W/cm². The common ponderomotive forces of the laser pulses arrange the plasma electrons to form a transient density grating (see lower left corner), which reflects a part of the pump pulse similar to Bragg reflection. The fast decay of the density grating ceases the reflection of the pump pulse leading to a further shortening of the signal pulse. While the signal is being amplified, the process becomes more efficient and the pump is depleted even stronger. Finally, the amplified signal pulse reaches intensities of 10^{18} W/cm² and a duration of 7 fs for a pump wavelength of 800 nm.

cannot be created by lasers based on stimulated emission.

Two approaches to SRA were tried. First, the original scheme was modified by using pump and signal pulses at the same frequency. Numerical simulations have shown, that SRA is possible after a second signal pulse has been launched at the correct frequency. This scheme is easiest to implement, because the same laser source can be used for the pump and signal pulses without the need to shift one of the pulses in wavelength. SRA was not clearly visible in this scheme. The second approach uses the original scheme with detuned input pulses. The experiments showed an unequivocal footprint of SRA directly related to the dynamics of the electrons trapped in the light field.

Outline

The thesis is divided into four major chapters and an outlook. The appendix covers further technical aspects.

Chapter 2 introduces the theoretical background to SRA, Raman amplification, and the differences between the two schemes. It lays the foundation to the interpretation of the experimental results in the chapters 4 and 5. The Particle-in-Cell computer code used to illustrate the theory and interpret the experimental results is described briefly.

Chapter 3 first considers the fundamental requirements to be met when implementing of an SRA experiment. The following sections describe the ATLAS system delivering the pump

pulses, the various attempts for the signal pulse generation, and the actual implementation. Finally, the setup inside and outside the target chamber and the diagnostics are presented.

The results of the early amplification experiments using pump and signal pulses at the same wavelength are covered in chapter 4 ending with the impediments by stimulated Brillouin scattering. Chapter 5 reports on the first unambiguous observations of SRA after returning to the original scheme using a red-shifted signal pulse. They include combined measurements of energy, spectrum and pulse duration. The last section presents the near- and far-field patterns of the input and amplified signal pulses.

The outlook extends the one-dimensional SRA scheme considered so far to diverging signal pulses that spread the energy over an increasing area and thus admit to higher powers. An analytic solution is derived for this scenario starting from a simplified model.

The appendix deals with the calibration measurements of the plasma electron density, the propagation of the pump pulse through the plasma and the derivation of the relations referred to in the outlook.

2 Superradiant Amplification: Theoretical Background

This chapter introduces to the theory of SRA. It starts with basic facts about laser plasma interaction necessary for the description of SRA in section 2.3 and for the similar process of Raman amplification in section 2.5. Numerical simulations illustrate and extend the SRA theory in section 2.4. Finally, section 2.6 summarizes characteristic footprints of SRA, which allow to verify the observation of SRA in an experiment.

2.1 Laser Plasma Interaction

The theoretical treatment of the laser plasma interaction [47] describes the distribution and evolution of the electric and magnetic fields and the particles in the plasma. The electric and magnetic fields are obtained from Maxwell's equations. They comprise both the fields of the laser radiation and those originating from charges and currents in the plasma.

The plasma constituents, electrons and ions, are usually described with a fluid or kinetic model, depending on the state of the plasma. The fluid description considers the electrons and ions as separate, charged gases. They have Maxwellian velocity distributions with a defined temperature and average velocity obtained as ensemble averages over small plasma volumes. The fluids are compressible but adjacent plasma volumes do not penetrate each other. They interact only by the thermal pressure and the electromagnetic forces. The fluid model is well suited for plasmas in thermodynamic equilibrium. It is used to describe collective effects in the plasma as outlined in the sections 2.1.3 and 2.1.4.

The advent of ultra-strong and fs-laser pulses allowed to create plasmas strongly out of the thermodynamic equilibrium. In particular, subpopulations of the plasma electrons often achieve relativistic velocities. Furthermore, single particle effects can appear that cannot be treated in the fluid model.

The kinetic theory can handle these non-equilibrium plasmas, because it tracks the distributions functions $f_i(\mathbf{r}, \mathbf{v}, t)$ of the complete phase space of all species i . The evolution of the distribution functions is given by a set of hierarchically structured equations that involve interactions, i.e. collisions, of an increasing number of particles. In the simplest case, the many particle interactions are neglected and the particles interact only via their averaged, collective fields. This case is described by Vlasov's equation.

Finally, it is instructive or in some cases even indispensable to follow the dynamics of the individual particles. This approach is taken in the description of SRA, where the motion of the particles is dominated by the laser radiation. Effective charge distributions and currents are given by the ensemble average over many electrons.

The equations for the fields and particles are coupled on the one hand by the Lorentz force $q_i(\mathbf{E} + \mathbf{v} \times \mathbf{B})$ that enters the momentum equation of the particles and on the other hand by

the charge density and current distributions in the plasma that represent the source terms in Maxwell's equations.

Because of their large mass, the plasma ions hardly move on the fs-time scale set by the laser pulse. The theoretical treatment usually disregards their motion on timescales much smaller 1 ps. This holds true as long as the laser intensities are less than 10^{23} W/cm², where the ions reach relativistic velocities in the laser field.

2.1.1 Laser-Electron Interaction

The optical laser field not only causes the electrons in a plasma to oscillate rapidly but also exerts a secular force on them. The dynamics can be studied in the idealized case of a single electron in the laser field. The field is characterized by its vector potential $\mathbf{A} = \hat{\mathbf{A}}(\mathbf{r} - \mathbf{v}_{\text{gr}}t) \cos(\mathbf{k} \cdot \mathbf{r} - \omega t)$. Here, \mathbf{k} is the wave vector and ω the frequency of the laser radiation and v_{gr} the group velocity of the envelope. The electron is driven by the Lorentz force of the light wave

$$\frac{d\mathbf{p}}{dt} = -e(\mathbf{E} + \mathbf{v} \times \mathbf{B}). \quad (2.1)$$

The electric and magnetic fields are expressed by the vector potential, $\mathbf{E} = -\partial\mathbf{A}/\partial t$ and $\mathbf{B} = \nabla \times \mathbf{A}$. The electron motion is dominated by the quiver oscillation in the transverse electric field. Neglecting the effect of the magnetic field and relativistic corrections, it is given by

$$\mathbf{p} = e\mathbf{A} \quad \longrightarrow \quad \mathbf{v} = \frac{e}{m_e}\mathbf{A} = \mathbf{a}c, \quad (2.2)$$

where c is the speed of light. The normalized vector potential $\mathbf{a} = e\mathbf{A}/m_e c$ is a convenient quantity to distinguish between different regimes of laser plasma interaction. SRA and the competing plasma effects take place in the non-relativistic regime, $|\mathbf{a}| \ll 1$. Relativistic effects are not important in this work; they are disregarded. The dynamics becomes relativistic for $|\mathbf{a}| \approx 1$, where the quiver velocity of the electron is already close to c . For $|\mathbf{a}| \gg 1$ the dynamics is called ultra-relativistic.

In Eq. (2.2), additional higher-order terms in the amplitude \mathbf{a} , are neglected. They cause harmonics at $2\omega, 3\omega, \dots$. Averaging Eq. (2.1) over the short time scale of the laser oscillation yields the equation of the secular motion of the electron,

$$\left\langle \frac{d\mathbf{p}}{dt} \right\rangle_{\text{av}: 2\pi/\omega} = -\frac{1}{4}m_e c^2 \nabla \hat{\mathbf{a}}^2. \quad (2.3)$$

The secular force acting on the electron is due to the $\mathbf{v} \times \mathbf{B}$ term and is called *ponderomotive force* [47, 48, 49]. It is given by the gradient of the slowly varying amplitude of the radiation field and expels the electrons from regions of high electromagnetic energy density. Since the force is proportional to a gradient, a potential can be assigned,

$$\phi_{\text{pond}} = \frac{1}{4}m_e c^2 \hat{\mathbf{a}}^2, \quad (2.4)$$

called the *ponderomotive potential*. The ponderomotive force is paramount for SRA, because it exceeds the other forces and dominates the electron dynamics.

2.1.2 The Propagation of Light in a Plasma

The electrons quivering in a plasma represent accelerated charges and hence radiate at the laser frequency shifted in phase with respect to the laser radiation field. This leads to the dispersion relation of electromagnetic waves of frequency ω and the wave number k in a plasma

$$\omega^2(k) = \omega_{pe}^2 + c^2k^2. \quad (2.5)$$

Here, $\omega_{pe} = \sqrt{n_e e^2 / (\epsilon_0 m_e)}$ is the *electron plasma frequency*, which is explained in the following section. The dispersion relation implies that an electromagnetic wave with a frequency lower than ω_{pe} cannot propagate in a plasma but is reflected at the surface. Seen from a different point of view, a wave of frequency ω_0 can only propagate if the electron density is smaller than the so called *critical density*

$$n_{\text{crit}} = \frac{\epsilon_0 m_e \omega_0^2}{e^2}. \quad (2.6)$$

Plasmas with a lower density are called underdense. Since many plasma effects scale with the laser frequency, it is often useful to give the electron density as a fraction of the critical density. The index of refraction of a plasma is derived from Eq. (2.5)

$$n_{\text{refr. ind.}} = \frac{v_{\text{ph}}}{c} = \frac{\omega}{kc} = \sqrt{1 - \frac{\omega_{pe}^2}{\omega^2}} = \sqrt{1 - \frac{n_e}{n_{\text{crit}}}} \approx 1 - \frac{n_e}{2n_{\text{crit}}}. \quad (2.7)$$

The last approximation holds for thin plasmas, $n_e \ll n_{\text{crit}}$.

2.1.3 Collective Effects in a Plasma

In the simplest description of a plasma, collision between the particles are neglected. Instead, the particles interact only via averaged electrostatic fields caused by charge inhomogeneities and the magnetic fields generated by plasma currents. They give rise to different kinds of oscillations. Two types are relevant for the present work: the electron plasma waves (Langmuir waves) and the ion sound waves.

Electron plasma waves (Langmuir waves)

Langmuir waves are electron density waves. They are the fastest collective phenomenon in a plasma. For densities used in the present experiments, their oscillation period is about 50 – 70 fs. Since the ions are much heavier than the electrons, they are considered as immobile. They form a homogeneous, positively charged background distribution. The restoring force of the oscillation is given by the electrostatic fields trying to balance the charge distribution. The energy oscillates forth and back between the kinetic energy of the electrons and the potential energy of the electrostatic field. The oscillation frequency is called *Langmuir frequency* or *electron plasma frequency* [50],

$$\omega_{pe}^2 = \frac{n_e e^2}{\epsilon_0 m_e}. \quad (2.8)$$

In the fluid model, the plasma frequency is derived from the conservation equations of mass and momentum and Poisson's equation. Including corrections due to the electron pressure at

the temperature T_e assuming adiabaticity, the dispersion relation of the electron plasma wave read [50]

$$\omega_p^2(k) = \omega_{pe}^2 + \frac{3k_B T_e}{m_e} k^2, \quad (2.9)$$

called *Bohm-Gross relation*. Here, $k_B = 1.38 \times 10^{-23}$ J/K denotes Boltzmann's constant. However, for the present SRA experiments, the temperatures are small and the correction can be neglected.

Ion acoustic waves

The ions make up almost the whole mass of the plasma. Therefore, an ion density wave is actually an acoustic wave. In a plasma this wave is not only driven by the ion pressure, but also by the electron pressure. The electrons follow the ions, except for a small deviation caused by their thermal pressure. The slight charge separation increases the restoring force. The resulting dispersion relation of the ion waves is [50]

$$\frac{\omega}{k} = \left(\frac{Zk_B T_e + \gamma_i k_B T_i}{m_i} \right)^{1/2} \equiv c_s, \quad (2.10)$$

where c_s is the sound velocity, T_i the temperature of the ion component, m_i the ion mass, Z the charge state, and $\gamma_i = 5/3$ the adiabatic coefficient of the ions. The adiabatic coefficient for the electrons is 1 corresponding to an isothermal compression. The electrons thermalize, because the collisions between them are more frequent than for the ions. The ion contribution to the restoring force, $\gamma_i k_B T_i$ can be neglected for plasmas created by fs-laser pulses because of $T_e \gg T_i$. The laser pulses predominantly heat the plasma electrons and the time required for the thermalization of electrons and ions is much longer than the time-scale, on which the effects occur that are studied here.

2.1.4 Stimulated Raman and Brillouin Scattering

There are four major instabilities and scattering processes that occur in laser-plasma interaction. They are dealt with in textbooks [50, 47, 51] and are treated only briefly, here. They are three-wave parametric processes that can be driven resonantly. Two of them are not relevant for SRA: the decay of the electromagnetic wave into (1) two electron plasma waves and (2) an electron and an ion plasma wave. They can only occur for higher electron densities, $n_e = n_{\text{crit}}/4$, and $n_e \approx n_{\text{crit}}$, respectively.

The other two instabilities can also occur for low plasma densities. Here, the electromagnetic wave decays into a plasma wave and a second electromagnetic wave. If an electron plasma wave is excited the process is called Raman scattering. In case of an ion plasma wave it is called Brillouin Scattering. As parametric processes, the secondary waves obey a resonance condition. They are amplified exponentially in the small signal regime. The two electromagnetic waves drive the plasma wave further by their common ponderomotive force. For Brillouin scattering the force is mediated to the ions by the electrons. The electron density gets modulated, thereby setting up an electrostatic field driving the ions. On the other hand, the plasma waves represent phase gratings scattering the irradiated laser wave into the second electromagnetic wave.

	resonance conditions		growth rate
Stimulated Brillouin (backward) scattering (SBS)	$\omega_0 = \omega_1 + \omega_{pi}$	$k = 2k_0 \left(1 - \frac{c_s}{c}\right) \approx 2k_0$	$\gamma = \frac{1}{2\sqrt{2}} \sqrt{\frac{c}{c_s}} \omega_{pi} a_0$
Stimulated Raman forward scattering (SRFS)	$\omega_0 = \omega_1 + \omega_{pe}$	$k = \frac{\omega_{pe}}{c}$	$\gamma \approx \frac{1}{2\sqrt{2}} \frac{\omega_{pe}^2}{\omega_0} a_0$
Stimulated Raman backward scattering (SRBS)	$\omega_0 = \omega_1 + \omega_{pe}$	$k = 2k_0 \left(1 - \sqrt{\frac{2\omega_{pe}}{\omega_0}}\right)$	$\gamma \approx \frac{1}{2} \sqrt{\omega_{pe}\omega_0} a_0$

Table 2.1: Resonance conditions, wave number of the plasma wave and growth rates for Brillouin backward and Raman forward and backward scattering taken from *Kruer* [47]. ω_0 , k_0 , and a_0 are the frequency, the wavenumber, and normalized vector potential of the irradiated electromagnetic wave; ω_1 is the frequency of the amplified light wave; ω_{pi} and ω_{pe} denote the electron and ion plasma frequencies, respectively, k is the wave number of the plasma wave; c_s is the sound velocity in the plasma. The Raman growth rates are approximated for $\omega_0 \gg \omega_{pe} \gg \gamma$, and a low electron temperature such that the temperature term in the dispersion relation of the electron plasma wave can be neglected.

Table 2.1 lists the growth rates and the resonance conditions for Raman and Brillouin scattering derived in *Kruer* [47]. It is assumed that the irradiated electromagnetic wave is much stronger than the scattered wave. For Brillouin scattering, the dispersion relations of the sound and electromagnetic waves in a plasma only allow backward scattering. For Raman scattering, both electromagnetic waves can propagate into the same direction, which is called *forward scattering* (SRFS), or into opposite directions called *backward scattering* (SRBS). Finally, for Raman side scattering the incoming electromagnetic wave is scattered sideways. Although the growth rate lies between that of SRFS and SRBS, it is of little importance here, because the scattered light immediately leaves the region of the incoming focused laser pulse and is lost for the parametric process. It comes into play only for much higher intensities than those used in this work. Anti-Stokes processes, where the plasma waves is already present initially, are also not considered here.

Raman and Brillouin instabilities can cause significant losses to laser pulses traveling through a plasma. However, the backscattering processes are uncritical if the pulses are shorter than the time that the instability needs to grow from noise to a substantial level. Since the electrons are more mobile than the heavier ions, Raman scattering occurs on a faster time scale than Brillouin scattering. For typical plasmas considered in this work, pulses shorter than 10 ps are not affected by SBS. For SRBS, the critical durations are a few 100 fs.

The growth rate for Raman forward scattering is by $(\omega_{pe}/\omega_0)^{3/2}/\sqrt{2}$ smaller than that of Raman backward scattering. Since the secondary light wave travels along with the primary wave in the same direction, it has more time to resonantly grow and excite the plasma wave. Hence Raman forward scattering not only depends on the length of the laser pulse but also on the propagation length in the plasma. However in the present experiments, Raman forward scattering was not found to be crucial.

2.2 Amplification of Laser Pulses in a Plasma

Plasma as an amplifier medium has the advantage that it can sustain arbitrarily high intensities. Conventional high power laser systems often suffer from damages due to the high-field strengths and specific measures are necessary to avoid them, like stretching of the laser pulse in time and increasing its diameter.

Unlike conventional laser amplifiers, a plasma amplifier medium for optical pulses does not store the energy during a pump process to release it later by induced emission when the laser pulse passes the medium. Instead the energy is transferred directly from a pump laser pulse to a signal pulse mediated by the electrons, similar to optical parametric amplification in a nonlinear crystal.

Since a homogeneous electron distribution does not scatter the pump laser, the electron density must be modulated by some ordering process. In the case of backscattering, the density is modulated by a period of about half the laser wavelength to scatter the pump pulse coherently. According to Eq. (2.7), the index of refraction exhibits the same modulation, which is equivalent to a phase grating leading to the Bragg reflection of the pump laser pulse back into the signal pulse [52].

The microscopic picture allows a different view on the mechanism. A single electron emits a dipole wave while it is oscillating in the radiation field of the laser pulse. This process is called *Thomson scattering* [53, 54]. For a homogeneous electron distribution, the radiation resulting from all dipoles is incoherent except for the propagation in the direction of the laser pulse. If the electron density is modulated with a period of about half the laser wavelength, the dipole emission due to the single electrons superimposes coherently in the backward directions, while the radiation in lateral directions is still incoherent.

Three plasma processes can cause such a periodic electron density grating able to backscatter the pump pulse. The density modulation is always imprinted by the common ponderomotive force of the counter-propagating pulses. However, they differ in the response of the plasma.

1. *SRA*: If the ponderomotive force is stronger than the electrostatic force in the plasma, the bunching of the electrons is due to the dynamics of the independent electrons in the ponderomotive potential. This mechanism is discussed in detail in the following sections.
2. *SRBS*: If the ponderomotive force is smaller, collective plasma oscillations govern the electron dynamics. If the resonance condition for SRBS is satisfied, a plasma wave is excited, which backscatters the pump pulse. This scheme is also called (backward) Raman amplification and is treated in section 2.5 because of its seemingly similarity to SRA and its relevance for the presented experiments.
3. *SBS*: If the laser pulses satisfies the resonance condition for SBS, an ion acoustic wave is excited from which the pump pulse is backscattered.

The last scheme can be distinguished very well from the other two. Since the ions are involved, the frequency detuning between the light waves is only very small and the typical time scales are on the ps-level. It is therefore not appropriate for the amplification of fs-laser pulses and disregarded.

The parameter regimes of SRA and Raman amplification are adjoining making the smooth transition from the Raman to the SRA regime possible. Therefore, it is essential for this work to identify the features by means of which the two processes can be separated from each other.

2.3 Mechanism of Superradiant Amplification

SRA is an amplification regime prevailing at high pump and signal intensities. If the ponderomotive forces of the light waves become stronger than the electrostatic forces in the plasma, the collective plasma wave disintegrates and the dynamics of the electrons is that of individual particles interacting with the radiation field. The initial conditions of the electrons and their dynamics arranges them to a density grating, which finally reflects a portion of the pump pulse into the signal pulse.

The following section starts by specifying the ponderomotive potential created by the interference of the counter-propagating laser pulses. A threshold for the laser intensities is found, where the ponderomotive force exceeds the electrostatic force so that the single electron approximation becomes valid. The dynamics of the electrons in the ponderomotive potential is analyzed leading to the bunching of the electrons and establishing a density grating. Its dynamics also causes the shortening of the amplified signal pulse. Analytic formulas for the intensity and energy amplification as well as the duration of the signal pulse are derived. Finally, the last section enlightens the origins of SRA in free-electron laser.

2.3.1 Ponderomotive Potential of the Counter-propagating Laser Pulses

The pump and signal pulses are circularly polarized with opposite helicity. While SRA is also possible for linearly polarized pulses, the circular polarization simplifies the analytic treatment and is in accordance with the experimental situation. However, SRA also works for linearly polarized pulses. The pulses are described by their normalized vector potentials

$$\mathbf{a}_s(z, t) = \frac{1}{\sqrt{2}}(\hat{\mathbf{e}}_x + i\hat{\mathbf{e}}_y)a_s(z, t)e^{i\theta_s} + c.c., \quad (2.11a)$$

$$\mathbf{a}_p(z, t) = -\frac{1}{\sqrt{2}}(\hat{\mathbf{e}}_x + i\hat{\mathbf{e}}_y)a_p(z, t)e^{i\theta_p} + c.c., \quad (2.11b)$$

where $\hat{\mathbf{e}}_{x,y}$ are the unit vectors in the respective directions, $a_{s,p}$ denote the envelopes and $\theta_{s,p}$ the phases of the laser pulses. Here and throughout the rest of this work, the indices p and s refer to the pump and signal pulses, respectively. The only exception are the pump pulse frequency ω_{pu} and the wave vector \mathbf{k}_{pu} to avoid confusion with the corresponding symbols for the plasma wave. The phases of the counter-propagating pulses are $\theta_s = k_s z - \omega_s t$ and $\theta_p = -k_{pu} z - \omega_{pu} t$. The pump wave vector and frequency are slightly larger than those of the signal pulse, $\omega_{pu} \gtrsim \omega_s$, $k_{pu} \gtrsim k_s$. The short signal pulse has a duration of a few laser cycles. The optimal duration will be specified later. Since the pump pulse is much longer, its amplitude is assumed constant for the following considerations.

The pulses given by Eqs. 2.11a are plane waves. The 1D approximation is justified, because the longitudinal length scale given by the interference structure of the pulses, $\approx \lambda/2$, is much smaller than the beam waist, r_\perp . Hence the longitudinal gradients are much larger than the

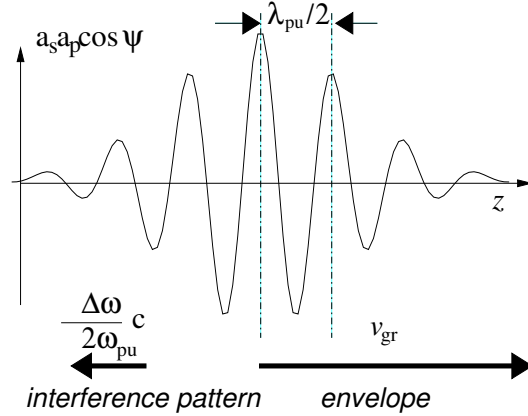


Figure 2.1: Ponderomotive potential of the interference term: The potential has a small phase velocity to the left, whereas the envelope travels with the velocity of the signal pulse to the right.

transverse gradients and the electrons move transversely on a slower time scale than longitudinally. In the experiment, the radius of the beam waist is $r_{\perp} \approx 15 \mu\text{m}$ and $\lambda/2 \approx 0.4 \mu\text{m}$.

The common ponderomotive potential of the pulses according to Eq. (2.4) is

$$\begin{aligned} \frac{\Phi_{\text{pond}}}{m_e c^2} &= \frac{1}{2} \langle (\mathbf{a}_s + \mathbf{a}_p)^2 \rangle = \frac{|a_s|^2}{2} + \frac{|a_p|^2}{2} - \frac{1}{2} (a_s a_p^* e^{i\psi} + c.c.) \\ &= \frac{|a_s|^2}{2} + \frac{|a_p|^2}{2} - a_s a_p \cos \psi, \end{aligned} \quad (2.12)$$

where the phase ψ of the slowly oscillating interference pattern of the two pulses reads

$$\psi(z, t) \equiv \theta_s - \theta_p = (k_s + k_{pu})z + (\omega_{pu} - \omega_s)t = k_I z + \Delta\omega t, \quad (2.13)$$

with $\Delta\omega = \omega_{pu} - \omega_s \ll \omega_{pu}, \omega_s$ and the wave number of the interference $k_I = k_{pu} + k_s \approx 2k_{pu}$. The ponderomotive force in the longitudinal direction according to Eq. (2.12) is mainly given by the interference term, because it has the steepest gradient. The derivative of the pump amplitude vanishes as a_p is almost constant. The remaining terms are approximated by

$$\frac{\partial}{\partial z} \frac{|a_s|^2}{2} \approx \frac{|a_s|^2}{2c\tau_s} \ll \frac{\partial}{\partial z} a_s a_p \cos \psi \approx k_I a_s a_p \sin \psi, \quad (2.14)$$

where τ_s is the duration (FWHM) of the signal pulse. Because of $k_I \gg 1/(2c\tau_s)$, the inequality holds true even if the signal amplitude exceeds the pump amplitude. Therefore, the force due to the interference structure dominates the dynamics of the plasma electrons if the electrostatic forces can be neglected.

Fig. 2.1 depicts this interference pattern. Since a_p is approximately constant, the shape of its envelope is given by the envelope of the amplitude a_s of the signal pulse. It travels to the right almost at the speed of light, $v_{gr} \approx c$. The phase velocity v_{ph} of the interference structure is obtained by solving Eq. (2.13) for the condition $\psi = 0$.

$$v_{ph} = -\frac{\Delta\omega}{k_I} = -\frac{\Delta\omega}{\omega_{pu} + \omega_s} c. \quad (2.15)$$

This means the phase structure under the signal envelope moves *opposite* to this envelope at a rather small velocity. For typical plasma densities, one finds $|v_{ph}|/c \approx 0.02 \dots 0.05$.

2.3.2 A Single Electron in the Ponderomotive Potential

The dynamics of a single electron trapped in a potential well of the interference structure is given by its equation of motion

$$m\ddot{z}_j = F_{\text{pond}} = -a_s a_p k_I m c^2 \sin \psi(z_j, t), \quad (2.16)$$

where z_j is the position of the electron. It is convenient to follow the motion of the electron in the frame of reference of the slowly moving interference structure by choosing the new coordinate $\zeta_j = z_j + v_{ph}t$. Rewritten in this reference frame, Eq. (2.16) reads

$$k_I \ddot{\zeta}_j + \omega_b^2 \sin(k_I \zeta_j) = 0, \quad (2.17)$$

where ω_b is the so-called *bouncing frequency*,

$$\omega_b = \sqrt{a_s a_p} k_I c = \sqrt{a_s a_p} (\omega_s + \omega_{pu}). \quad (2.18)$$

Here, the refractive index was set to 1, which is a valid approximation for thin plasmas. Eq. (2.17) is just the equation of motion of a mechanical pendulum. For small displacements the electron oscillates with the bouncing frequency around the potential minimum. As the force in Eq. (2.17) is non-harmonic, the oscillation frequency decreases for larger amplitudes.

2.3.3 Threshold Condition for SRA

The intensity threshold for the onset SRA is obtained from the condition that the ponderomotive force, F_{pond} , acting on a plasma electron must be larger than the electrostatic force, $F_{\text{stat}} = -eE_{\text{stat}}$. In the following, a simpler and more intuitive approach is chosen to derive an expression for the threshold condition than in the original work by Shvets [44]. The maximum electrostatic force is derived from Poisson's equation while the plasma wave still exists. Its longitudinal component reads

$$\frac{\partial E_{\text{stat}}}{\partial z} = \frac{e}{\epsilon_0} \{Zn_i - [n_{e0} + \delta n_e(z, t)]\}, \quad (2.19)$$

where Z is the charge number and n_i is the density of the ions; $n_{e0} = Zn_i$ is the undisturbed electron density and

$$\delta n_e(z, t) = -\delta \hat{n}_e \cos(k_I z - \Delta \omega t) \quad (2.20)$$

the density modulation. The wave number k_I and the oscillation frequency $\Delta \omega$ are imprinted by the driving ponderomotive force so that the phase of the cosine is just ψ . The negative sign is chosen without loss of generality to shift the minimum of the electrostatic potential to $z = 0$. Integration of Eq. (2.19) yields

$$E_{\text{stat}} = \frac{e \delta \hat{n}_e}{k_I \epsilon_0} \sin \psi = \frac{m_e}{ek_I} \frac{\delta \hat{n}_e}{n_{e0}} \omega_{pe}^2 \sin \psi. \quad (2.21)$$

The maximum amplitude of the plasma wave is limited to $\delta \hat{n}_e/n_{e0} \leq 1/2$ by the onset of wavebreaking [55]. The equation of motion for a test electron in this electrostatic potential reads

$$\ddot{\zeta}_j = \frac{-eE_{\text{stat}}}{m_e} = -\frac{\omega_{pe}^2}{2k_I} \sin(k_I \zeta_j). \quad (2.22)$$

Again the position of the electron ζ_j is given in the frame of reference of the ponderomotive phase structure. A comparison with Eq. (2.17) yields the threshold condition for $F_{\text{pond}} > F_{\text{stat}}$

$$\boxed{\omega_b^2 > \frac{1}{2}\omega_{\text{pe}}^2} \iff a_s a_p > \frac{n_e 0}{8n_{\text{crit}}}. \quad (2.23)$$

This inequality sets a lower limit for the product of the pump and signal amplitudes, for which the ponderomotive force becomes larger than the electrostatic force of the plasma wave. The electrostatic forces are neglected and the electron dynamics is described by the pendulum equation Eq. (2.17). Eq. (2.23) is no hard threshold, but there is a transition around the regime $\omega_b = \omega_{\text{pe}}/\sqrt{2}$, where the dynamics slowly changes from the collective motion of the plasma wave to that of single independent electrons trapped in the ponderomotive potential.

Compared to the criterion derived in [44, 46], $\omega_b > \omega_{\text{pe}}$, Eq. (2.23) sets an even lower threshold. The prior works used $\delta\hat{n}_e/n_e = 1$ for the maximum amplitude of the plasma wave, which is already beyond the wavebreaking limit.¹

2.3.4 Electron Trapping, Oscillation and Bunching

Electron trapping and oscillation

Having confirmed that the dynamics of the plasma electrons is governed by the ponderomotive force of the two laser pulses if the relation (2.23) holds, it is now inspected how an ensemble of independent electrons gets arranged by the oscillation in the ponderomotive potential.

It is important to point out again that the ponderomotive potential depicted in Fig. 2.1 does not arrive as a fixed structure at the position of the electron, because the phase and group velocities differ. The envelope of the arriving signal pulse moves like a window over the slow interference structure and selects a section. In Fig. 2.2a, the trapped electron (1) does not enter the potential well from the side over the crest but it gets trapped when the edges of the potential well rise on both sides with the arrival of the signal pulse.

Before the signal pulse arrives, all electrons are uniformly distributed in space with an initial velocity $\check{\zeta} = v_{\text{ph}}$ with respect to the potential structure. The velocity spread due to the initial temperature is negligible. When the ponderomotive potential builds up, the total energy of the electrons is shifted by the potential energy. There exist two classes of electrons: (1) Those that are trapped in the potential structure; they are closer to the dip of the well and their total energy is smaller than the energy associated with the crests of the potential energy. (2) Electrons that can surmount the crest and pass on to the adjacent well. If the frequency detuning of the laser

¹In the limit of a *highly* nonlinear plasma wave, the amplitude of the electron distribution can be approximated by

$$\delta n_e(z) = \frac{n_e 0}{2} \left\{ 1 + \sum_{m \in \mathbb{Z}} 2\pi \delta \left(k_I z - 2\pi \left(m + \frac{1}{2} \right) \right) \right\},$$

where δ is Dirac's *delta*-function. The electrostatic field obtained by integrating Poisson's equation rises linearly with z to the maximum value $E_{\text{stat}} = (en_e 0 \pi) / (\epsilon_0 4k_I)$, which yields the threshold condition $\omega_b^2 > \frac{\pi}{4} \omega_{\text{pe}}^2$. However, this is an extremely idealized plasma wave. In reality, wavebreaking sets in earlier. Furthermore, the nonlinear plasma wave mainly increases the field near the electron peaks, while Eq. (2.23) is true, where $\sin \psi \approx \psi$ holds. In conclusion, this excursion illustrates the statement above that Eq. (2.23) does not set a strict threshold, but rather defines a transition regime, $\omega_b = 0.7 \dots 0.85 \omega_{\text{pe}}$, where SRA gradually sets in by trapping more and more electrons in the ponderomotive potential.

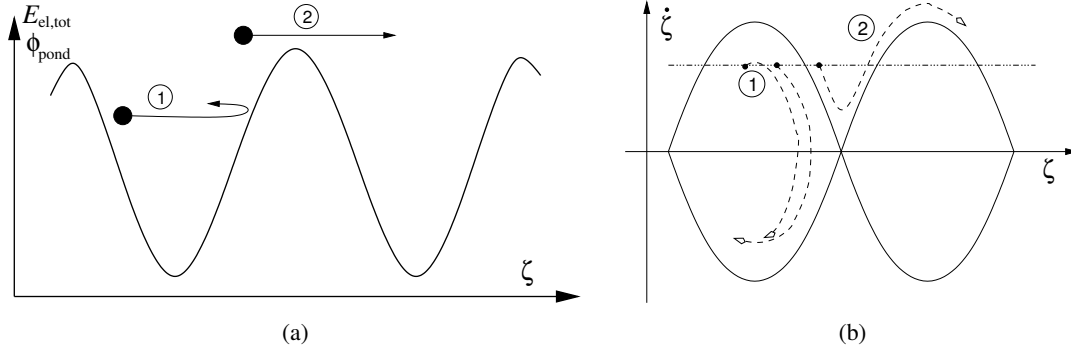


Figure 2.2: (a) Energy diagram showing the total electron energy and the ponderomotive potential; (b) phase space of electrons with the separatrices separating the areas with electrons trapped in the potential from those outside. Electron (1) is trapped and oscillates: it bounces forth and back between the edges of the potential well in (a) and rotates inside the separatrix in (b). Electron (2) is not trapped and can surmount the potential crest; it oscillates along the separatrices in (b).

pulses and hence v_{ph} becomes larger the fraction of the second type increases, because the number of electrons that are inside the separatrices in Fig. 2.2b decreases.

Bunching of an ensemble of electrons by the oscillation

Fig. 2.3 illustrates the bunching of the electrons to thin layers of high density as a consequence of their individual motion in the ponderomotive potential. It consists of a series of snapshots obtained from numerical simulations at the indicated times during one full oscillation cycle, $T_b = 2\pi/\omega_b$. The simulations were performed with the particle-in-cell code described in section 2.4. Each snapshot shows the electron phase space in the upper half with a sample ensemble of electrons indicated as dots. In the lower half, the electron density (blue line) and the ponderomotive potential (red line) of the pump and signal pulse are plotted. For illustration purposes, the signal pulse is chosen semi-infinite.

When the signal pulse arrives, the initially uniformly distributed electrons (a) get trapped in the ponderomotive potential, start oscillating (b) and are bunched in space on a very short distance at $T_b/4$ for the first time (c). The electron density peaks appear on the right edges of the potential wells, where on average they scatter the pump light into the signal pulse. As the electrons continue their oscillation, the electron density grating decays. The bunching of the electrons is basically a consequence of their small velocity at the return points on the edges of the well leaving late electrons time to catch up with the early ones. At time step $T_b/2$, the electrons are again approximately uniformly distributed in space (d), disregarding the regions around the potential maxima, where the electrons are mostly expelled.

At $3/4T_b$ the electrons bunch a second time in space, this time on the opposite edge of the potential well. Here on average, they scatter the signal pulse back into the pump pulse, causing the signal to be attenuated. The peaks in the electron density are nearly as high as during the first bunching. Even the non-trapped electrons close to the separatrices have moved on to the adjacent potential well and almost join the trapped, bunched electrons. The ongoing oscillations of the trapped electrons make the electron density peaks decay again and the elec-

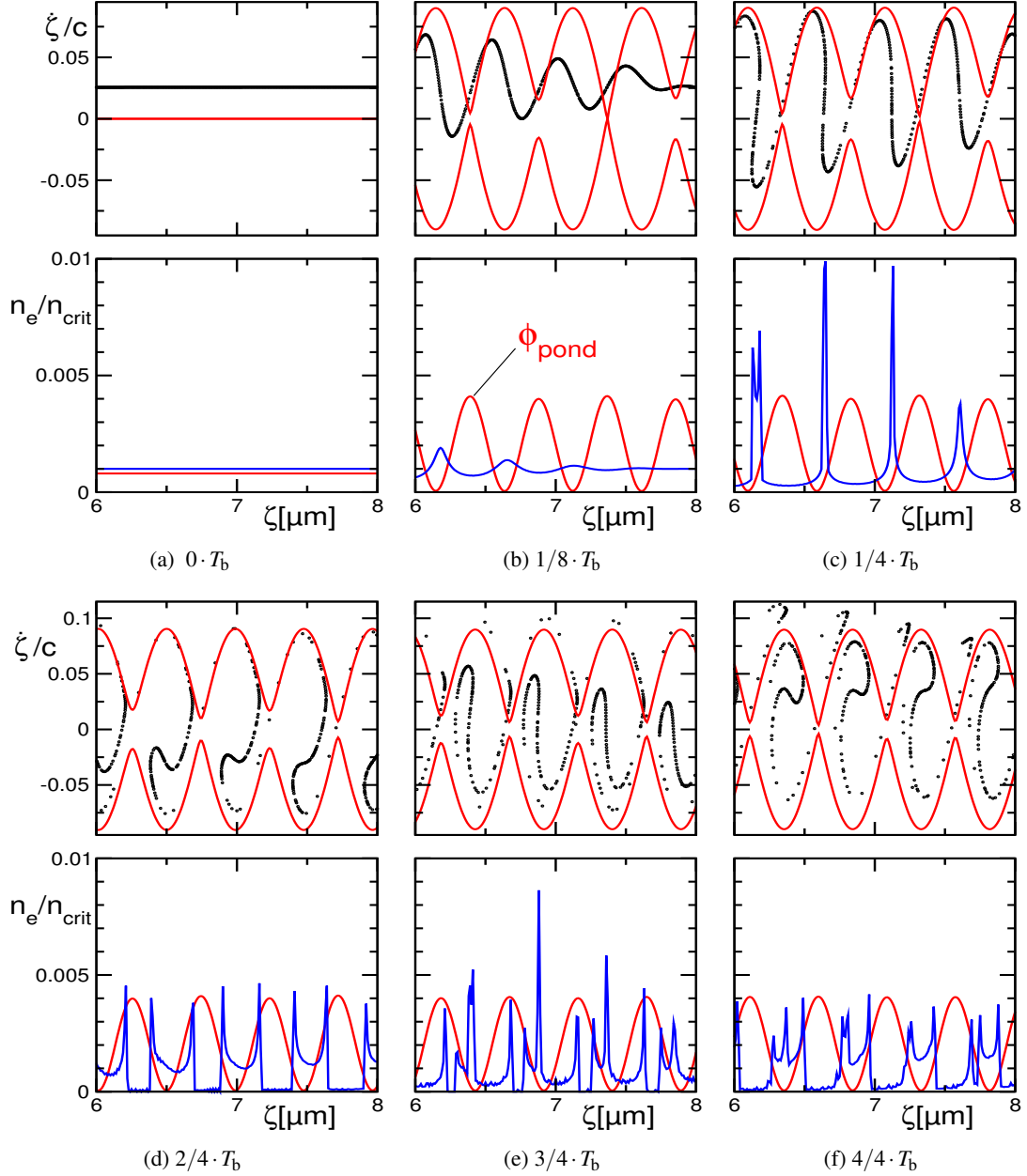


Figure 2.3: PIC simulations illustrating the electron motion. The abscissa is the signal pulse propagation distance in μm in the rest frame of the ponderomotive potential; the signal pulse propagates to the right, the pump pulse to the left (both not shown). The individual frames are snapshots at successive time steps during one oscillation cycle. The upper frames show the electron phase space with the electrons marked as black dots, which appear as a solid line if they are narrowly spaced. The red lines indicate the separatrices set by the ponderomotive potential. Electrons inside the separatrices are trapped and rotate in the phase space. Electrons outside the separatrices are not trapped, they propagate on oscillating curves along the separatrices. (Remark: It is due to the finite numerical resolution of the abscissa that the upper and lower halves of the separatrices do not touch at every node.) The lower frame shows the ponderomotive potential (bottom, red line) and electron density (bottom, blue line).

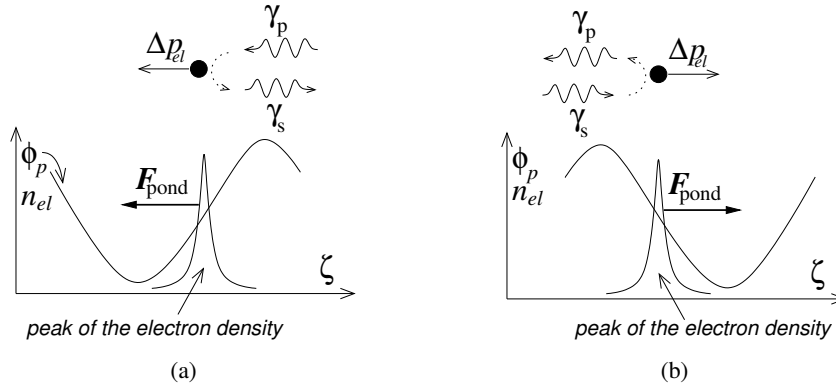


Figure 2.4: Direction of the energy flow of the light scattered from an electron density peak; the signal pulse travels to the right, the pump pulse to the left side. The ponderomotive force acting on the electrons corresponds to the net recoil momentum per unit time, that the electrons gather by scattering photons of the pump and signal pulses. (a) Electron peak on the right side: net scattering of pump photons back into the signal pulse leading to the amplification of the signal pulse. The opposite case is depicted in (b).

trons get distributed again after one full oscillation cycle. Since the oscillation frequency of the electrons is smaller near the separatrix, they are not perfectly homogeneously distributed, however on the average, there is no net scattering of light between the two pulses.

Seen from a different point of view, the electron distribution oscillates between a broad distribution in space with a narrow velocity distribution and a peaked distribution in space with a broad velocity spread. This consideration is idealized because the electrons have slightly different oscillation frequencies due to the non-harmonic potential. Actually, they gradually smear out in the phase space.

Direction of the energy flow of the scattered light

The position of the electron peak within the ponderomotive potential determines the direction of the energy flow from the pump pulse to the signal pulse or vice versa, because it determines the phase relation between the waves of the pump and signal pulses at the position of the scattering electrons. This fact is more easily understood in the picture of electrons backscattering pump and signal photons, as depicted in Fig. 2.4. The ponderomotive force acting on an electron can be interpreted as the sum of the recoil momenta that the electron gathers per unit time by scattering laser photons. If the electron experiences a net ponderomotive force in one direction, e.g., in the direction of the pump pulse, it scatters more photons from the pump into the signal pulse than vice versa, which results in a net amplification of the signal (Fig. 2.4a). The same holds true the other way around: If the net force goes into the direction of the signal pulse, the pump is amplified at the expense of the signal pulse.

2.3.5 Signal Shortening and Optimal Frequency Detuning

Contraction of the signal pulse and amplification bandwidth

The signal pulse is attenuated by the backscattering of the signal pulse during the second bunching around $3/4T_b$. In the optimal case, the signal pulse is short enough that the attenuation occurs just on its rear edge and constricts its duration. The pulse duration can be approximated by half an oscillation period,

$$\tau_s \approx T_b/2 = \frac{\pi}{\omega_b} = \frac{\pi}{\sqrt{a_p a_s}(\omega_{pu} + \omega_s)} \approx \frac{T_{pu}}{4\sqrt{a_p a_s}}. \quad (2.24)$$

The last step uses the approximation $T_s \approx T_{pu}$. When the signal pulse is amplified by SRA, the ponderomotive potential becomes deeper and the bouncing frequency ω_b increases (Eq. (2.18)). Hence the signal is shortened even further, because the generation and destruction of the electron grating by the oscillation occurs faster.

For the signal pulse to shorten, its bandwidth has to increase. The large amplification bandwidth is a consequence of the velocity spread that the electrons exhibit, when they are bunched. All the electrons backscatter the pump pulse Doppler shifted by their individual velocity. The deeper the ponderomotive potential, the larger becomes the spread and hence the amplification bandwidth.

Optimal detuning of the laser pulses

The initial velocity of the electrons with respect to the ponderomotive potential is $\zeta = v_{ph}$, which is by Eq. (2.15) proportional to the frequency detuning $\Delta\omega$ between the pump and signal pulses. Half an oscillation period later, after the electron has contributed to the amplification of the signal pulse and has been reflected from the edge of the potential well, it has approximately the velocity $\zeta = -v_{ph}$. Therefore, its contribution to the amplification is larger for a higher frequency detuning. According to the previous section, the change of its momentum corresponds to the net number of photons it has scattered from the pump into the signal pulse.

On the other hand for a higher detuning, less electrons are trapped and bunched in the potential. There exists an optimal detuning, for which the overall amplification becomes largest. In [46], it is shown numerically and analytically that the optimal detuning is $\Delta\omega = \omega_{pu} - \omega_s \approx \omega_b$. However, this is not a strict resonance. Fig. 2.7 shows that the amplification starts for a large range of detunings and shifts the spectrum towards the optimal detuning.

2.3.6 Amplification by Coherent Emission from Bunched Electrons

The plasma electrons scatter the light pulses by classical Thomson scattering with the scattering cross section [53]

$$\frac{d\sigma}{d\Omega} = \frac{1}{2}(1 + \cos^2\theta)r_e^2 \quad (2.25)$$

into the solid angle $d\Omega$ under the angle θ with respect to the wave vector of the incoming radiation. Here, $r_e = e^2/(4\pi\epsilon_0 m_e c^2) \approx 2.8$ fm is the classical electron radius. The phase of the scattered radiation is shifted by π with respect to the incoming wave. If the electrons are

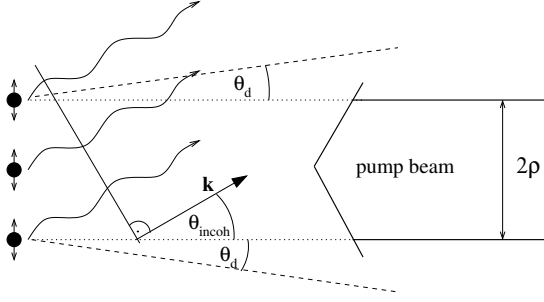


Figure 2.5: For a pump beam diameter of 2ρ , the electrons scatter the light coherently into a cone with the half-opening angle θ_d . For larger angles some of the electron radiate out of phase.

homogeneously distributed in space, their scattering amplitudes, a_{scat} , add incoherently when superimposed.

During the amplification however, the electrons are nonuniformly distributed and a net scattering wave remains. In particular, the bunching of the electrons to thin layers with a thickness much smaller than the laser wavelength as depicted in Fig. 2.3(c) and (e), makes them scatter coherently. Because of the periodicity of the potential, the waves reflected from the adjacent electron bunches are in phase as well. Therefore, the total signal amplitude is proportional to the number of scattering electrons \mathcal{N} ,

$$a_s = \mathcal{N}a_{\text{scat}} + a_{s0}, \quad (2.26)$$

where a_{s0} is the initial signal amplitude, which can be neglected for sufficiently large \mathcal{N} . The signal intensity hence grows with the square of the number of electrons, $I_s \propto a_s^2 \propto \mathcal{N}^2$.

Growth of signal intensity in the superradiant regime

Fig. 2.5 shows the geometry of the amplification by scattering from the plasma electrons. For the backscattering from the pump into the signal, the angle θ in Eq. (2.25) is approximately π , hence $1 + \cos^2\theta \approx 2$. A pump beam of diameter 2ρ is scattered coherently within a cone with the half-opening angle θ_d . Outside the diffraction angle, the radiation emitted from the electrons partly cancels. For a Gaussian transverse beam profile one finds $\theta_d = \sqrt{2}/(k_s\rho)$ [56] corresponding to the solid angle $\Delta\Omega = 2\pi(1 - \cos\theta_d) \approx \pi\theta_d^2$ [57, Eq. 3.135]. Using these relations, the radiation power scattered by a single electron can be written as

$$P_e = \frac{d\sigma}{d\Omega} \Delta\Omega I_p = \frac{2\pi r_e^2}{(k_s\rho)^2} I_p. \quad (2.27)$$

Ideally, all electrons scatter the pump pulse coherently and the signal intensity as well as its power grows quadratically with the number of participating electrons \mathcal{N} , which is given by the number of electrons in the volume passed by the signal pulse $\mathcal{N} = \pi\rho^2 z n_e$. This allows to compute the total signal power

$$P_s = \pi\rho^2 I_s = \mathcal{N}^2 P_e = (\pi\rho^2 z n_e)^2 P_e, \quad (2.28)$$

where z is the amplification length in the superradiant regime. From the last two equations an analytic expression for the the signal intensity as function of the propagation distance is derived,

$$I_s = \frac{P_s}{\pi\rho^2} = \frac{\omega_{pe}^4}{8k_s^2 c^4} z^2 I_p = \frac{1}{8} \left(\frac{n_e}{n_{\text{crit}}} \right)^2 (k_{\text{pu}} z)^2 I_p. \quad (2.29)$$

Again the frequencies of the pump and signal pulses were taken equal, $\omega_s \approx \omega_{pu}$ or $k_s \approx k_{pu}$, and the refractive index was approximated for small densities, $n_{\text{refr. ind.}} \approx 1$ or $\omega_{s/p} \approx ck_{s/p}$. Extensive numerical simulations yielded a somewhat smaller pre-factor: $\approx 1/16$ instead of $1/8$ [46]. The analytic value is higher, because it was assumed that the peak of the signal pulse is amplified maximally, whereas the numerical simulation in Fig. 2.10(a) shows that the maximal amplification of the signal actually occurs only on its leading edge. At the pulse maximum, the electron grating already decays due to the ongoing oscillation.

Limits of SRA

In numerical simulations SRA amplifies the signal pulse up to relativistic intensities, $a_s \approx 0.5$. Then another nonlinear process sets in and the pulse starts to break up [46]. At relativistic intensities the ponderomotive force due to the envelope cannot be neglected any longer, because it becomes as strong as the force due to the interference pattern. The trapped electrons gain an additional momentum, which shifts the position of the electron peak from the right edge of the potential well as depicted in Fig. 2.3(c) over the crest to the left edge of the adjacent well, where it attenuates the signal pulse.

A consequence of the limitation on the signal intensity, the minimally achievable pulse duration according to Eq. (2.24) is approximately two laser cycles.

2.3.7 Remark on the Carrier Envelope Stability

Recently, the absolute phase of few-cycle laser pulses has attracted a lot of attention because of its relevance for the generation of attosecond pulses [32, 33]. Single as-pulses can be generated for a specific phase relation, called the cosine pulse, meaning that the maximum of the carrier wave coincides with the maximum of the pulse envelope [58]. A laser amplifier for these pulses inserts a phase shift between the carrier and the envelope, but this shift must not be random, so that it can be pre-compensated. Therefore, the amplifier can maintain the carrier-envelope stabilization if the jitter added to the absolute phase is much less than $\pi/2$.

Using SRA as an amplifier, the jitter stems mainly from the fluctuations of the plasma density and length. The phase shift between the carrier traveling at $v_{ph} = c/n_{\text{refr. ind.}}$ and envelope traveling at $v_{gr} = cn_{\text{refr. ind.}}$ is

$$\Delta\phi = k_s(v_{ph}\tau - v_{gr}\tau) \approx k_s L \frac{n_e}{n_{\text{crit}}}, \quad (2.30)$$

where $\tau = L/v_{gr}$ is the time the signal pulse needs to pass the plasma of length L with an idealized flat top density profile. The fluctuation of $\Delta\phi$ due to the changes in the plasma length and density is

$$\delta \left(k_s L \frac{n_e}{n_{\text{crit}}} \right) = k_s \left(\delta L \frac{n_e}{n_{\text{crit}}} + L \frac{n_e}{n_{\text{crit}}} \frac{\delta n_e}{n_e} \right). \quad (2.31)$$

For typical parameters of the present work, $L = 1$ mm, $n_e/n_{\text{crit}} = 0.002$ and $\lambda \approx 800$ nm, the jitter of $\Delta\phi$ stays smaller than $\pi/2$ if $\delta L \ll 100 \mu\text{m}$ and $\delta n_e/n_e \ll 0.1$. Although this appears feasible, it requires a large control over the gas jet and is usually not trivial to achieve.

2.3.8 Scaling Laws for Intensity, Duration, and Energy

Table 2.2 summarizes characteristic scalings of the SRA regime derived in the previous sections. A coarse estimate for the signal energy is added. The third column gives the scalings for fixed energy and duration of the pump pulse. They are more appropriate with regard to an experiment, where the pump energy and duration can be directly controlled. The given scalings only refer to the superradiant regime. Therefore, a minimum pump intensity I_p is required to satisfy the threshold condition for SRA.

Threshold condition	$\omega_b \gtrsim \omega_{pe}/\sqrt{2} \Leftrightarrow a_s a_p \gtrsim \frac{n_e 0}{8n_{crit}}$	
Intensity	$I_s = \frac{1}{8} \left(\frac{n_e}{n_{crit}} \right)^2 (k_{pu} z)^2 I_p$	$\propto (n_e \omega_{pu})^2 E_p \tau_p$
Duration	$\tau_s \approx \frac{\pi}{\omega_b} \propto ((\omega_s + \omega_{pu}) a_s a_p)^{-1/2} \propto (I_s I_p)^{-1/4}$ $\propto (n_e k_{pu} z I_p)^{-1/2}$	$\propto (n_e \omega_{pu} E_p)^{-1/2}$
Energy	$E_s \approx \pi \rho^2 \tau_s I_s \propto (n_e k_{pu} z)^{3/2} \pi \rho^2 I_p^{1/2}$	$\propto (n_e \omega_{pu})^{3/2} \rho E_p^{1/2} \tau_p$

Table 2.2: Scaling laws for the threshold condition, and the signal intensity, duration, and energy. A constant pump amplitude is assumed; z is the amplification length. In the third column the pump intensity is expressed by its energy E_p and duration τ_p , where $I_p \approx E_p/(\pi \rho^2 \tau_p)$ is used, with the beam diameter 2ρ . The amplification length is approximated by $z = c\tau_p$. These scaling expressions are more appropriate for the experiment, where the pump energy and duration can be directly controlled.

An interesting feature is the scaling of the duration with the pump wavelength λ_{pu} . The minimally achievable signal duration is directly proportional to λ_{pu} if the same values for a_p and n_e/n_{crit} are used and the same maximum amplitude of the amplified signal a_s is assumed. Therefore, shorter amplified pulses can be achieved just by using a pump of shorter wavelength. Table 2.3 lists the minimal pulse duration and the according energy fluences for possible pump sources that can deliver picosecond, high-power laser pulses suitable for SRA. In particular, KrF and Nd:glass or Nd:YAG systems can deliver kJ-pulses allowing to amplify signal pulses up to multi-Petawatt peak powers, far beyond the 1 PW-level of today. At the same time, much shorter pulse durations can be achieved than it is possible nowadays for high-power laser systems with durations of at least 25 fs.

pump laser	wavelength λ_p	min. signal duration τ_s	max. fluence J_s
Ti:sapphire	800 nm	7 fs	6 kJ/cm ²
Nd doped, 2 ω	530 nm	4.5 fs	9 kJ/cm ²
KrF	248 nm	2 fs	20 kJ/cm ²

Table 2.3: Minimal durations and maximal fluences of the signal pulse for different pump wavelengths. The maximum signal amplitude $a_s \approx 0.45$ was obtained from numerical PIC simulations and allows a minimal signal duration of 2-3 laser cycles.

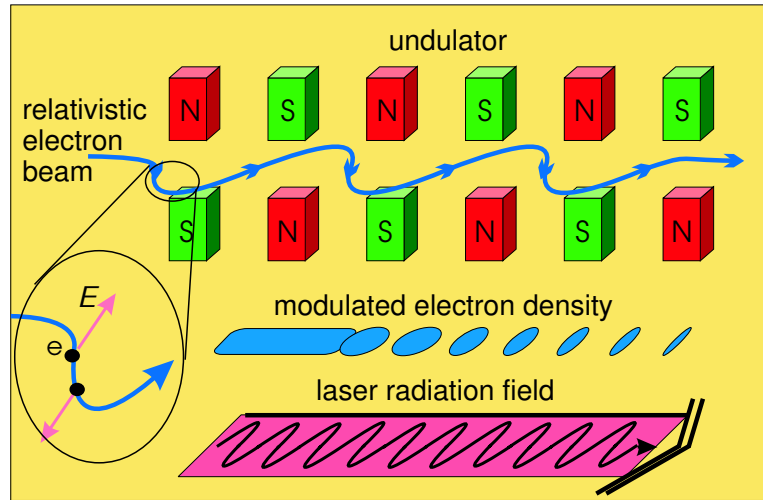


Figure 2.6: In a FEL, a relativistic electron beam oscillates transversely in the alternating magnetic fields of the undulator or wiggler. The additional radiation field of the signal pulse is necessary to cause the breakup and bunching of the electron beam. In the superradiant Compton regime, the oscillating electrons radiate coherently thereby amplifying the signal pulse. The FEL is transformed into the superradiant plasma amplifier by a Lorentz transformation into the reference frame of the initially uniform electron beam. The relativistic electron beam becomes the uniform plasma at rest. The magnetostatic undulator field transforms into a counter-propagating electromagnetic wave, which represents the pump pulse.

2.3.9 Analogy to Free-Electron Lasers

This section compares the SRA plasma amplifier to a Free-Electron Laser (FEL), which actually works according to the same basic mechanism. The comparison reveals similarities, which can help to transfer some of the theory already worked out for FELs to the theory of the plasma amplifiers, but it also states several differences concerning the operation and the output.

In a FEL [59, 56, 60, 61], a relativistic electron beam is sent through a periodic magnetostatic structure called undulator or wiggler (Fig. 2.6). In the alternating magnetic field, the Lorentz force makes the electrons oscillate and radiate. Since the electrons move at a velocity close to the speed of light, their radiation peaks in forward direction. The radiation superimposes incoherently and is weak as long as the electrons are uniformly distributed. The undulator field and the radiation field create a ponderomotive potential causing the bunching of the electrons in space. The bunching increases the coherence of the scattering electrons thus leading to amplification of the radiation field. FELs exist as oscillators and as single pass amplifiers. In an oscillator, the radiation is confined in a cavity. A certain radiation level is build up after a short operation time so that a radiation field is already present, when the electrons enter the undulator. Oscillators typically have a small gain. In single pass amplifiers, there is no initial radiation field. Instead the radiation is generated by *self-amplification of spontaneous emission* (SASE). SASE-FELs need a high gain to achieve a noteworthy output.

In the beginning, the electron bunching and the radiation field form a feedback loop. The radiation field contributes to the ponderomotive potential causing the electron bunching. The

stronger the radiation field is the faster the electrons get bunched, and in turn: the better the electrons are bunched the more coherently they radiate leading to stronger amplification. Such feedback loops often give rise to exponential growth in the small signal regime, which is also found in the FEL [56, 60, 61]. The bunching is numerically described by the so-called *bunching parameter* b . It ranges between 0 and 1, where 0 corresponds to uniformly distributed electrons radiating incoherently and 1 corresponds to perfectly bunched electrons radiating coherently.

The similarity between the FEL and the plasma amplifier becomes apparent by a Lorentz transformation to the reference frame of the relativistic electron beam. The resting electrons form the plasma. The magnetostatic undulator field transforms into an electromagnetic wave propagating in opposite direction to the laser radiation field, which is exactly the configuration of the plasma amplifier. Unlike the FEL, SRA corresponds to a single pass amplifier with an initial signal pulse present. In both amplifiers, the bunching of the electrons is caused by their longitudinal oscillation in the ponderomotive potential. Since their dynamics is similar, corresponding quantities often satisfy analog relations. Table 2.4 compares the undulator (pump pulse), the radiation field (signal pulse), and the electron beam (plasma) of the SRA plasma amplifier and the FEL. Despite the similarity, some of the quantities like the bunching parameter and the duration of the pulses differ significantly entailing a different behavior in some aspects. In the following comparison, both amplifiers are viewed in the rest frame of the average electron motion and the terminology of the plasma amplifier is used.

The electron bunching is much smaller in the FEL resulting in exponential but small amplification. For SRA, the bunching reaches this level already in the leading edge of the signal pulse. It continues to almost perfect bunching at the pulse center, where all electrons radiate coherently. If the bunching parameter approaches 1 in the FEL, the amplification is no longer exponential and the FEL is called *saturated*. Since the electrons radiate in phase, their single scattering amplitudes add up linearly to the amplitude of the signal pulse. Therefore, the intensity grows quadratically with the number of electrons and, for a homogenous plasma, quadratically with the propagation distance.

Even a saturated SASE-FEL still differs significantly from the superradiant plasma amplifier concerning the pump and signal pulse durations. In an FEL, the pump pulse is much shorter. In the optimal case, it is just long enough that the electrons get bunched perfectly one time, which happens after a quarter rotation in the ponderomotive potential as it is shown in Fig. 2.3(c). On the other hand, the signal pulse duration given by the length of the electron beam is typically much longer, in particular in the reference frame of the relativistic electron beam. This means the roles of the pump and signal pulses are reversed as compared to SRA. There, the signal pulse is limited to half an oscillation period in the ponderomotive potential, whereas the pump pulse occupies the whole plasma length.

This is of importance for the instabilities that can occur in an FEL and a plasma amplifier. For SRA, the long pump pulse is likely to be subject to instabilities, while it is traveling through the plasma without interacting with the signal pulse. In particular, the Raman and Brillouin instabilities can occur. The latter is obviously not an issue for an FEL, because no ions are present. Raman effects only play a role if the electron beam has a high current density and the relativistic factor γ is small, which results in a higher electron density. While in an FEL, the electron beam is prone to transverse instabilities, the ions neutralize the electron charge and prevent this instability in the plasma amplifier. The long signal pulse of an FEL can be subject

	FEL	SRA plasma amplifier
undulator / pump pulse	magnetostatic undulator ($K < 1$) or wiggler ($K > 1$)	electromagnetic wave
wavelength	undulator period: λ_u in electron rest frame: λ_u/γ	$\lambda_{pu} \approx \lambda_s$
frequency	static field in electron rest frame: $\gamma c/\lambda_u$	$\omega_{pu} \approx \omega_s$
amplitude acting on electrons	$K = \frac{\lambda_u e B}{2\pi m_e c} = \frac{e A_u}{m_e c}$ $K \approx 1$	$a_p = \frac{e E}{\omega_{pu} m_e} = \frac{e A_p}{m_e c}$ $a_p \approx 0.03$
length	40 - 200 periods in electron rest frame shorter than signal pulse	1000 - 3000 periods adapted to length of plasma $\tau_p \gg \tau_s$
radiation field / signal pulse	electromagnetic wave	electromagnetic wave
wavelength	$\lambda_R = \frac{\lambda_u}{2\gamma^2}(1 + K^2)$ in electron rest frame: $\lambda_u/\{\gamma(1 + K^2)\}$	$\lambda_s \approx \lambda_{pu}$
frequency	$\omega_R = 2\pi c/\lambda_R$	$\omega_s \approx \omega_{pu}$
initial amplitude	SASE: $a_{R0} = 0$	$a_{s0} \approx a_p$
final amplitude	$a_R = 10^{-4} \ll K$	$a_s \approx 0.5 \gg a_p$
duration	duration of electron pulse + undulator length/ (γc)	$\tau_s \approx \pi/\omega_b \ll \tau_p$
intensity growth	$I_R \propto e^{z/l_g}$	$I_s \propto z^2$
beam / plasma	relativistic electron beam	electrons and ions
longitudinal oscillation frequency	synchrotron frequency: $\Omega_s^2 = 4a_R K \omega_R k_u c / \gamma^2$	bouncing frequency: $\omega_b^2 = 4a_s a_p \omega_s \omega_{pu}$
bunching time	usually: $\ll \pi/\Omega_s$	$\approx \pi/\omega_b$
bunching parameter	usually: $b \ll 1$ for saturation: $b \approx 1$	$b \approx 1$

Table 2.4: Comparison of the free-electron laser and the plasma amplifier in the SRA regime. The undulator acts on the electron with the wiggler constant K (sometimes also denoted a_w). B is the average magnetic field in the undulator; γ is the relativistic factor of the electron beam. The fields are expressed by their corresponding vector potentials using the relations $B = k_u A$ for the FEL and $E = \omega_{pu} A$ for the plasma amplifier. l_g is the gain length in the FEL. The synchrotron frequency is given for a helical undulator and the bouncing frequency for circularly polarized light. For the linear configuration the values are smaller by a factor 2. The wavenumber of the undulator (wiggler) is $k_u = 2\pi/\lambda_u$. (compiled from [60, 61]) (Remark: DESY at Hamburg plans to build an FEL with an undulator of several thousand periods. However, also this much longer undulator just corresponds to the saturation bunching time.)

to a backward wave instability, whereas the signal pulse in the superradiant plasma amplifier is too short for this to occur.

For long undulators, the *synchrotron instability* [60] can show up in an FEL. Here, the electrons are trapped in the ponderomotive potential for several oscillations. As described earlier for the SRA regime, this leads to an alternate sequence of amplification and attenuation of the signal pulse causing a break-up into a train of pulses. This effect usually does not occur for the superradiant amplifier, because the signal pulse is so short that the electrons only perform half an oscillation. However, in the experiments in chapter 5, the input signal pulse is longer. The observed pulse break-up corresponds to the synchrotron instability in an FEL.

Finally, there exists an FEL theory being the exact equivalent to SRA: The superradiant Compton regime described by Bonifacio *et al.* [62, 63]. There, the common ponderomotive force of the laser pulse and the wiggler field is larger than the electrostatic force between the electrons. The electrons get trapped in the ponderomotive potential, where they perform longitudinal oscillations and are bunched very efficiently with a bunching parameter close to 1. In this regime, the intensities of the radiation field in the FEL grows quadratically and the duration is constricted to half an oscillation cycle. It was G. Shvets, who transferred this FEL scheme to a plasma to propose a new kind of amplifier.

2.4 Numerical Particle-In-Cell Simulations

The dynamics in a plasma is usually so complex that approximations and restrictions have to be made when treating the laser plasma interaction analytically. Numerical simulations obtained from the integration of the basic equations represent virtual experiments performed in a computer allowing to study and visualize the complex plasma dynamics in much greater detail than possible in an analytic treatment. However as opposed to a real experiment, the conditions are idealized.

2.4.1 Particle-In-Cell codes

The best way to simulate the interaction of intense femtosecond laser pulses with a plasma numerically is usually by means of a Particle-in-Cell (PIC) code [64, 65]. It traces the motion of the particles in the plasma by integrating their equations of motion with the Lorentz force acting on them, $\dot{\mathbf{p}} = q(\mathbf{E} + \mathbf{v} \times \mathbf{B})$. The electric and magnetic fields are directly obtained from Maxwell's equations. To reduce the computational effort, macro particles are used representing a larger number of actual particles. The electric and magnetic fields are computed on a grid, which represents also the corner points of cells, through which the particles move. The charge and current densities are computed for each cell by adding the contribution of all particles that are partially inside the cell. In a Leap-Frog scheme, the algorithm computes alternately for fixed time steps the particle motion and the fields.

The kinetic treatment of the particles is suitable, because laser-plasmas often show a very nonlinear behavior, in particular, the phase space of the electrons gets mixed strongly and small electron populations can get accelerated to high velocities. If the particles overtake each other, a fluid description of the plasma breaks down. Vlasov-codes, which compute the distribution functions for electrons and ions from the Vlasov equations in a defined area in the phase space, are inappropriate, because most parts of the phase space are usually empty and are computed

in vein. The macro particles in a PIC simulation can be regarded as tracer particles that allow to determine the distribution functions without confining the phase space.

The drawback of PIC codes is their large consumption of computational power. This restricts the simulations to frames of the femtosecond-time scale and rather thin plasmas or low dimensions. The interaction of femtosecond laser pulses with an underdense plasmas is therefore the ideal field of application for PIC codes. Codes simulating 1, 2, or 3 spatial dimensions (1D, 2D, 3D) are common nowadays.

The simulations in the present work are performed with the 1D code *Virtual Laser Plasma Laboratory* (VLPL1D) written by A. Pukhov and extended by myself in the framework of my diploma thesis [46]. To reduce the computational effort, the plasma is usually simulated only around the interaction region of the pump and signal pulses in a simulation box co-moving with the signal pulse.² All simulations of this work were performed with this code on ordinary PCs.

2.4.2 Numerical Study of SRA

Confirmation of Analytic Findings

In [46] the analytically derived scaling laws for intensity, energy and duration given in Table 2.2 in the previous section could be reproduced by the numerical simulations with slight changes of the pre-factor. For the intensity scaling, the numerically obtained value is approximately 0.067, which is half the theoretically predicted value. The rough theoretical estimate of the signal duration could be refined to $\tau_s = 1.2\pi/\omega_b$.

Also the transition from SRBS to SRA described in section 2.5.3 is observed. If the initial signal pulse is too weak to directly enter the SRA regime, it is amplified by SRBS until its intensity has grown large enough to satisfy the threshold condition, $\omega_b > 0.7\omega_{pe}$. An upper intensity limit for SRA was found for relativistic intensities. Further non-linear effects cause the pulse breakup [46, Fig. 5.2], which has been discussed in section 2.3.6.

Amplification for same initial frequencies of pump and signal pulse

In Fig. 2.7 taken from my diploma work [46], the amplification process is studied when varying the detuning $\Delta\omega = \omega_{pu} - \omega_s$ between the input signal and pump pulses. Fastest growth occurs for a specific frequency detuning. This optimal frequency is approximately ω_b if the threshold condition Eq. (2.23) is satisfied prior to amplification. For smaller initial intensities, the signal pulse is first amplified in the Raman regime requiring the frequency detuning $\Delta\omega = \omega_{pe}$.

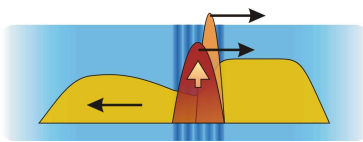


Figure 2.8: Generation of a new signal pulse by SRBS if the detuning between the pump and signal pulses is far from the optimum.

However, the signal pulse is also amplified if the initial detuning is far off the optimal value. In particular, the case $\Delta\omega = 0$ is of great interest, because it is experimentally much easier to generate both laser pulses the same frequency from a single source. Therefore, this choice was the first approach in the present work and is described in chapter 4. However, it was found that the delayed start of the strong amplification gives instabilities of the pump pulse more time to significantly grow and deteriorate the amplification process preventing the success of this approach.

²The simulation is still performed in the reference frame of the resting electrons, not in the Lorentz-boosted reference frame of the signal pulse.

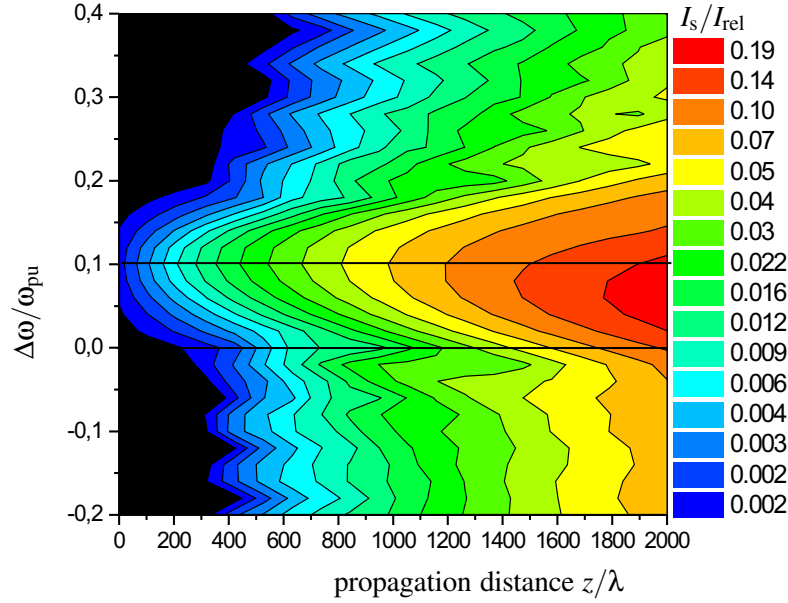


Figure 2.7: Evolution of the peak signal intensity for varying the frequency detuning $\Delta\omega/\omega_{\text{pu}} = (\omega_{\text{pu}} - \omega_{\text{s}})/\omega_{\text{pu}}$ between the pump and input signal pulses. The intensity is color-coded and given in units of the relativistic intensity $I_{\text{rel}}(\lambda = 1 \mu\text{m}) = 2.76 \times 10^{18} \text{ W/cm}^2$, for which the normalized vector potential of circularly polarized light equals 1. The initial signal intensity is below the intensity threshold for SRA, hence the amplification starts in the Raman regime, where fastest growth is found if the resonance condition $\Delta\omega = \omega_{\text{pe}} = 0.1\omega_{\text{pu}}$ is satisfied. For different detunings, a new signal pulse is created at the correct frequency detuning. The amplification sets in delayed, because the generation of the new signal pulse takes some time, but finally the same intensities are reached as for the optimal initial detuning. When the pulses have the same frequencies initially, the interaction length has to be increased by $600 \mu\text{m}$ later to achieve intensities of equal strength.

The amplification far off the optimum frequency detuning is possible, because the signal pulse is not amplified at its original frequency. Instead it launches a plasma wave, which scatters back some of the pump light at the Stokes frequency $\omega_{\text{pu}} - \omega_{\text{pe}}$. This light is quickly amplified in the Raman regime. When it becomes strong enough to pass the threshold for SRA, the amplification mechanism changes to SRA and the new signal pulse is also shortened. Hence the original input pulse at the wrong frequency only launches the generation of a new signal pulse with the correct frequency detuning.

Instabilities of the Pump Pulse

Instabilities are only relevant for the pump pulse, but not for the signal pulse, because it is too short. To investigate their influence on SRA, the whole plasma is simulated for the time the pump pulse needs to pass it.

The most likely instabilities are Raman forward and backward scattering. The simulations show only backward scattering due to its much larger growth rate. This agrees with the experimental observation in appendix B.2. Furthermore, the instabilities never occur in the section of the plasma that the signal pulse has already passed. The phase-space plot in Fig. 2.10a explains this finding: The electrons leaving the ponderomotive potential have a very large ve-

locity spread. When they mix with electrons trapped in the adjacent potential wells, they are heated to keV temperatures.

Instabilities occurring ahead of the signal pulse deteriorate the amplification process in two ways. First, the initially cold, homogeneously distributed electrons are pre-heated and pre-bunched. The trapping and bunching mechanism of SRA becomes less efficient and the amplification rate falls off. Second, the pump light backscattered by the instabilities appears as weak long precursor of the main signal pulse. This decreases the contrast, which impedes experiments with solid targets, where the occurrence of a pre-plasma is detrimental.

The inspection of the growth rates in Table 2.1 reveal that Raman backward scattering can be decreased by reducing the electron density and the pump intensity. Since this affects the growth rate of SRA, too, the optimal parameter set for the actual experiment is a tradeoff between maximizing the amplification of the signal pulse and minimizing the instabilities. Further options for the reduction of the instabilities have been proposed in theoretical investigations of Raman amplification of short pulses [66, 67]. Some of these are likely to work for SRA, too, e.g., using strongly chirped pump pulses [68] or plasmas with density gradients that limit the necessary resonance for SRBS to rather short distances, thus reducing the gain length of the instabilities.

The computational analysis of the instabilities for the parameters of the experiment presented in this work revealed that they are small and just about to set in. The main simulation problems arise from the proper implementation of the temperature distribution and the nuclei of the instabilities. The latter are stochastic; they depend on statistical fluctuations of the plasma density and can hardly be modeled reliably. The temperature models used in numerical simulations seem oftentimes inappropriate for rather low temperatures in the initial plasma (≈ 10 eV). Several different algorithms have been implemented in the present code. Although they all used the same average temperature, the results differ rather strongly. Hence the influence of the temperature on the instability thresholds and the growth damping could not be analyzed reliably. The correct modeling of low-temperature plasmas appears to be a general problem of PIC codes.

2.5 Raman Amplification versus SRA

Stimulated Raman backward scattering (SRBS) described in section 2.1.4 can amplify laser pulses for intensities and plasma densities close to those of SRA. Indeed, it is used in the present experiments in chapter 4 to pre-amplify the weak input pulse. The proximity of the two regimes sometimes causes confusion, which mechanism dominates for certain conditions and even whether SRA is a separate regime at all. To establish a clear distinction in the experiments, it is therefore important to discuss the similarities and differences between these two amplification schemes, starting with a more detailed description of Raman amplification.

2.5.1 Amplification by Stimulated Raman Backward Scattering

SRBS has been proposed as an amplification scheme for laser beams since the 1960s, first in Raman-active gases [69, 70], later also in plasmas [71, 72, 73]. However, several disadvantages impeded its application in plasmas until recently. The resonance condition, $\omega_{\text{pu}} = \omega_{\text{pe}} + \omega_{\text{s}}$, is difficult to strictly satisfy, because small gradients of the electron density already

change ω_{pe} considerably and the amplification ceases. It is very demanding to provide plasmas homogeneous enough over lengths of several mm or even cm and hence to achieve sufficient amplification.

The second disadvantage of SRBS is its small gain bandwidth, $\Delta\omega_{\text{SRBS}}$, which rules out the amplification of very short laser pulses. The gain bandwidth is given by twice the growth rate,

$$\Delta\omega_{\text{SRBS}} = 2\gamma = \sqrt{\omega_{pe}\omega_{pu}}a_p. \quad (2.32)$$

For typical parameters of Raman amplification ($n_e = 0.001 \dots 0.05n_{\text{crit}}$, $a_p = 0.005 \dots 0.03$), the gain width only allows for pulses longer than a few hundred fs in the visible. These durations are not very attractive, because they can be achieved by well-established laser technology based on induced emission. The reason for these long durations is apparent: The plasma wave continues to exist once it has been excited by the pump and signal pulses. It backscatters the pump pulse on its whole length creating a backscattered pulse of the same length although the original signal pulse is short.

2.5.2 Raman Amplification in the Pump Depletion Regime

Recently, the theoretical analysis of Raman amplification made a breakthrough to solve this problem by including a simple detail known from three wave interaction: the depletion of the pump [45]. If the pump pulse has a rather low intensity ($I_p = 10^{12} \text{ W/cm}^2 \dots 10^{15} \text{ W/cm}^2$) and the plasma density high enough ($n_e/n_{\text{crit}} = 0.01 \dots 0.1$), the pump pulse is completely reflected over the length of the signal pulse. When the pump is exhausted, the energy flow reverses and the signal pulse is backscattered into the pump thus attenuating the signal. The signal pulse does not only stay short but shrinks even further, because the plasma wave is excited faster and the pump depleted earlier, while the signal amplitude grows due to the amplification.

This phenomenon is analogous to the energy transfer between mechanical pendulums coupled by a spring. If only one pendulum swings initially its energy is gradually transferred to the other pendulum by the spring. When the energy transfer is completed, the process reverses: The amplitude of the first pendulum increases again but shifted in phase by π . The same happens between the pump and the signal pulse, which are coupled by the plasma wave. The main difference is the fact that the electromagnetic waves propagate in opposite directions and the mutual energy transfer can only occur, where the pulses overlap. The final signal is actually a pulse train, due to the ongoing forth and backscattering. The zeros of the pump and signal pulses take turns. Each time one pulse is depleted the carrier wave shifts its phase by π and the energy transfer reverses.

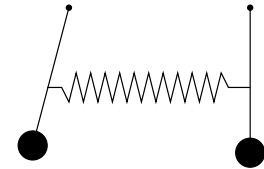


Figure 2.9: Coupled mechanical pendulums

The pump depletion regime of SRBS has received considerable interest in the recent years, analytically [45, 74, 75, 76, 77, 78, 67], numerically [79, 80, 81, 82, 83] and experimentally [84, 85, 86, 87, 88]. Though the experiments would not yet directly prove the occurrence of the pump depletion, the pulse shortening was observed by Ping *et al.* [88].

The pump-depletion regime looks very attractive, because the whole pump is reflected eventually. However, only the energy in the first lobe of the signal pulse train is attractive for an application. It contains around 50 % of the signal energy. Furthermore a fraction of

$\omega_{pe}/\omega_{pu} \approx 10\%$ is lost in the idler plasma wave. The trailing pulses could turn out to be disadvantageous when used in a follow-up experiment. They could interfere or destroy plasma structures trailing the main pulse, e.g, the electrons that are accelerated by the electrostatic field in the wake of a short strong laser pulse [22, 24, 25]. It might be possible to cut the trailing pulses by instantaneous wave breaking at the expense of the rate of the pump depletion, which would drop to less than 30% [80].

The pulse shortening is approximately inverse to the propagation length, $\tau_s \propto 1/z$. However, the signal pulse lengthens in the beginning as long as the signal is too weak and the excited plasma wave too small to fully deplete the pump. The duration increases to the ps-level before it starts shrinking. Though the analytic treatment claims that pulses as short as 10 fs are possible ($\lambda_{pu} = 1 \mu\text{m}$), a duration of 50 fs is more realistic but was not yet confirmed in simulations [76, 80].

Other problems may arise from the requirement that the pump intensities stay below the wave breaking limit to achieve full depletion. This entails low intensities and hence interaction lengths much longer than those for SRA to achieve the same energy transfer. Large homogeneous plasmas are required and the long travel distances of the pump pulse in the plasma gives the instabilities time to grow. Several publications deal with these issues and propose solutions [78, 67, 81, 82, 83, 66], which could in part also be useful to suppress instabilities of the pump pulse in the SRA regime.

2.5.3 Distinction between SRA and Raman Amplification

In the pump depletion regime, SRA and Raman amplification look quite similar on the first glance: Both exhibit amplification and pulse shortening and have about the same parameters of the plasma and the laser pulses. However, there are also differences in a number of characteristic features. Some of them have already been stated in the previous sections. In the following paragraphs, they are compiled and compared versus each other in total. Fig. 2.10 is a graphical illustration of these features using results from numerical simulations. The main relations for the two regimes are given in Table 2.5.

SRA: The ponderomotive forces exceed the electrostatic forces. The SRA dynamics is envisaged as that of independent electrons getting trapped in the ponderomotive potential of the two laser pulses. The oscillation in the ponderomotive potential arranges the electrons and creates the density modulations with sharp peaks, which backscatters the pump pulse into the signal pulse. The electron phase space is strongly mixed up. The ongoing electron oscillation destroys the grating structure of the electron density but recreates it π/ω_b later, shifted in phase by π so that the signal pulse is now backscattered into the pump thus attenuating the rear side of the signal pulse and limiting its duration to π/ω_b . The destruction and phase-shifted revival can occur several times for long signal pulses.

SRBS: Below the threshold for SRA, the electrons are coupled by their electrostatic forces and collective effects dominate their dynamics. The ponderomotive potential of the laser pulses excites a plasma wave. The associated electron modulation backscatters the pump pulse into the signal pulse. After the signal pulse has passed, the plasma wave stays intact and continues to backscatter the pump pulse.

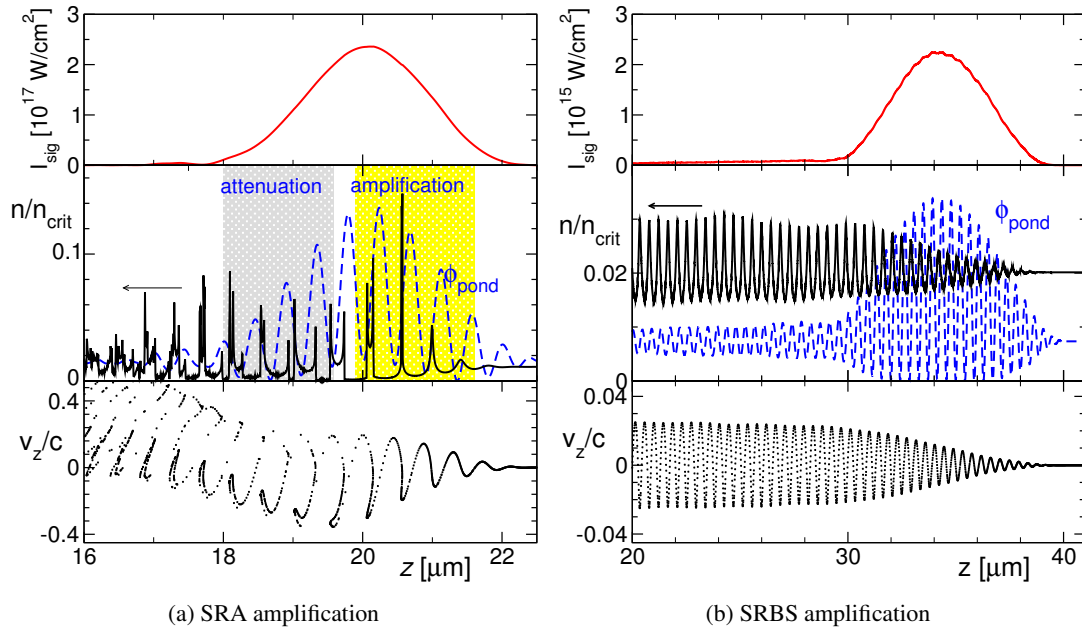


Figure 2.10: One-dimensional Particle-In-Cell simulations to illustrate the Raman and SRA amplification regimes. The plots show the intensity profile of the signal pulse traveling to the right (top), the electron density and the ponderomotive potential (middle), and the electron phase space (bottom). (a) In the SRA case, the signal intensity is chosen higher by a factor of 100 and the initial electron density lower by a factor of 2 compared to the Raman case so that the threshold condition $\omega_b > 0.7\omega_{pe}$ is satisfied and the electron dynamics is dominated by the ponderomotive potential. The electron density grating is set up within two laser cycles ($\lambda_{pu} = 0.8 \mu\text{m}$). The peak densities are 15 times higher than the initial density. Within the next two cycles, the grating first decays but then recovers whereby it attenuates the rear side of the signal pulse. The phase space can be interpreted as the temporal evolution when read from the right to the left side. It shows first regular oscillations and then the mixing of the electrons, i.e. small volumes of the initially homogeneous plasma overtake each other. After the signal pulse has passed, the plasma is heated up strongly, because the electrons have a large velocity spread and start distributing in space. No clear structure in the electron density is left. (b) In the Raman case, the plasma wave stays intact over long distances. Even after the signal pulse has passed, the pump is further backscattered. The electron phase space also remains ordered. The modulation depth of the electron density and the longitudinal velocity of the individual electrons are much smaller than in the SRA case.

The narrow gain bandwidth of SRBS causes a lengthening of the signal pulse unless the pump gets depleted. The minimal signal pulse duration is restricted to a period of the plasma oscillation, which is the time needed to establish the plasma wave. If the pump is depleted, the energy flow reverses and the pump is amplified again shifted in phase by π . This also causes the ponderomotive potential to shift its phase by π with respect to the plasma wave.

As can be seen in Fig. 2.10(b), the electron phase space stays regular, the electrons do not overtake each other. The minimal electron density is half the background density.

Evolution of SRBS to SRA When in the SRBS regime the signal amplitude has grown sufficiently large to satisfy the threshold condition $\omega_b > 0.7\omega_{pe}$, the amplification can switch to

	SRA	SRBS
parameter region	$\omega_b > 0.7\omega_{pe}$	$\omega_b < 0.7\omega_{pe}$
characteristic frequency	bouncing frequency: $\omega_b = \sqrt{a_s a_p (\omega_s + \omega_{pu})}$	plasma frequency: $\omega_{pe} = \frac{n_e e^2}{\epsilon_0 m_e}$
wave number of electron density modulation	$k_s + k_{pu}$	$k_s + k_{pu}$
resonance condition	$\omega_{pu} - \omega_s \approx \omega_b$ no strict resonance; signal is red shifted when ω_b increases	$\omega_{pu} - \omega_s = \omega_{pe}$ less stringent for short signal pulses
amplification bandwidth	$\Delta\omega_{SRA} \approx \omega_b$	$\Delta\omega_{SRBS} = 2\gamma_{SRBS}$ in the linear regime

Table 2.5: Comparison of SRBS and SRA regimes

SRA. Although the two amplification regimes can be clearly distinguished by their different features (Fig. 2.10), the transition from SRBS to SRA occurs gradually. While the signal amplitude is amplified, the increasing ponderomotive potential traps more and more electrons and the density peaks become more pronounced. In the transition regime, the electron dynamics is governed by the ponderomotive forces for the trapped electrons and by the plasma wave for the rest. Numerical simulations show a smooth change of the amplified signal intensity from the exponential growth with distance typical for Raman amplification to the growth quadratic in distance, which is characteristic for SRA [46, Fig. 5.3-5].

2.6 Detection of SRA

For the analysis of the experiment described in chapters 4 and 5, criteria are needed that allow to determine, whether SRA has been achieved. In particular, the SRA regime has to be distinguished from the Raman regime by some of the features listed in the previous section. Several footprints for SRA are given below, which can be verified by measurements. The most favorable of these are the strong spectral broadening combined with the pulse shortening. They are easy to verify and allow the clear discrimination of SRBS.

Energy Gain

According to Table 2.2, the maximum signal intensity grows quadratically with the amplification distance, z , and the electron density, n_e . Because of the pulse shortening, the signal energy grows with $(n_e z)^{1.5}$ only. While these scalings seem to be a very clear feature in theory, it is difficult to measure them in an experiment. The amplification length is difficult to control without changing other parameters. Using gas jets of different lengths is very cumbersome. An easier way is by changing the delay between the pulses. This shifts the interaction range partly out of the plasma and the effective amplification length is reduced. However in case of sub-sonic gas jets, the plasma has a long density gradient at the edges, which complicates the

quantitative comparison with the theoretical scalings.

Checking the scalings by varying the plasma density changes the results even more if the amplification does not start in the superradiant regime. The initial amplification in the Raman regime depends strongly on the exact resonance conditions for SRBS. Furthermore, the SRBS growth is exponential in the small signal regime. Both effects shift the position, where the transition from SRBS to SRA takes place and hence they change the actual amplification length in the superradiant regime.

All these side-effects have to be considered when adapting the theoretical scalings to the experimental situation. Even if these were verifiable in principle, they might be difficult to prove in a real experiment. First, they are derived under the assumption of perfect electron bunching. Furthermore, the temporal profile of the pump is usually not flat-top. For a proper comparison with the experiment, the scalings have to be integrated over the actual temporal profile instead of just multiplying by some average pump intensity approximated to a flat-top profile. Finally, the typically large fluctuations in plasma experiments could decrease the visibility of the scalings further.

Although the energy measurement itself is not the first choice for proving the amplification in the SRA regime, it allows to verify, whether the signal is amplified. With the duration the signal intensity and the important bouncing frequency ω_b can be determined.

Spectral Broadening

The spectral broadening is relatively easy to observe experimentally. It rules out usual Raman amplification, which usually exhibits narrow spectra except for two cases, where spectral broadening occurs also for Raman amplification.

- *The strongly coupled regime:* [89, 90] For high plasmas densities, the growth rate and hence the gain bandwidth can exceed the plasma frequency. However in the SRA experiments presented in this work, the plasma densities are deliberately kept at low values to avoid Raman instabilities of the pump.
- *The pump depletion regime:* A contraction of the signal pulse is also found in the pump depletion regime described in 2.5.2. It entails the broadening of the spectrum. If pump depletion occurs, a significant energy transfer ($\gg 10\%$) from the pump to the signal pulse has to take place. Unless this is observed, the pump depletion regime can be ruled out, too.

Pulse Shortening

The contraction of the signal pulse can be measured with an autocorrelator. Together with the energy measurement and the known focus diameter the signal intensity can be determined, which allows to directly check the relation $\tau_s \approx \pi/\omega_b$ by evaluating Eq. (2.24). The pulse shortening due to other mechanisms than SRA can be excluded easily. Again, there exist two further possibilities:

- *The amplification in the pump depletion regime* leads to pulse shortening. As already stated above, the pump depletion must be accompanied by a significant energy transfer from the pump to the signal pulse. Furthermore, the shortest pulses are still much longer

than expected for SRA. Even in optimal cases the shortest durations are at least 50 fs [80].

- In the measurements reported about in section 5.1, a train of short pulses is observed, which could be created by *the beating of light at two separate wavelengths*. In our case these could be due to the signal pulse and Raman backscattered pump light. However, two distinct components have then to be identified in the spectrum. The detuning $\Delta\omega$ of their central frequencies has to match the temporal spacing of the pulses, $\Delta T = 2\pi/\Delta\omega$.

Wave Breaking

The amplification in the Raman regime creates a plasma wave with the wavelength $\lambda_{pe} \approx \lambda_{\text{Laser}}/2$, which still exists after the signal pulse has already passed by. One could look for this long, regular plasma wave by making use of its regular structure, which represents a phase grating. It can diffract a probe pulse irradiated from the side. A portion of the light will be diffracted to a higher order, which can be detected. In the SRA regime, the density modulation in the plasma is rather short-living and, as apparent from Fig. 2.10a, the grating structures on the front and the rear side of the signal pulse are displaced by half a period with respect to each other. Hence their contribution to the diffraction of the probe pulse cancels.

From the theory of linear gratings [91], it is known that the wavelength of the probe pulse must be shorter than twice the length of the grating period in order to observe a maximum of the diffracted light. This means the probe pulse must have a shorter wavelength than the pump pulse. One could therefore use a frequency doubled sample of the pump pulse. It has to be focused into the interaction region of the pump and signal pulses. By moving the focus along the interaction region, the transition from Raman Amplification to SRA can be identified by a decrease of the scattered light.

However, the disappearance of the plasma wave is not a strong criterion insofar as it does not necessarily exclude the Raman regime. If the plasma wave is driven very strongly, the onset of wavebreaking can destroy the plasma wave within the range of the short signal pulse, though the amplification itself still occurs by an orderly plasma wave [80].

One prerequisite for this diagnostics is a gas jet that is accessible from the side. This is not possible for the experiments of this work presented in chapter 5. Hence the auxiliary-beam diagnostics can not be applied.

3 Experiment

This chapter outlines the experimental concept and actual setup used to demonstrate superradiant amplification. Section 3.1 first considers general issues of the implementation and then focuses on the parameters and sketches the layout of the experiment. The ATLAS system providing the laser pulses is presented in section 3.2. It proved to be difficult to generate the input signal pulse appropriate for the amplification in the superradiant regime. The various attempts are dealt with in section 3.3, while the approach used in this work is described in section 3.4 and its implementation in section 3.5. The final section 3.6 discusses the setup of the amplification experiment in the target chamber and the required diagnostics.

3.1 Implementation

The basic requirements and difficulties encountered when implementing the SRA experiment are analyzed here. Reasonable parameters for the pump and signal laser pulses and the plasma are defined, a solution for the separation of the laser pulse is offered, and the necessary diagnostics is specified.

The pump pulse is provided by the ATLAS-2 system, a chirped-pulse amplification (CPA) laser at the MPQ described in section 3.2. ATLAS-2 delivers about 200-mJ pulses at 792 nm. The pulse duration is easily adjusted in the range of 0.13-5 ps by changing the distance between the compressor gratings.

The parameters required for the signal pulse depend on the plasma density and the pump pulse intensity. Table 3.1 collects the required mean intensities of the two pulses needed to satisfy the SRA threshold for different electron densities. Obviously, these intensities can only be achieved if the pulses are focused. Several aspects have to be considered, when choosing the focus diameter:

- The focus must be small enough to achieve the required intensities with the available pulse energies. Somewhat smaller intensities for the signal pulse are acceptable, because it will be amplified.

n_e/n_{crit}	n_e	$\sqrt{a_s a_p}$	$\sqrt{I_s I_p}$	τ_{sig}
0.001	$1.7 \times 10^{18} \text{ cm}^{-3}$	0.013	$6.8 \times 10^{14} \text{ W/cm}^2$	64 fs
0.003	$5.2 \times 10^{18} \text{ cm}^{-3}$	0.022	$2.0 \times 10^{15} \text{ W/cm}^2$	37 fs
0.01	$1.7 \times 10^{19} \text{ cm}^{-3}$	0.04	$6.8 \times 10^{15} \text{ W/cm}^2$	20 fs

Table 3.1: Electron density, n_e , and corresponding threshold conditions for SRA at $\lambda \approx 800 \text{ nm}$: mean normalized vector potentials for pump and signal pulses, $\sqrt{a_s a_p}$, mean pump and signal intensities, $\sqrt{I_s I_p}$, minimal signal pulse duration at the onset of SRA, $\tau_{\text{sig}} \approx 1.2\pi/\omega_b$.

- To obtain a one-dimensional configuration with almost plane waves, the Rayleigh length must be much longer than the diameter of the focus and comparable to the interaction length of the laser pulses. In this case, the diameter of the focus is also much larger than the period of the electron grating, $\lambda/2$. The one-dimensional configuration is favored for the first SRA studies, because the analytical theory and the numerical simulations mainly deal with this geometry. An extension of the amplification scheme to divergent beams is discussed in section 6.3.
- The maximum duration τ_p of the pump pulse limits the interaction length to $1 \dots 2 \times \tau_p/(2c)$ depending on the pulse profile. This interaction length sets a reasonable value for the Rayleigh length.
- To fit into the target chamber, twice the focal length of the parabolas must be smaller than the diameter of 80 cm.

The experiment uses a focus diameter of $25 \dots 30 \mu\text{m}$ with a corresponding Rayleigh length of $600 \dots 900 \mu\text{m}$ which provides enough interaction length to observe significant amplification. For the given diameter, the signal pulse needs to have an energy of several hundred μJ . The pump and signal pulses are focused from opposite directions into the plasma by off-axis parabolic mirrors. The setup is described in detail in section 3.6.1.

The input signal pulse has to be synchronized with the pump pulse with a jitter of less than 1 ps, so that the two pulses actually meet in the plasma. There are two options to achieve this. Either the pulses share the same source, i.e. oscillator, so that they are inherently synchronized, or they have separate sources synchronized by appropriate means. The different approaches and the involved difficulties are discussed in section 3.3. For the present work, the input signal pulse is generated from a fraction split off from the ATLAS pulse. It is spectrally broadened by self-phase modulation in a gas-filled hollow fiber, spectrally filtered, and then compressed (see sections 3.4 and 3.5).

The plasma mediating the amplification has a rather low density and is typically generated in a gas jet. Hydrogen or helium are used, because these atoms can be ionized completely by an intense laser pulse. A fully ionized plasma is preferable to avoid that the amplified signal pulse is attenuated, when it becomes strong enough to ionize the atoms further. Moreover, ionization instabilities are reduced if the atoms are ionized quickly. The gas is ionized either by a separate laser pulse or by the leading edge of the pump pulse. Using an additional laser pulse separates the ionization process from the interaction process of the pulses, so that neither pump nor signal pulses are affected. However, it complicates the setup significantly, because the additional pulse has to be focused into the same gas volume without obstructing the setup of the pump and signal pulses. A numerical simulation of the ionization process shows that that the leading edge of the pump pulse can ionize the gas reliably. Therefore, we refrained from adding the extra ionization pulse.

A important issue is the most suitable way to separate the beam paths of the two counter-propagating laser pulses after their interaction. The pump pulse must not follow the signal path back into the setup for the signal pulse generation, where it would cause severe damage. Furthermore, the amplified signal pulse must be separated and sent to the diagnostics. There are two possible approaches to accomplish the separation: First, dielectric mirrors can separate the pulses by their different colors. They can be manufactured such that their reflectivity decreases

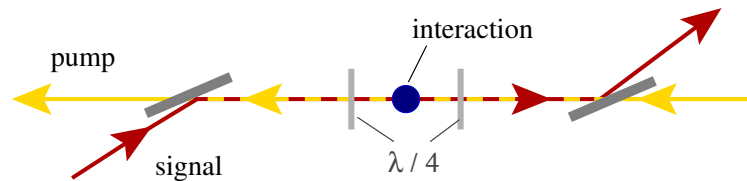


Figure 3.1: Schematic drawing of how to separate the pump and signal beam paths. The signal pulse is reflected into and out of the common beam path by (a) polarizing beam splitters or (b) dielectric mirrors with an adapted coating transmitting the pump pulse and reflecting the signal pulse. If polarizing beam splitters are used the signal pulse is s-polarized and the pump pulse p-polarized. Their polarizations have to be changed to circular polarization by quarter waveplates ($\lambda/4$) to enable the interaction.

over a range of about 5 – 10 nm from close to 1 to almost 0; *vice versa* the transmission rises from 0 to 1. This scheme cannot be applied here, because the experiments in chapter 4 use pump and signal pulses with the same central wavelength. Even for detuned pump and signal pulses, the dielectric mirrors are unfavorable: The transmission oscillates near the edge with an amplitude of up to 20 – 30 % (Fig. 3.15). Several reflections are necessary to suppress the pump pulse sufficiently. Finally, the location of the rise in the spectrum has a manufacturing tolerance of about 5 % and is sensitive to the incidence angle.

The second option used here separates the pulses by their different polarizations. It is explained in detail on page 61. The spectral overlap of pump and signal pulses is not a problem in this scheme. The suppression is about a factor 100, which is sufficient to prevent damages in the setup of the short pulse generation and the ATLAS system. However, the beam splitters have to be aligned very carefully. A small change of the incidence angle increases the crosstalk into the wrong channel significantly. Furthermore, the broad spectrum and large apertures make the required beam splitters and waveplates rather expensive.

Certain diagnostics has to be set up to characterize the input and amplified signal pulses (see 3.6.1 and 3.6.4). The amplification is ascertained by measuring the energy. The spectrum and the autocorrelation of the amplified pulse allow to prove, whether it has been amplified in the superradiant regime (2.6). Moreover, the near and far-field patterns are recorded to check, whether the amplified pulse has a good quality and can be refocused again for a following experiment. Finally, additional diagnostics has to be set up allowing to assure that the pump and signal pulses actually meet in the gas jet. Section 3.6.3 describes the diagnostics used to verify the temporal and spatial overlap in the focus.

3.2 The ATLAS System

The *Advanced Titanium-Sapphire Laser* system (ATLAS) at the MPQ is the laser source used in the present work. It is a CPA laser delivering 130-fs pulses with a central wavelength at 792 nm, 10-Hz repetition rate, and energies of up to 200-mJ. The MPQ report [19] describes the system in depth. Fig. 3.2 depicts it schematically.

The mode-locked Ti:sapphire oscillator delivers a train of 100-fs pulses. The pulses are stretched to 150 ps to avoid nonlinear effects, like self-focusing or self-phase modulation, and damages to the optical components in the following amplification stages. After the amplification, the pulse is recompressed and sent to the target chamber through an evacuated tube system.

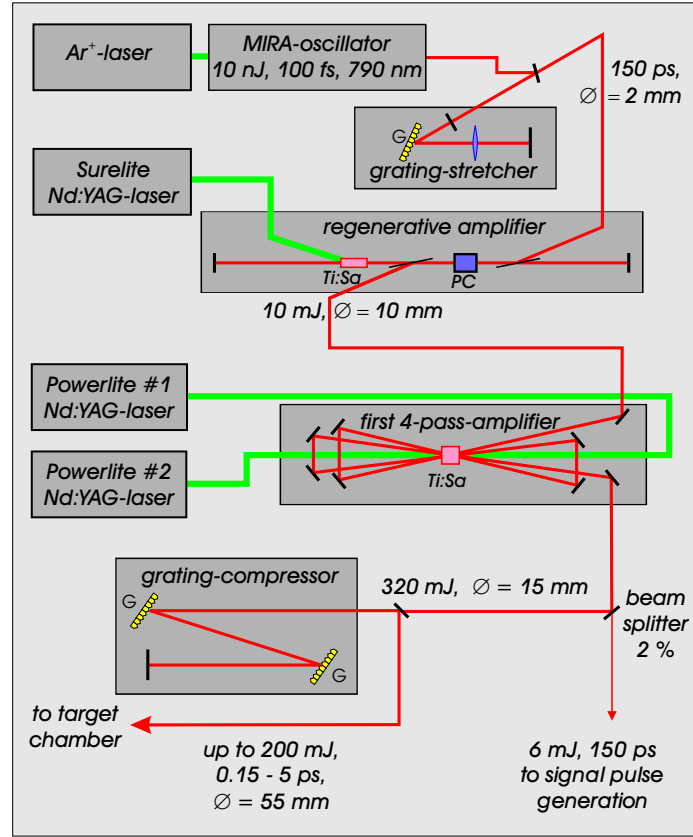


Figure 3.2: Schematic setup of the ATLAS system. Ti:Sa = Titanium doped Sapphire crystal, G = Grating, PC = Pockels Cell.

Modifications to satisfy the SRA experiment

For the SRA experiments, the ATLAS system has been modified in two ways:

1. A beam splitter is inserted before the final compressor. It splits off 2 % of the stretched pulse used to generate the input signal for the amplification (see section 3.5).
2. The distance of the compressor gratings is changed from its optimal value to increase the final pulse duration to a few picoseconds. For smaller distances, the pulse is not fully recompressed and the output pulse has a positive chirp or up-chirp, i.e. the instantaneous frequency increases with the time. Reversely, a negative chirp or down-chirp is imprinted on the pulse by increasing the distance between the gratings. The resulting pulse duration is given by [92]

$$\tau_p = \frac{\Delta d}{d_{opt}} \tau_{stretched}, \quad (3.1)$$

where Δd is the change of the grating distance and $d_{opt} = 660$ mm is the optimal grating distance that compresses the stretched pulse of duration $\tau_{stretched} = 150$ ps to its minimal duration of ≈ 120 fs. Eq. (3.1) is correct if $\tau_p \gg 120$ fs. In the experiments, the pulses are usually negatively chirped, because the mechanical constrictions of the compressor permit longer larger values of Δd and thus longer pulse durations. The maximal duration used in the experiments is 5.6 ps.

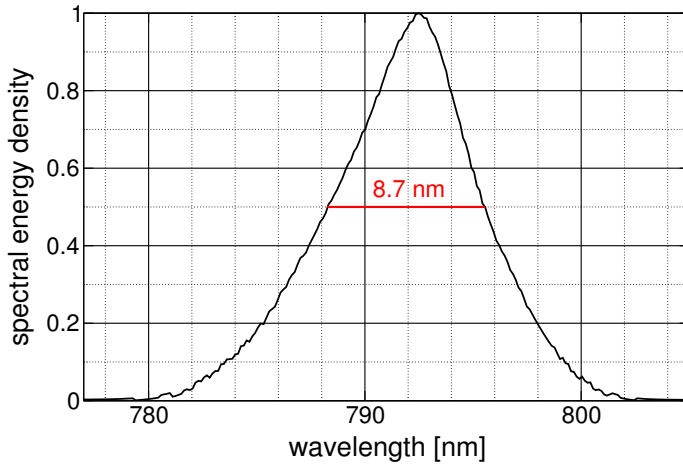


Figure 3.3: Spectrum of the ATLAS pulse after the multi-pass amplifier with the indicated FWHM bandwidth.

Since the pump pulses are strongly chirped, their temporal profile is actually given by their spectrum (Fig. 3.3). The bandwidth of 8.7 nm corresponds to the FWHM duration τ_p . The short wavelength part of the spectrum arrives first for negatively chirped pulses.

3.3 Generation of the Input Signal Pulse

While the pump pulse for the experiment is easily obtained from the ATLAS system, it is much more difficult to provide a suitable input signal pulse. The requirements are a short duration of 20-40 fs and the shift of the carrier frequency by ω_b (2.3.4) towards a lower frequency. The shift is naturally of the order of the plasma frequency, because SRA sets in when the threshold condition $\omega_b \gtrsim 0.7\omega_{pe}$ is satisfied.

Furthermore, signal and pump pulse have to be synchronized, so that they arrive in the plasma at the same time. For a plasma of about 1 mm length and a pump pulse duration of several ps, the jitter has to be less than 1 ps to ensure the interaction of pump and signal pulses in the plasma. There are basically two options to accomplish the synchronization. Either both laser pulses have the same oscillator, or their oscillators have to be coupled. In the first scheme, the original pulse is split at some point into a pump and a signal pulse. The pulses are perfectly synchronized and the arrival times are matched if the optical path lengths are equal for both pulses. They may have a small jitter, e.g., due to density fluctuations of the air caused by turbulences, but this jitter is small and can be neglected. After the separation, the central wavelength of one of the pulses has to be shifted and the durations have to be customized. This is achieved by non-collinear optical parametric amplification (section 3.3.1), by spectral broadening in a hollow-fiber waveguide (section 3.4), or by starting from a common oscillator with a broad spectrum (section 3.3.2).

Using two independent oscillators, the desired wavelengths and pulse durations can be chosen independently for each oscillator. However, certain means have to be taken to couple the oscillators and synchronize their output: Their round trip frequencies have to be matched and, in addition, the time lag between the pulses must be fixed, which corresponds to a phase-lock of their round trips. Establishing the synchronization is the major difficulty in these concepts. This path is taken with the 2-color-oscillator in section 3.3.3, and two electronically synchronized oscillators in section 3.3.4.

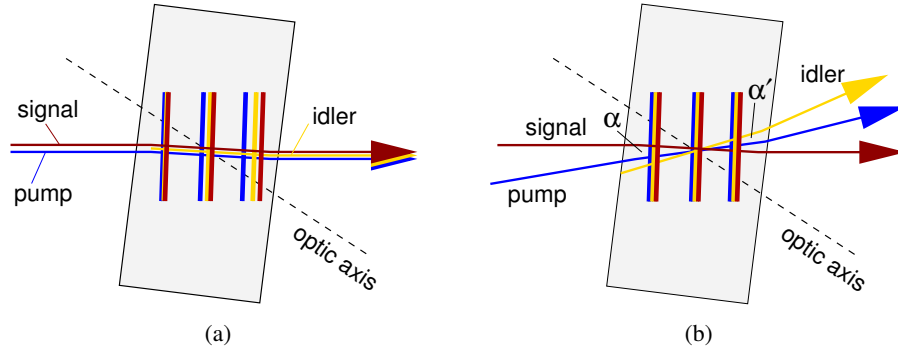


Figure 3.4: Collinear versus non-collinear optical parametric amplification in case of short laser pulses. α is the angle between the propagation directions of the pump and signal pulses, α' that between the pump and idler pulses.

The following sections discuss all approaches that have been investigated within this work. The actual amplification experiments have been carried out with the signal pulse generated by self-phase modulation in a gas-filled hollow fiber (3.4).

3.3.1 Non-Collinear Optical Parametric Amplification of a Whitelight Spectrum

Non-Collinear Optical Parametric Amplification

This scheme uses optical parametric amplification (OPA) to intensify a spectrally broad pulse from a continuous white-light spectrum [93, 94, 95, 96, 97]. OPA is a resonant three-wave process in a nonlinear optical crystal [3, 56]. A signal wave is amplified at the expense of a pump wave of higher frequency accompanied by the generation of an idler. To guarantee that the pump and signal waves stay in phase while propagating through the crystal, their phase velocities have to be matched by adjusting the angle between the optic axis of the nonlinear, birefringent crystal and the wave vectors of the laser pulses.

For very short pulses with a broad spectrum, this is not sufficient, because the group velocities of pump, signal, and idler still differ due to group velocity dispersion illustrated in Fig. 3.4a. The overlap between signal and pump pulse gets lost and the gain drops. *Non-collinear Optical Parametric Amplification* (NOPA) solves this problem by matching the group velocities geometrically. The pulses run at small angles α, α' (Fig. 3.4b) through the crystal such that the projection of the slightly higher signal and idler velocities to the propagation direction of the pump equals the group velocity of the pump pulse

$$v_{gr,pump} = v_{gr,sig} \cos \alpha \approx v_{gr,id} \cos \alpha'.$$

Using β -Barium Borate (BBO) [98] as a nonlinear crystal, α is about 7° for $\lambda_{pump} = 395$ nm and $\lambda_{sig} = 830$ nm. The second benefit of NOPA is the improved phase matching for a broader frequency range [99, 100, 101, 102]. For certain angles between the propagation directions of the pump and signal pulses with respect to the optical axis of the nonlinear crystal, phase-matching is possible for a spectral band of more than 200 nm, depending on crystal properties and pump wavelength [103, 104, 41, 42]. This is particularly important, when amplifying ultra-short laser pulses.

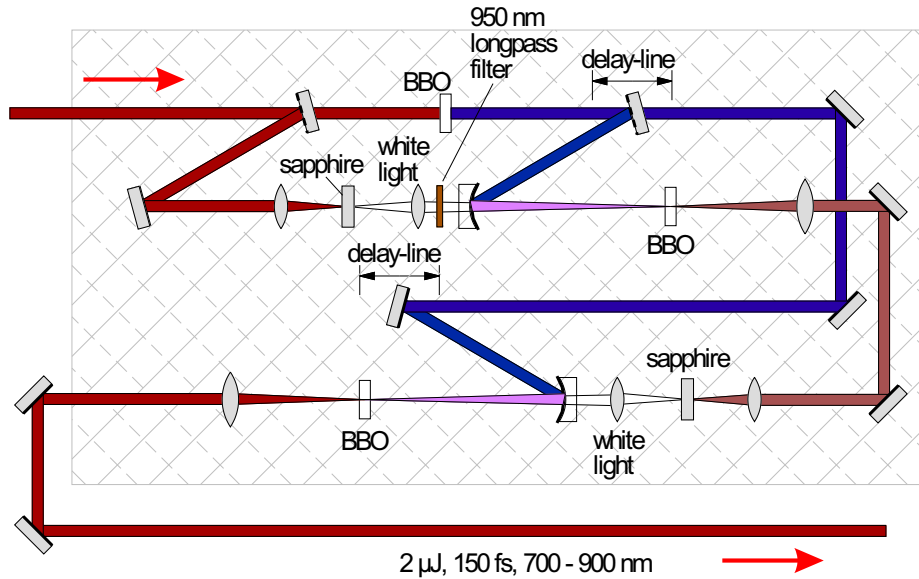


Figure 3.5: Two-stage NOPA setup to generate a frequency-shifted, short input signal pulse.

For a perfect overlap of the pump and signal pulses, the amplitude front of the pump pulse has to be tilted by α with respect to its propagation direction. However, this is not required if both pulses are focused, so that their longitudinal and transversal dimensions are about the same inside the crystal, because their intensity distribution is approximately spherical and a tilt has no effect.

NOPA applied to generate a short, wavelength shifted pulse from a whitelight continuum

A commercial system [105, 93, 94, 95] depicted in Fig. 3.5 was used to implement the NOPA scheme. As input pulse for the system 1 – 2 % of the main ATLAS pulse are split off after the multi-pass amplifier (Fig. 3.2) and compressed in a separate grating compressor to 120 fs. A small fraction of the pulse is focused into a 1-mm thick sapphire plate, where self-phase modulation (SPM) generates a whitelight spectrum [106, 107, 108, 109]. The rest of the input is frequency doubled with an efficiency of about 30 % and provides the pump for the NOPA. The NOPA stages amplify the whitelight spectrum around the desired wavelength with the bandwidth of about 40 nm.

The whitelight spectrum in Fig. 3.6 has a pronounced maximum around the central wavelength of the incoming pulse and falls off rapidly on both sides. On the short wavelength side, it is followed by a plateau, which drops off at 500 nm and ends approximately at 400 nm. On the near infrared side, the spectrum falls steadily. The whitelight pulse is linearly chirped and the desired spectral band is selected by changing the delay between the whitelight and the pump pulse. The amplified pulse is compressed by removing the chirp in a prism compressor. However, the range around the original wavelength at 792 nm is not linearly chirped and it is not possible to directly obtain short pulses in the wavelength region around 830 nm.

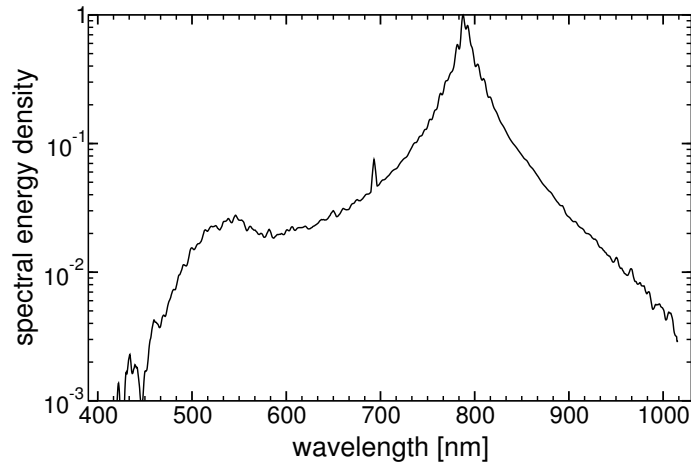


Figure 3.6: Measured spectrum after first whitelight generation.

Instead, the whitelight is spectrally filtered, blocking the wavelengths below 950 nm. The first NOPA stage amplifies the remaining spectrum around 1000 nm. The pulse is focused again into a sapphire plate to generate a second whitelight spectrum. The desired wavelength range for the signal pulse lies now in the plateau region and is amplified in the second NOPA stage. Changing the delay between the chirped whitelight pulse and the pump pulse allows to tune the wavelength of the amplified pulse between 700 nm and 900 nm.

Because the pulses are focused into the BBO crystals, the cross section of the pulses is small and the achievable energies are limited to a few μJ . For the SRA experiment, a signal pulse of several hundred μJ energy is required. A multi-pass amplifier with Ti:sapphire as laser medium was projected for the further amplification followed by a prism compressor to remove the chirp and compress the final pulse to 30 fs.

Problems impeding the use of NOPA pumped by ATLAS

The NOPA, the white-light generation and the frequency doubling are all nonlinear processes. The energy fluctuations of the incoming pulse delivered by ATLAS are increased in each stage unless the stages work in saturation. The present NOPA implementation, however, has been designed for a kHz pump laser system with good pulse-to-pulse stability. This ensures that the NOPA output fluctuates by only a few percent. The ATLAS system, on the other hand, is optimized for peak powers. The resulting shot-to-shot fluctuations of up to 5 % are too large to accomplish the stable operation of the NOPA system. Operating the frequency doubling in saturation [110] can help to reduce the sensitivity of the system but is not sufficient.

Furthermore, the low repetition-rate of the ATLAS system makes the adjustment very demanding. Several requirements must be met at the same time: (1) the foci of pump and signal pulse have to overlap in the crystal; (2) the delay has to be adjusted very precisely due to the short pulse durations; (3) the correct angles between signal pulse, pump pulse, and the crystal axis have to be found. Since the 10-Hz repetition rate of ATLAS reduces the average power by a factor of 100 as compared to a kHz system, it is difficult to observe a weak signal, if the pulses overlap only partially, or if the angles or the delay are not correctly adjusted. For these reasons, the NOPA option was not further pursued.

3.3.2 One Common Oscillator with a Broad Spectrum

This option makes use of the spectral proximity of the required pump and signal pulses. One starts with a common short pulse oscillator delivering 15-fs-pulses with 60 nm bandwidth and a central wavelength at 830 nm as they are commercially available [111]. The pulses are split into a pump and a signal pulse. The signal pulse is stretched to a few picoseconds, amplified in a multi-pass amplifier and recompressed by a prism compressor.

The pump pulse is amplified in the the ATLAS system after it has been cut on the short wavelength side, shaping the spectrum such that it resembles the one of the original ATLAS oscillator with the central wavelength near 790 nm and a bandwidth of about 10 nm. This is important, because the stretcher, amplifiers, compressor, and optical components are specifically designed and set up for these parameters.

In pre-experiments it has been investigated, whether the spectral shaping can be accomplished by spectral filtering to remove the components above 800 nm. The short pulse arm of the two-color-oscillator was used as a source with a bandwidth of 40 nm and the central wavelength shifted to 820 nm to have more energy around 790 nm. However, it was not possible to obtain a reasonably shaped spectrum with the available dielectric filters. Apart from the maximum at 790 nm, the spectrum had several further spikes towards longer wavelengths. Moreover, the pulse energy was attenuated so much that it could not be compensated for in the regenerative amplifier of ATLAS. Because of these disadvantages, the option using a common oscillator was abandoned.

3.3.3 Two-Color-Oscillator

A two-color-oscillator couples two mode-locked laser cavities by the common Ti:sapphire amplifier crystal [112, 113]. The wavelengths and pulse durations can be adjusted separately for each cavity, because their dispersion is controlled independently. The laser crystal is pumped by two almost parallel Nd-YAG laser beams focused with a single objective lens to two slightly overlapping foci near the surface of the Ti:sapphire crystal. In the mode-locked state, the circulating pulses interact in the overlap region by the mutually induced Kerr effect. After a first accidental encounter in the crystal, the interaction synchronizes them during the following round-trips. For the coupling to work properly, the round trip periods must be equal, i.e. the lengths of the two cavities have to be matched to the μm -scale. The typical jitter of the output pulses is much smaller than the pulse durations.

The amount of overlap is a crucial parameter for the stable operation of the two-color-oscillator. The foci have to overlap by about 10 % to ensure sufficient interaction. If it is less, the coupling is too weak and the pulses will not get synchronized. For a larger overlap the gain competition of the pulses becomes dominant. The stronger pulse is more strongly amplified at the expense of the weak pulse. The round trip gain of the latter becomes too small and the mode-locking finally stops.

Our two-color-oscillator was a replica of the system first built by A. Leitensdorfer [112]. One arm of the oscillator was intended to replace the ATLAS oscillator. It generated 100 fs-pulses at 790 nm. To serve as a source for the signal pulse, the second cavity was tuned to 830 nm with a four times larger bandwidth of 40 nm, which corresponded to a pulse duration of 25-30 fs.

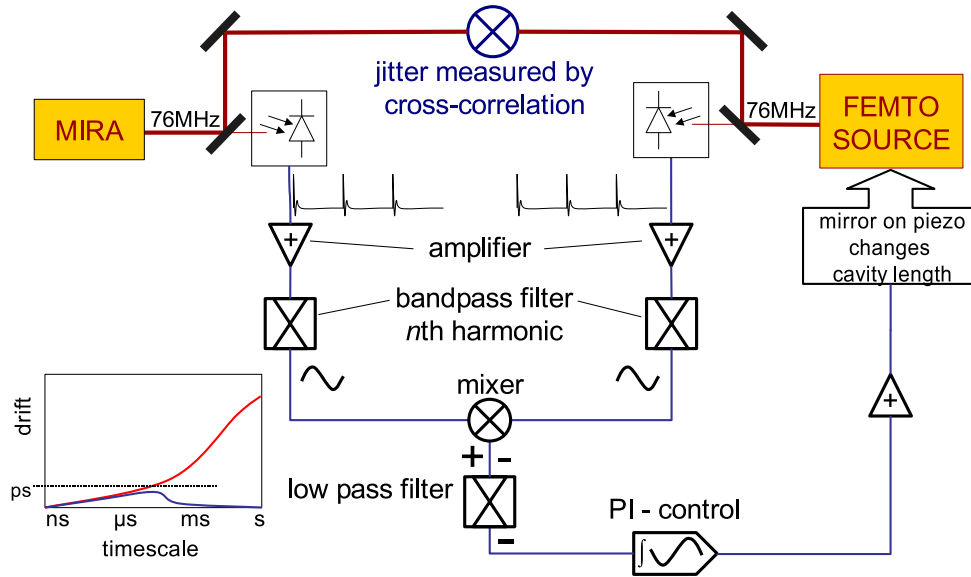


Figure 3.7: Electronically coupled oscillators: Schematic drawing of the PLL circuit for the synchronization of the ATLAS oscillator and a Femtosource short-pulse oscillator. The graph in the lower left corner sketches the jitter occurring on different time scales (red curve). Large fluctuations appear on slow time scales and can be compensated for by the rather slow piezo transducer resulting the blue curve for the jitter.

However, a stable everyday operation of the oscillator could not be achieved. The large temperature drifts in the laboratory were identified as the main reason for the failure. They caused changes in the cavity lengths and deviations of the beam directions, which affected the overlap of the pulses in the Ti:sapphire crystal.

3.3.4 Electronically Coupled Oscillators

Recently, it was shown that two independent fs-oscillators can be coupled electronically by a phase-locked-loop (PLL) control circuit such that their output pulses are synchronized with a residual jitter on the fs scale [114, 115, 116, 117, 118]. The PLL synchronizes the pulse trains of the two oscillators: It equalizes the round-trip frequencies of the pulses in the cavities, in particular, it fixes the temporal offset of the pulse trains, which corresponds to a phase-lock of the round trip phase.

Fig. 3.7 depicts a schematic circuitry for the control loop. It starts by detecting the output of the two oscillators with fast photodiodes. The bandpass filters select a certain harmonic of the pulse trains, i.e. a multiple of the round-trip frequency of 76 MHz. Using a higher harmonic makes the PLL more sensitive, but also increases the demands on the electronic components. The two sinusoidal harmonics are mixed in a phase detector. The output signal has the sum frequency as carrier frequency with the modulation of its amplitude equal to difference frequency. A low-pass filter selects the latter. The integrated signal is used to control the length of one of the oscillator cavities by means of a piezo transducer that has one of the cavity mirrors attached to it. As soon as the relative phase of the pulse trains starts to

drift, the integrated signal deviates from zero, causes a change of the cavity length and thereby changes the round-trip time until the relative phase has returned to its original value.

The slowest component in the control loop is the piezo transducer with a bandwidth of a few 10 kHz. Its electric capacity and the inertia of the mirror attached to it cause the slowdown of its response. However, it is possible to achieve a femtosecond synchronization because the jitter of the round-trip frequencies becomes random only on the 10 μ s time scale [115]. On shorter time scales, the turbulences of the air and the power fluctuations of the pump laser of the oscillator cause only linear, monotonic drifts, which can be compensated for with quite a slow actuator. The jitter can be reduced to less than 1 fs [116]. Even larger drifts due to temperature changes in the laboratory become important only after minutes or hours and are compensated by a motorized translation stage supporting the piezo transducer.

In first experiments at the MPQ, a ‘‘Femtosource 20’’ oscillator from Femtolasers GmbH has been locked with the ATLAS oscillator. Using the 14th harmonic of the round trip frequency, the synchronization was established with a jitter of less than 500 fs. The pulses exiting the oscillator have to be pre-amplified in a multi-pass-oscillator to several hundred μ J to serve as input pulses for the SRA experiment. The generation of the signal pulse from an independent oscillator coupled electronically to the oscillator of the pump laser appears to be the most promising approach for a future implementation of the SRA experiment. It is able to reliably deliver short signal input pulse at the desired wavelength.

3.4 Signal-Pulse Generation with the Hollow-Fiber Technique

The signal pulse is generated from a small fraction split off from the ATLAS pulse. The scheme uses *Self-Phase Modulation* (SPM) in a gas-filled hollow fiber to broaden the spectrum and compress the pulse further to about one fifth of the original duration [119, 120, 121, 122, 123, 124].

3.4.1 Self-Phase Modulation (SPM) at High Intensities

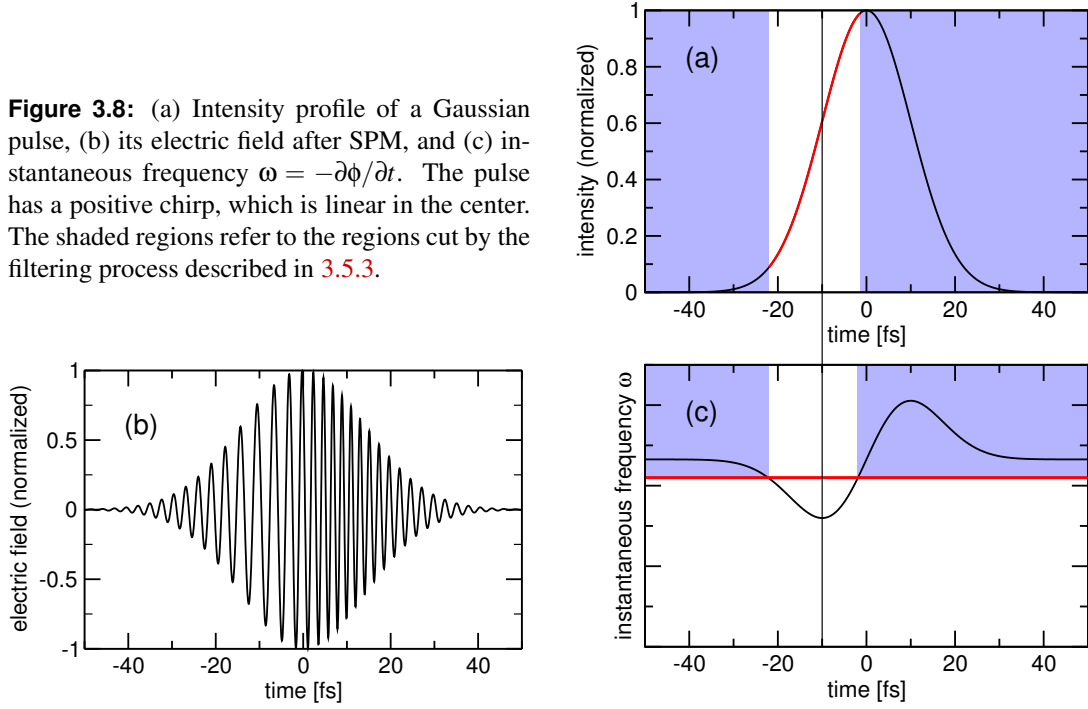
SPM is caused by the nonlinear dependence of the refractive index n on the laser intensity [52, 125]

$$n = n_0 + n_2|E(t)|^2 = n_0 + \bar{n}_2 I(t). \quad (3.2)$$

Here n_0 is the linear refractive index, valid for low intensities, n_2 and $\bar{n}_2 = 2n_2/(\epsilon_0 c n_0)$ are the nonlinear index coefficients to express the change of n in terms of the electric field E and the intensity I , respectively. Since the nonlinear refractive index is a result of a third order optical nonlinearity, n_2 can be expressed by the third order polarizability tensor $\chi^{(3)}$, $n_2 = 3\chi^{(3)}/(8n_0)$. Far from resonances, n_2 is positive. As the intensity of the fs-laser pulse is time and space dependent, different parts of the pulse experience different refractive indices. An intensity profile with the maximum in the center focuses the pulse in space. When this focusing overrides diffraction, self-focusing can occur. The temporal dependence leads to the spectral broadening and a chirp of the resulting pulse, because the effective optical path length depends on the intensity. The phase $\phi(z, I)$ of the laser pulse reads

$$\phi(z, t, I(t)) = k(I(t))z - \omega_0 t = k_0 z + k_0 z \frac{\bar{n}_2}{n_0} I(t) - \omega_0 t$$

Figure 3.8: (a) Intensity profile of a Gaussian pulse, (b) its electric field after SPM, and (c) instantaneous frequency $\omega = -\partial\phi/\partial t$. The pulse has a positive chirp, which is linear in the center. The shaded regions refer to the regions cut by the filtering process described in 3.5.3.



$$= \phi_0(z, t) + k_0 z \frac{\bar{n}_2}{n_0} I(t), \quad (3.3)$$

where $\phi_0 = k_0 t - \omega_0 t$ and $k_0 = 2\pi n_0/\lambda$ are the phase and the wavenumber in the linear case, respectively, and z is the propagation distance in the nonlinear medium. The instantaneous frequency ω is given as the time derivative of ϕ ,

$$\omega = -\frac{\partial\phi(z, t)}{\partial t} = \omega_0 - k_0 z \frac{\bar{n}_2}{n_0} \frac{\partial I(t)}{\partial t}. \quad (3.4)$$

The example in Fig. 3.8 shows the phase and the frequency modulation for a Gaussian pulse. For the body of the pulse, which contains most of the energy, the temporal shape can be approximated by a parabola. Therefore, $\partial I(t)/\partial t$ is linear, which implies that the body of the pulse mainly carries a linear positive chirp and can be compressed afterwards by standard means.

Eqs. 3.3 and 3.4 assume an instantaneous response of the nonlinear medium to the electric field, i.e., there is no time delay between the acting electromagnetic wave and the change $\bar{n}_2 I$ of the refractive index. This assumption is justified, because the 120 fs-pulse is much longer than the response time of an electronic nonlinearity, which is of the order of 1 fs. For pulses short compared to the response time, the pulse envelope becomes tilted towards later times, i.e. its maximum lags behind [125, Fig. 3.14].

The *nonlinear interaction length*

$$L_{NL} = \frac{n_0}{\bar{n}_2 k_0 I_{\max}}. \quad (3.5)$$

defines the length scale, on which the phase-shift due to SPM becomes significant. It allows to write the maximum phase shift in Eq. (3.3) as z/L_{NL} . The spectral broadening

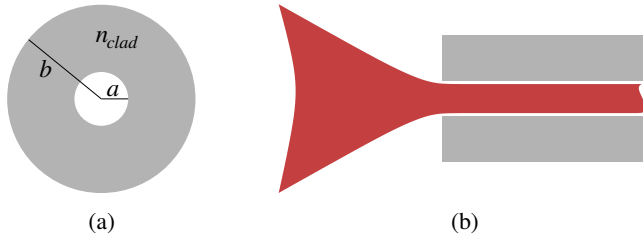


Figure 3.9: (a) Front of the hollow fiber. (b) Coupling into the fiber: The focus of the laser pulse is positioned at the fiber entrance.

$\delta\omega$ (FWHM) derived from Eq. (3.4) can be approximated by $\delta\omega = \frac{z}{L_{NL}} \frac{1}{\tau_0}$, where τ_0 is the FWHM of the input pulse. A detailed derivation for a Gaussian pulse with the intensity profile $I(t) = I_{\max} \exp(-4 \ln 2 (t/\tau_0)^2)$ yields [125]

$$\delta\omega\tau_0 = 4\sqrt{2}\ln(2) \frac{z}{L_{NL}}. \quad (3.6)$$

The time bandwidth product of a fully compressed Gaussian pulse is $\delta\omega\tau_0 \approx 2.77$, whereas it is about 3.4 for the compressed ATLAS pulse. To achieve large values of z/L_{NL} , the laser pulse is guided in a fiber. With the implementation described below, values of $z/L_{NL} \approx 8-10$ and $\delta\omega\tau_0 \approx 30-40$ are accomplished. Typical values for L_{NL} are given in Table 3.2 on page 52. For $z/L_{NL} \geq 3$, the resulting broadened spectrum starts to break up into more and more parts [125, Fig. 3.13].

3.4.2 Pulse Propagation as Fiber Mode

Spectral broadening of ps- and fs- laser pulses in single-mode optical fibers has been applied since the early 1980s [126, 127]. Compression down to 6 fs were achieved by careful compensation of the nonlinear chirp [128]. The optical fiber acts both as a waveguide and as a nonlinear medium that causes the SPM. However, the use of solid-state fibers restricts the pulse energies to the nJ-level. More recently, Nisoli *et al.* replaced the solid state fibers by dielectric hollow fibers made from fused silica [119], also called capillaries. They are filled with different kinds of gas, typically Argon or Krypton. They merely serve as waveguide, while the SPM is predominantly caused by the gas.

The hollow fibers have bore diameters between a few ten μm up to a few hundred μm (Fig. 3.9a). The fused silica wall has the refractive index $n_{\text{clad}} = 1.485$, whereas for the gas inside it is $(n_{\text{gas}} - 1) \approx 10^{-4}$. The propagation through the fiber can be envisaged in two pictures:

1. In a simple picture, the pulse is guided by multiple total internal reflections from the walls. Beams with larger reflection angle are not completely reflected. They suffer from higher losses and are attenuated stronger. Adjusting the focus diameter at the entrance minimizes the angle and hence the losses (Fig. 3.9b).
2. The pulse entering the fiber is decomposed into a superposition of fiber modes propagating independently through the hollow fiber disregarding nonlinear coupling at the moment. This mode picture is used in the following discussion.

The solution of the wave equation for electromagnetic waves in a cylindrical waveguide leads to a set of propagation modes [129, 130] characterized by a set of orthogonal functions

describing the field distribution. They are categorized in three classes with specific properties of the electric and magnetic fields.

- For transverse electric modes (TE_{0m}), the electric field has no longitudinal component. Lines of constant electric field strength are concentric circles centered on the propagation axis. The magnetic field has both a transverse and longitudinal component.
- For transverse magnetic modes (TM_{0m}), the situation between the electric and magnetic fields is reversed.
- Hybrid modes (EH_{nm}) have all components of the electric and magnetic fields, whereby the contributions in the propagation direction are small.

The individual modes are further distinguished by their mode numbers n and m , where m refers to the number of nodes in the radial direction and n refers to their number in the azimuthal direction. In the case of a hollow fiber with dielectric walls the modes are called *leaky*, because losses occur as the evanescent field spreads through the wall material and an electromagnetic wave is radiated outside. The losses typically increase with the mode numbers. If the fibers are long enough, only the mode with the lowest attenuation survives, whereas the others are depleted. The TE_{01} mode has the smallest attenuation [130, 131]. However, the dispersion relation shows that electromagnetic waves can propagate in this mode only if the ratio of the refractive indices of wall material and gas satisfies the condition $v = n_{\text{wall}}/n_{\text{gas}} > 2.02$, which is not true for fused silica. Here, the EH_{11} mode is attenuated least. The propagation of electromagnetic waves through the fiber is characterized by its complex wavenumber γ , also called *propagation constant*. Its real and imaginary parts are given by the phase constant β and the attenuation α , respectively, [130]

$$\beta = \text{Re } \gamma = k \left[1 - \frac{1}{2} \left(\frac{u_{11}\lambda}{2\pi a} \right)^2 \right], \quad (3.7)$$

$$\alpha = \text{Im } \gamma = \left(\frac{u_{11}}{2\pi} \right)^2 \frac{\lambda^2}{a^3} \frac{v^2 + 1}{2\sqrt{v^2 - 1}}, \quad (3.8)$$

where a is the bore radius of the fiber and $u_{11} = 2.405$ is the first root of the Bessel function J_0 . For the bore diameter $2a = 250 \mu\text{m}$ used in the experiment, the attenuation of the fiber is $\alpha = 0.07 \text{ m}^{-1}$. The resulting transmission for the fiber lengths $l = 0.6 \dots 0.75 \text{ m}$ is $\exp(-\alpha l) \approx 94 \%$.

The attenuation constant increases significantly if the hollow fiber is bent. For the EH_{11} mode, the dependence on the radius of curvature R is given by [130]

$$\alpha_{11}(R) = \alpha_{11}(\infty) \left\{ 1 + \frac{4}{3} \left(\frac{2\pi a}{u_{11}\lambda} \right)^4 \left(\frac{a}{R} \right)^2 \left[1 - \frac{1}{u_{11}^2} + \frac{3}{4} \frac{\text{Re}\sqrt{v^2 - 1}}{\text{Re}\frac{v^2 + 1}{\sqrt{v^2 - 1}}} \cos 2\theta \right] \right\}, \quad (3.9)$$

where θ is the angle between the electric field and the plane of curvature and $v = n_{\text{wall}}/n_{\text{gas}}$. Using the experimental parameters and $\theta = 0$, the attenuation doubles for $R = 30 \text{ m}$. Over a length of 2 cm , this is equivalent to a lateral deviation of only $10 \mu\text{m}$ from the perfectly straight

alignment. Therefore, great care has to be taken to assure that the fiber is kept straight in its mount.

Another critical issue for a high energy transmission is the proper focusing of the pulse into the fiber. Firstly, the incoming pulse and the fiber have to be coaxial. Secondly, the focal radius r_0 has to be adapted to the bore radius. Efficient energy coupling to the fiber is achieved if the incoming pulse matches the desired fiber mode best, i.e., the integral of the overlap of the fields has to be maximized. A focal radius of $r_0 \approx 0.7a$ maximizes the coupling efficiency to the mode EH_{11} and reduces coupling to fiber modes of higher order exhibiting larger transmission losses [121]. Here, r_0 is the $1/e^2$ waist radius of the Gaussian intensity profile. A mismatch of 10 – 15 % is acceptable.

3.4.3 Spectral Broadening by SPM in the Gas-Filled Hollow Fiber

Several practical aspects have to be considered when using hollow fibers filled with a noble gas for spectral broadening.

Dispersion

SPM in a non-absorbant medium does not increase the pulse duration or change the shape of its profile. However, the group velocity dispersion (GVD) in the medium causes significant pulse lengthening, if the propagation distance becomes longer than the dispersion length, $L_D = \tau_0^2/k_0''(\omega)$ [125], where τ_0 is the duration of the fully compressed pulse. The GVD parameter $k_0''(\omega)$ has contributions both from the gas and the fiber. For the hollow fiber, k_{fiber}'' is obtained by differentiating Eq. 3.7 twice

$$k_{\text{fiber}}''(\omega) = \beta''(\omega) = -\left(\frac{u_{nm}}{a}\right)^2 \frac{1}{(2\pi)^3 c^2} \lambda^3 = -0.258 \text{ fs}^2/\text{m} \cdot \frac{\lambda[\mu\text{m}]}{a[\text{mm}]}. \quad (3.10)$$

For $a = 0.125 \text{ mm}$ and $\lambda = 0.8 \mu\text{m}$, the GVD parameter is $-2.0 \text{ fs}^2/\text{m}$. The GVD of the gas is derived from its wavelength dependent refractive index given in [132] for all noble gases. At pressure p and temperature T , one finds the dispersions

$$k_{\text{Ar}}''(\omega_0) = -20.0 \text{ fs}^2/\text{m} \cdot p[\text{bar}] \frac{293 \text{ K}}{T}, \quad (3.11)$$

$$k_{\text{Kr}}'(\omega_0)' = -40.3 \text{ fs}^2/\text{m} \cdot p[\text{bar}] \frac{293 \text{ K}}{T} \quad (3.12)$$

for the center frequency $\omega_0 = 2\pi c/792 \text{ nm}$ of the ATLAS pulses. Hence the dispersion due to the gas dominates the total GVD. In the experiment, gas pressures of several 100 mbar are used resulting in dispersion lengths of the order

$$L_D = \frac{\tau_0^2}{k_0''(\omega)} \approx 0.5 \dots 1 \text{ km}. \quad (3.13)$$

It is therefore easy to find a regime, where the fiber is long enough to cause sufficient spectral broadening by SPM, whereas it is short enough to avoid pulse lengthening by dispersion: $L_D \gg \text{length of the fiber} \gg L_{LN}$.

Table 3.2: Ionization threshold [135], nonlinear refractive index n_2 [136], and nonlinear interaction length L_{NL} of noble gases. n_2 and L_{NL} are given for $T = 295$ K, $p = 1$ bar, and $I_{\max} = 2.5 \times 10^{13}$ W/cm².

	$I_{\text{ionize}} [\text{W}/\text{cm}^2]$	$n_2 [\text{cm}^2/\text{W}]$	$L_{NL} [\text{m}]$
He	12×10^{14}	0.36×10^{-24}	1.078
Ne	7×10^{14}	0.65×10^{-24}	0.599
Ar	2.2×10^{14}	8.5×10^{-24}	0.046
Kr	1×10^{14}	23×10^{-24}	0.017
Xe	0.7×10^{14}	68×10^{-24}	0.0057

Effective fiber length l_{eff} and effective intensity I_{eff} in the fiber

While the pulse propagates through the hollow fiber, the nonlinearity $\bar{n}_2 I$ becomes smaller, because the intensity of the pulse decreases. The total phase change $\Delta\phi$ due to SPM is obtained by integrating the second term in Eq. (3.3) over the length of the fiber l ,

$$\Delta\phi = \int_0^l k_0 \frac{n_2}{n_0} I(t) e^{-\alpha z} dz = k_0 \frac{n_2}{n_0} I(t) \frac{1 - e^{-\alpha l}}{\alpha}. \quad (3.14)$$

The attenuation is included in a simple way in Eq. (3.3) by replacing the physical length l by the *effective fiber length* $l_{\text{eff}} = (1 - e^{-\alpha l})/\alpha$.

The effective intensity accounts for the transverse intensity pattern of the pulse. It is computed as the average transverse intensity weighted with the power

$$I_{\text{eff}} = \langle I \rangle = \frac{\int I \cdot IdA}{\int IdA} = \frac{\int I^2 dA}{P_{\text{tot}}}. \quad (3.15)$$

For pulses with Gaussian transverse profile, the result is $I_{\text{eff}} = I_{\max}/2$.

Choice of the gas as to obtain a broad spectrum and maximum energy transmission

The SRA experiment needs a sufficiently strong and short input pulse to start in the superradiant regime. Therefore, a configuration is required that permits a high-energy transmission through the fiber and a large spectral broadening. The energy transmission is primarily limited by the cross section of the fiber bore and the maximum intensity. The choice of the fiber diameter $2a = 250 \mu\text{m}$ is explained in section 3.5.1. The intensity has to be kept clearly below the ionization threshold for the gas filled into the hollow fiber (Tab. 3.2). For intensities very close to the ionization threshold, the spectrum gets shifted towards shorter wavelengths by ionization blueshift [133, 134]. This is undesirable because the SRA experiments ideally needs an input signal pulse shifted towards longer wavelengths with respect to the pump pulse. Therefore, their higher ionization thresholds render the lighter noble gases more favorable. On the other hand, a significant broadening ($l/L_{NL} \gg 1$) must be achieved for a reasonable fiber length ($l \leq 1$ m) and reasonable pressures ($p \leq 1.5$ bar). This is only possible for the heavier gases with higher atomic polarizabilities.

Apart from the gas, the hollow fiber sets a limit to the maximum intensity, too, since the input pulse is not perfectly focusable. Light diffracted from the central focal disc hits the wall material and can ionize it. The plasma at the entrance prevents a proper coupling of the pulse energy into the fiber. For the evacuated fiber, the maximum intensity is limited to about

$5 \times 10^{13} \text{ W/cm}^2$.¹

An analysis of the data in Tab. 3.2 shows that only Ar and Kr are suitable filling gases. In the experiment, Ar is used because it allows a slightly higher energy transmission. The lower polarizability is compensated by increasing the gas pressure and the pulse intensity. Subtracting the light lost at the entrance, the effective intensity in the experiment was about $3 \times 10^{13} \text{ W/cm}^2$.

Self-focusing in the waveguide

The change in the refractive index $n_2 I$ causes SPM in the temporal domain, but also focuses the pulse spatially. At sufficiently high intensities, self-focusing scatters light from the fundamental mode, EH_{11} , into higher-order modes, which have stronger attenuation. The threshold for the onset of self-focusing in Argon is given by $Pp = 18.4 \text{ GW} \cdot \text{bar}$ [137, 138], where P is the pulse power and p the gas pressure. For experimental parameters, the product of power and pressure was at most $5.0 \text{ GW} \cdot \text{bar}$ and hence well below the limit for self-focusing.

Compression

The choice of the compressor to remove the chirp from the spectrally broadened pulse depends on the initial pulse duration. For rather long input pulses $> 100 \text{ fs}$, a prism compressor is adequate. The minimum pulse duration is around $\approx 20 \text{ fs}$, [119]. 20-fs input pulses can be compressed to 5 fs but means have to be taken to remove higher-order dispersion, e.g., using chirped mirrors. The prism compressor can be combined or replaced with specifically designed chirped mirrors [124].

3.5 Implementation of the Short Pulse Generation and Characterization of the Input Pulse

3.5.1 Setup

Fig. 3.10 depicts the setup for the generation of the signal input pulse for the SRA experiment. A partially transparent mirror splits off 2 % ($\approx 6 \text{ mJ}$) from the uncompressed ATLAS-2 pulse after the multi-pass amplifier (Fig. 3.2). A combination of a $\lambda/2$ -waveplate and polarizing beam splitter allows the fine tuning of the energy. The pulse is compressed to 120 fs in a grating compressor equivalent to the ATLAS compressor. After the compression, a telescope² reduces the diameter of the pulse³ from 12 mm to 4 mm. A lens focuses the pulse to the entrance of the hollow fiber. While the pulse propagates as a fiber mode, it is spectrally broadened by SPM. After the fiber, a mirror recollimates the diverging pulse. The optional filter (F) absorbs or reflects the short wavelength part of the pulse. A prism compressor removes the chirp that

¹ Actually, residual gas - Ar, Kr or air - could be responsible for the limitation of the intensity. The vacuum pump connected to the fiber allowed only for a vacuum on the mbar level. The residual gas could have been ionized. If this was the case, the maximum transmitted intensity should increase when the fiber is flooded several times with He and evacuated again, because of the higher ionization threshold of He. However, an increase of the maximum intensity was not observed.

²The telescope is not mandatory in the present setup but would have been necessary when using NOPA.

³The pulse diameter refers to twice the radius, where the intensity has dropped to $1/e^4$ of its maximum [139].

the pulse has obtained by the SPM in the hollow fiber. Finally, a second telescope increases the pulse diameter to 38 mm.

The hollow fiber is placed in an Argon atmosphere inside a plexiglass tube. To keep the fiber straight, it rests in a V-groove milled into a aluminum bar, which is slightly shorter than the fiber itself. The ends of the tube are closed by brass caps with small, 0.5 mm-thick, AR-coated entrance and exit windows for the laser pulse.

To obtain a high-energy throughput, a fiber with a large bore cross section is necessary because the maximum intensity inside the fiber is limited by the ionization threshold of the Argon gas. Furthermore, a larger diameter reduces the attenuation of the pulse by the fiber as seen from Eq. (3.7). On the other hand, the attenuation becomes more sensitive to bending (cf. Eq. (3.9)). The handling of the fiber is more difficult and the demands for a precise manufacturing of the fiber as well as the suspension V-groove increase. Moreover, a larger diameter requires a weaker focusing with a smaller f-number, i.e. a longer focal length. This decreases the beam diameter on the entrance and exit windows if the length of the plexiglass tube is kept constant. At the same time, the pulse energy is higher, because the larger bore cross section can carry more energy. However, the increased flux on the windows well below their damage threshold and effectively limits the maximum bore diameter.

In the experiment, fibers with bore diameters of 250 μm and 0.65 m length are used. The maximum possible input energy of the pulses is ≈ 1.4 mJ and is limited by the onset of ionization at the entrance. The transmission starts fluctuating and the spatial profile of the fiber output degrades. The observed transmission of 50-60 % is much smaller than the theoretical value of 94 % given by Eq. (3.7). The further losses can be attributed to a number of deviations from the ideal conditions:

- The input pulse is not ideally Gaussian (Fig. 3.11a). Parts of the pulse hit the wall and do not enter the fiber. Furthermore, the imperfect focus favors the coupling to fiber modes of higher order, which are attenuated stronger.
- The attenuation increases due to bending Eq. (3.9) because the fiber does not rest ideally straight in the V-groove.
- Due to faults in the manufacturing process, some of the hollow fibers show density inhomogeneities or cracks along the inner side of the wall. The transmission is reduced by more than 30 % making these fibers not suited as waveguides.
- The coupling efficiency gradually decreases over a longer operation period, because the stray light hitting the wall material around the fiber entrance gradually destroys the wall and creates a kind of funnel.

For the evacuated tube with a residual pressure ≤ 1 mbar, the output energy is around 0.72-0.82 mJ. The higher value refers to a fiber entrance with intact walls and the latter to the degraded case after a longer operation period. Filled with 650 mbar Argon, the output decreases to 0.63-0.71 mJ.

After the primary setup, the coupling to the fiber has to be readjusted during the alignment procedure before the experiment and during the experiment if thermal drifts of ATLAS cause a change of the propagation direction and the focus position at the fiber entrance. To align the fiber, the surrounding tube is mounted on linear translation stages that allow to move

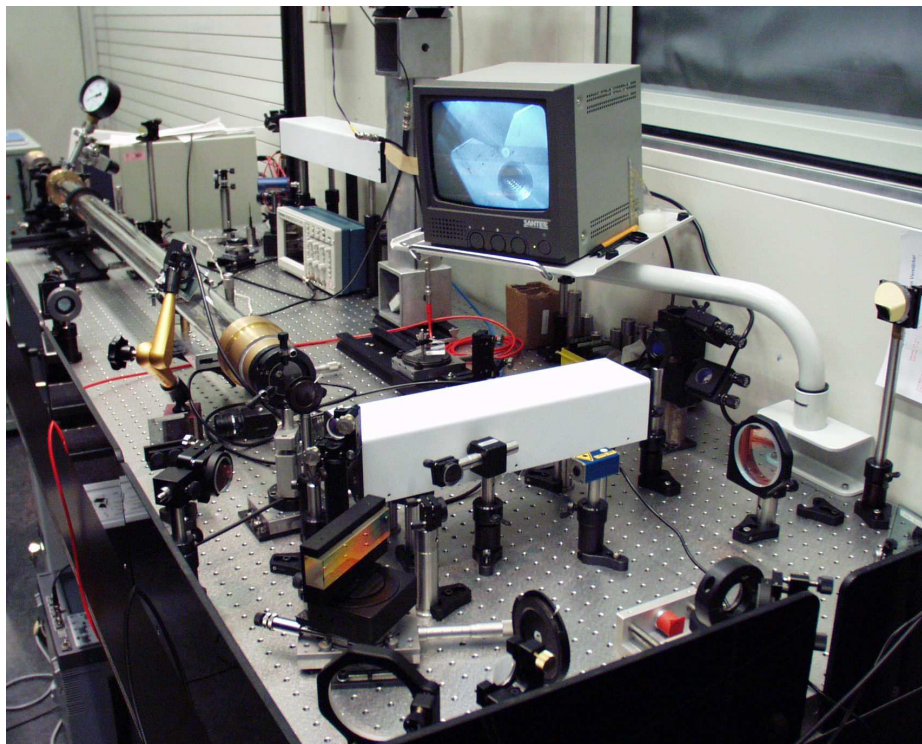
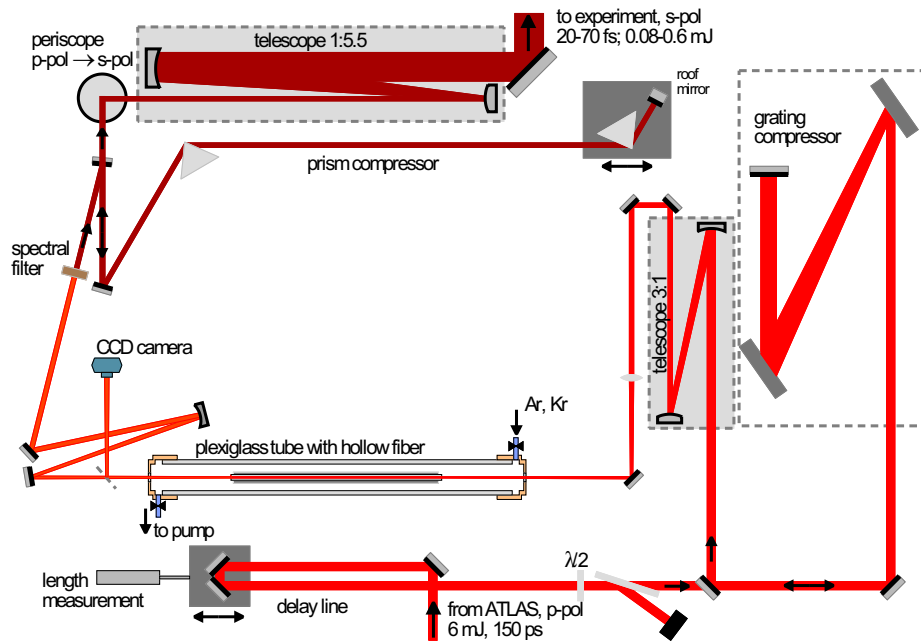


Figure 3.10: Schematic drawing (top) and photo (bottom) of the setup for the generation of the input signal pulse. The monitor in the photo shows the view on the entrance of the hollow fiber with a bore diameter of $250 \mu\text{m}$ resting in the V-groove.

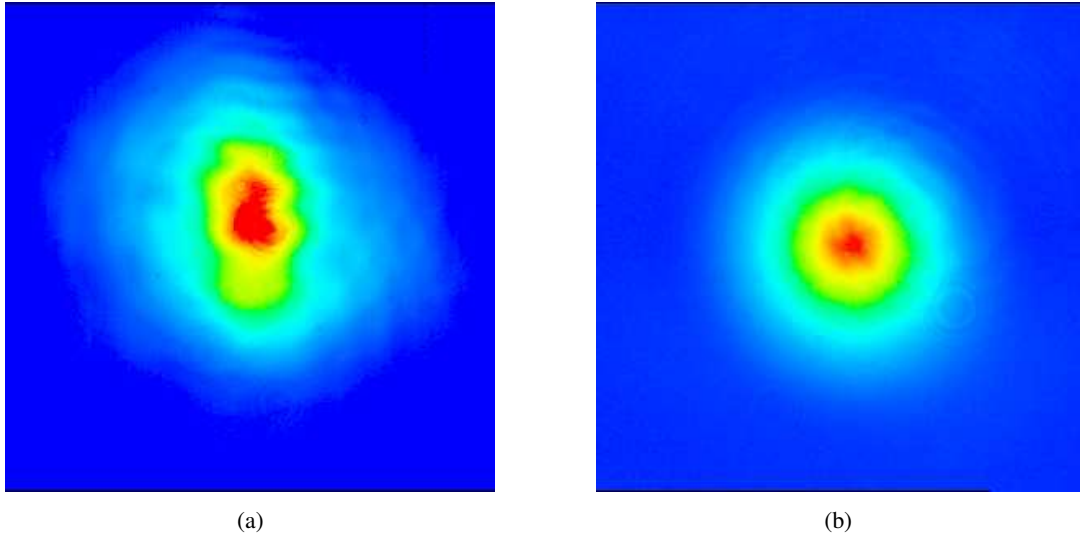


Figure 3.11: Near-field patterns of the signal pulse before and after the passage through the hollow fiber.

both ends independently in the transverse directions. One of the supports of the tube is fixed directly below the entrance of the hollow fiber and is used to match the fiber entrance and the laser focus. This way the orientation of the fiber can be changed by shifting the second support without moving the position of the entrance. The alignment is checked by observing the output behind the fiber with a CCD camera.

3.5.2 The Resulting Short Input Signal Pulse

Fig. 3.12 shows the signal spectrum before and after the passage through the hollow fiber. The plexiglass tube is filled with about 600 mbar Argon and Krypton, respectively. The broadening for Krypton is much larger than that for Argon, but the spectrum is shifted strongly to shorter wavelengths due to the ionization blueshift, which renders the resulting pulse unfavorable as an input for the SRA experiment.

The theoretical values for the spectral width computed by Eq. (3.6) with the effective intensity I_{eff} from Eq. (3.15), the effective length from Eq. (3.14), the nonlinear interaction length L_{NL} from Eq. (3.5), and the nonlinear constants given in [136] is about 80 nm for Ar and 100 nm for Kr. For Ar the value agrees well with the observed broadening, while it is somewhat smaller for Kr. The larger bandwidth in the experiment is most likely due to further broadening by ionization blueshift, which is not included in the computation.

The autocorrelation in Fig. 3.13 is taken after the prism compressor. The FWHM of the peak is 32 fs corresponding to a pulse duration of 23 fs if a pulse with a Gaussian temporal profile is assumed. The autocorrelation trace has an offset indicating that the signal pulse has a rather long pedestal. This is a common feature for the pulses broadened by SPM because the pulse receives a nonlinear chirp. While the body of the pulse has a linear positive chirp and is compressed, the contributions of the leading and trailing parts have negative chirps (cf. Fig. 3.8) [119]. They are stretched by the prism compressor and cause pre- and after-pulses or a pedestal.

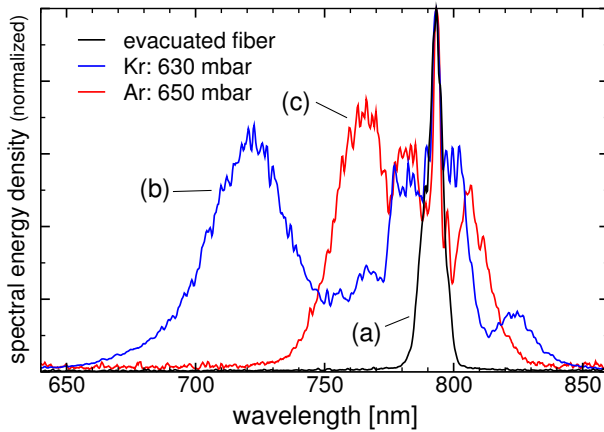


Figure 3.12: Spectrum after the passage through the hollow fiber in (a) vacuum with some residual gas, (b) Krypton, and (c) Argon. Krypton shows a larger spectral broadening but also a strong ionization blue shift. The weighted central wavelength is shifted towards shorter wavelengths, which is unfavorable for the following SRA experiment.

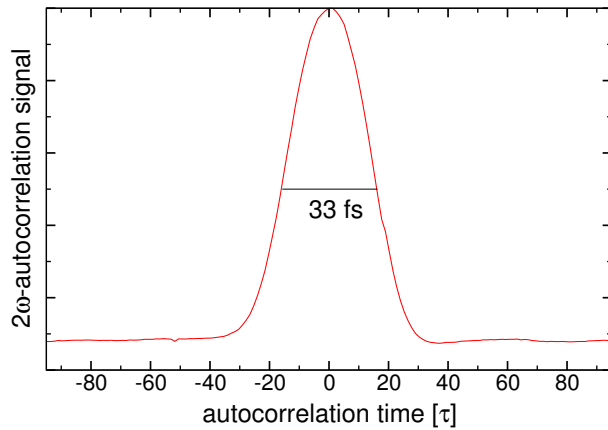


Figure 3.13: Autocorrelation trace of the signal pulse broadened in a Ar-filled hollow fiber after the final compression in the prism compressor. The FWHM of 33 fs corresponds to a pulse duration of 23 fs

3.5.3 Red-Shifting of the Central Wavelength by Filtering

Though the numerical simulations in section 2.4.2 suggest that SRA is possible starting with an input pulse with the same central wavelength as the the pump pulse, the experiments have shown that SBS instabilities rule this scheme out. A simple approach to obtain a pulse shifted towards longer wavelength is by spectral filtering the fiber output. Filters that absorb or reflect the short wavelength part of the spectrum effectively shift the central wavelength of the remaining pulse to the NIR.

Two types of filters are used, absorbing glass filters and dielectric coated filters. RG glass filters absorb the visible light and transmit the IR part. They are denoted by the wavelength, where the light is attenuated to 50 % after passing a 3-mm distance inside the filter. They are industrially manufactured for a few specific wavelengths of which only RG780 and RG830 are suitable in the present application. 4-mm RG780 glass cuts most of the short wavelength part of the fiber output, as shown in Fig. 3.14. However, there is still a significant amount of light left in the region of the original ATLAS spectrum, which could still trigger the SBS instability. It can be suppressed by a combination of 2-mm RG780 and 1-mm RG830 at the expense of the attenuation of the desired long-wavelength part of the spectrum. The remaining pulse becomes too weak to be used as input pulse for the SRA experiment.

A second filter option are dielectric mirrors. They reflect the short wavelength part of the

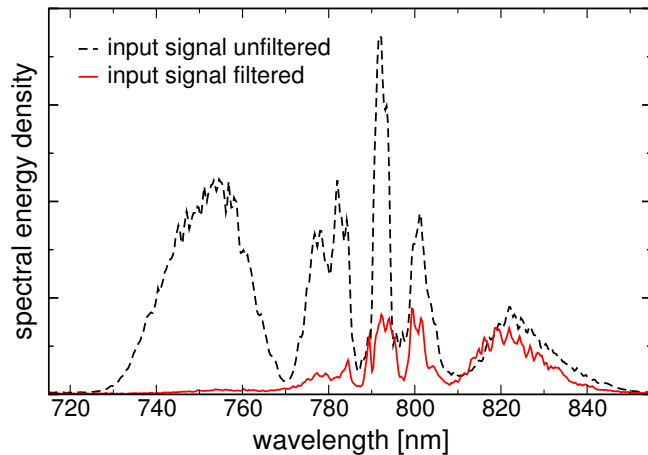


Figure 3.14: Spectrum before and after filtering by 4 mm of RG780 glass.

spectrum, in particular, the spectral band of the pump pulse. Fig. 3.15 shows the transmission curves of the applied filters. They have been designed such that the transmission increases sharply around 805 nm. This steep edge in the transmission is an advantage of dielectric filters compared to RG glass filters, which have a much slower rise and separate nearby wavelengths only poorly. The rising edge of the transmission curve can be shifted towards shorter wavelengths by increasing the angle of incidence. The oscillations of the transmission are a characteristic but undesirable feature of dielectric filters, because they influence the spectral shape of the transmitted pulse in the desired region above 800 nm. However, the measured spectrum in Fig. 3.16 shows that this is a minor effect. The obtained spectrum is smooth, non-ragged with a maximum at about 815 nm. To avoid any undesired interference with the residual short-wavelength contribution around 750 nm, the pulse is additionally cleaned by a 2 mm RG780 filter.

Filtering affects the compressibility of the self-phase modulated pulse a lot. Firstly, the bandwidth is narrowed to about 17 nm, which increases the minimal pulse duration to about 60 fs due to the time-bandwidth product. Furthermore, the theoretical curves of the instantaneous frequency in Fig. 3.8 show that the remaining pulse has only a partially linear, positive chirp. Only the low frequency parts pass the filter (unshaded regions). On the right side of the vertical line, the chirp is positive though not completely linear. This part is compressed in the prism compressor. The part left of the vertical line has a negative chirp and is stretched even further. Therefore, one expects that the compressed pulse is longer than the unfiltered case.

The measured autocorrelation trace is shown in Fig. 3.17. One can deduce a pulse duration of about 80 fs and a pedestal of 200-300 fs. The latter value is ambiguous because the actual shape of the pedestal is unknown. However, one can assume that the pedestal is asymmetric with respect to the pulse and extends farther to the front, in the propagation direction, because the non-compressible parts of the pulse having the negative chirp are leading before the prism compressor (Fig. 3.8) and also pass the compressor faster than the body of the pulse.

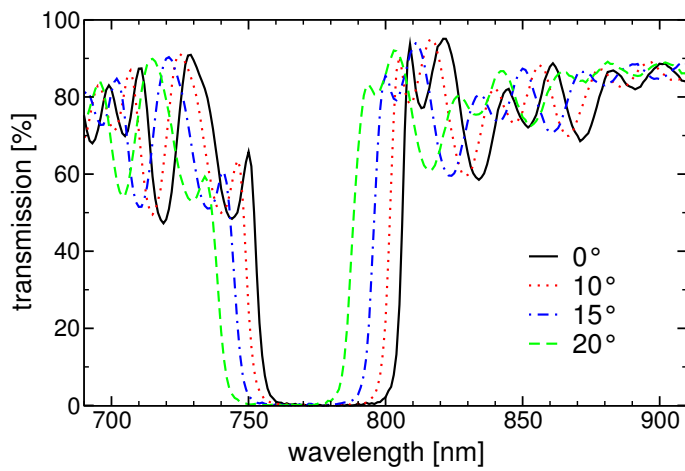


Figure 3.15: Transmission curves of the dielectric filter for different incidence angles.

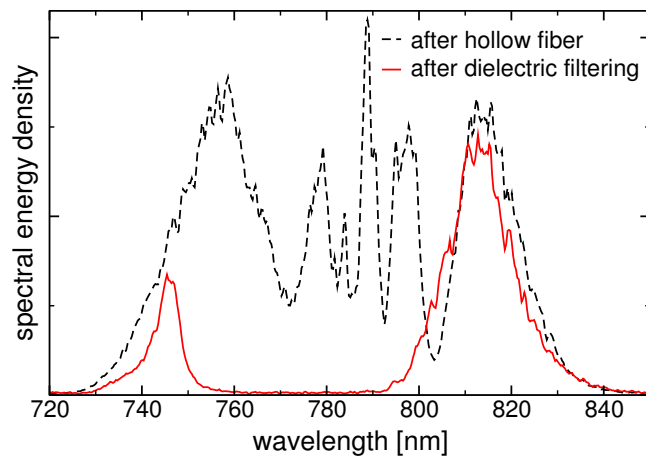


Figure 3.16: Spectrum before and after filtering using dielectric filters with a steeper edge of the transmission curve.

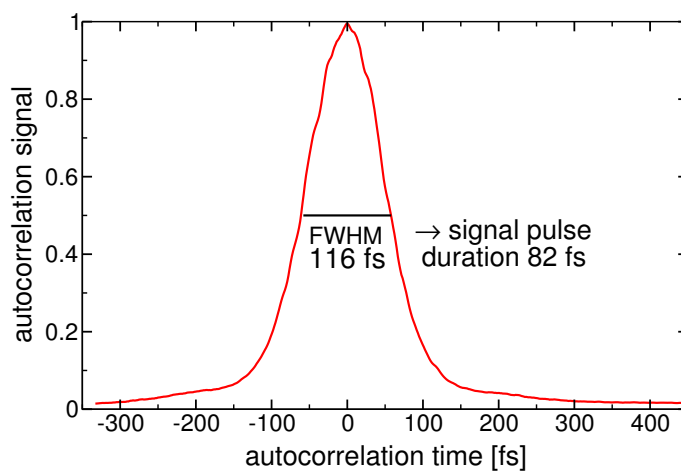


Figure 3.17: Autocorrelation trace of the dielectrically filtered signal pulse after the compression in the prism compressor.

3.6 Setup and Alignment of the Amplification Experiment

3.6.1 Target Chamber

Focusing

Fig. 3.18 depicts the target chamber setup for the SRA experiment. The signal and pump pulses are focused from opposite directions into a gas jet by off-axis parabolic mirrors (OAP). The OAPs are identical. They have a diameter of 2 inch, a focal length of 12 inches and the effective focusing number is approximately $f/12$ (cf section 3.1). The foci of the signal and the pump pulses have a diameter of $25 - 30 \mu\text{m}$ and a Rayleigh length is $L_R \approx 600 \dots 900 \mu\text{m}$. To achieve approximately the same focusing parameters for signal and pump pulses, their diameters are adjusted by telescopes before. Fig. 3.19b shows the intensity distribution of the focused pulses image-relayed to a CCD camera. A hard aperture in the second telescope causes the slight Airy rings around the signal focus

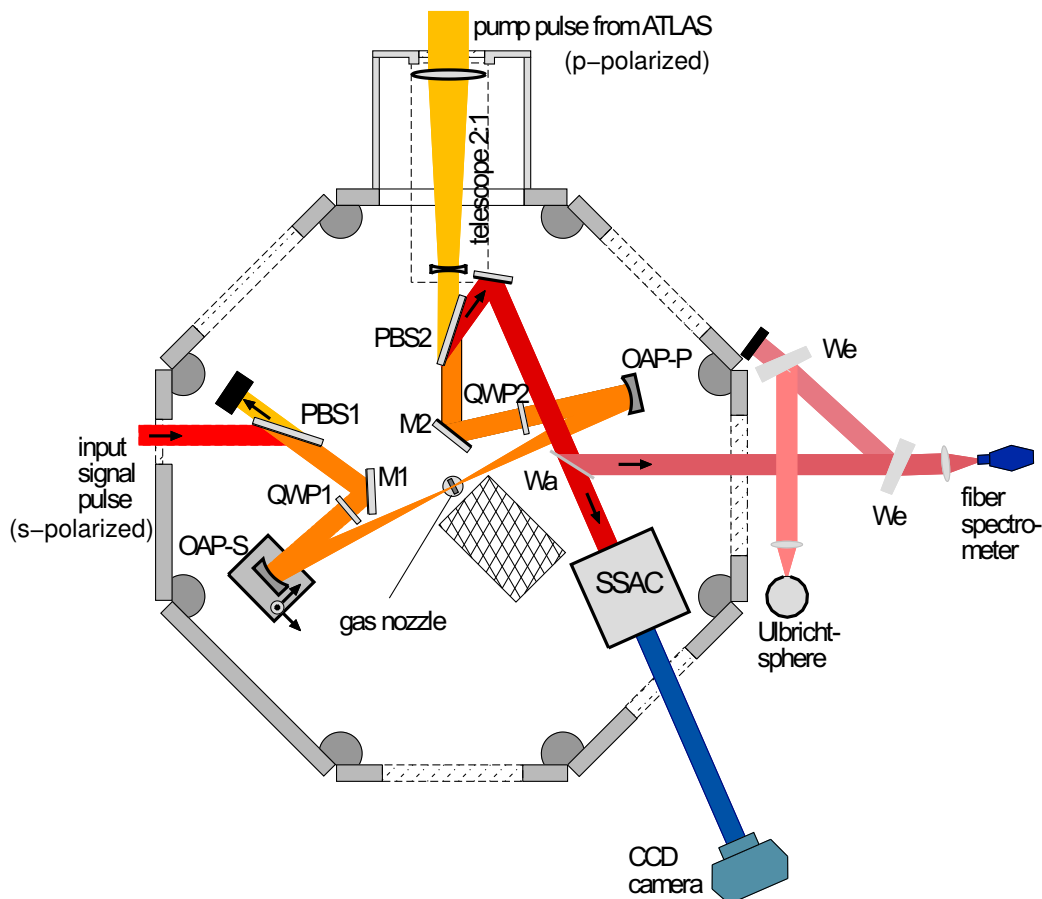


Figure 3.18: Layout of the target chamber for the SRA experiment: PBS1, PBS2 - polarizing beam splitters; QWP1, QWP2 - quarter waveplates; M1, M2 - dielectric mirrors; OAP-S, OAP-P - off-axis parabolic mirrors to focus signal and pump pulses, respectively; Wa - 0.5 mm thin wafer, single sided AR-coated; SSAC - single-shot autocorrelator, see Fig. 3.22; We - wedges. The hatched area contains additional diagnostics for ensuring the pulse overlap and is depicted separately in Fig. 3.21.

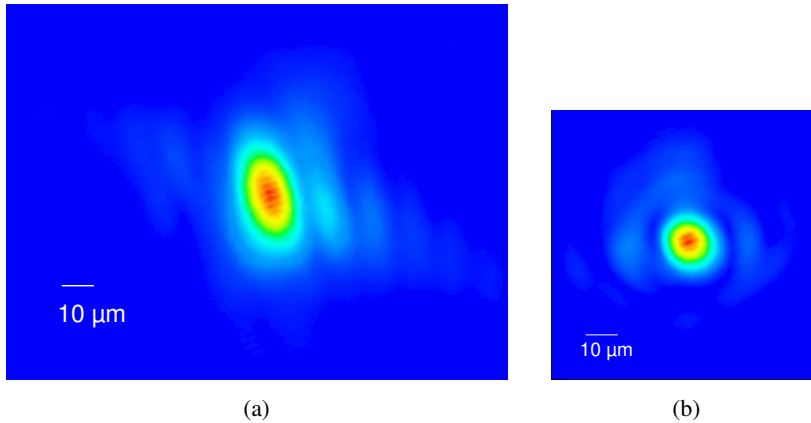


Figure 3.19: Focus of (a) the pump pulse and (b) the signal pulse (dielectrically filtered). The images of the foci are taken at reduced energy with the target chamber filled with air.

Separation of pump and signal beam paths

One of the main difficulties of the implementation is to find a proper way of separating the beam paths of the counter-propagating signal and pump pulses. The pump pulse follows back the input path of the signal pulse, is recollimated by the signal OAP and, unless taken care of, would cause severe damage, when running into the setup for the signal pulse generation. In the same way, the signal pulse has to be separated from the common beam path, not only to prevent damages to the ATLAS system but also to send it to the diagnostics for its characterization.

In this setup, a combination of polarizing beam splitters (PBS1 and PBS2 in Fig. 3.18) and broadband waveplates (QWP1 and QWP2) is used to separate the pulses by their different polarizations. Both pulses are linearly polarized, when they enter the target chamber. The signal pulse is s-polarized, i.e., perpendicular to the plane of propagation, while the pump pulse is p-polarized, i.e., in the plane of propagation. The signal is reflected by PBS1 and the quarter ($\lambda/4$) waveplate QWP1 changes the linear polarization to circular polarization. After focusing, passing the gas jet and recollimation, QWP2 restores the original polarization of the signal pulse. The second beam splitter PBS2 reflects it from the common beam path. The same happens to the pump pulse, except that it passes through PBS1 and PBS2 and has the opposite helicity, while it is circularly polarized. The opposite circular polarization is required so that the signal and pump pulses couple in the plasma.

With this setup, the pump and signal pulses can be separated with an efficiency of about 99 %. It is limited by the coating of the beam splitters, a possible change of the circular polarization to a slight elliptical polarization by the reflection from the OAPs, and by the precision of the alignment. The residual pump pulse has an energy of less than 2 mJ and does not cause any damage in the setup for the signal pulse generation, unless it refocuses near one of the optical components. This could happen if the distance between the OAPs is slightly longer than twice their focal length, so that the pump pulse is not recollimated but refocused by the second OAP.

The layout of the optical components and their alignment is slightly sophisticated, because both the beam-splitters and the OAPs have fixed angles of incidence and, moreover, the pump and signal pulses should enter the target chamber perpendicular to the chamber walls. Only the dielectric mirrors M1 and M2 tolerate small deviations from the specified angle of incidence. The optical components have to be pre-aligned carefully using diode lasers coupled into the optical path of the pump and signal pulses.

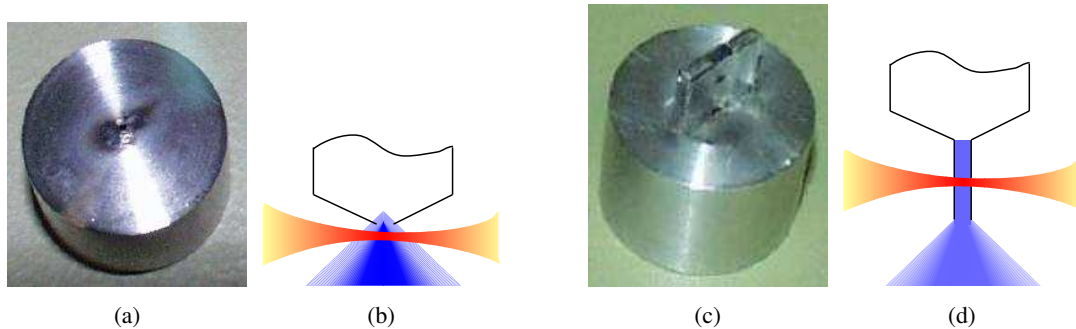


Figure 3.20: Gas nozzles used in the experiment with the corresponding schematic side views showing the density profile: (a,b) conical nozzle with a soft density gradient; (c,d) chimney nozzle with steep density gradient.

Gas jet

The interaction of the signal and pump pulses takes place in a subsonic hydrogen or helium gas jet in the center of the chamber. While subsonic gas jets lack the top-hat density profile of supersonic jets, they have the advantage that the density can be changed without affecting the shape of the density profile. Different kinds of nozzles are used to generate the jet:

- Ordinary nozzles (Fig. 3.20a) releasing a conical gas jet. The transverse density profile (Fig. 3.20b) is approximately Gaussian shaped [140] and has long density gradients. Furthermore, their density is quite sensitive to the distance from the mouth of the nozzle as depicted in Fig. A.3.
- Chimney shaped nozzles (Fig. 3.20c) that guide the gas jet as shown in Fig. 3.20d. The laser pulses enter through small holes in the foils covering the sides of the chimney. The density profile is more homogeneous and has steeper edges. The gradient at the edges is formed by small amounts of gas streaming through the entrance holes. However, also the chimney nozzle has disadvantages: The jet is not accessible to an interferometric measurement of the plasma density from the side. The density is determined from the Raman instabilities of the pump pulse in the plasma, by observing the shift of the Stokes-lines described in appendix A.

Diagnostics

After the amplification and separation from the common optical path, the output signal pulse is characterized by measuring its energy, spectrum, and autocorrelation trace. A thin wafer (0.5 mm) and two wedges split the pulse into different samples allowing for simultaneous measurements. The autocorrelator is described in section 3.6.4. The spectrometer is a fiber spectrometer from the company “Ocean Optics”. The energy of the sample pulse is too low for a measurement with a pyroelectric detector, while it is too large to be measured directly with an integrating photodiode. Therefore, the energy is measured inside an Ulbricht sphere as a voltage signal from a photodiode, which is calibrated by measuring the energy of the full pulse inside the chamber with a pyroelectric detector.

Furthermore, the near- and far-field patterns are measured by replacing the spectrometer and the first wedge by a cardboard, on which the near field is observed with a CCD camera. To observe the far field, a lens with a long focal length focuses the pulse directly to a CCD camera

3.6.2 Precise Alignment of the Focusing Parabolas

This section deals with the details of the alignment procedure that have to be assured to achieve a good focus quality, the overlap of the pump and signal foci as well as the precise counter-propagation at the same time. After the first rough alignment of all optical components, the foci of the OAPs are optimized by fine tuning of their orientation with respect to the incoming pulses. The foci are checked by a CCD camera capturing their relayed and magnified images (see Fig. 3.19). Since the procedure requires that the OAPs are slightly turned around their horizontal and vertical axis, the exact counter-propagation of the pulses between the OAPs and the overlap of the foci are lost. The realignment has to be accomplished without deteriorating the foci again, which means that incidence angles of the pulses on the respective OAP must be kept fixed.

The fine tuning benefits from the fact that the position of the focus is fixed with respect to the OAP. Therefore, the overlap of the foci is accomplished by shifting the OAPs in space.

The propagation directions are made parallel separately for the horizontal and vertical angular deviation. In the plane of incidence, the beam path of the signal pulse is rotated around the focus by translating the mirror M1 along the direction of the incoming beam. The focus position stays fixed because the OAP is not moved. The direction of the pump pulse is changed in the same way. To remove the remaining angular deviation in the vertical direction, it is important that both pulses have the same height on their focusing OAPs, respectively, i.e. that the plane the pulse propagation is parallel to the chamber floor. Then, the OAPs can be rotated around the axis parallel to the symmetry axis of the full paraboloid, which is just the direction of the incident pulse. The focus moves on a circle around this axis without being deteriorated and the pulses are raised or lowered on the opposite OAP. In principle, the vertical translation and the rotation of the OAP have the same effect. In the latter case however, larger changes can be made, because the relative position of pulse on the focusing OAP is not shifted.

3.6.3 Diagnostics to Assure the Spatio-Temporal Overlap

The exact overlap of the foci of the pump and signal pulses has to be ensured at the beginning of every experiment. In particular, the transverse overlap of the foci is very critical. Furthermore, the arrival times of both pulses in the focus have to be synchronized. Fig. 3.21 depicts the additional diagnostics to check the overlap.

To measure the time lag, a small prism (uncoated glass) with an apex angle of 90° is moved to the position of the focus. It reflects small fractions of the attenuated counter-propagating pulses. They are colinearly sent out of the chamber to the entrance slit of a streak camera (Hamamatsu 500), which has a temporal resolution of a few picoseconds. The length of the delay line in the setup for the generation of the signal pulse (Fig. 3.10) is changed to remove the measured time lag. The residual error of the delay is less than 3 mm and is caused by (i) the resolution of the streak camera and (ii) the uncertainty of the placement of the prism

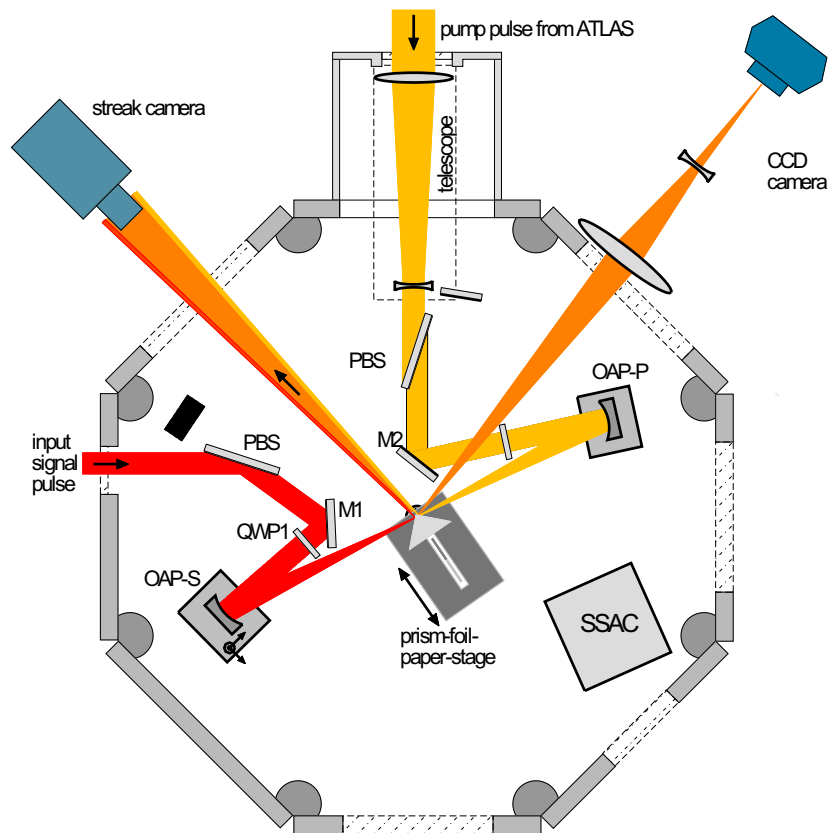


Figure 3.21: Additional diagnostics implemented to assure the spatio-temporal overlap of the signal and pump pulses. Notations are the same as those in Fig. 3.18.

with respect to the actual focus. The fine tuning is done during the experiment by changing the delay in small steps until the maximum amplification of the signal pulse is found. This is cumbersome if the gas jet allows only single-shot operation, but is quickly accomplished for 10-Hz operation with a motor-controlled delay line.

The transverse overlap is verified in two steps. First, a thin paper is moved to the focus. The attenuated signal and pump pulses illuminate the paper. The scattered light is collected by a telescope outside the chamber and relayed to a CCD camera. The paper has to be thin enough that some light of the signal pulse is transmitted. The foci are matched on the paper by moving OAP-S in the transverse direction. Because the paper has a rough structure and the scattered light is partially blocked by other optics, the foci are not resolved and the procedure is not very accurate. To optimize the overlap further, the paper is replaced by a thin aluminum foil. A tiny hole of the size of the foci is shot into the foil using the attenuated pump pulse. It acts as pinhole, which the signal focus has to be moved to. The CCD observes the signal light transmitted and scattered from the edge. The intensity is maximized by shifting OAP-S again.

After having verified the overlap, the prism-foil-paper-stage is moved out of the focal area and the gas nozzle is lowered into the focus.

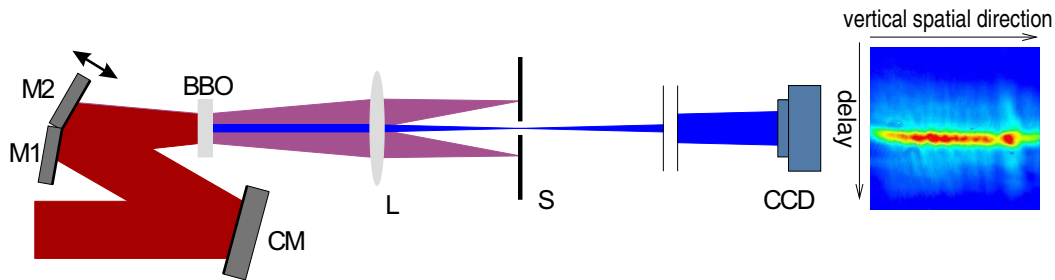


Figure 3.22: Layout of the single-shot autocorrelator (top view): CM - cylindrical mirror, cyl. axis is in the drawing plane; M1, M2 - mirrors enclosing the angle 2θ ; BBO - SHG crystal; L - lens images the intensity pattern at the BBO onto the CCD; S - slit in focal plane of L; CCD - CCD camera (8- or 14-bit). The CCD camera is placed outside the target chamber at a long distance from the lens. M2 is shifted for the calibration experiment. A typical CCD readout is shown next to the camera.

3.6.4 The Single-Shot Autocorrelator

A second-order autocorrelator has been designed meeting the following requirements:

- It captures the complete autocorrelation in single-shot operation.
- It works for small pulse energies down to $50 \mu\text{J}$.
- It works for pulses with large bandwidths ($> 100 \text{ nm}$) and short durations $< 20 \text{ fs}$. Therefore, no transmitting optics are tolerable up to the thin crystal for the second harmonic generation (SHG).
- It is sufficiently compact to fit into the target chamber. A measurement outside the chamber would lead to a pulse lengthening when the pulse passes the chamber window.

Fig. 3.22 shows the layout of the autocorrelator. The incoming pulse is split into two halves by the mirror pair M1, M2, which encloses the small angle 2θ . The two halves overlap in a $100 \mu\text{m}$ -thick β -barium-borate (BBO) crystal⁴ and generate three second-harmonic signals: Two in the direction of the incoming pulses by SHG of the individual pulses and a third one between them by sum-frequency generation of both pulses. Since the incoming signal pulse is very weak, it is focused in the vertical direction by a cylindrical mirror. The BBO crystal is placed a few mm in front of the line focus, where the intensity is large enough to obtain a strong second-harmonic signal.

The common sum-frequency generation by the two pulse halves maps the delay between the pulses to the crystal plane. The lens L collects the light and images the autocorrelation pattern at the crystal on a CCD camera outside the target chamber. Because the mapping of the time axis to a spatial axis is already done, the dispersion of the window does not affect the measurement any more. In the focal plane of the lens, the three beams are focused to horizontally different locations. The slit S blocks the fundamental and the second harmonic light of the two halves of the original signal pulse. The autocorrelation signal passes the slit and is measured without background.

⁴ The crystal is thin enough to measure the autocorrelation of the observed pulses. They created a stronger SHG signal than thinner crystals, which would have to be used for even shorter pulses.

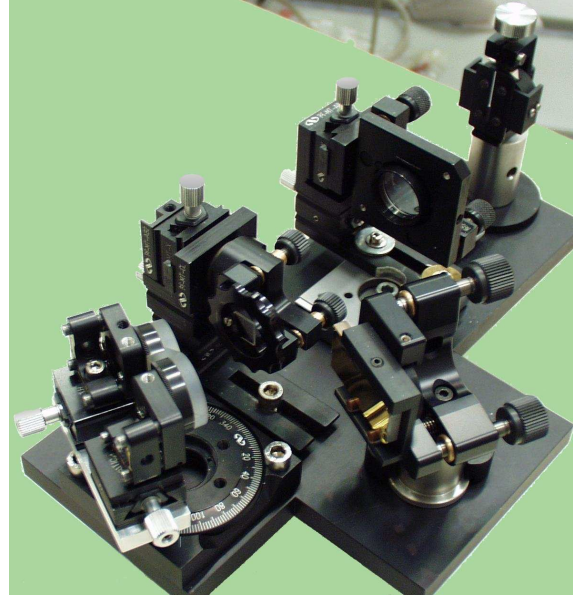


Figure 3.23: Foto of the single-shot autocorrelator (CCD camera not shown).

The image captured by the CCD camera carries the autocorrelation information in the horizontal direction. The vertical dimension is related to the vertical profile of the pulse. The autocorrelation delay τ as a function of the horizontal distance x_{CCD} on the CCD camera reads

$$\tau = \frac{2n_{\text{gr}} \sin \theta_{\text{ext}}}{n_{\text{ph}} c M} \Delta x_{\text{CCD}}, \quad (3.16)$$

where M is the magnification of the image relayed by L , c is the speed of light, $n_{\text{gr/ph}}$ are the refractive indices for the group and phase velocities in BBO, respectively, and θ_{ext} the half angle enclosed by the two halves of the pulse outside of the crystal. For small angles θ_{ext} and using practical units, the expression reduces to

$$\tau[\text{fs}] \approx \frac{2\theta_{\text{ext}}}{0.3M} \Delta x_{\text{CCD}}[\mu\text{m}]. \quad (3.17)$$

The relation has been verified by a calibration measurement: $x_{\text{CCD}}(\tau)$ was measured by shifting the mirror $M2$ in the direction of the incoming laser pulse. The delay τ was computed from the measured translation of $M2$. The results given in Fig. 3.24 are in good agreement with the theoretically derived expression.

An example of the captured images is next to the CCD camera in Fig. 3.22. The autocorrelation trace is retrieved as a line-out of the image by averaging it over several rows.

Since the two pulses form an interference pattern in the crystal, the autocorrelation actually has a substructure. The envelope given by the intensity autocorrelation

$$I_{2\omega}(\tau) \propto \int_{-\infty}^{\infty} I_s(t - \tau) I_s(t) dt \quad (3.18)$$

is modulated with the period $\lambda / \sin \theta_{\text{int}} \approx 10 - 20 \mu\text{m}$ of the interference pattern. Here $\theta_{\text{int}} \approx \theta_{\text{ext}} / n_{\text{ph}}$ is the internal half-angle between the pulses. However, this is not visible for two reasons: The diameter of L is only 20 mm and limits the resolution of the relayed image.

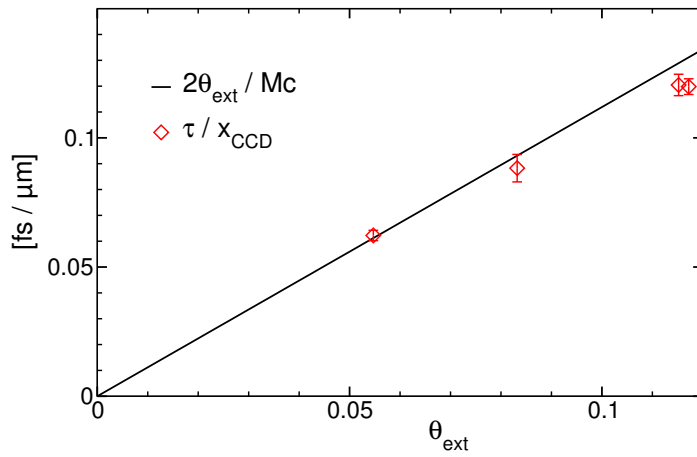


Figure 3.24: Comparison of the theoretically derived curve for τ/x_{CCD} according to Eq. (3.17) (solid line) with a calibration measurement. The angle θ_{ext} is given in radians.

Even more important is the Fourier filtering [52] done by the slit located in the focal plane of the lens. It blocks not only the two halves of the original pulse, but also the diffraction side maxima needed to resolve the fringe pattern.

4 Results with an Unshifted Signal Pulse and Discussion

The first experiments are carried out with the input signal pulse and the pump pulse at the same central wavelength. As described in section 3.4, the signal pulse is obtained by spectral broadening in a hollow fiber and subsequent compression in a prism compressor to 25 fs. SRA is expected to be achieved after launching the formation of a Raman backscattered pulse at the Stokes frequency. The new pulse is first amplified in the Raman regime and later by SRA after its intensity has grown sufficiently large to satisfy the threshold condition. The formation of the new pulse is confirmed and first evidence for SRA is found in sections 4.1-4.3. Full access to the superradiant regime is anticipated when increasing the amplification distance by using longer pump pulses. However, this is presently prevented by the sudden onset of stimulated Brillouin backscattering.

4.1 Energy Amplification

Before the amplification experiment, the spatio-temporal overlap of the pump and signal pulses in the focus has to be assured. The temporal overlap is fine-tuned during the experiment by optimizing the energy gain of the output signal. The dependence of the signal output energy on the delay between the pump and signal pulses is plotted in Fig. 4.1. A significant amplification in energy is found in a short range of the delay. This proves that the pulses meet indeed in the plasma and hence the major challenge of the accurate pulse alignment is under control.

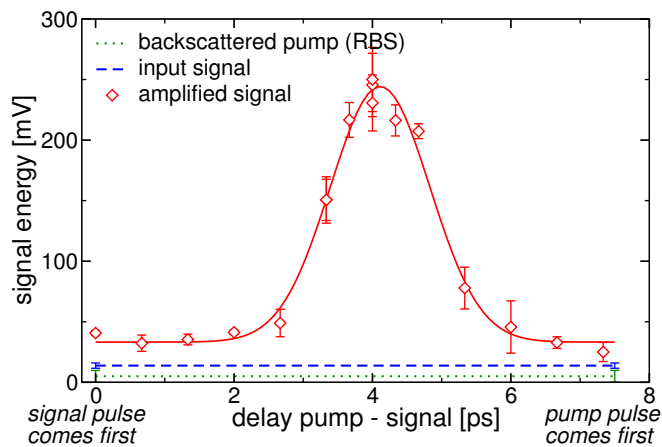


Figure 4.1: Dependence of the output energy on the delay between the pump and signal pulses. Energy is given in terms of the voltage peak measured at the photo diode attached to the Ulbricht sphere. The input signal is measured without the pump pulse and the H₂ gas, the level of the backscattered pump light (mainly due to Raman backward scattering) is measured with the input signal blocked. Error bars are given as statistical deviation over 2-4 shots. The red solid line is a Gaussian fit to the measured data points to improve the visibility of the gain curve.

In the experiment shown, the pump pulse has a duration of $\tau_p = 1.8$ ps and contains 90 mJ energy, yielding an intensity of 5×10^{15} W/cm² in the focus. The electron density is $n_e = 3.4 \times 10^{18}$ cm⁻³ = $0.0019 n_{\text{crit}}$. The signal output energy is 17 times higher than that of the input pulse. However, it was found later on that this value is too large due to a systematic error in the early energy measurements. To avoid over-steering of the photodiode attached to the Ulbricht sphere, the sample of the output signal was first attenuated by absorbing filters instead of the wedges shown in Fig. 3.18. These filters tend to saturate for higher intensities and get bleached so that they transmit the amplified pulse over-proportionally resulting in too large values of the measured signal energy. To remove this source of error, the signal pulse was attenuated by reflections from wedges in later experiments.

A Gaussian curve is fitted to the measured points in Fig. 4.1. It has a width of 1.4 ps (FWHM) corresponding to a length of 425 μm . The width of the gain curve is limited by three parameters:

- *The pump pulse duration* $\tau_p = 1.8$ ps (FWHM), which sets the maximal interaction length $1 \dots 2 \times c\tau_p/2 = 300 \dots 600 \mu\text{m}$ of the pulses;
- *The length of the plasma* of about 500 μm in the case of the conically shaped, single-shot nozzle. This sets the maximum length over which the the plasma couples the pump and signal pulses;
- *The Rayleigh length* of about 600 μm , where the pump and signal pulses are most intense and therefore the energy transfer into the signal pulse is largest.

Computing an exact relation for the width of the gain curve involves the precise knowledge about the kind of amplification, i.e., SRBS or SRA, and their share to the total energy gain. Actually, the amplification takes place in a transition stage from SRBS to SRA, where the mechanisms are mixed to some extent. A detailed analysis is therefore almost impossible. However, it is plausible that the amplification is largest, if the region, where the pump and signal pulses meet, lies both within the densest part of the plasma and within the Rayleigh length. So, the given lengths set upper limits on the width of the gain curve.

The green dotted curve in Fig. 4.1 represents the level of the pump light scattered back due to plasma instabilities, of which Raman backward scattering (RBS) starting from thermal noise is most important. The scattered light has the same polarization as the signal pulse and occupies the same spectral range. Therefore, it can neither be separated by the polarizing beam splitter in Fig. 3.18 nor by a subsequent dichroic mirror. Instead, it results in a pedestal added to the signal pulse and has to be kept small to ensure a good signal-to-noise ratio.

An upper limit of RBS is obtained by measuring the level of the backscattered pump light with the input signal pulse blocked. The obtained value is higher than the actual value in the amplification experiment, because the pump pulse can be scattered back over the full length of the plasma column. On the other hand, the interaction of the pump and signal pulse in the SRA regime mixes the electrons in the phase space and heats them up to keV temperatures. This suppresses the instabilities strongly in the region already passed by the signal pulse [47] and reduces the effective length over which pump instabilities can occur.

In the experiment the observed RBS energy level is well below that of the amplified signal pulse resulting in a satisfactory signal-to-noise ratio. As the Raman scattered light is usually

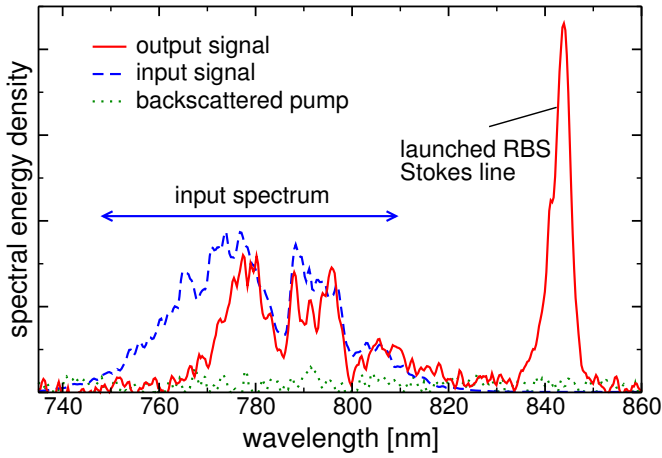


Figure 4.2: Spectra of the signal pulse before and after amplification and the Raman scattered pump light for $\tau_p = 1.15$ ps and $n_e = 5.9 \times 10^{18} \text{ cm}^{-3}$. The delay is adjusted to maximize the energy amplification.

much longer than the duration of the signal pulse, the energy is distributed over a longer time which reduces the intensity even further.

A specific feature of the energy vs. delay plot in Fig. 4.1 and also in Fig. 5.1 is the slightly higher level of the energy output if the signal pulse arrives first in the gas jet (left in Fig. 4.1). In this case the signal pulse ionizes the gas so that the pump pulse interacts with an already pre-ionized plasma. This leaves more time for RBS instabilities to set in and higher RBS levels are expected. If the pump pulse arrives first and pre-ionizes the gas, the signal pulse passes the plasma without being affected much, because it is too short to be subject to RBS and too weak to cause other non-linear plasma interactions. The measured output energy drops to the sum of the RBS level plus the signal input energy (right side in Fig. 4.1).

4.2 Analysis of the Spectra

Figs. 4.2 and 4.3 show the spectra of the amplified signal pulse for two different pump pulse durations and electron densities. A narrow Stokes line due to SRBS is observed, if a short pump pulse and the high electron density are used (Fig. 4.2). Unlike the RBS thermal instability, the Raman scattering is launched by the initial signal pulse as explained in section 2.4.2. This creates the new signal pulse that is to be amplified by SRA, when its intensity becomes large enough to satisfy the threshold condition.

The second measurement in Fig. 4.3 uses a longer pump pulse, thereby increasing the interaction length. Furthermore, the lower electron density decreases the SRA threshold intensity. The spectrum of the amplified pulse exhibits significant broadening at the base of the originally narrow Stokes line, which is evidence for the onset of SRA. While the amplification by stimulated Raman backward scattering (SRBS) is characterized by a narrow gain bandwidth according to Eq. (2.32) resulting in a long pulse, the signal pulse is shortened in the SRA regime, which entails the broadening of the spectrum. Other possible explanations for the spectral broadening are ruled out in section 5.3, where the spectra of later experiments are discussed.

The measurements suggest, that the SRA regime can be fully reached by increasing the duration and energy of the pump pulse, thereby increasing the interaction length, while maintain-

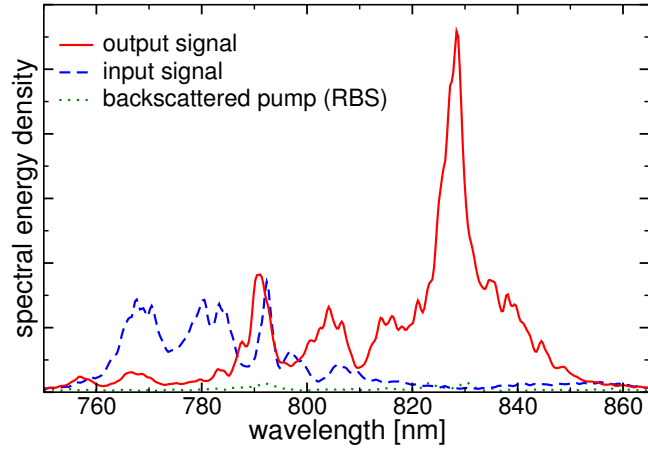


Figure 4.3: Spectra of the signal pulse before and after amplification and the Raman scattered pump light for $\tau_p = 1.8$ ps and $n_e = 3.4 \times 10^{18} \text{ cm}^{-3}$. The delay is adjusted to maximize the energy amplification.

ing the intensity of the pump. These experiments are presented in section 4.6. In the spectra, presented in Fig. 4.2 and Fig. 4.3, the energy level of the pump light backscattered due to the Raman instability is much lower than that of the amplified signal pulse whose spectrum is therefore not masked by the presence of the RBS light.

4.3 Autocorrelation and Streak Measurements

Fig. 4.4 presents typical results of autocorrelation measurements. The autocorrelation traces are obtained as calibrated line-outs from these images (cf. Fig. 5.5) by averaging over 10 to 20 rows. The rows are selected in a range, where the 2ω -signal is maximal but not yet clipped to make use of the whole dynamic range of the CCD 8-bit camera. Actual autocorrelation traces are retrieved in section 5.4, where the traces are analyzed quantitatively.

The signal pulse in Fig. 4.4a is 25 fs long but has a longer pedestal. The traces of the amplified pulses in Fig. 4.4b and c are much longer (> 150 fs). In particular, the last image exhibits a slight periodic modulation of the intensity. During the first stage of the amplification pulse lengthening is expected, when the new pulse is formed from SRBS launched by the short input pulse. The resonant three-wave process has a narrow spectral gain width in the small signal regime causing a long Raman scattered pulse (section 2.5.1).

The theory predicts, that the newly formed signal pulse starts to shrink once the SRA regime is reached. Since the measured spectra suggest that SRA is about to set in, first evidence of the pulse shortening is expected to become visible in the autocorrelation traces. As figured out later in section 5.4, the modulation in Fig. 4.3 is actually a footprint of SRA.

The restricted time window of the autocorrelation does not allow to resolve, whether there are any further contributions to the signal pulse on a longer time-scale. We measured its temporal structure on a longer time scale with the streak camera also used to establish the temporal overlap as outlined in section 3.6.3. The comparison of the measurements of the input and amplified pulses shown in Fig. 4.5 does not reveal any further features. Therefore, the amplified signal pulse must have a duration shorter than 2 ps, which is the resolution of the streak camera.

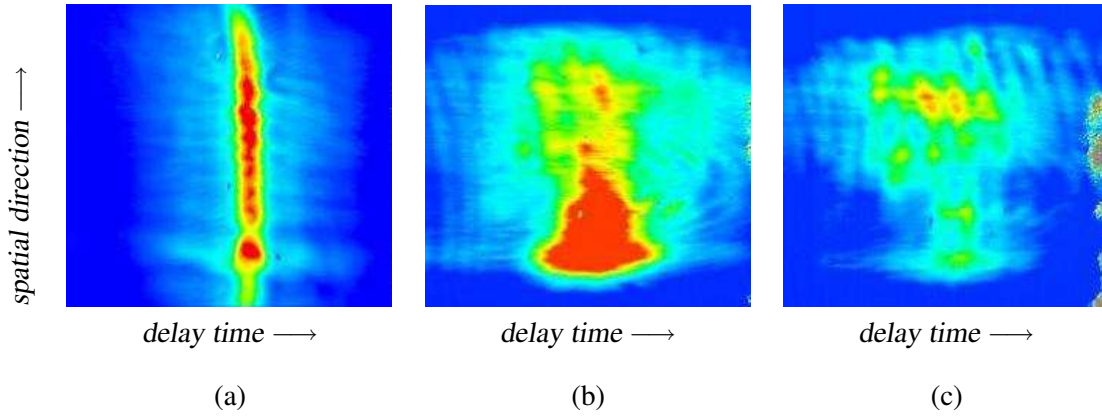


Figure 4.4: 2ω single-shot autocorrelation patterns captured by the CCD camera (cf. Fig. 3.22). The horizontal direction represents the delay. The width of the images corresponds to a time window of ≈ 220 fs. The vertical direction corresponds to the vertical spatial axis of the autocorrelated pulses. The autocorrelation patterns refer to (a) the 25-fs input signal pulse, (b) and (c) two examples of the amplified pulse: (b) a smooth wide autocorrelation; (c) an overall wide autocorrelation modulated with a short period.

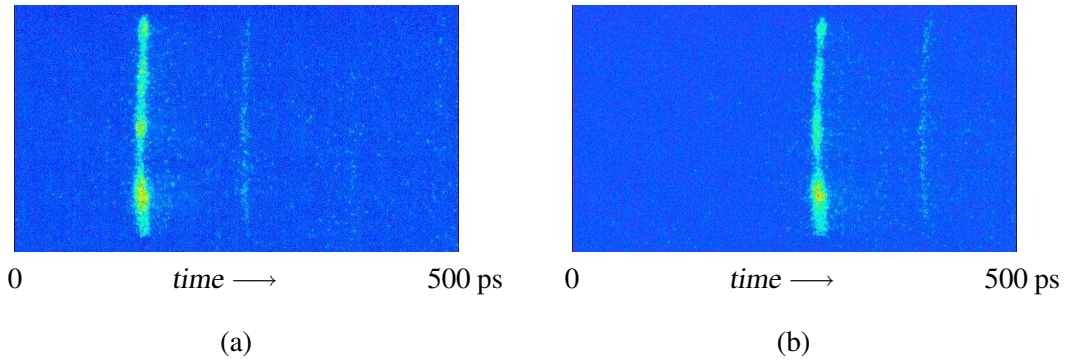


Figure 4.5: Streak measurements of the signal pulse (a) before and (b) after the amplification. Time goes from left to right and covers 500 ps. The jitter of the electronic trigger signal causes the horizontal shift of the lines. The weak line ≈ 130 ps right of the main line is due to an internal reflection at the 12-mm thick window that the pulse passes on exiting the vacuum chamber.

4.4 Density Dependence of the Amplification

With the delay set to maximize the energy output, the amplified signal energy is measured for various backing pressures of the gas jet, thus changing the electron density in the plasma. The electron density n_e is determined from the Stokes shift of the Raman backscattered pump light as explained in appendix A.

The output energy increases strongly with the electron density as shown in Fig. 4.6. Since the pump and signal pulses are coupled via the plasma electrons, a larger number of electrons leads to a larger energy transfer from the pump to the signal pulse and to the triggered SRBS pulse, which is also reflected in the dependence of the growth rates in the SRBS and the SRA regime on n_e .

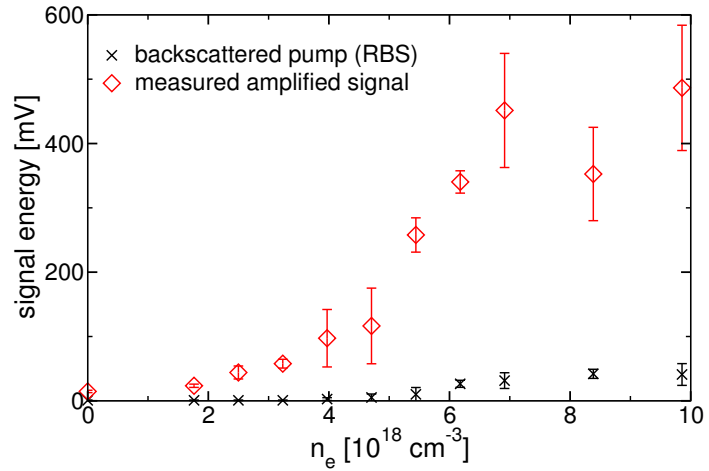


Figure 4.6: Energy of the amplified signal pulse as a function of the electron density n_e . The error bars indicate the statistical deviation of several shots.

Reproducing the data of Fig. 4.6 quantitatively by an analytic expression is very difficult, because several important parameters are not ascertained:

- The input signal launches the formation of a new signal pulse by SRBS. However, it is unknown, where this starts exactly.
- PIC simulations show, that the growth rate of a SRBS pulse is changed if it has a precursor, because the electron density gets already modulated by the precursor. It is difficult to rate the effect of the input signal pulse on the launched SRBS pulse.
- The transition from SRBS to SRA is smooth and the growth rate changes smoothly, too. The exact growth rate during the transition and the length of the transition zone are difficult to determine.
- The newly formed pulse is long while amplified in the SRBS regime (Fig. 4.3), but approaches the duration $\approx \pi/\omega_b$ in the SRA regime. While still in the early stage of the SRA regime, the pulse trailing edge still contributes a large share to the measured signal energy. Only after a longer amplification in the superradiant regime, the energy contribution of the pulse trailing edge becomes negligible.

Although this multitude of difficulties seems to rule out a quantitative analysis at all, most of them are relevant only in the early amplification stage. They do not affect the analysis for later times when the SRA is fully established and contributes most of the overall amplification of the signal pulse.

4.5 Further Detailed Analysis of the Amplified Spectra

4.5.1 Chirped Input Pulses

Fig. 4.7 shows the spectra of the amplified signal pulse for an input pulse that is not completely compressed. Positive or negative chirping is realized in the prism compressor that is part of the setup for the generation of the input pulse (Fig. 3.10). The chirped pulses have durations

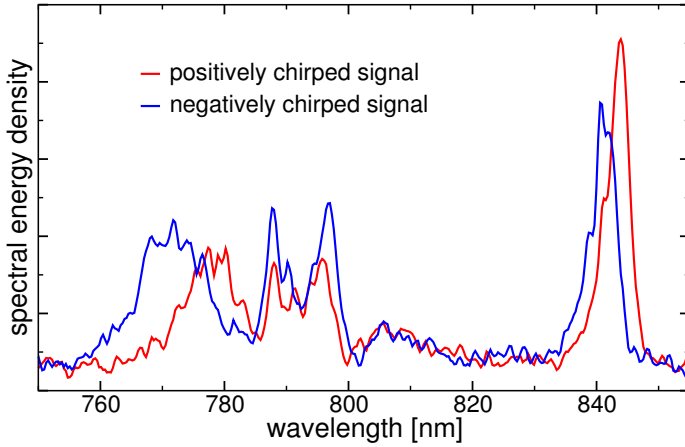


Figure 4.7: Spectra of the amplified signal pulse when it is initially either positively or negatively chirped. The other experimental parameters are equal to those given in Fig. 4.3

of about 40 fs. Apart from this change, the experimental parameters are the same as in section 4.2, where the broadening of the Stokes line was observed.

The output spectra of the initially positively or negatively chirped input pulses look very similar. Again SRBS is triggered by the input signal, but the beginning broadening of the Stokes line is absent similar to the experiment with the shorter pump pulse depicted in Fig. 4.2. Hence the longer and less intense signal pulse is less effective in the formation of the SRBS pulses than the fully compressed pulse. On the other hand, the sign of the chirp does not play a role. Opposite to the duration of the signal pulse, its chirp does not appear to be important.

4.5.2 Dependence of the Amplified Spectrum on the Delay

Changing the delay t_d between the pump and signal pulses shifts the interaction region first within the plasma and finally out of the plasma. From a different point of view, the interaction length in the most dense region of the plasma is shortened. Furthermore, the signal pulse interacts with a different part of the negatively chirped pump pulse in this region. It sees a blue shifted pump, if it arrives earlier, and a red shifted pump in the opposite case. Because the amplification is dominated by the resonant SRBS initially, the spectra should reflect the shift of the pump pulse wavelength.

In fact, the spectra shown in Fig. 4.8 for different delays t_d prove that the amplification maximum of the signal pulse shifts to shorter wavelengths if the signal pulse arrives earlier. It lies around 835 nm for the maximal energy amplification ($t_d = 0$ ps), moves to about 825 nm for $t_d = 0.66$ ps and to a minimal value of about 820 nm for $t_d = 1.33$ ps. For the last two delay settings the maximum remains, but the overall energy gain becomes much smaller. Obviously, the interaction length of the signal and pump pulses is already significantly decreased.

The spectra in Fig. 4.8 also suggest, that the signal input pulse itself might be amplified by SRBS, if a part of its spectrum satisfies the resonance condition for Raman scattering. This is also observed when varying the plasma density as described in the following section.

4.5.3 Dependence of the Amplified Spectrum on the Backing Pressure

The spectra in Fig. 4.9 are taken for increasing backing pressure and hence increasing plasma density while the delay is set to maximize the energy amplification. As expected, the Stokes

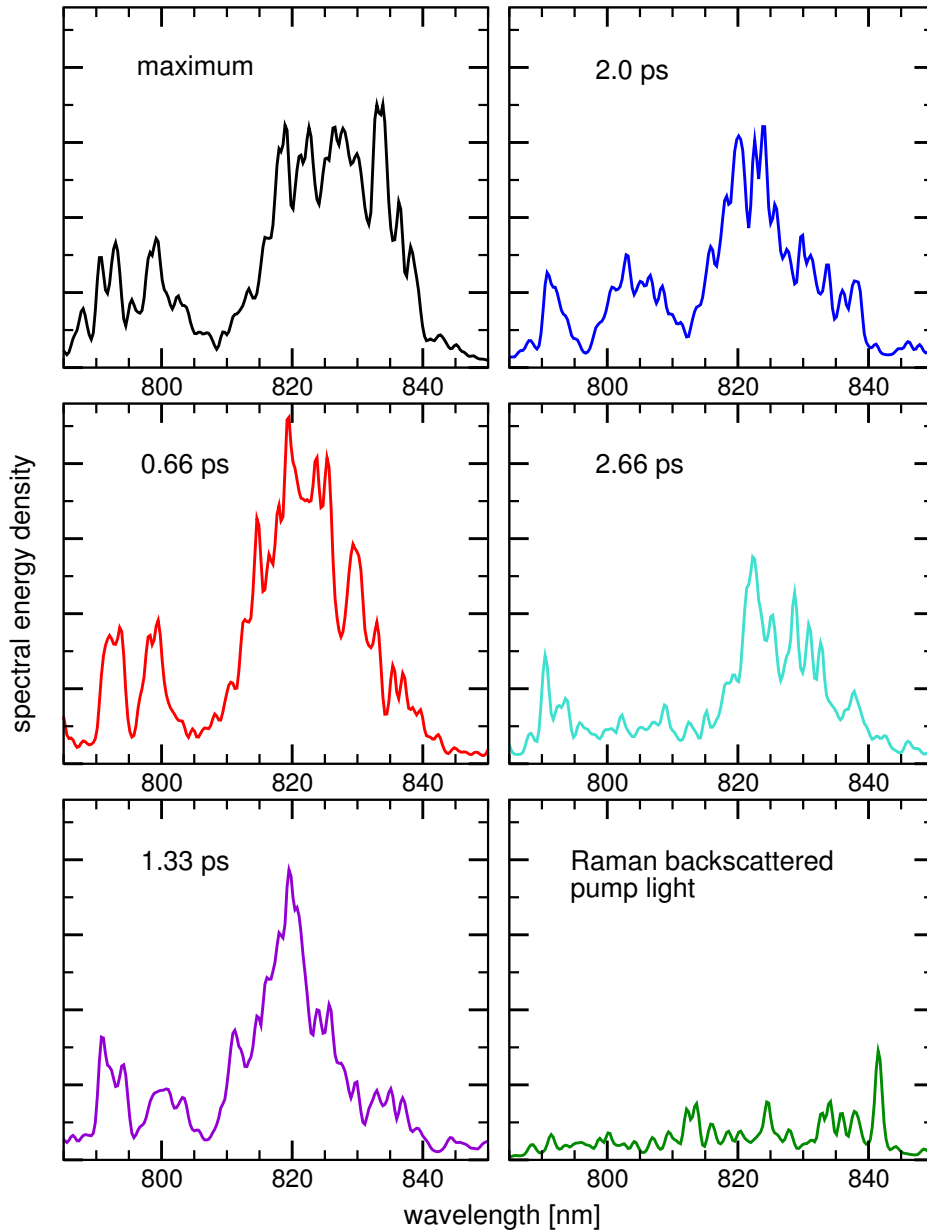


Figure 4.8: Spectra of the amplified signal pulse for different delays between the pump and signal pulses. Starting from the maximum of the energy vs. delay curve, the signal pulse arrives earlier by 0.66 ps from one plot to the next. The last spectrum shows the Raman backscattered pump light in absence of the signal input pulse. All graphs have the same scaling of the ordinate.

line due to SRBS shifts to longer wavelengths when the plasma density increases. For high pressures, the Stokes line finally appears separated from the input spectrum.

Furthermore, a sharp line at 793 nm is observed, which becomes stronger for increasing pressure. It is caused by stimulated Brillouin scattering and is discussed in next section.

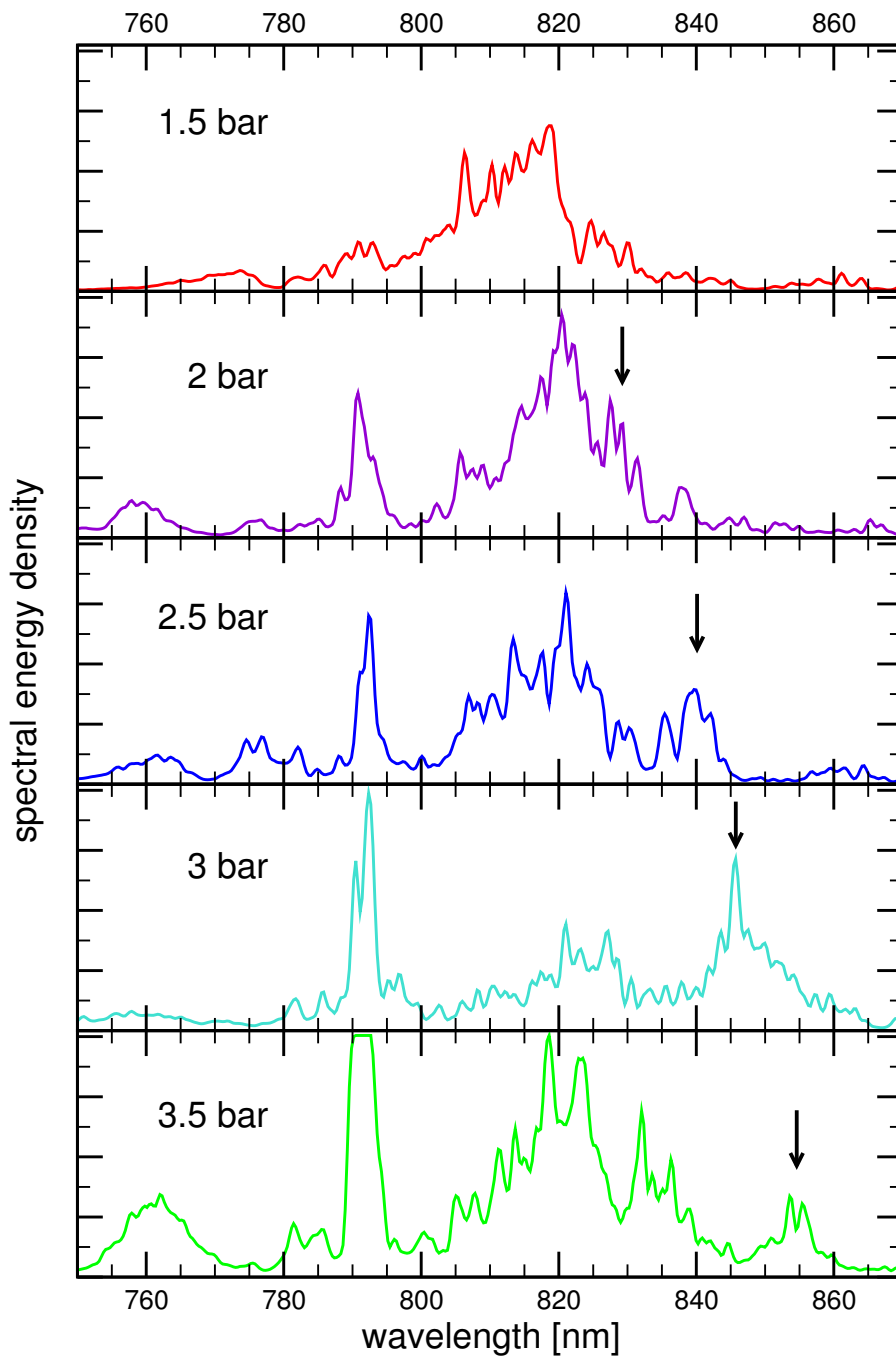


Figure 4.9: Set of spectra for different backing pressures of the gas jet. For higher pressures and hence higher electron densities, the spectrum extends further to longer wavelengths. For 1.5 bar the Stokes line lies completely within the spectrum of the incoming signal pulse. In the plots, it shifts for increasing pressure to 830 nm, 840 nm, 847 nm, and 855 nm.

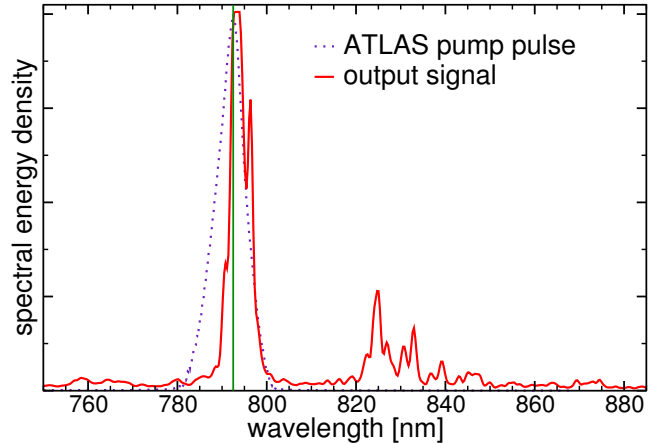


Figure 4.10: For longer pump pulses, SBS starts to dominate the spectrum of the signal output pulse.

4.6 Stimulated Brillouin Scattering for Longer Pump Pulses

We have observed a pulse amplified at the Stokes frequency of the pump pulse with characteristic SRBS features, which proves that launching the new pulse works. For longer pump pulses and a rather low plasma density, its spectrum starts to broaden. These first results suggest that the SRA regime can be fully entered by using longer pump pulses and hence longer interaction lengths. When the pump pulse duration is extended to 3.7 ps at an the energy of 140 mJ, a narrow peak close to the central pump wavelength appears in the spectrum of the amplified signal pulse shown in Fig. 4.10. This feature became already apparent in the density scans shown in Fig. 4.9.

The position of the line and its narrow width suggest that it is caused by stimulated Brillouin scattering (SBS), the scattering from an ion density wave. It shifts the backscattered light by the ion plasma frequency ω_{ion} . For the plasma densities in our experiments, this corresponds to wavelength shifts of 0.5 – 2 nm. At the first glance, the occurrence of SBS is surprising, because in comparison to RBS the inertia of the heavier ions reduces the SBS growth rate. Typical build-up time of SBS is around 20 ps¹. For few ps-pulses, SBS has been observed in rare cases [141], when the plasma is turbulent, has hot spots and a higher density than that used here. In our experiments, SBS is observed only if the signal pulse is injected. SBS is absent in the RBS measurements, when the signal pulse is blocked. On the other hand, an input pulse of about 30 fs duration is much too short to make the heavy ions move and create a density modulation during the time it is present.

In order to understand this finding, PIC simulations using the experimental parameters were performed covering the full plasma length instead of only the small co-moving window around the signal pulse. They revealed that SBS sets in only a long time after the signal pulse has passed. Though the signal pulse is too short to cause a density modulation of the ions while it is passing, the electron density grating set up by the interaction of the signal and pump pulses exerts a strong, periodic electrostatic force on the ions and imprints a velocity distribution without actually moving the ions much. After the signal pulse has passed, the initial velocity distribution transforms into a density modulation, which is just the sound wave that

¹This time-scale is valid for a monochromatic laser pulse. The chirp of the pump pulse used here even reduces the effective time, during which the pump pulse, the backscattered wave, and the ion acoustic wave stay resonant.

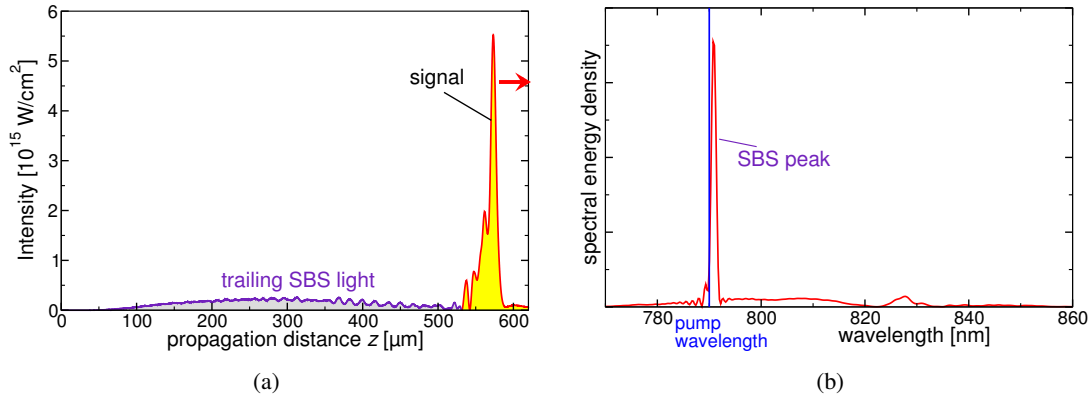


Figure 4.11: 1D-PIC simulation using the experimental parameters. (a) Intensity of the radiation going into the direction of the signal pulse (propagating to the right) after the indicated interaction distance between signal and pump pulse. The short, amplified signal pulse has a long tail of Brillouin scattered light. (b) Spectrum of the backscattered radiation. Although the SBS light has a much lower intensity level than the amplified signal pulse, its total energy is larger than that of the signal pulse.

backscatters the pump pulse. This takes about a quarter of the oscillation period of this sound wave corresponding to $\pi/(2\omega_{\text{ion}}) \approx 0.5 \cdot 1$ ps. The critical point is that this process is almost resonant, because the input signal and the pump pulse have the same wavelengths. They can satisfy the resonance condition for SBS $\omega_{\text{pu}} = \omega_{\text{s}} + \omega_{\text{ion}}$, because ω_{ion} is smaller than the spectral width of the pulses.

One could think that SBS is tolerable, since the SBS light runs behind the amplified signal pulse. However, it disturbs the study of SRA if it dominates the spectrum and the energy of the signal output pulse. It is not advantageous to split off the SBS radiation by using dielectric mirrors, because those have significant oscillations in their transmission curve (cf. Fig. 3.15). Several reflections would be necessary to suppress the SBS light sufficiently, which would also affect the ultra-short signal pulse.

Two approaches are possible to suppress or at least reduce the SBS instability. The first option is to return to the original scheme with an input signal pulse shifted properly with respect to the pump pulse. SBS would not be launched resonantly any more and would thus appear only for much longer pump pulses. Moreover, the properly detuned signal pulse can be amplified directly by SRA. The time consuming launching of a second signal is omitted and higher intensities of the signal can be achieved with the same pump duration and energy.

The second remedy to restrain SBS is using a gas with higher mass number, e.g. helium instead of hydrogen. The larger inertia of the ions lowers the growth rate of SBS, $\gamma \propto m_{\text{ion}}^{-1/4}$ (see Table 2.1 on 11). The downside of this approach are the higher laser intensity needed to fully ionize the gas and the multiple ionization states. Full ionization is necessary to avoid the depletion of the signal pulse when its intensity surpasses that of the pump pulse so that it can strip the remaining electrons from the ions. Furthermore, the different ionization states increases the likelihood for the modulational instability at the ionization front [142]. For the pump pulse intensities and durations used in our experiments, helium is still fully ionized, but not nitrogen or argon.

Both options have been implemented. It turned out that shifting the input signal sufficiently

suppresses SBS. On the other hand, the gas type does not change the results significantly; they are therefore omitted here. Since hydrogen can be ionized faster and for lower intensities, the time for ionization instabilities to set in is even shorter. Therefore helium was abandoned again in later experiments.

5 Observation of SRA for a Red-Shifted Signal Input Pulse

This chapter presents and discusses the experiments performed with the original SRA scheme using a signal input pulse red-shifted with respect to the pump pulse. The combined measurements of the energy amplification, the spectral broadening, and the autocorrelation allow to conclude that SRA in an early stage has been accomplished. In particular, the pulse break-up in the autocorrelation measurement is directly related to the electron dynamics in the SRA regime. The interpretation is supported by a numerical simulations. The measurements for different gas densities are compared. The final section 5.6 analyzes the spatial pattern of the amplified signal pulse. The following, first section summarizes the improvements implemented after the first measurements of the previous chapter.

5.1 Improvements of the Experimental Setup

The various improvements include exchanging the gas jet, shifting the central wavelength of the signal input pulse, and improvements of the energy measurement and the overlap check.

10 Hz Gas Jet with Chimney Nozzle

The main disadvantage of the former gas jet is its large gas exhaust due to its large gas reservoir and long opening time. Each shot increases the pressure level in the vacuum chamber to 10^{-2} - 10^{-1} mbar. Breaks of about 10 sec are necessary between the shots until the pressure level has returned to 10^{-2} mbar. The breaks make the measurements and, in particular, the search for the correct temporal overlap very cumbersome. Furthermore by an indirect effect, they cause fluctuations of the energy and the spectrum of the input signal pulse. The reason for this is that the Ti:sapphire crystal in the multi-pass amplifier of ATLAS is also pumped if the system shutter is closed, because the shutter is located between the regenerative and the multi-pass amplifier. As the energy is not extracted by the laser pulse, the crystal is slightly stronger heated, which changes its index of refraction. When the shutter is reopened the next time, the laser pulse experiences a different thermal lensing in the crystal, which changes its divergence compared to the 10-Hz operation. In the setup for the short pulse generation, the changed divergence shifts the position of the focus relative to the entrance of the hollow fiber. The pulse is not coupled optimally to the fiber mode, the transmission decreases and the spectral broadening is different. This leads to larger shot-to-shot fluctuations of the signal input pulse compared to the 10-Hz operation.

We replaced the gas jet with a type that has a shorter opening time, thus releasing less gas and enabling 10-Hz operation rate with a vacuum level of 10^{-4} - 10^{-3} mbar in the target chamber. The increased operation rate not only simplifies the search for the exact delay setting but

also allows to obtain better statistics and to optimize the amplification during the experiment by changing the spatial overlap of the foci.

Furthermore, we have changed the shape of the nozzle from a conical sub-sonic nozzle with a divergent gas jet that has a large density spread (cf. Fig. 3.20a/b) to the chimney type shown in Fig. 3.20c/b, which guides the gas between its walls and restricts it to a 1D flow. The transverse profile in the main interaction region of the laser pulses is rather flat top like, affected only slightly by small amounts of gas leaking through the entrance and exit holes for the laser pulses. Furthermore, the gradient along the direction of the flow is smaller, which reduces the sensitivity of the exact distance from the nozzle orifice to the focus (cf. appendix A). A nozzle with a width of 1 mm yielded the best results; widths of 0.7 mm and 1.5 mm were also used.

Spectral Filtering to Shift the Signal Wavelength

The conclusions drawn in the previous section advise to return to the original SRA scheme using an input signal pulse with a central wavelength slightly longer than that of the pump pulse. The options to generate such a signal pulse are thoroughly discussed in section 3.3. Within the frame of this work, the only reliable option to obtain such pulses synchronized with the pump pulse was by spectrally filtering the signal pulse after the hollow fiber. The central wavelength of the filtered pulse is around 816 nm, the energy in the target chamber about 80 μ J, and its duration about 80 fs.

Change of the Gas

We temporarily switched from hydrogen to helium for the experiments, because its larger mass number decreases the growth rate of SBS. Since no significant improvements were observed after having shifted the wavelength of the input signal pulse, hydrogen was employed again. Its lower ionization threshold assures its early ionization by the pump pulse before the interaction of the signal pulse with the body of the pump pulse starts.

Improved Energy Measurements

As mentioned in section 4.1 as to the energy measurements, the absorbing filters used to adjust the amount of light entering the Ulbricht sphere are bleached by the high intensities of the amplified signal pulses. To remove this source of error, the absorbing filters were replaced by two wedges as depicted in Fig. 3.18. Furthermore, the energy measurement was computerized to record the data at 10 Hz. Along with the computer controlled delay line, fully automated scans of the energy amplification became possible.

5.2 Energy Amplification to the mJ Level

In Fig. 5.1 the energy amplification of the signal pulse is plotted versus the delay between the pump and signal pulses for the following parameters:

	pulse duration (FWHM)	energy	focal intensity
pump pulse	5.6 ps	210 mJ	3.7×10^{15} W/cm ² ,
signal input pulse	80 fs	80 μ J	1.4×10^{14} W/cm ² .

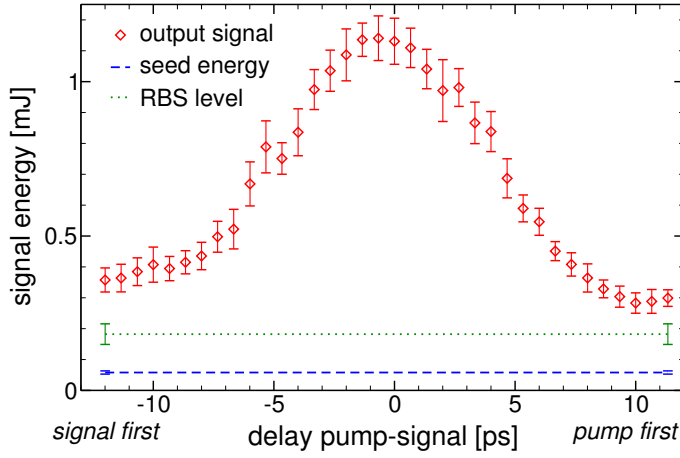


Figure 5.1: Energy vs. delay between input signal and pump pulses. The pump pulse is 5.6 ps long, the gas jet is 1 mm wide. The signal pulse is amplified by a factor of 19 to ≈ 1.15 mJ. Each point is averaged over 20 shots with the error bar indicating the standard deviation. (See section 4.1 for the different levels of the amplified signal on the left and right hand side of the maximum.)

About 70-80 % of the energy of both pulses are contained in the foci of 26-30 μm diameter. The plasma density is $n_e = 3.5 \times 10^{18} \text{ cm}^{-3} = 0.002 n_{\text{crit}}$. The new curve is definitely smoother than that depicted in Fig. 4.1 and has improved statistics, both a result of the continuous 10-Hz operation. At its maximum, the output signal contains 1.15 mJ, which is 19 times higher than that of the input signal pulse, if compared to the energy contained in the central disk of the focus. This is justified, because outside this disk the intensities of the pump and signal pulses are too weak to lead to significant amplification and the contributions to the input energy are irrelevant when considering the amplification (cf. Fig. 3.19).

Combined with the AC measurement in section 5.4, the intensity of the still focused signal pulse after the amplification is computed to $3.6 \times 10^{15} \text{ W/cm}^2$. The intensities of the pump and signal pulses allow to compute the ratio $\omega_b/\omega_{\text{pe}}$, which indicates whether the pulse is amplified by SRBS or by SRA. The ratio increases from $\omega_b/\omega_{\text{pe}} = 0.58$ before to $\omega_b/\omega_{\text{pe}} = 1.30$ after the amplification. Hence the signal pulse seems to be amplified first by SRBS and later by SRA. To verify the amplification in the superradiant regime, further evidence is gained by inspecting the spectrum and the autocorrelation of the amplified pulse.

The initial amplification in the SRBS regime is possible although the resonance condition for Raman amplification $\omega_{\text{pu}} = \omega_s + \omega_{\text{pe}}$ is not satisfied strictly for the parameters in the experiments. The Stokes-line is expected at 829 nm. The small frequency mismatch $\Delta\omega = \omega_{\text{pu}} - \omega_s - \omega_{\text{pe}} = 0.36\omega_{\text{pe}} = 0.016\omega_{\text{pu}}$ becomes important only if the amplified pulse is longer than $\pi/\Delta\omega \approx 85$ fs. This is analogous to optic parametric amplification in a nonlinear crystal, where a mismatch of the wave-vectors, Δk , causes decoherence only if the crystal is longer than $\pi/\Delta k$.

The RBS value indicated in Fig. 5.1 is measured with the signal pulse blocked and gives an upper limit for the RBS level during the experiment. The input signal pulse has a lower intensity than in the earlier experiments, because the spectral filtering to shift its central wavelength reduces its energy and at the same time increases its duration. The electron density has been reduced to lower the threshold for SRA and to avoid that the pump light backscattered by instabilities (RBS) becomes much stronger than the signal pulse to be amplified. However, lowering the electron density decreases the gain, since the coupling between the pulses is weakened.

5.3 Spectral Broadening of the Amplified Pulse

The observed spectra depicted in Fig. 5.2 reveal additional contributions that do not belong to the signal pulse or the Raman backscattered pump light. They represent pump light reflected from the walls of the chimney nozzle, in particular around the entrance holes for the laser pulses. There, the pump intensity is too small to burn the aluminum foil covering the sides. The pump light is reflected from the foil and enters the spectrometer together with the desired signal. Its contribution is measured separately injecting only the pump pulse without the signal pulse and without releasing gas. Subtracting this spectrum from the raw data yields the spectra of the amplified signal pulse and the RBS of the pump pulse in Fig. 5.3. The same correction has been carried out for the energy measurement in the previous section.

The signal pulse is broadened significantly from 17 nm (FWHM) for the input to 30 nm for the amplified output. Furthermore on the long wavelength side, an additional wing extends from 830 nm up to 870 nm. The sharp Stokes line, that dominated the spectrum in the first experiments (Figs. 4.2 and 4.3) is absent, suggesting that SRBS contributes only little to the amplification. Instead, the amplification has switched to the SRA regime at some point accompanied by the pulse shortening and spectral broadening. The bandwidth theoretically estimated in section 2.3.5 ranges from the pump wavelength up to 865 nm, which corresponds very well to the end of the long-wavelength wing in the spectrum. Assuming the wing is due to SRA, the intensity ratio of the wing and the main spectrum suggests that SRA is still in an early stage.

It has to be excluded that SRBS causes the observed broadening. While SRBS is characterized by the narrow bandwidth of the backscattered light for small signal gain, two other regimes exist that entail broader spectra (cf. section 2.6): (i) The *strongly coupled Raman regime* [89, 90] and (ii) the *pump depletion regime* [45]. Their spectra can have widths greater than the plasma frequency. The pump depletion regime cannot take place because it requires the pump pulse to be completely depleted from some point on during the interaction with the signal pulse. This is ruled out by the small energy transfer of less than 1 % from the pump pulse to the signal pulse.

The strongly coupled Raman regime is characterized by a growth rate γ exceeding ω_{pe}

Figure 5.2: The unprocessed original spectrum contains pump light reflected from the side walls of the chimney nozzle around the entrance holes. The black curve is taken when injecting only the pump pulse without gas and signal pulse. The spectra in Fig. 5.3 are obtained by subtracting this spectrum from the measured spectra of the signal output and Raman backscattered pump, respectively.

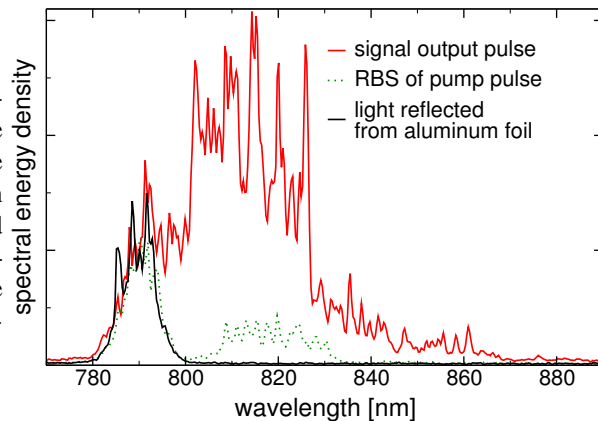


Figure 5.3: Spectra of the signal input and output pulses and of the Raman backscattered pump light. The amplified spectrum is smoothed (black line) to infer its bandwidth. The bandwidth increases from 17 nm (FWHM) of the input signal pulse to 30 nm for the amplified output.

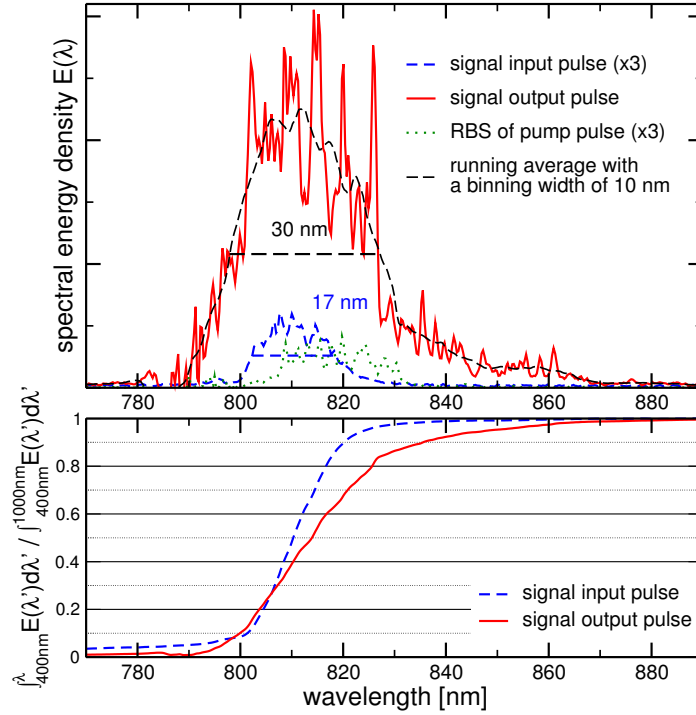


Figure 5.4: Integrated energy distributions of the spectra for the input and output signal pulses show that 15 % of the energy of the amplified pulse are contained in a long wing extending from 830 nm to 870 nm.

substantially. The SRBS growth rate from Table 2.1 for our parameters is computed to

$$\gamma = \frac{1}{2} \sqrt{\omega_{pe} \omega_{pu}} a_p = 0.068 \omega_{pe} \ll \omega_{pe} \quad (5.1)$$

using the approximation $\omega_{pump} \gg \omega_{pe}$, $a_p = 0.029$ (from experiment), and $\sqrt{\omega_{pe}/\omega_{pump}} = \sqrt[4]{n/n_{crit}} = \sqrt[4]{0.002} = 0.21$. Therefore, the weakly coupled regime prevails with the gain bandwidth

$$2\gamma_0 = 0.14 \omega_{pe} = 0.0061 \omega_{pu} \quad (5.2)$$

corresponding to 5 nm. Including the 8.7-nm bandwidth of the chirped pump pulse, the total gain bandwidth in the Raman regime is still significantly smaller than the observed spectral broadening.

A special feature in Fig. 5.3 are the narrow peaks on top of the amplified spectrum. It appears that they might be caused by RBS, because they are narrow and they end around 830 nm on the long-wavelength side, where the Stokes line for the maximum electron density is expected. However, they are not very prominent in the pure RBS measurement when the signal pulse is blocked. Thus they have to be due to the interaction of the signal and pump pulses. This is only possible in the pedestal or a precursor of the signal pulse, because the intense maximum of the signal pulse is amplified in the SRA regime, thus the plasma wave is broken and Raman scattering ceases. It is not yet fully understood, whether the peaks in the spectrum could also be produced by SRA.

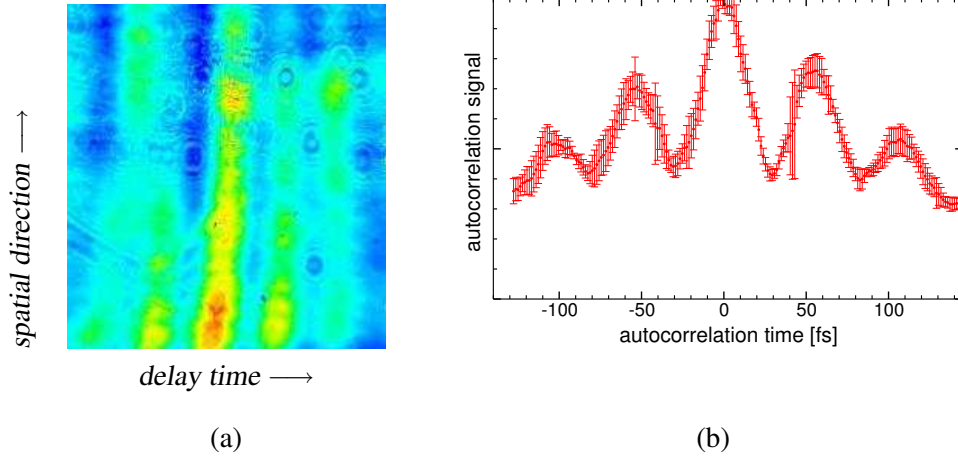


Figure 5.5: (a) Single-shot autocorrelation of the amplified signal pulse captured by the CCD camera. (b) Line-out averaged over several rows with statistical deviation vs. the calibrated time axis. The rows were taken near the bottom of the image, where the 2ω -signal is maximal but not yet clipped.

5.4 Autocorrelation Measurement

Fig. 5.5a shows the image of a typical autocorrelation measurement captured by the CCD. The autocorrelation trace is obtained as a line-out over up to 20 rows. They are chosen in a region, where the 2ω -signal is maximal without being clipped so that the full dynamic range of the CCD camera is used. The error bars represent the statistical deviation with respect to the average curve. For clarity they are omitted in the following figures.

The periodic modulation of the autocorrelation trace indicates that the output signal actually consists of a train of equidistant pulses. Their temporal spacing is equal to the spacing between the peaks of modulation in the autocorrelation trace. The five peaks of the trace refer to three pulses in the train. In Fig. 5.6a, the autocorrelation trace of the signal output is compared to that of the signal input. The individual pulses of the train must be much shorter than the input pulse, whereas the hole pulse train is slightly longer.

We fitted a train consisting of three \cos^2 -pulses¹

$$I_s(t) = \sum_{j=1}^3 I_j \cos^2\left(2\pi \frac{t-t_j}{T_j}\right) + I_0 \quad (5.3)$$

such that its autocorrelation²

$$I_{ac}(\tau) \propto \int_{-\infty}^{\infty} I_s(t) I_s(t-\tau) dt \quad (5.4)$$

¹The cosines are restricted to the first half period around 0, i.e.

$$\cos^2(t) \equiv \begin{cases} \cos^2(t) & |t| \leq \pi/2 \\ 0 & |t| > \pi/2 \end{cases}$$

²Actually, the autocorrelator generates the second harmonic of the *amplitudes* in the BBO crystal causing a fringe pattern with a spacing $2\lambda/\sin(\theta/2)$ inside the crystal, which are not visible here, as explained in the description of the autocorrelator in 3.6.4. The effective signal captured by the CCD camera is proportional to Eq. (5.4).

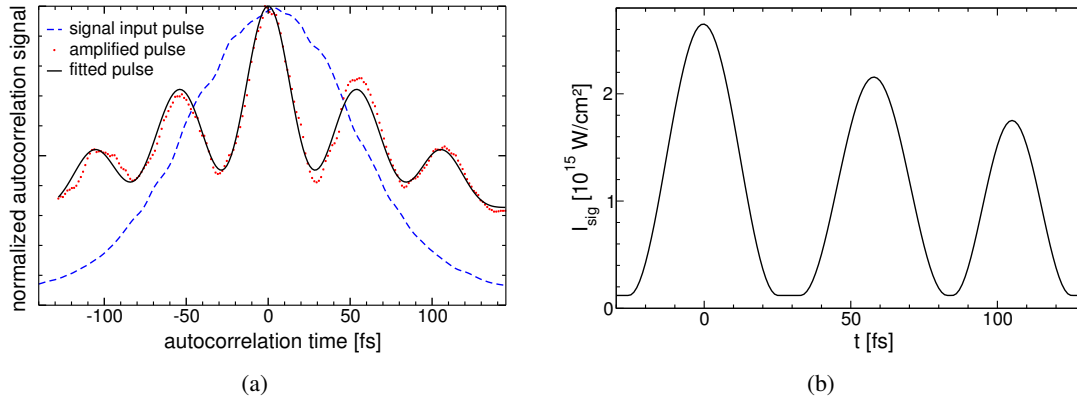


Figure 5.6: (a) AC traces of input and output signal pulses. The periodic modulation of the amplified signal implies that it consists of a train of pulses. The pulse train in (b) is fitted such that it reproduces the measured autocorrelation trace best.

	T_j [fs]	t_j [fs]	I_j [a.u.]	contained energy [%]
Pulse 1	23	0	0.19	36
Pulse 2	26	56	0.12	26
Pulse 3	32	105	0.074	20
offset	140 ^(a)	—	0.016	18

Table 5.1: Parameters of the fit shown in Fig. 5.6b.

^afull length of the pedestal

matches the measured trace best. Its temporal profile and its computed autocorrelation trace are shown Fig. 5.6. In Eq. (5.3), the T_j 's are the FWHM durations of the pulses and the t_j 's are their temporal offsets. Table 5.1 lists the parameters of the fitted pulse train plotted in Fig. 5.6b. The offset (0) should not be regarded as independent of the pulses, but rather adds up to them in equal shares. Fig. 5.6a leaves open whether there are more modulations outside the measured time window. We repeated the fitting procedure including a 4th pulse. The results became somewhat arbitrary for the 3rd and 4th pulse insofar as the pulses overlapped partially. We use the 3-pulses-fit, to avoid the arbitrariness and because the two leading pulses are the strongest and have approximately the same parameters in both fits.

5.4.1 Origin of the Pulse Breakup

The pulse breakup is a direct consequence of the SRA acting on a long signal pulse, i.e., a pulse long enough to trap the electrons for more than one oscillation cycle $T_b = 2\pi/\omega_b$ in the ponderomotive potential. The electrons continue to get bunched periodically such that they first scatter the pump light back into the signal pulse, then the signal back into the pump during the next bunching and so forth, as it is illustrated in Fig. 2.3 on page 18. The long signal is amplified and attenuated periodically while it is interacting with the pump pulse. The attenuation finally splits the signal into a train of pulses with the temporal spacing T_b and a pulse duration of about $T_b/2$. To check this explanation, values of T_b from Table 5.1 are compared with those computed from $\omega_b = \sqrt{a_s a_p (\omega_s + \omega_{pu})}$. For the computation the

intensities of the pump and signal pulses are needed.

Although the measurement with a 2nd-order autocorrelator is ambiguous as to which is the front and which is the rear side of the fitted pulse train, it is reasonable to assume that the most intense pulse leads the train. There are two arguments, why the SRA favors the amplification of the first pulse inherently:

1. The electrons oscillating in the ponderomotive potential have different oscillation periods because the potential is non-harmonic. Therefore, they de-phase after several oscillations, their bunching becomes less perfect, the backscattering of the pump is no longer fully coherent and hence less efficient.
2. The bunching causes a velocity spread of the electrons equivalent to the depth of the ponderomotive potential which is proportional to the amplitude of the signal pulse. If the amplitude of the leading pulse has grown already slightly larger, the subsequent pulses cannot trap the electrons as efficiently any more. Less electrons get bunched and participate in the backscattering of the pump.

The stronger growth of the leading pulse is also observed in the numerical simulations in Fig. 5.7.

Using the values from Table 5.1 the intensity of the main peak of the signal pulse is computed to $I_s = 3.6 \times 10^{15} \text{ W/cm}^2$ and its amplitude to $a_s = 0.036$. To determine the intensity of the pump pulse, its temporal profile must be taken into account and the intensity evaluated at the position of the signal pulse at the time, when the amplification drops off significantly. Although the exact position and time are difficult to ascertain, the value of ω_b is not affected too much, because it depends only weakly on the pump intensity, $\omega_b \propto I_p^{1/4}$. Consulting numerical simulations of SRA, a reasonable intensity level is 40 % of the maximum, $I_p \approx 1.5 \times 10^{15} \text{ W/cm}^2$ or $a_p = 0.014$. For the given pump and signal intensities, the resulting bouncing frequency is $\omega_b = 0.043 \sqrt{\omega_{pu} \omega_s} = 1.1 \times 10^{14} \text{ Hz}$ and the period $T_b = 2\pi/\omega_b = 58 \text{ fs}$. This value compares well with the distance t_1 between the first two pulses given in Tab. 5.1. The observed pulse duration is slightly shorter than the computed one, $T_s \approx T_b/2 = 29 \text{ fs}$. However, the agreement is good, considering that the \cos^2 -profile used for the fit is only a rough estimate that may differ from the actual profile.

The good agreement of the computed and measured values of T_b confirms the assumption that the pulse breakup is caused by SRA and the amplification of the signal pulse in the super-radiant regime can be concluded from this observation. Other effects that might cause a pulse train with such equidistant pulses can be excluded. The two possible explanations are again related to the Raman regime:

- *Beating of two waves:* The beating of two light waves with close but not identical central wavelengths can cause a periodic pulse train. In this case, two distinct components should appear in the spectrum related to the incoming signal pulse and the Raman backscattered pump light. These distinct components, however, are not visible in the measured spectrum depicted in Fig. 5.3.
- *Nonlinear pump depletion regime:* In the regime described by Malkin [45], the scattering of the pump pulse back into the signal pulse from the electron plasma wave becomes so strong that the pump is completely depleted. The energy transfer then reverses and

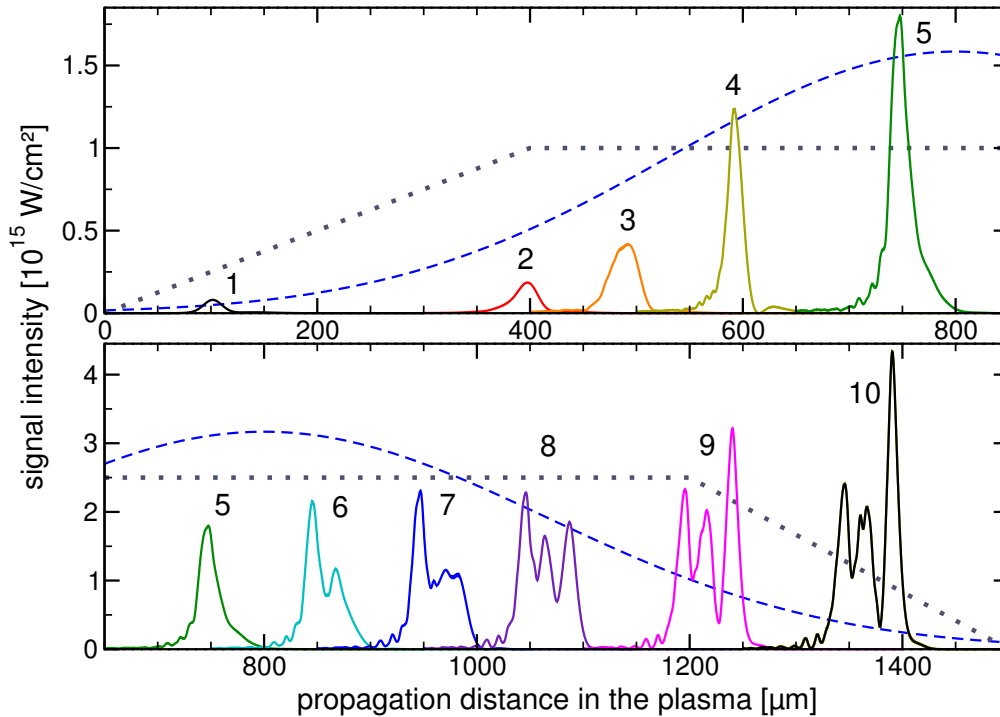


Figure 5.7: PIC-simulation illustrating the pulse breakup. Snapshots of the signal pulse are given for several propagation distances. The upper plot shows the first half of the interaction region, the lower plot the second half. The blue dashed line indicates the intensity of the pump pulse seen by the signal pulse at the respective position. (In the upper graph its intensity is divided by 2 to fit the scale.) The grey dotted line indicates the density profile of the plasma. The signal pulse (5) at $700 \mu\text{m}$ (green curve) is plotted in both graphs to act as a reference.

the pump is amplified again shifted in phase by π . As explained earlier, the pump depletion can be excluded due to the small total energy transfer of less than 1% from the pump to the signal pulse.

5.4.2 Numerical Simulation of the Pulse Breakup in the SRA Regime

Fig. 5.7 illustrates the pulse break up by means of a numerical PIC simulation. It also clarifies, why the complete length of the output signal pulse increases slightly. The parameters used for the pump and signal pulse and the plasma are close to the experimental ones. The pump pulse is negatively chirped and has the bandwidth of the ATLAS pulse. The signal pulse is modeled using two pulses. The main pulse with 70 fs duration at 818 nm contains most of the energy. A longer negatively chirped pedestal stretches out about 150 fs to the front side of the main pulse and has 6% of the peak intensity. This part originates from the generation of the short pulse by self-phase modulation in the hollow fiber, filtering, and compression and has been discussed in section 3.4 on p. 57. The plasma density profile is approximated by adding ramps on both sides to model the mostly flat top density profile in the chimney nozzle with some gas leaking through the entrance holes of the laser pulses.

The weak input pulse (1st pulse, black line) is first amplified in the Raman regime, thereby

increasing its duration slightly (3rd pulse, orange line). Up to $700 \mu\text{m}$, the pulse is further amplified but the pulse starts shortening by attenuation of its rear side, which indicates the onset of SRA. At the same time, the pedestal has been amplified significantly. Although still in the Raman regime, it perturbs the electron phase space strongly enough to prevent the further amplification of the trailing main pulse beyond $800 \mu\text{m}$ up to the end. The emerging front of the signal has time to get amplified and finally overtake the original main pulse in intensity. Between $850 \mu\text{m}$ and $950 \mu\text{m}$, the leading pedestal is amplified until it forms a plateau at about the threshold intensity for SRA. This is possible, because the amplification of the leading edge of the plateau prevents the amplification behind. After the pedestal has been amplified to full length of about 150 fs , the further growth of the plateau stops. SRA sets in and leads to the breakup of the pulse by the mechanism explained in the previous section. Finally, the leading pulse of the train starts to outgrow the other pulses of the train. Simulations with longer interaction lengths show, that the leading pulse is amplified strongly up to an intensity of several times 10^{17} W/cm^2 and dominates the residual pulses, which are too weak to trap all the electrons released from the ponderomotive potential after the first pulse has passed. The trailing pulses keep their intensity level and become negligible compared to the main pulse.

The simulation nicely visualizes the processes of the amplification, lengthening and pulse breakup, and supports the analysis of the experimental results. On the other hand, it also indicates how sensitive the actual signal pulse shape depends on the exact input parameters while the amplification is still in the transition region $\omega_b \approx \omega_{pe}$ or in the early stage of SRA.

5.5 SRA at Different Densities

Changing the backing pressure and thus the electron density in the plasma has various, in some respect antagonistic effects on the amplification:

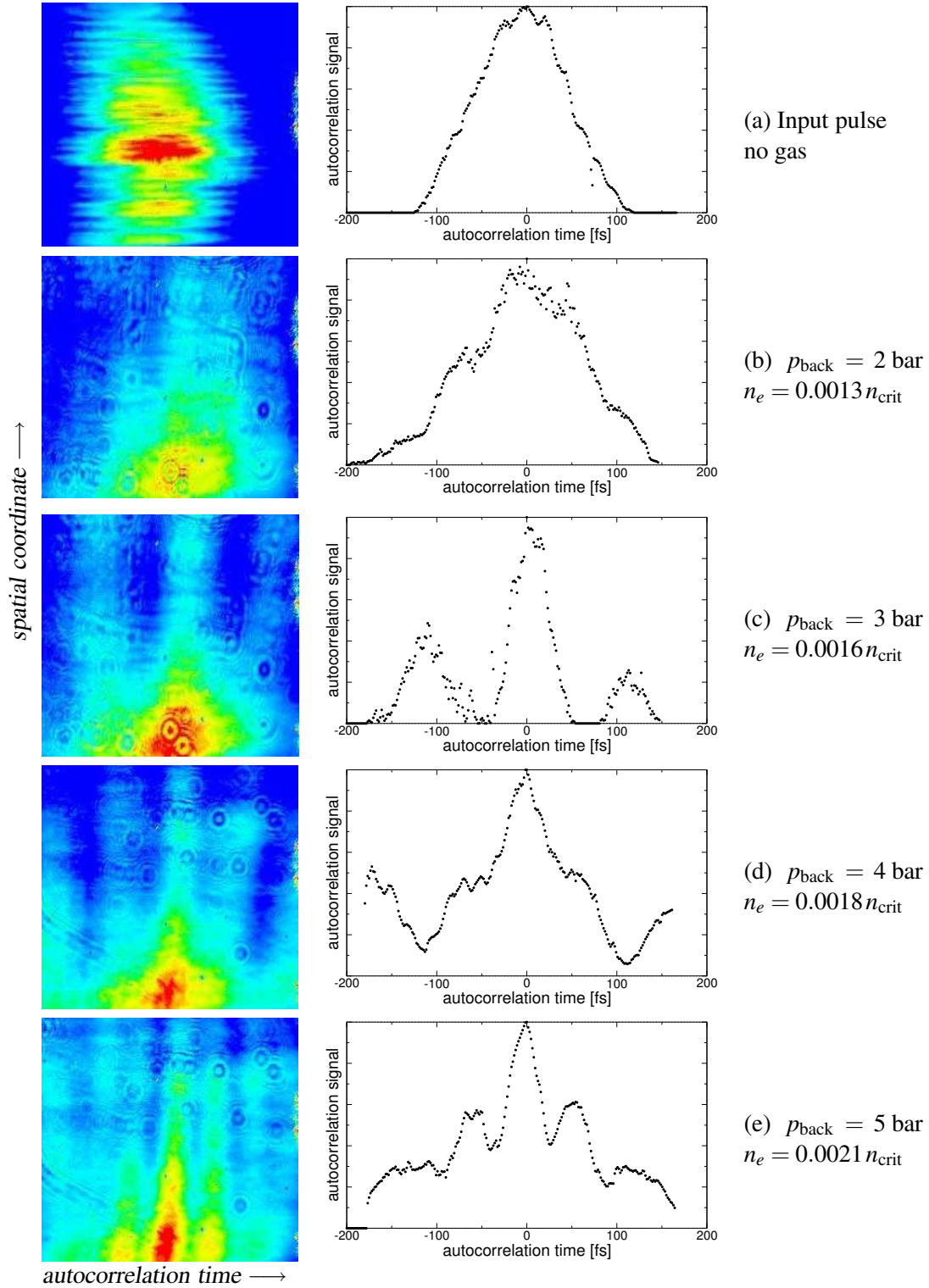
1. Because of the higher electron density, more electrons scatter the pulses and the two pulses are coupled stronger. Thus the signal is amplified stronger.
2. In a denser plasma, collective effects become stronger. The higher n_e also entails a higher plasma frequency ω_{pe} . Therefore, the threshold intensity for the onset of SRA increases. This is particularly important, because the input signal pulse becomes much weaker after spectral filtering.
3. The RBS instabilities of the pump pulse become larger, which not only lowers the signal-to-noise ratio of the output pulse but also perturbs the initially homogeneous and quiet plasma. As seen in the previous section, this can reduce the amplification.

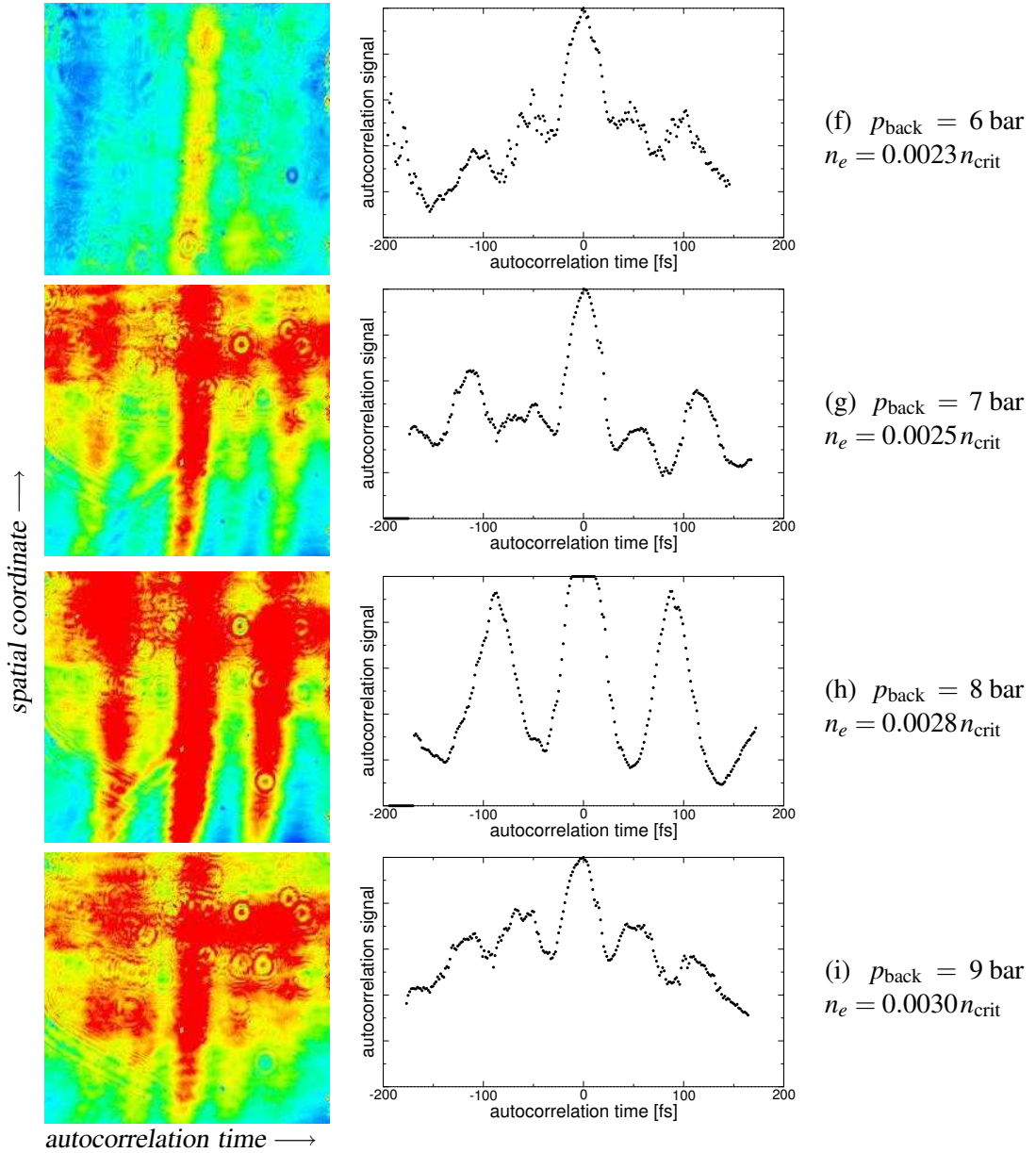
Two questions are addressed in the following sections: Is SRA quenched for higher densities because the threshold intensities cannot be reached any longer? How do the energy amplification and the autocorrelation change for higher intensities?

5.5.1 Autocorrelation Measurements

Fig. 5.8 shows the captured CCD images and the line-out of the autocorrelation traces for increasing backing pressure of the gas jet. The signal pulse breaks up and a modulation in the

Figure 5.8: Single-shot autocorrelation images and line-outs for different backing pressures in the reservoir of the gas jet resulting in different plasma densities. The line-outs depicted in the right column are obtained by averaging over several rows of the CCD image, where the 2ω -signal is maximal but not yet clipped. Error bars in the line-outs are omitted for clarity. The asymmetry of the images are dealt with in the text.





autocorrelation becomes apparent. It is barely visible at the lowest pressure (b), but becomes clearer for higher pressures and amplification. With increasing density, the periods of the modulations become shorter. Finally, some of the fringes merge with the adjacent ones (g) & (h). At the same time, the pedestal below the modulation in the autocorrelation trace increases.

Most obviously the shorter periods for higher densities are explained by the higher signal intensity that results in a higher value for ω_b and thus a shorter period $T_b = 2\pi/\omega_b$. But this explanation does not reach far enough. Actually, the break-up that determines the period occurs only once when the signal and pump intensities become large enough to satisfy the threshold condition. The period of the modulation becomes shorter because the transition from SRBS to SRA occurs for a higher ω_b . Later on, the first pulse of the train is amplified preferentially as it

was explained in the previous section. Its intensity increases further and hence the local value of ω_b causes only the leading pulse to shrink. Its length is then shorter than half the period of the pulse train, $T_s < T_{b,\text{breakup}}$, which is not clearly visible in the data. The trailing pulses get out of phase with respect to the first pulse so that the resulting autocorrelation traces smears out, i.e., the modulation of the trace becomes less deep. The fringes merge or disappear and the pedestal of the trace rises. The reconstruction of the actual pulse profile is difficult in this case.

The autocorrelation traces of the pulses that are amplified longest in the superradiant regime show a dominant central peak due to the larger amplification of the leading peak of the pulse train. This appears most clearly for the pressure range from 5 to 7 bar in the Figs. (e) to (g). At 8 bar the central peak decreases again, i.e. the leading pulse is not as dominant any longer. For the highest pressure at 9 bar, the modulation is less pronounced and has a much larger pedestal, which might indicate that the breakup due to SRA is just about to set in, but is not yet complete.

The apparent asymmetries in the autocorrelation images are not yet fully understood. There are possible explanations, but the necessary preconditions for them are not satisfied. First, it could be a distortion of the wave front causing a shift of the line focus of the cylindrical mirror in the autocorrelator in Fig. 3.22. However, a similar shift was not noticed in the measurements of the far-field in 5.6.1. Second, the extension of the signal pulse spectrum to the NIR could change the phase matching condition for the second harmonic generation in the BBO crystal. For a different fundamental wavelength, the 2ω -signal is emitted in a slightly different direction, which shifts the image relayed to the CCD camera. This trend should continue for higher densities, where the spectra extend even further to the NIR. However, this is not found in the captured autocorrelation images (f)-(i).

5.5.2 Energy Dependence on Density

The signal energies corresponding to the preceding autocorrelations are plotted in Fig. 5.9a for densities from $0.001 n_{\text{crit}}$ to $0.003 n_{\text{crit}}$. The range below $0.001 n_{\text{crit}}$ is missing, because the density in the gas jet does not go to zero linearly for small backing pressures (Fig. 5.9b). The signal output energy is slowly increasing with the electron density and fluctuates increasingly for higher densities. Although there are more electrons to take part in the signal amplification for higher densities, the overall amplification is affected by the increasing instabilities of the pump pulse, which pre-heats the plasma and thereby affect the bunching of the electrons during the signal-pump interaction. The statistic behavior of the RBS instabilities therefore contributes to the larger energy fluctuations of the amplified signal pulse. As concluded from the autocorrelation measurements, the SRA regime is not reached safely any longer.

In the actual experiment, the RBS instabilities are weakened by the signal amplification (see section 4.1). The net signal energy is therefore larger than the difference between the total signal output and the level of the RBS light in Fig. 5.9a, so that the highest effective signal energies are found around $n_e = 0.002 n_{\text{crit}}$. This is just the density range, where the autocorrelation traces in Fig. 5.8 show the formation of a strong short pulse expected when the signal pulse is amplified longer in the superradiant regime.

As the input signal is weak in these energy-density measurements, the threshold for the superradiant regime is reached only late. The amplification length in the superradiant regime is

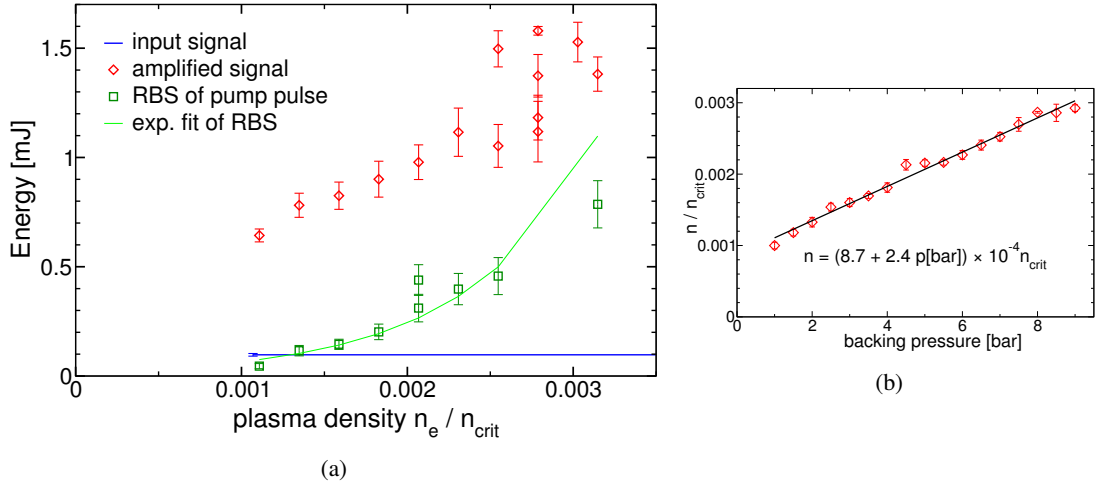


Figure 5.9: (a) Energy dependence on density for $\tau_p = 5.6$ ps. The data refers to the previous autocorrelation measurements in Fig. 5.8. (b) Calibration curve for the relation between backing pressure and electron density.

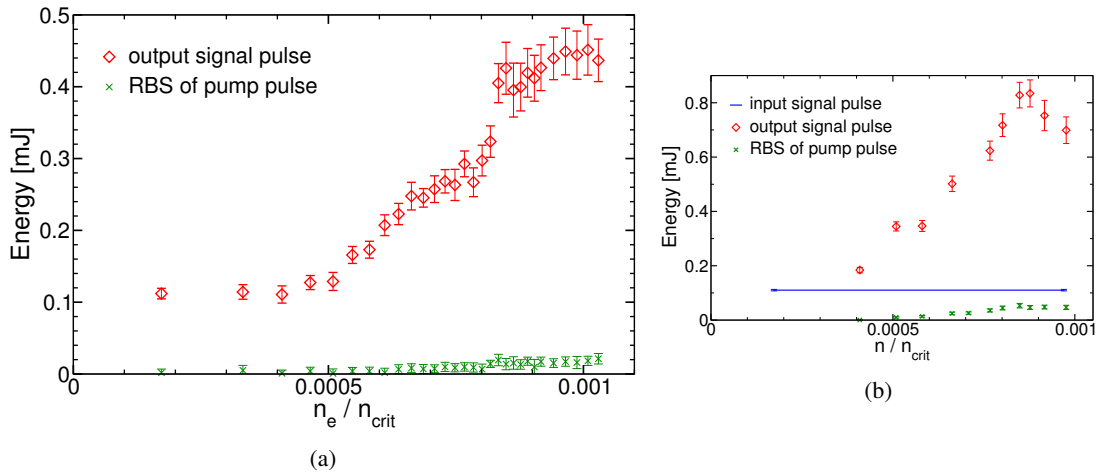


Figure 5.10: Dependence of the signal output energy on n_e for low densities and $\tau_p = 4.3$ ps. The records are obtained from different measuring campaigns. The differences in the energy show that deterioration of the alignment of the off-axis parabolas between several measurement campaigns can cause a significant decrease of the amplification.

rather short and the contribution of SRA to the total amplification does not yet dominate. Only if SRA prevails for a longer time so that traces of the initial conditions and of the transition regime become negligible, one can expect to find the theoretically predicted scaling laws.

In a second experiment shown in Fig. 5.10a, the electron density has been controlled differently to achieve lower electron densities. Instead of changing the backing pressure, the opening time of the gas jet and the delay between releasing the jet and arrival time of the laser pulses are changed while the backing pressure is fixed at 2 bar. For such low densities, the instabilities of the pump pulse almost vanish. Below $0.0004 n_{crit}$, the signal pulse is not significantly amplified, the energy of the input and output pulses are equal; above $0.0005 n_{crit}$, the energy increases approximately linearly with the gas density.

The low plasma densities enable SRA even for low signal intensities. However, the amplification is not very efficient and the bouncing frequency ω_b is so small that no pulse shortening can be observed. This agrees with the autocorrelation measurement in Fig. 5.8a for $n_e = 0.001 n_{\text{crit}}$.

Finally, the data plotted in Fig. 5.10b demonstrates the influence of the accurate alignment on the amplification. Though the pump and signal pulse parameters and the plasma densities are the same as in Fig. 5.10a, the signal output energy is significantly higher. The data was taken earlier, shortly after an overall realignment of the complete setup in the target chamber. The accuracy of the alignment degrades over a series of experiments and hence the observed amplification. In particular, the alignment of the two off-axis parabolic mirrors ensuring the exact counter-propagation of the pulses is crucial. The misalignment can also be identified in the far field images of the signal pulses as obvious from Fig. 5.11d and e. In the present setup, it is too cumbersome to realign the parabolas before every experiment, because various other components have to be removed for the procedure. For future experiments, it is preferable to install a diagnostic that allows a quick and precise realignment.

5.6 Spatial Profiles of the Amplified Pulse

5.6.1 Near- and Far-Field Patterns

The quality of the near and far-field patterns of the amplified pulse are of paramount importance for the application of SRA as an amplifier stage in an actual laser system, because this determines whether the pulse is well focusable, i.e. whether the energy of the pulse can be concentrated in a small spot to achieve high peak intensities.

The near and far-fields for the input and output signal pulses and for the Raman backscattered pump light are presented in Fig. 5.11. The near-field profiles are observed on a cardboard by a CCD camera, the far fields are refocused by a lens of long focal distance (10 m) and captured directly by a CCD camera. The long focal distance was chosen to minimize the distortion of the far-field profile by a possible misalignment of the lens.

All near-fields have a smooth intensity distribution. The profile is approximately super-Gaussian for the input pulse and Gaussian with an additional broader base for the output pulse. The pattern of the input pulse has a hole, which is due to a damage in the coating of the signal focusing parabola. The spot is smoothed out by the amplification and disappears in the output signal pulse. The Raman scattered pump light is so weak that it is hardly detectable.

The far-fields of the signal pulses show slight fringes that do not appear for the Raman scattered pump light. Therefore, a misalignment of the focusing lens can be excluded. Instead they are caused by a misalignment of the off-axis parabolic mirrors focusing and recollimating the signal pulse. If they are tilted with respect to each other, here in the horizontal plane of the chamber, the pulses are not exactly counter-propagating any more but are still reasonably well focused. However, the recollimation imprints a tilt on the wavefront preventing an optimal refocusing.

Disregarding this effect, which can be remedied by a proper realignment, the amplified output pulse does not only prove to be well refocusable, but also to be cleaned from wave front deformations: Some of the fringes are removed and more energy is concentrated in the central part of the signal pulse. Indeed, this is expected in case of a good overlap of the pump

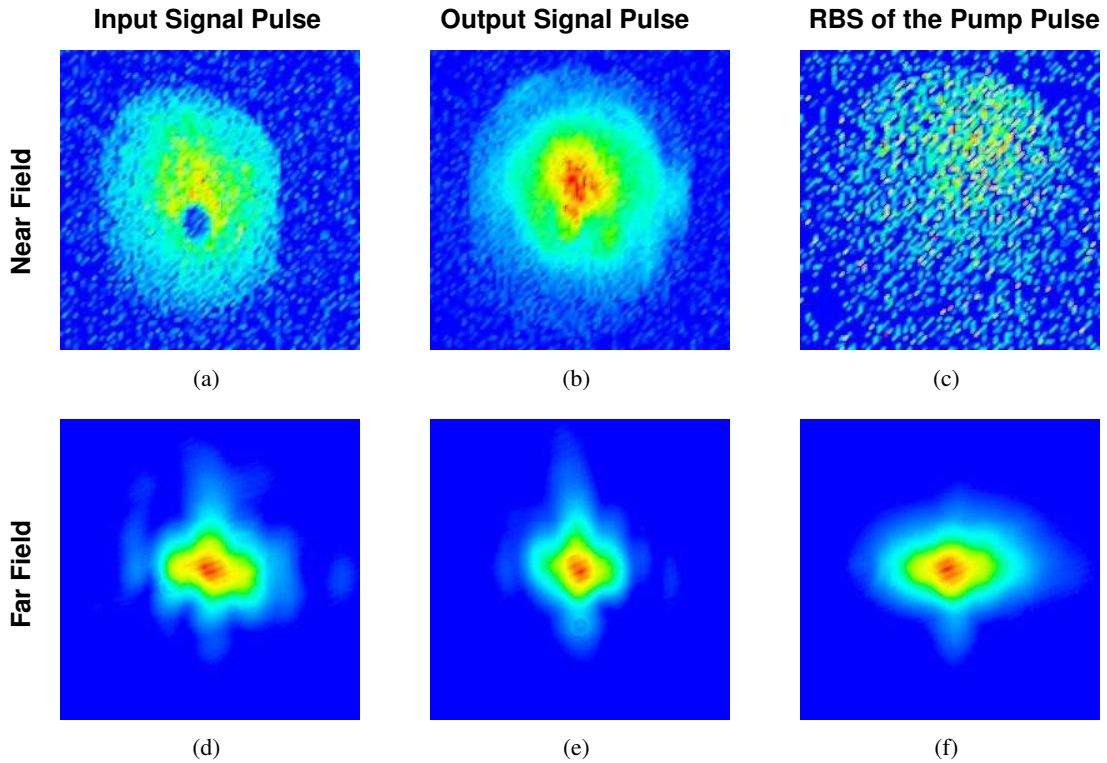


Figure 5.11: Spatial profile of the near fields (upper row) and far fields (lower row) of the input signal pulse (left column), amplified pulse (central column), and RBS light of the pump pulse alone (right column).

and signal pulses in the focus. First, because the amplification has the highest gain, where both pulses have the highest intensities. This favors the central part of the focus, while the outer parts are attenuated relatively to the center. Moreover, the amplification is gain guided and the signal pulse is effectively drawn into the direction of the pump pulse, which is possible if the interaction length ($\approx 600 \mu\text{m}$) is much longer than the focus diameter. The tilt between the phase fronts of the signal and pump pulses, which is due to the misalignment, is reduced and the amplified signal pulse emitted from the plasma is better recollimated by the second off-axis parabola.

5.6.2 Using Near-Field Profiles as Overlap Diagnostics

During the experiments, the observation of the near-field of the signal output pulse has also proved to be a useful on-line diagnostics to check the overlap of the signal and pump foci. If the foci are displaced laterally, fringes appear in the near-field pattern resembling interference fringes shown in Fig. 5.12. It can be excluded that they are caused by the gas jet by diffraction at the edges of the entrance holes for the laser pulses. The holes have a diameter of several $100 \mu\text{m}$ and are much larger than the diameter of the foci.

When the mismatch becomes larger, the number of fringes increases. They become narrower and more tightly spaced, and the amplification gain decreases. The fringes are oriented at right angles to the direction of the displacement, which makes it easy to retrace the origin

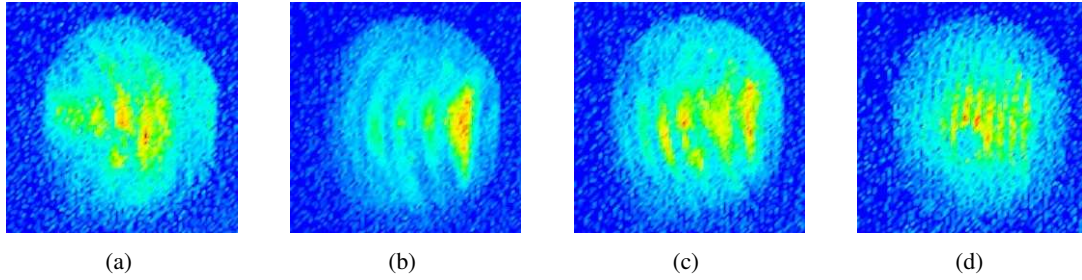


Figure 5.12: Fringes appear for a lateral displacement of the pump and signal foci. The displacement increases from left to right. The energy gain upon amplification decreases.

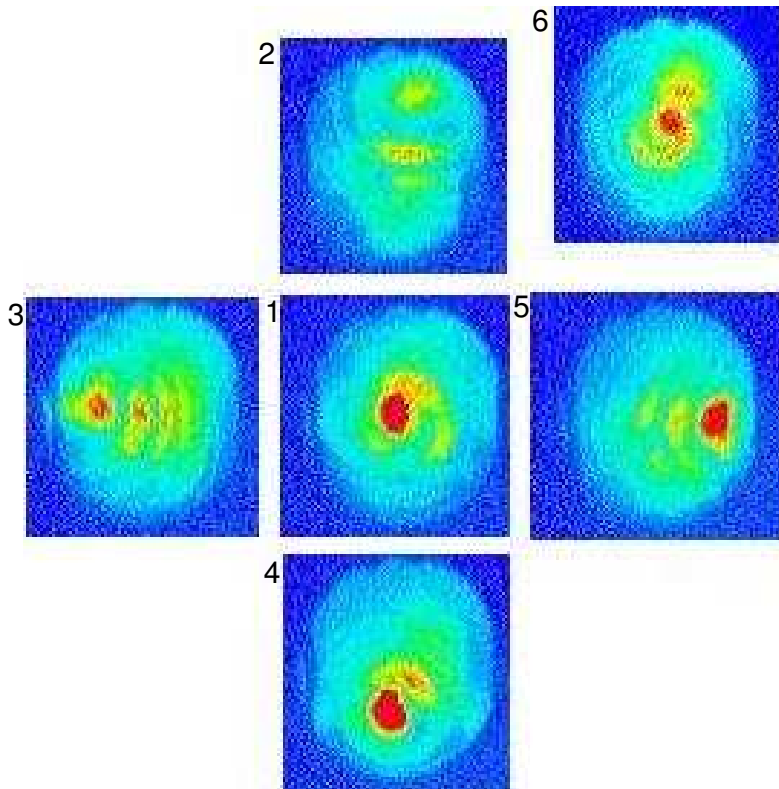


Figure 5.13: Near-field patterns as overlap diagnostics: The fringes are oriented perpendicular to the direction of the displacement. The central image (1) shows the best overlap. Images taken for displacements in the upward (2), left (3), downward (4), and right (5) direction. The image (6) shows the near-field pattern for a large longitudinal displacement. An annular intensity structure appears.

of the mismatch (Fig. 5.13). Finally, annular intensity maxima and minima appear if the foci are displaced longitudinally by a larger distance (see upper right image in Fig. 5.13).

The inspection of the near-field pattern makes it possible to optimize the spatial overlap of the laser pulses online during the experiment, simply by shifting one of the focusing parabolas, thereby shifting the corresponding focus by the same distance, until all fringes have disappeared.

The origin of the fringes is not yet fully understood. When the signal focus is displaced only a narrow strap of the signal profile is amplified. In addition, the remaining part of the signal is outside the pump focus, where the gas is not or only partly ionized. The two halves of the transverse profile experience a different refractive index, which could lead to an interference in the near-field. 3D PIC simulations could help in understanding this effect.

6 Summary, Conclusions, and Outlook

6.1 Summary of the Present Measurements

The first demonstration of SRA has been achieved. As described in detail in chapter 5, its existence is proved by (i) the energy amplification enabling to pass the theoretically given threshold for SRA; (ii) the spectral broadening by a factor of two joined by an even longer tail extending to the NIR (Fig. 5.3); both findings indicate the pulse shortening; (iii) the breakup of the long input signal pulse into a train of short pulses (Fig. 5.6). Their duration and separation agree with the expected values determined from the bouncing frequency of the electrons in the ponderomotive potential (Eq. (2.24)). Other explanations of the observed data could be excluded.

The proof-of-concept of SRA is the first step towards its application in a novel kind of amplifier stage for generating few-cycle, high-power pulses. In this context, the observed near- and far-field patterns are very encouraging: The pulse not only maintains a good profile but is even spatially cleaned by the amplification process. This feature makes SRA additionally attractive.

Two schemes were studied differing in the initial frequency detuning of the pump and signal pulses. The simpler approach in chapter 4 uses pump and signal pulses at the same wavelength. The theoretically predicted formation of a new frequency-shifted signal pulse is confirmed by the experiments up to the point, where the transition from Raman amplification to SRA is indicated by the beginning spectral broadening. The sudden onset of Brillouin scattering of the pump pulse frustrates further studies, because the backscattered light overpowers the still weak signal pulse.

The experiments in chapter 5 were done with the original SRA scheme using a red-shifted input signal pulse. Brillouin is not relevant in these experiments, because it is not resonantly driven by the pump and signal pulses. The input signal pulse is weaker and longer due to spectral filtering, but it is instantly amplified without the detour of launching a second signal pulse. After an initial amplification in the Raman regime, it passes the threshold for SRA. This early stage of SRA is sufficient to imprint characteristic features on the signal pulse, from which the occurrence of SRA is concluded. However, a longer amplification by SRA is needed to study the mechanism quantitatively and to check the theoretical scalings over a wider range.

The generation of the red-shifted signal input pulse synchronized with the pump pulse turned out to be the major complication in present SRA experiments. Among the various approaches examined, only the hollow-fiber technique turned out to give access to SRA. However, this method provided a weak, long input pulse with a weak temporal contrast. It allowed the verification of SRA, but did not permit further detailed studies.

6.2 Future Studies of SRA

An efficient superradiant amplifier delivering a single short pulse requires above all a much improved input signal pulse. A shorter, more intense pulse with a higher temporal contrast is needed red-shifted by 5-10 % of its wavelength compared to the pump pulse. Nowadays, 20-30 fs laser pulses in the mJ-range are reliably produced by commercially available Ti:Sapphire based laser systems. The electronic phase-locked loop described in section 3.3.4 allows to synchronize the oscillators of the pump and signal pulses. Pre-studies performed in this work yielded less than 500 fs jitter between the pump and signal pulses, which is already sufficient for the SRA application. Using a separate laser system for the signal pulse generation has the advantage that its parameters can be adjusted independently from those of the pump pulse thus minimizing the mutual influence of the two lasers. PIC simulations modeling experiments with the present setup of the target chamber showed that the improved input signal is amplified to 10-30 mJ, while its duration shrinks to 10-15 fs.

These pulses are exclusively amplified in the SRA regime and allow more detailed studies of SRA. The theoretical scalings can be checked, in particular, the dependence of the amplification on the plasma density and the continuous shortening of the duration for stronger amplification. Both effects are barely visible while still in an early stage of SRA.

Future investigations also have to consider the propagation of the pump pulse through the plasma. In particular, the Raman backward instability (SRBS) needs to be controlled. While this was not crucial in the present experiments, the instability could emerge as an obstacle when the plasma density is increased and a longer and more intense pump pulse is used to enhance the amplification. Several options are conceivable to suppress SRBS. Its growth length can be limited by restricting the resonance of the pump, signal and plasma wave to short distances: (a) by using a plasma with a density gradient [67] or (b) by using pump pulses with a large chirp [68, 143]. Furthermore, the plasma temperature can be increased by using two additional laser pulses to ionize the plasma and heat it to a temperature of up to 100 eV [144]. This increases the threshold for the onset of SRBS [89, 47] but affects SRA only weakly, because the ponderomotive potential that governs the electron dynamics reaches a depth of up to 1 keV and still traps most of the electrons. The separate ionization of the plasma has the further advantage that ionization instabilities of the pump pulse are excluded.

Finally, if SRA is to be applied in the final stage of a high-power laser system the geometry must be changed from the amplification in the Rayleigh zone used in this work to the region, where the signal pulse strongly diverges so that due to the larger cross sections higher pulse powers can be realized. The following outlook will unfold this idea in greater detail.

6.3 Outlook: Amplification of Divergent Beams

In the present experiments, the amplification of the signal pulse takes place within the Rayleigh zone around the beam waist, where the intensities of the pump and signal pulses are highest and the wavefronts are approximately plane (Fig. 6.1a). Furthermore, the period of the interference pattern created by the pump and signal pulses is $\lambda/2$ and thus much smaller than their focal diameters. Hence the geometry is approximately one-dimensional and matches the existing theory elaborated in previous works.

However, this configuration is inconvenient when aiming for much higher powers, which

is easily seen by the following example. Since the maximally achievable intensity is limited to about 10^{18} W/cm² in the visible, one has to increase the cross sections. To carry 1 PW, the signal pulse needs a diameter of about $300\ \mu\text{m}$. For the one-dimensional configuration with this beam waist, the Rayleigh length is about 9 cm. To avoid damage on the next optical component, the intensity has to drop by 6 orders in magnitude meaning the pulse diameter has to increase by a factor of 1000, which is reached 90 m behind the focus. Such long focal lengths are obviously impracticable. Furthermore, the large focal diameter requires a much stronger input signal pulse to achieve the intensities necessary for SRA, initially.

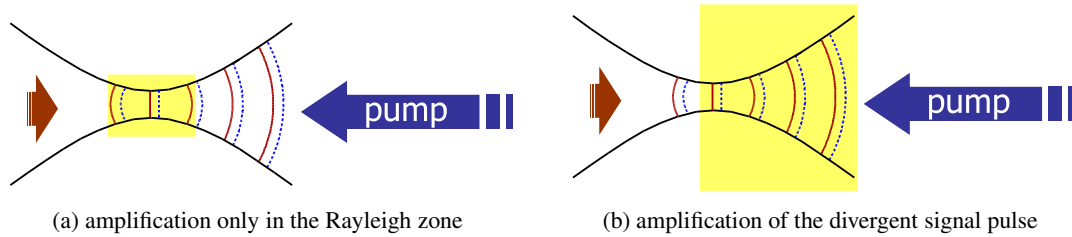


Figure 6.1: Amplification configurations: (a) In the low-energy case, the amplification can be restricted to one Rayleigh length around the beam waist. (b) The achieve high energies, the signal pulse is focused tighter. The amplification can now start with a weaker signal in the focus. While the signal pulse diverges, its energy is distributed over a larger cross section. It stays below the relativistic limit and collects a large total power. If the f-numbers for the pump and signal pulses are equal, their wavefronts are locally parallel everywhere and the electron bunching by SRA occurs in layers along the curved wavefronts.

These inconveniences are solved by a tighter focusing of the pump and signal pulses. This extends the amplification to the domain outside the Rayleigh range, where the signal pulse diverges rapidly. Since the wavefronts of the pulses are locally parallel, i.e. their normal vectors have the same direction everywhere, the bunching by SRA occurs along the wavefronts resulting in curved electron layers reflecting the pump pulse.

The tight focusing also allows to start with an input signal pulse of low energy. When the signal pulse starts diverging, it is already amplified sufficiently strong to stay above the SRA threshold. On the other hand, the signal intensity is kept below the relativistic intensity limit by distributing its power over a larger cross section. While its diameter increases, the signal pulse can collect the desired large energies for high-power applications. Due to the tight focusing, the Rayleigh length is short and the pulse diameter grows quickly after the amplification, which keeps the distance to the following optics short, as required

An exact analytic description of SRA in this configuration must include the dependence on the propagation distance and the distance from the optical axis. Relevant higher dimensional effects are the diffraction of the pulse causing the divergence, gain effects affecting the diameter by relatively stronger or weaker amplification of the center as compared to the edges of the pulse, and mutual guiding [145, 146] of the pump and signal pulses leading to focusing or defocusing. In three dimensions, filamentation instabilities can also occur.

In appendix C, an expression for the signal-pulse amplification is analytically derived considering only diffraction. It is introduced in a heuristic way by assuming that the pulse area A grows according to the free-space solution. For a Gaussian beam, this is $A(z) = \pi r_0^2 (1 + z^2/L_R^2)$, where r_0 is the radius at the waist and $L_R = \pi r_0^2/\lambda$ is the Rayleigh length.

The growth of the signal intensity is described by an ordinary differential equation (Eq. (C.7)). It includes terms for the gain by the amplification and the loss by the energy spreading. It can be solved analytically and the total power of the amplified pulse is obtained by integrating over the power of the pump pulse and the plasma density (Eq. (C.11)). The integral is evaluated in the case of a constant pump power (Eq. (C.13)), a linear rising pump power (Eq. (C.14)), and a pump pulse with a Gaussian temporal shape (Eq. (C.17)), which is closest to the usual experimental situation.

The solutions are illustrated in Fig. 6.2. They inherit the quadratic dependence on the plasma density from the one-dimensional case. The temporal shape of the pump entails different evolutions of the signal duration, because the latter depends on the product of the pump and signal intensities, $\tau_s \propto (I_s I_p)^{-1/4}$. One would like to choose a configuration, in which the signal pulse shrinks or, at least, keeps its duration. The analytic solution is yet to be checked by a comparison with numerical simulations. The large computational effort of a full three-dimensional Particle-in-Cell simulation did not allow to include numerical results in this work.

Though several effects have been neglected in the derivation of this analytical solution, it can be used to estimate and optimize the interaction length and focusing of the pump and signal pulses for a given energy of the pump pulse.

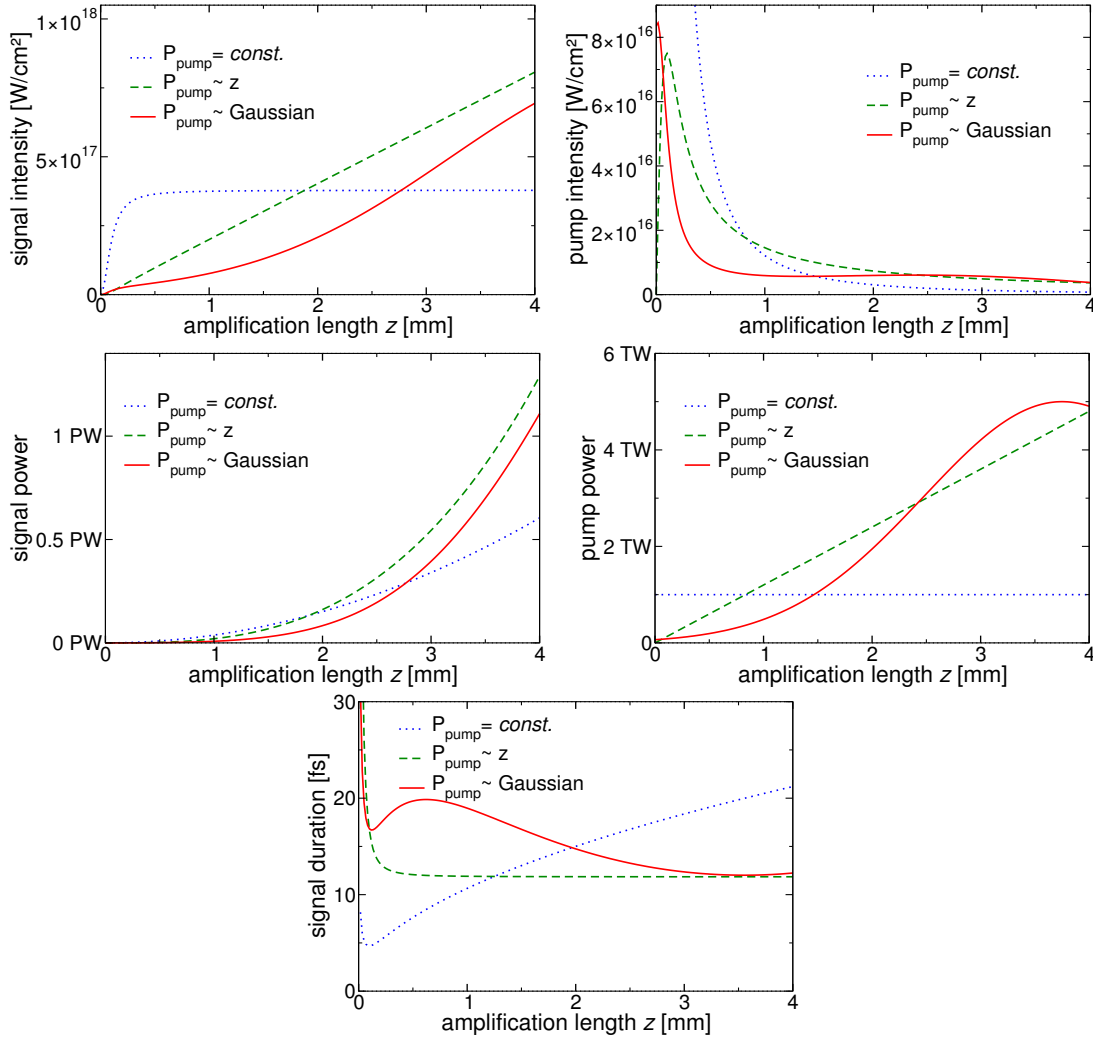


Figure 6.2: Illustration of the analytical solution for the cases of constant pump intensity (blue, dotted curve), linearly increasing intensity (green, dashed curve), and a pump pulse with a Gaussian temporal profile (red, solid curve). The free space solution of a beam with a Gaussian transverse profile is used to compute the increasing cross section. The waist radius is $5 \mu\text{m}$ with the corresponding Rayleigh length of $100 \mu\text{m}$ at a 800-nm pump wavelength. After 4 mm amplification length the radius has increased to about $200 \mu\text{m}$. The pump power is given at the respective position of the pump-signal interaction meaning the total pump duration is $2 \cdot 4 \text{ mm}/c \approx 13 \text{ ps}$. The initial pump intensity for the case of constant pump power is outside the plotted range at $6.7 \times 10^{17} \text{ W}/\text{cm}^2$. The plasma density was set to $0.002n_{\text{crit}}$.

A Density Calibration

Two approaches are common to determine the electron density n_e in a plasma: (1) interferometry and (2) measuring the shift of the first Stokes line of the Raman scattered laser light.

A.1 Measurement Techniques

Density Measurement by Interferometry

Interferometry allows space and time resolved measurement of the gas density in the jet and can be done in a separate experiment. Various implementations are possible, e.g. Mach-Zehnder interferometry [147], shearing interferometry [140], or using polarized beams [148]. Interferometry needs an additional setup and the measured data has to be deconvoluted to infer the space-resolved density. If the electron density is to be determined during the amplification experiment, the additional setup must not obstruct the experiment. Finally, the gas jet has to be accessible for the interferometric test beam.

The online interferometry is difficult to add to the present setup because of the diagnostics for the overlap check of the pulses, which is aligned perpendicular to the paths of the pump and signal pulse (cf. Fig. 3.21). Moreover, a chimney nozzle is used in later experiments Fig. 3.20. It is closed on the sides except for entrance holes for the pump and signal pulses, which rules out interferometry at all.

Electron Density Inferred from Raman Stokes Line

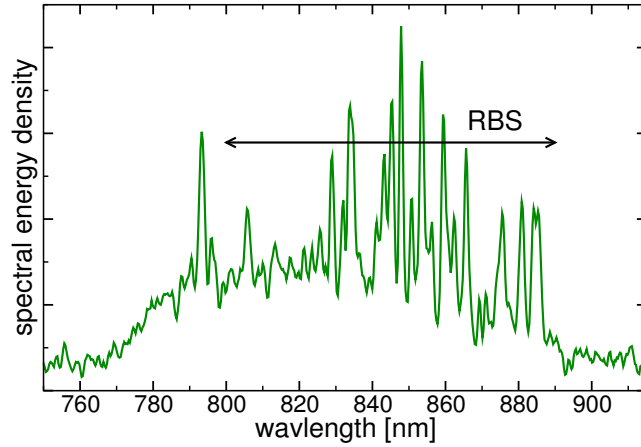
In our experiments, n_e is retrieved from the shift of the Raman Stokes line. This allows to determine n_e at the time the pump pulse passes the plasma. The spectrum of the pump light backscattered from thermal Raman instabilities is recorded with the signal pulse blocked. The frequency difference of the incident pump and the reflected Stokes pulse is the electron plasma frequency $\omega_{pe} = \omega_{pu} - \omega_{Stokes}$ ¹, from which n_e is computed as:

$$n_e = \frac{\omega_{pe}^2 \epsilon_0 m_e}{e^2}, \quad (\text{A.1})$$

where e is the unit charge. The method is limited, because no density profile can be inferred. However, the scattering from the most dense part of the plasma usually dominates, because the growth rate for RBS is largest there. Even if light is also scattered from regions of lower density, the maximum n_e is easily recognized, because it causes the largest red shift of the backscattered pump light. The corresponding Stokes line lies at the long wavelength edge of

¹Actually, the correct plasma frequency is given by the dispersion relation $\omega_p^2 = \omega_{pe}^2 + 1.5k^2 k_B T_e / m_e$ (Eq. (2.9)), where T_e is the electron temperature and $k \approx 2k_{pu}$. However, for the rather low laser intensities used, the plasma temperatures are around 10 eV [149] initially, and hence so small that the thermal correction can be neglected.

Figure A.1: RBS spectrum of an intense pump pulse traveling in a dense plasma. The laser light is backscattered at different positions along the plasma channel. The region with the maximum n_e causes the largest spectral shift at 885 nm.



the spectrum, as can be seen in Fig. A.1. If the gas jet has already been characterized interferometrically before, as it is the case for the single-shot nozzle used in the first experiments in chapter 4 [150], the maximum of the interferometrically obtained profile can be scaled to the measured value of n_e .

The chimney nozzle is designed in such a way that its density profile is rather flat top, because the gas is guided along the channel (Fig. 3.20c/d). There will be a slight decrease towards the entrance holes for the laser pulses, but it is much less than in case of the conical free-streaming nozzle (Fig. 3.20a/b).

A.2 Calibration Measurements

Dependence on Backing Pressure

Fig. A.2a shows the spectra of the Raman backscattered pump light for different backing pressures in the reservoir of the gas jet. The incident pulse has an energy of 90 mJ and a duration of 3.7 ps. The wavelengths of maxima of the Stokes lines can easily be identified in the spectra. Because the pump pulse has a broader spectral width and is negatively chirped, there is an ambiguity as to which wavelength is actually scattered and has to be referred to when computing ω_{pe} . The central wavelength is most likely, because the pertaining amplitude and hence RBS gain is largest.

The calibration curve relating n_e to the backing pressure is given in Fig. A.2b for three wavelengths of the incident pulse: the central wavelength at 792.5 nm and the wavelengths, where the spectral energy density dropped to half of its maximum at 788 nm and 795.5 nm, respectively. The corresponding curves are shifted up and down, respectively. The variations are, however, small and do not influence the qualitative and quantitative behavior in the energy vs. density plots presented in in Figs. 4.6 and 5.9 much.

Dependence on Distance from Nozzle

The gas is not guided below the conical nozzle and gets diluted by free 3D expansion. Its density decreases rapidly with growing distance from the nozzle orifice. This dependence is

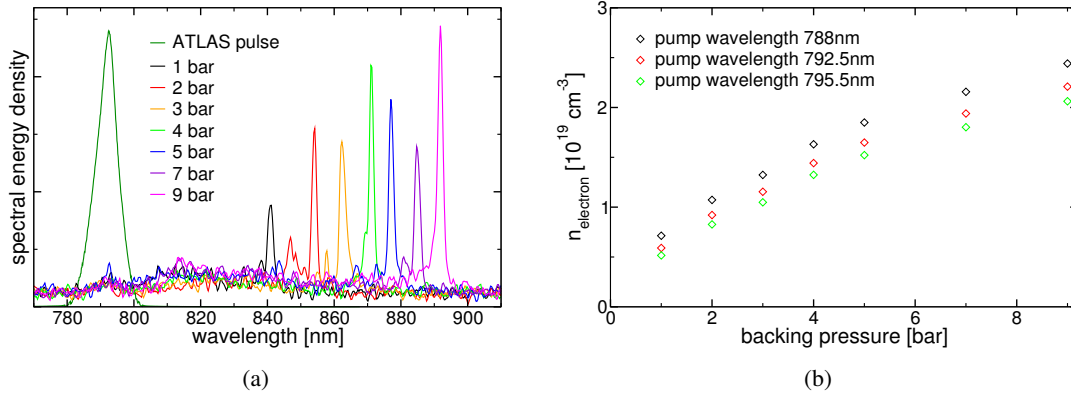


Figure A.2: (a) RBS spectra for various backing pressures of the gas jet. The corresponding electron densities are inferred from the shift of the Stokes line with respect to the incident pump pulse. (b) Calibration curve for the relation between backing pressure and electron density inferred from Fig. A.2a for three different wavelengths of the pump pulse spectrum in Fig. 3.3.

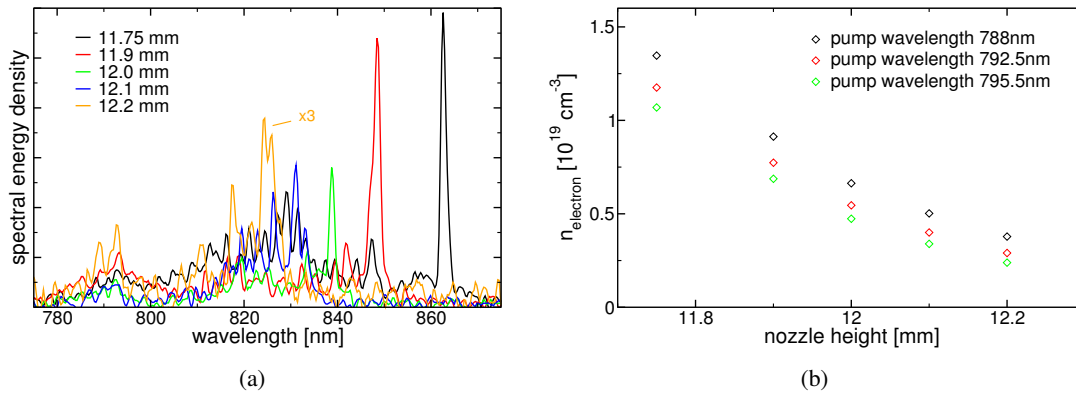


Figure A.3: RBS spectra (a) and computed electron densities (b) for different distances of the laser focus from the orifice of the conical gas nozzle. The height of 11.75 mm refers to the closest possible distance; for shorter distances, the laser pulse hits the orifice thereby creating a spark due to ionization of nozzle material. The backing pressure is fixed to 5 bar; the pump pulse has an energy of 120 mJ and a duration of 3.7 ps.

important, because the nozzle is removed to create free space for the overlap diagnostics and put back to its position before each experiment. The RBS spectra in Fig. A.3 illustrate how sensitively the electron density depends on the distance of the laser focus from the nozzle orifice. This sensitivity renders a once measured calibration curve as that in Fig. A.2b useless unless the distance can be determined very precisely. Under everyday experimental conditions, this turned out to be rather difficult. Thus we decided to measure the RBS spectra during the very amplification experiment for the backing pressures used.

The problem is less critical for the chimney nozzle used in the later experiments, because the walls of the chimney prevent the lateral expansion of the gas and restrict it to a 1D flow.

B Propagation of the Pump Pulse through the Plasma

B.1 Nonlinear Plasma Phenomena Affecting the Pump Pulse

A prerequisite for the amplification experiment is that the pump pulse can propagate to the focus without being significantly scattered or impaired by instabilities. A number of mechanisms exist, that influence the propagation through the gas jet: First while the gas is not yet ionized, next, at the ionization front, and finally in the fully ionized plasma.

While the pulse is far outside the focus, the intensities are still below the ionization threshold of the gas. Here, the nonlinear refractive index $n_2 I_p$ (3.4.1, [125]) induces self-focusing (1).

When the pulse approaches the focus, its intensity becomes large enough to quickly ionize the hydrogen or helium gas at $10^{13} - 10^{15} \text{ W/cm}^2$. A plasma is created, which strongly modifies the index of refraction. At the ionization front, the pulse is subject to (2) self-modulation [151] altering the temporal profile, (3) ionization defocusing [152, 153], and (4) ionization induced scattering [142] both affecting the spatial profile. Furthermore, (5) the ionization blue shift [154, 134, 155] broadens the pulse spectrum towards the blue. This blue shift arises from the sudden decrease of the refractive index from $n_{\text{ref,He}} \approx 1$ to $n_{\text{ref,plasma}} = \sqrt{1 - n_e/n_{\text{crit}}}$ at the ionization front. The trailing part of the pulse travels in the plasma at a higher phase velocity, $c/n_{\text{ref,plasma}}$, and thereby catches up with the pulse front moving at slower speed. This shortens the wavelength at the ionization front. Although this effect is present whenever ionization occurs, it can be neglected in the SRA experiment, because the gas is already completely ionized far in the pulse leading edge so that the body of the pulse enters a homogeneous, fully ionized plasma. In Fig. B.1 the ionization of the plasma is computed using the ADK-ionization-model [156].

Finally, while traveling in the fully ionized plasma, the body of the pulse is subject to several

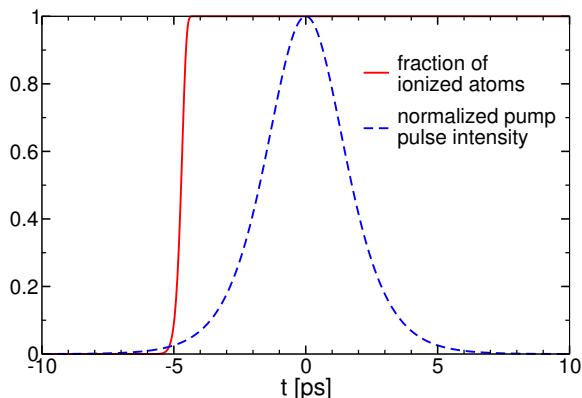


Figure B.1: Ionization state of the hydrogen gas as seen by the pump pulse. The computation uses the ADK model. The pump pulse duration is 3.4 ps, its maximum intensity is $4 \times 10^{15} \text{ W/cm}^2$, and its temporal profile is sech^2 . (Computed by M. Geissler)

plasma instabilities. Its temporal profile can get distorted by (6) the relativistic modulation instability [157, 158, 159], and Raman (7) forward and (8) backward scattering. The spatial profile is influenced by (9) Relativistic self-focusing [157, 160]. The Brillouin instability [47] can be disregarded, because it is caused by the slow ion density waves and comes into play only for pulses longer than 20 ps or in a strongly turbulent plasmas [141].

The self-modulation at the ionization front (2) and the relativistic modulation instability (6) neither need to be considered, because they require higher intensities of the pump pulse and higher electron densities than used here. For the relativistic self-focusing (9) to set in, the pulse power must be larger than the critical power, $P_{cr} \approx 17 \text{ GW} \cdot \omega^2 / \omega_{pe}^2$. For our plasma densities, $P_{cr} > 5 \text{ TW}$ is larger than the peak power of the fully compressed ATLAS-2 pulse, hence relativistic self-focusing is not critical either.

The only relevant processes for the SRA experiment are (3) ionization defocusing, (4) ionization induced scattering and the Raman instabilities (7+8). They are checked in a separate pre-experiment presented in the following section. As regards the Raman instabilities, it is sufficient to control the backscattering, because its growth rate $\gamma_{rbs} = a\sqrt{\omega_{pe}\omega}/2$ is much larger than that of the forward scattering $\gamma_{rfs} = \gamma_{rbs}(\omega_{pe}/\omega)^{3/2}/\sqrt{2}$ (see Table 2.1 on 11).

B.2 Pre-experiment to Check Pump Pulse Propagation

In a pre-experiment shown in Fig. B.2a, the influence of the helium gas on the focus profile and the transmission of the pump pulse through the plasma was investigated. The focus is image-relayed to a 8-bit CCD camera. A small portion of the pulse is split off at the wedge W and sent to the camera. The main fraction passes the wedge W. Outside the chamber, the energy meter EM1 measures the pulse energy to detect losses due to back and side scattering. The Raman backscattered light reflected from the plasma travels back along the incoming optical path and is separated by the polarizing beam splitter PBS. A second energy meter EM2 detects its energy.

Ionization instabilities are expected to be more pronounced in helium, because it has a higher ionization potential than H_2 . The ionization rate is smaller for the same laser intensity and the instability has more time to develop. The pump pulse has a duration of 1.2 ps and an energy of up to 90 mJ corresponding to a maximum intensity of $7.5 \times 10^{15} \text{ W/cm}^2$.

The images captured in Fig. B.3 show the focus of the pump pulse in vacuum and for two different electron plasma densities. The effect of the density on the spatial profile proves to be small. For higher densities a slight focusing is visible, which might be explained by self-focusing in the neutral gas before the focus or ionization defocusing after the focus.

During the amplification experiments, a small high-intensity spot sometimes appears in the near-field pattern of the pump pulse after its passage through the plasma. It is about 4 mm in diameter. The intensity in the spot can be so high that the coating of the signal parabola is completely blown off, both for a gold coating and for a high-power dielectric coating. This is observed, e.g., in the near-field pattern of the signal pulse in Fig. 5.11. The origin of this hot spot is not fully understood, as it was not observed in all experiments. Particularly, it appears less frequently when using the chimney nozzle or longer and less intense pump pulses. Since the effect does not seem to interfere with the amplification experiment, it was not further investigated in the scope of this work.

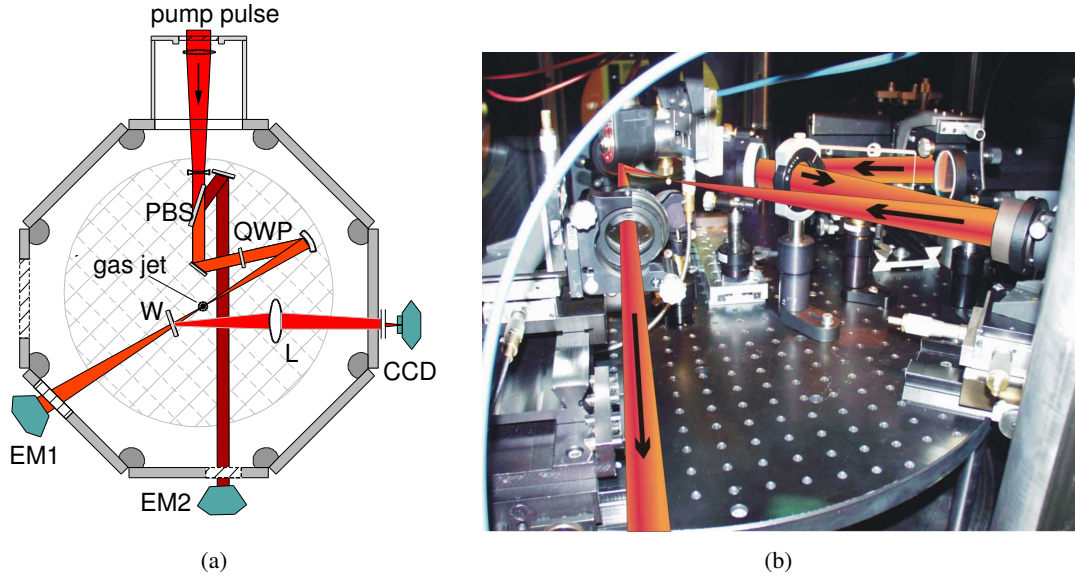


Figure B.2: (a) Setup of the pre-experiment: The wedge W splits off a small fraction of the pump pulse after the He-gas jet. The lens L image relays the pump focus to the CCD camera. The energy meter EM1 (Laser Systems 380401 with power meter 374) measures the energy of the pump light transmitted through the gas jet, EM2 (Gentech ED-200) measures the fraction back-reflected in the plasma. The back-reflected light has the opposite helicity as the incoming light and is separated by the polarizing beam splitter in the same way as the amplified signal pulse. (b) View into the target chamber from the position of the CCD camera. The arrows indicate the propagation direction of the laser pulse.

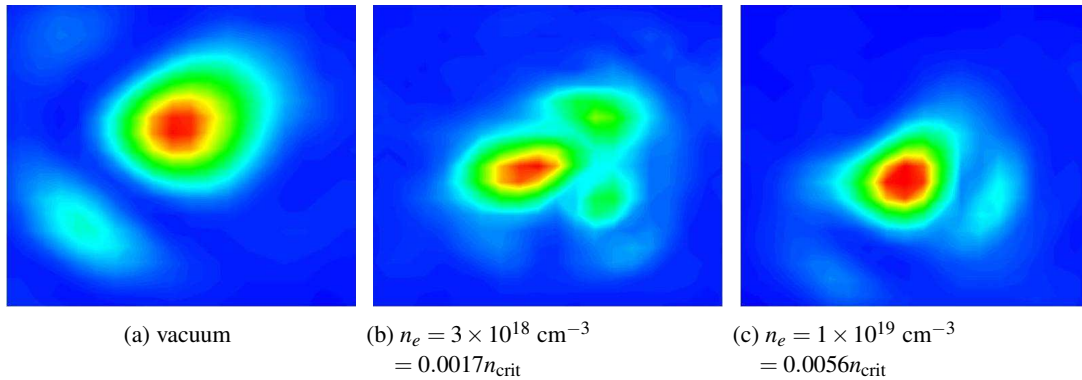


Figure B.3: Focal fluence patterns of the pump pulse image-relayed to the CCD camera captured for different electron densities.

Within the accuracy of the high-power energy meter EM1 ($\approx 5\%$), the energy measurement yielded the same pulse energy independently on whether the plasma was present or absent. The backscattered light was measured with the pyroelectric meter EM2. The observed energies were on the sub-mJ level, which is low enough not to affect the amplification experiment.

C Analytic Solution of the Amplification in Divergent Beams

An analytic expression is derived for the amplification of a divergent signal pulse as depicted in Fig. 6.1b. A simple model is used considering only the intensity growth due to amplification and the reduction of the signal intensity due to the spreading of the signal energy over an increasing cross section. The depletion of the pump pulse is disregarded. The final results shows that the result depends on the pump amplitude rather than its intensity. Hence the error will be less than $\approx 10\%$ as long as the pump depletion stays below about 20% .

At a given position, the overall growth rate of the signal intensity is the sum of two terms, one accounting for the gain at constant cross section and the other for the reduction due to expansion at constant pulse power

$$\frac{dI_s}{dz} = \left. \frac{dI_{s,\text{amp}}}{dz} \right|_{A=\text{const.}} + \left. \frac{dI_{s,\text{diff}}}{dz} \right|_{P_s=\text{const.}}. \quad (\text{C.1})$$

The intensity growth rate for constant cross section is taken from the one-dimensional case. The relation Eq. (2.29) for the intensity growth signal is derived for constant plasma density and pump intensity. By the same reasoning a more general expression for the growth rate of the signal amplitude, $a_s \propto \sqrt{I_s}$, is found

$$\frac{d}{dz} \sqrt{I_s} = \frac{1}{\sqrt{8}} \left(\frac{n_e}{n_{\text{crit}}} \right) k_{\text{pu}} \sqrt{I_p} \quad (\text{C.2})$$

which is also valid for varying density and intensity. The growth rate reads then

$$\left. \frac{dI_{s,\text{amp}}}{dz} \right|_{A=\text{const.}} = 2C_1 \sqrt{I_p I_s}, \quad (\text{C.3})$$

where the constant

$$C_1 = \frac{1}{\sqrt{8}} \frac{n_e}{n_{\text{crit}}} k_{\text{pu}} \quad (\text{C.4})$$

is introduced to simplify the notation. When substituting $I_{s,\text{amp}}|_{A=\text{const.}}$ by I_s in Eq. (C.3), higher orders of dI_s were neglected. The intensity decrease for constant power due to diffraction is obtained from

$$\frac{dP_s}{dz} = \frac{d}{dz} \left(A I_{s,\text{diff}}|_{P_s=\text{const.}} \right) = 0. \quad (\text{C.5})$$

One finds

$$\left. \frac{dI_{s,\text{diff}}}{dz} \right|_{P_s=\text{const.}} = -I_{s,\text{diff}}|_{P_s=\text{const.}} \frac{dA}{A dz} \approx -I_s \frac{dA}{A dz}. \quad (\text{C.6})$$

The last approximation neglects again higher orders of dI_s . Substituting Eqs. C.3 and C.6 in Eq. (C.1) yields an equation for the growth of the signal intensity,

$$\frac{dI_s}{dz} = 2C_1 \sqrt{I_p I_s} - I_s \frac{dA}{Adz}. \quad (\text{C.7})$$

This ordinary differential equation is of the Bernoulli type [161]. Using the substitution $\mathcal{E} = \sqrt{I_s}$ and deviding by $2\mathcal{E}$ allows to rewrite it as a linear first-order differential equation,

$$\frac{d\mathcal{E}}{dz} = C_1 \sqrt{I_p} - \frac{dA}{2Adz} \mathcal{E} \quad (\text{C.8})$$

This equation can be integrated and has the analytic solution

$$\mathcal{E}(z) = \exp\left(-\frac{1}{2} \ln \frac{A(z)}{A(z_0)}\right) \left\{ \mathcal{E}(z_0) + \int_{z_0}^z C_1 \sqrt{I_p(\tilde{z})} \exp\left(\frac{1}{2} \ln \frac{A(\tilde{z})}{A(z_0)}\right) d\tilde{z} \right\}, \quad (\text{C.9})$$

where the amplification starts at z_0 with initial value $\mathcal{E}(z_0) = \sqrt{I_{s0}}$. The equation is simplified to

$$\mathcal{E}(z) = \frac{1}{\sqrt{A(z)}} \left\{ \mathcal{E}(z_0) \sqrt{A(z_0)} + \int_{z_0}^z C_1 \sqrt{I_p(\tilde{z}) A(\tilde{z})} d\tilde{z} \right\}. \quad (\text{C.10})$$

The signal intensity is given by the square of this expression, $I_s = \mathcal{E}^2$. The radicand of the square root is just the power of the pump pulse $P_p = I_p A$. Since the cross section of the diverging pulse increases, it is also of interest to look at the power of the amplified pulse,

$$P_s(z) = \left\{ \sqrt{P_s(z_0)} + \int_{z_0}^z C_1 \sqrt{P_p(\tilde{z})} d\tilde{z} \right\}^2, \quad (\text{C.11})$$

where $P_s(z_0) = I_s(z_0)A(z_0)$ is the initial power of the signal pulse, which can be neglected for large amplification. The equation can be analytically or numerically integrated for arbitrary pump powers and plasma densities. In case of a homogeneous plasma, C_1 is constant and one finds an expression similar to that of the signal intensity in the 1D situation, Eq. (2.29),

$$P_s(z) = \frac{1}{8} \left(\frac{n_e}{n_{\text{crit}}} \right)^2 k_{\text{pu}}^2 \left(\int_{z_0}^z \sqrt{P_p(\tilde{z})} d\tilde{z} \right)^2. \quad (\text{C.12})$$

The quadratic scaling with the electron density remains as expected for the SRA regime.

In the following, this expression is evaluated for (1) a constant pump power, (2) a linearly rising pump power, and (3) a pump pulse with a Gaussian temporal profile. For simplicity, it is now assumed that the beam waist is located at $z = 0$ so that the area of the beam grows approximately as $A(z) \propto z^2$. Furthermore, the amplification is assumed to start at $z_0/z \approx 0$ and uses the whole length of the pump pulse $z = c\tau_p/2$; the division by 2 reflects the fact that the pulses are counter-propagating and the interaction length is thus half the length of the pump pulse.

Case I: Constant pump power

For $P_p \equiv \text{const.}$, the relations for the signal power and intensity read

$$P_s(z) = \frac{1}{8} \left(\frac{n_e}{n_{\text{crit}}} \right)^2 k_{\text{pu}}^2 z^2 P_p, \quad I_s(z) = \frac{1}{8} \left(\frac{n_e}{n_{\text{crit}}} \right)^2 k_{\text{pu}}^2 \frac{z^2}{A(z)} P_p. \quad (\text{C.13})$$

The expression for the power is equivalent to that of the signal intensity in 1D. However, the results are different, because the power is distributed over a larger cross section. Since $z^2/A(z) \approx \text{const.}$ holds true, the signal intensity remains approximately constant, instead of the quadratic intensity growth in 1D. Choosing a suitable focusing and pump power, one can adjust I_s to a large but still non-relativistic intensity, where SRA is most efficient. However, the signal duration will increase, because I_p decreases for increasing cross section and so does the bouncing frequency, $\omega_b \propto (I_s I_p)^{-1/4} \propto \sqrt{z}$. Furthermore, the constant pump power is experimentally impractical, because the pump intensity is very high at the beginning of the amplification, while it becomes rather low later on. A shaped temporal profile with an increasing power can compensate for this.

Case II: Linearly increasing pump power

The pump power is now given as $P_p(z) = z\tilde{P}$, where \tilde{P} is a constant. An additive constant P_{p0} is omitted for simplicity. The signal power and intensity then read

$$P_s(z) = \frac{1}{18} \left(\frac{n_e}{n_{\text{crit}}} \right)^2 k_{\text{pu}}^2 z^3 \tilde{P}, \quad I_s(z) = \frac{1}{18} \left(\frac{n_e}{n_{\text{crit}}} \right)^2 k_{\text{pu}}^2 \frac{z^2}{A(z)} z \tilde{P}. \quad (\text{C.14})$$

Again the signal intensity scales with the pump power, but this time it increases linearly with the amplification length. The product of the pump and signal intensity remains constant and so does the signal duration.

Case III: Gaussian temporal profile of the pump power

This case is of particular interest, because it is closest to the experimentally available pulse shape. Many laser pulses can be approximated by a Gaussian temporal profile,

$$P_p(z) = \hat{P}_p \exp \left(-4 \ln 2 \frac{(z - z_c)^2}{(c\tau_p/2)^2} \right). \quad (\text{C.15})$$

Half the pulse duration is used in the denominator because the signal and pump pulses counterpropagate so that the actual interaction time is only $\tau_p/2$. z_c is the position, where the signal pulse meets the center of the pump pulse. The integral in Eq. (C.10) yields

$$\int_{z_0}^z \sqrt{P_p(\tilde{z})} d\tilde{z} = \frac{c\tau_p \sqrt{\pi}}{8\sqrt{\ln 2}} \sqrt{\hat{P}_p} \left\{ \text{erf} \left(-16 \ln 2 \frac{(z - z_c)^2}{(c\tau_p)^2} \right) - \text{erf} \left(-16 \ln 2 \frac{z_c^2}{(c\tau_p)^2} \right) \right\}. \quad (\text{C.16})$$

Here $\text{erf}(z) = (2/\sqrt{\pi}) \int_0^z e^{-t^2} dt$ denotes the error integral [162]. The pump is focused strongly, where the amplification starts. The small power necessary to make SRA work is reached

already far in the pulse front. Hence z_c is large enough to approximate the second term in the braces by $\lim_{t \rightarrow -\infty} \text{erf}(t) = -1$. Now P_s can be computed by evaluating Eq. (C.10)

$$P_s(z) = \frac{1}{512 \ln 2} \left(\frac{n_e}{n_{\text{crit}}} \right)^2 k_{\text{pu}}^2 c^2 \hat{P}_p \tau_p^2 \left\{ \text{erf} \left(-16 \ln 2 \frac{(z - z_c)^2}{(c \tau_p)^2} \right) + 1 \right\}^2 \quad (\text{C.17})$$

$$\approx 0.006 \left(\frac{n_e}{n_{\text{crit}}} \right)^2 (\omega_{\text{pu}} \tau_p)^2 \hat{P}_p \approx 0.006 \left(\frac{n_e}{n_{\text{crit}}} \right)^2 \omega_{\text{pu}}^2 E_p \tau_p, \quad (\text{C.18})$$

where $E_p \approx \hat{P}_p \tau_p$ is the energy of the pump pulse, a quantity that is easily accessible experimentally. The erf-term has been approximated by 1/2 reflecting the fact that the amplification has to end before the pump intensity drops too fast thus leading to an increasing signal pulse duration. As regards the numerical pre-factor, one has to keep in mind that it has been obtained for the ideal case of perfect bunching of the electrons in the SRA regime. Numerical simulations reported in section 2.4 yielded a value that is about half as large.

D Publications

- M. Dreher, E. Takahashi, J. Meyer-ter-Vehn, and K.-J. Witte, *Observation of Superradiant Amplification of Ultrashort Laser Pulses in a Plasma*, Physical Review Letters **93**, 095001 (2004) (reprinted)
- M. Dreher, M. Jost, D. Habs, and K.-J. Witte, *Experimental Demonstration of Superradiant Amplification of Ultrashort Laser Pulses in a Plasma*, Inertial Fusion Sciences and Applications 2003, 616 (2004) (reprinted)
- M. Dreher, M. Jost, D. Habs, and K.-J. Witte, *Experimental Demonstration of Superradiant Amplification of Ultrashort Laser Pulses in a Plasma*, EPS 2004, O2_33
- M. Dreher, S. Yu. Kalmykov and J. Meyer-ter-Vehn, *Theoretical considerations concerning recent MPQ experiments on superradiant amplification (SRA) of short laser pulses.*, GSI Annual Report 2002 - High Energy Density Physics with Intense Ion and Laser Beams, p. 36

Observation of Superradiant Amplification of Ultrashort Laser Pulses in a Plasma

M. Dreher, E. Takahashi,* J. Meyer-ter-Vehn, and K.-J. Witte¹

¹Max-Planck-Institut für Quantenoptik, D-85748 Garching, Germany

(Received 12 December 2003; published 25 August 2004)

We demonstrate the amplification of a femtosecond signal pulse in an underdense plasma by a novel mechanism called superradiant amplification. The pulse is amplified by a counterpropagating few picosecond long pump pulse. In the superradiant regime, the ponderomotive forces exceed the electrostatic forces and arrange the plasma electrons to reflect the pump light into the signal pulse. We found a significant amplification in energy and intensity. The time structure of the amplified signal pulse carries intrinsic features of the superradiant regime. Sub-10-fs pulses of petawatt power appear feasible.

DOI: 10.1103/PhysRevLett.93.095001

PACS numbers: 52.35.Mw, 42.65.Re

The recent years have witnessed significant progress in increasing the peak powers of laser pulses up to the petawatt (PW) level [1,2] by perfecting the chirped-pulse amplification (CPA) technique [3]. Such pulses are indispensable for particle acceleration in plasma [4,5], high-harmonic generation [6], and x-ray lasers [7]. The minimal pulse duration is limited by the gain bandwidth of the amplifying medium. The presently broadest medium is Ti:sapphire yielding 28-fs pulses of PW power [1]. An alternative is optical parametric amplification. It provides larger amplification bandwidths enabling sub-10-fs pulses at currently the μJ level [8]. Its potential for high-energy amplification has yet to be proven.

Two plasma-based amplification schemes have been proposed recently able to directly amplify fs-laser pulses without stretching and recompression. Plasma acting as an amplifying medium can sustain almost arbitrarily high intensities without suffering damages. In both schemes, a short input signal pulse collides with a long counterpropagating pump pulse of slightly higher frequency in an underdense plasma. The electron density is modulated in the interaction region such that the electrons scatter pump light back into the signal pulse. The schemes differ in the way the electrons are arranged.

In this Letter, we experimentally demonstrate for the first time superradiant amplification (SRA) [9] that efficiently amplifies ultrashort pulses and simultaneously increases their bandwidth thereby leading to significant pulse shortening. In the SRA regime, the intensities of the pump and signal pulses are so strong that their common ponderomotive force exceeds the electrostatic forces due to charge separation. Hence the electrons perform forced oscillations at the frequency dictated by the ponderomotive potential. The term SRA implies that all participating plasma electrons coherently backscatter the pump pulse. SRA can amplify a signal pulse close to relativistic intensities at flux levels of several kJ/cm^2 . PW pulses with durations of two laser cycles can be obtained within a cross section of less than 1 mm^2 .

The second plasma amplification scheme [10,11] is based on stimulated Raman backscattering (SRBS).

Pump and signal pulses resonantly excite a plasma wave, which backscatters the pump pulse. The signal pulse is shortened only if the pump pulse is depleted. In general, SRA allows shorter pulse durations than SRBS.

The SRA dynamics can be described in terms of an ensemble of electrons. The motion of an individual electron is governed only by its initial conditions and the ponderomotive potential, while the electron-electron interactions are negligible. As the frequencies of the pump and signal pulses differ only slightly, the phase velocity of their interference pattern is small and most plasma electrons get trapped in the periodic structure of the ponderomotive potential (Fig. 1). The trapped electrons start oscillating with the bouncing frequency $\omega_b^2 = 4a_{\text{pu}}a_s\omega_{\text{pu}}\omega_s$ [9], where $a_{\text{pu/s}} = eA_{\text{pu/s}}/(m_e c)$ are the normalized vector potentials of the pump and signal pulses and $\omega_{\text{pu/s}}$ their frequencies, respectively. The initially uniformly distributed electrons are periodically bunched and unbunched. This results in narrow density peaks that appear in turn on the two edges of the confining potential wells. The first bunching after a quarter oscillation period leads to the scattering of pump light into the signal pulse. Because of the ongoing oscillation, the density peak decays and the reflection of the pump ceases. When the peak reappears half an oscillation period later on the opposite side of the potential well, the signal pulse is reflected back into the pump pulse and is thereby attenuated.

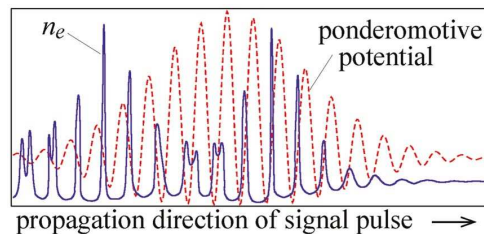


FIG. 1 (color). Snapshot of the electron density n_e in the ponderomotive potential. Potential wells from right to left indicate the evolution of the electron density grating.

Thus an initially short signal pulse is amplified on its leading edge while the attenuation on its rear edge restricts its duration to about one-half of an oscillation period, π/ω_b . Since ω_b increases as the signal amplitude grows, the pulse becomes shorter during the amplification. The coherent scattering follows from the almost perfect bunching of the electrons to layers much thinner than the laser wavelength in combination with the spatial periodicity of the potential. The threshold for the transition from SRBS to SRA is given by $\omega_b > \omega_{pe}$ [9] and sets a lower limit for the intensities of the laser pulses. Here, $\omega_{pe}^2 = e^2 n_e / (\epsilon_0 m_e)$ is the electron plasma frequency.

The Advanced Ti:S Laser (ATLAS) at the Max-Planck-Institute for Quantum Optics provides 200-mJ, 793-nm pulses at 10 Hz. To serve as pump pulses for our experiments (Fig. 2), they are not compressed to the bandwidth limit of 120 fs but only to a few ps by imparting them a negative chirp. The input signal pulse is generated from a small fraction split off from the fully stretched ATLAS pulse. It is separately compressed to 120 fs and broadened to a spectral range from 740 to 830 nm by self-phase modulation in an Ar-filled hollow fiber [12]. The fiber also filters the pulse spatially, yielding a Gaussian-like intensity distribution with a diffraction-limited beam quality ($M^2 \approx 1$). A dielectric filter blocks the wavelengths below 800 nm, thereby shifting the central wavelength to 815 nm. The nonlinear chirp of the filtered pulse prevents compression to the bandwidth-limited duration of 56 fs corresponding to its 17-nm bandwidth. The compressed pulse has an energy of 70 μ J, a duration of 80 fs (FWHM), and a negatively chirped pedestal that extends to about 170 fs at an intensity level of a few percent of the peak intensity.

In the target chamber, the pump and signal pulses are focused from opposite directions into a H₂ gas jet by off-axis parabolic mirrors of equal focal length. The diameters of the central focal disks extending to the first diffraction minimum are 30 and 26 μ m, respectively. Any

stray light outside these disks is so weak that it is negligible for the amplification process. About 70% of the pump pulse energy and 85% of the signal pulse energy is contained in the disks. In the focus, the initial intensities are $I_s = 1.3 \times 10^{14}$ W/cm² and $I_p = 5.7 \times 10^{15}$ W/cm² for a duration of $\tau_{pu} = 3.5$ ps. The Rayleigh length is ≈ 600 μ m and lies within the gas jet of 1-mm length. The spatial overlap of the two pulses in the plasma is established by making both pass through a pinhole. Their arrival times are synchronized by means of a streak camera measuring the time lag between them. The delay between both pulses is fine-tuned by optimizing the gain during the experiment.

As the gas nozzle is closed on the sides except for holes for the pulses, an interferometric measurement of the electron density, n_e , is not possible. Instead n_e is derived from the spectral shift of the Raman backscattered pump light by the relation $n_e = \omega_{pe}^2 \epsilon_0 m_e / e^2$. For the presented experiments, n_e is 3.5×10^{18} cm⁻³ corresponding to 0.002 times the critical density. The ionization blueshift is not relevant for this measurement because the H₂ gas is ionized by the low-intensity leading edge of the pump pulse [13], so that the main part of the pulse interacts with a fully ionized plasma.

After the interaction in the plasma, the reflection from the second off-axis parabola recollimates the two pulses. The individual beam paths are separated by a combination of polarizing beam splitters and $\lambda/4$ wave plates. On both beam splitters, the signal pulse is *s* polarized and the pump pulse *p* polarized, so that the pump pulse passes through them and the signal pulse is reflected. The first wave plates alter the polarization state of the incoming pulses to circular polarization of opposite helicity as best for the interaction. The passage through the second wave plate restores the original linear polarizations.

The diagnostics to characterize the signal pulse include the simultaneous measurement of its energy, spectrum, and autocorrelation (AC) by a single-shot, second-order background free autocorrelator (Fig. 2).

Figure 3(a) shows the energy of the amplified signal pulse versus the delay between both pulses. The output energy reaches its maximum when the region where the pulses meet lies completely within the plasma and the Rayleigh length. The maximal energy of ≈ 1 mJ corresponds to a gain of 19 with respect to the input energy contained in the central focal disk. Shot-to-shot fluctuations of the output energy can be explained by fluctuations of the plasma density and of the intensities of both input pulses. They are correlated because the two pulses originate from the same source.

Initially, the threshold condition for SRA, $\omega_b > \omega_{pe}$, is not satisfied; one finds $\omega_b^2 / \omega_{pe}^2 = 0.4$. By amplification the ratio increases to 1.75. The amplified signal intensity is computed from the measured output signal energy, the focus diameter, and the temporal profile obtained from

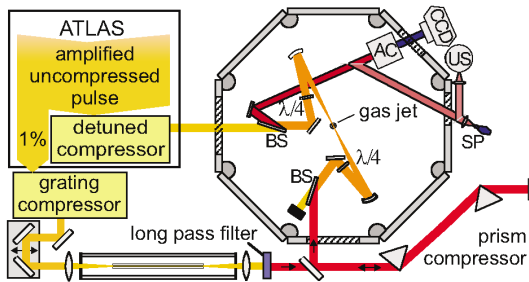


FIG. 2 (color). Experimental setup: BS: polarizing beam splitter; $\lambda/4$: quarter wave plate; AC: single-shot AC; CCD: charge coupled device camera; US: Ulbricht sphere for energy measurement; SP: spectrometer;

the AC measurement. Thus the interaction starts in the SRBS regime and enters the SRA regime during the amplification. Raman amplification is possible for short pulses even though the resonance condition is not satisfied strictly. The dephasing due to the frequency mismatch $\Delta\omega = \omega_{pu} - \omega_s - \omega_{pe}$ becomes important only for pulses longer than $\pi/\Delta\omega = 90$ fs.

The amplified signal has a background caused predominantly by the Raman instability of the pump pulse. The backscattered light has the same polarization and occupies the same spectral range as the signal pulse and cannot be separated by a beam splitter. It forms an undesired long weak precursor. The Raman instability is strongly suppressed in the region already passed by the signal pulse because the interaction of the two pulses heats the plasma electrons to keV temperatures corresponding to the depth of the ponderomotive potential. The energy level of the backscattered light is measured with the signal pulse blocked. Since the plasma is not heated by the pump-signal interaction, the pump pulse is scattered over the full length of the plasma and this measurable level will be higher than that in the presence of the signal pulse, which is not directly measurable.

The spectra in Fig. 3(b) reveal whether SRBS or SRA dominates the amplification. The spectral broadening from 17 nm (non-bandwidth-limited input pulse) to 29 nm after the amplification is expected for SRA because of the pulse shortening during the amplification. It is much larger than for pure SRBS, which has its Stokes line around 825 nm and a gain bandwidth $\gamma = \sqrt{\omega_{pu}\omega_{pe}a_{pu}} = 0.17\omega_{pe}$ in the weakly coupled regime [14] corresponding to 6 nm. Including the 8-nm bandwidth of the chirped pump pulse, this is still much less than the observed bandwidth. Bandwidth broadening by amplification in the pump-depleted Raman regime [10] can be excluded, because the observed energy transfer from the pump to the signal pulse is too small.

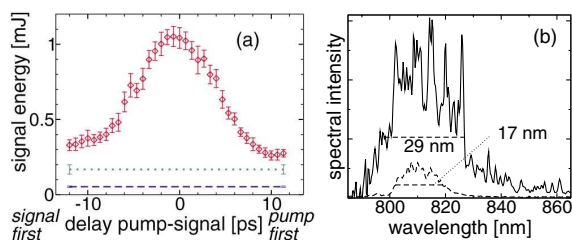


FIG. 3 (color). (a) Energy of the amplified signal vs delay between both pulses (diamonds), input signal energy (dashed line), and backscattered pump light (dotted line) in the absence of the signal pulse. The diamonds represent averages over 30 shots; statistical deviation is indicated by error bars. (b) Input (dashed line) and output (solid line) spectra of the signal pulse for the delay adjusted to maximum amplification.

The 2nd-order AC trace of the amplified signal pulse in Fig. 4 exhibits an oscillating behavior. Apparently, the signal pulse consists of a train of equidistant pulses. The five peaks of the AC trace correspond to three peaks of the amplified signal. Its temporal profile is retrieved by fitting a train of three \sin^2 pulses such that its computed AC trace matches the measured trace. The fitted pulses are each 26 fs long and spaced by 54 fs, i.e., each single spike is much shorter than the input pulse.

Although the AC trace is ambiguous as to which pulse leads the train, it is reasonable to assume that the pulse with the largest amplitude comes first, as explained later. The measured energy and known focus diameter yield an intensity of 2.6×10^{15} W/cm², about 17 times higher than that of the input pulse. To compute the bouncing frequency ω_b , the pump intensity I_p at the position of the signal pulse is needed. Although I_p changes during the amplification, the uncertainty of the exact value of I_p affects the value of ω_b only slightly because of $\omega_b \sim I_p^{-1/4}$. Assuming $I_p \approx 2 \times 10^{15}$ W/cm², which is 35% of the peak value, the calculated pulse duration is $\pi/\omega_b = 28$ fs and the temporal spacing of the succeeding pulses $2\pi/\omega_b = 56$ fs, very close to the measured data.

The breakup into a train of pulses is an intrinsic SRA feature. It appears if the signal pulse is so long that the electrons are trapped for several oscillation cycles in the ponderomotive potential of the signal and pump pulses. The signal pulse is amplified and attenuated periodically and, finally, the periodic attenuation splits it into a train of pulses at regular intervals of one oscillation period, $2\pi/\omega_b$, which is confirmed by the good agreement of the measured and computed durations and temporal distances of the signal pulses.

SRBS cannot cause a regular train of such short pulses. The pump depletion regime exhibiting a pulse train is excluded because of the small energy transfer from the pump to the signal pulse. A beating of a Raman Stokes line with the input signal pulse is ruled out by the absence of two distinct spectral components in the spectrum.

The bunching of the electrons becomes less perfect after several cycles because potential wells are nonhar-

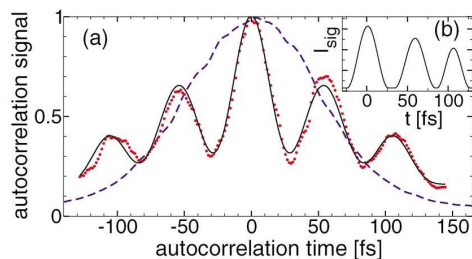


FIG. 4 (color). (a) Normalized AC traces of the input pulse (dashed), amplified output pulse (dots) and fitted signal pulse (solid). (b) Intensity profile of the fitted signal pulse.

monic and thus not all electrons have exactly the same oscillation period. Furthermore, the electrons receive an energy spread of the order of the depth of the ponderomotive potential after the first pulse has passed and cannot be trapped all by the smaller ponderomotive potential of the following pulses. Fewer electrons are bunched and the amplification becomes less efficient. Therefore, the leading pulse is more strongly amplified and finally outgrows the trailing pulses.

The pulse breakup by the amplification in the SRA regime can be reproduced by numerical simulations that we performed with a 1D particle-in-cell (PIC) code. The experimental data are used for n_e and the intensities and durations of the pump and signal pulses. The temporal pulse profiles are taken Gaussian like, the pump pulse is negatively chirped, and the signal pulse has an additional negatively chirped precursor whose intensity amounts to 6% $I_{s,max}$. The plasma length is 1000 μm with additional 250 μm -long ramps at the edges. The snapshots in Fig. 5 show that the SRA with subsequent pulse breakup sets in only after the signal has been amplified by SRBS. Furthermore, they reveal that the slight lengthening of the pulse train compared to the input pulse is caused by the amplification of the precursor. Although its intensity is very small in the beginning, it can catch up with the main pulse. Plots of n_e and phase space (not shown here) reveal the trapping of a fraction of the electrons when ω_b is still slightly smaller than ω_{pe} , which deteriorates the bunching and thus the amplification when the main pulse passes. Similarly, the signal trailing edge is not significantly built up by SRBS in the Raman regime at the beginning, because the fraction of trapped electrons affect the coherence of the plasma wave behind the signal pulse. In the simulation the energy and intensity amplification are about 2 times larger than those experimentally observed. This is a good agreement considering the idealized 1D plane geometry used in the PIC code.

Finally, the near and far fields of the amplified pulse were examined. The near field shows a smooth, Gaussian-like fluence distribution without hot spots. This indicates that only the central disk of the focus is amplified, where the intensities of both pulses are strongest, as is expected for a good transverse overlap. In the surrounding areas the intensities and hence the amplification is only small. These findings agree with the far-field measurement. The signal pulse was refocused with a lens of long focal length and captured by a CCD camera. Comparing the far-field fluence patterns of the input and amplified signal pulse shows an almost diffraction-limited beam quality of the amplified pulse. Shifting the foci of the pump and signal pulses transversely with respect to each other by a few μm causes interference fringes in the near field pattern, oriented at right angles to the direction of the shift. This sensitivity renders the inspection of the near field a valuable online diagnostic for an exact overlap.

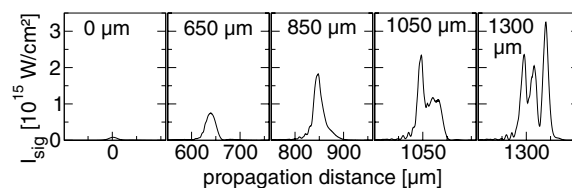


FIG. 5. A PIC simulation in the comoving rest frame illustrating evolution of the signal pulse. Snapshots of the signal intensity are displayed after a propagation distance indicated in the individual plots. The signal pulse travels to the right.

In conclusion, we have demonstrated SRA. This is proven by (i) an amplification of about 20 in energy and intensity, (ii) the breakup of the amplified signal pulse into a sequence of pulses of duration π/ω_b separated by $2\pi/\omega_b$, and (iii) by spectral broadening of the signal pulse. The effect (ii) causes the shortening of the pulse if it has an initial duration $\leq 2\pi/\omega_b$. The good focusability of the amplified signal pulse renders the SRA mechanism attractive as a final amplification stage of a CPA laser system. Furthermore, the results show that a weak input signal pulse is initially amplified in the Raman regime until its intensity becomes sufficiently large to enter the SRA regime. To start directly in the SRA regime, the intensity of the input signal can be increased by using tighter focusing of both pulses. This approach is appropriate for achieving PW powers, because the amplification starts within the short Rayleigh length and proceeds into the diverging beam, thus distributing the energy over an increasing area, and keeping the intensity below the relativistic level.

The authors thank G. Shvets, A. Pukhov, S. Kalmykov, M. Jost, and D. Habs for fruitful discussions. This work was supported by Euratom-IPP and by the DFG, under Contract No. WI1713/2-1.

*Present address: AIST, Tsukuba Ibaraki, 3058568 Japan.

- [1] M. Aoyama *et al.*, Opt. Lett. **28**, 1594 (2003).
- [2] M. D. Perry, *et al.*, Opt. Lett. **24**, 160 (1999).
- [3] D. Strickland and G. Mourou, Opt. Commun. **55**, 447 (1985).
- [4] R. A. Snavely *et al.*, Phys. Rev. Lett. **85**, 2945 (2000)
- [5] V. Malka *et al.*, Science **298**, 1596 (2002).
- [6] P. A. Norreys *et al.*, Phys. Rev. Lett. **76**, 1832 (1996).
- [7] T. Kawachi *et al.*, Phys. Rev. A **66**, 033815 (2002)
- [8] G. Cerullo *et al.*, Opt. Lett. **23**, 1283 (1998); A. Shirakawa *et al.*, *ibid.* **23**, 1292 (1998).
- [9] G. Shvets *et al.*, Phys. Rev. Lett. **81**, 4879 (1998).
- [10] V. M. Malkin *et al.*, Phys. Rev. Lett. **82**, 4448 (1999).
- [11] Y. Ping *et al.*, Phys. Rev. E **67**, 016401 (2003).
- [12] M. Nisoli *et al.*, Appl. Phys. Lett. **68**, 2793 (1996)
- [13] A. Scrinzi *et al.*, Phys. Rev. Lett. **83**, 706 (1999).
- [14] D.W. Forslund *et al.*, Phys. Fluids **8**, 1002 (1975).

EXPERIMENTAL DEMONSTRATION OF SUPERRADIANT AMPLIFICATION OF ULTRASHORT LASER PULSES IN A PLASMA

M. Dreher¹, M. Jost¹, D. Habs², and K.-J. Witte¹

¹*Max-Planck-Institut für Quantenoptik, Hans-Kopfermann-Str. 1, D-85748 Garching*

²*LMU München, Am Coulombwall 1, D-85748 Garching*

email: matthias.dreher@mpq.mpg.de

We demonstrate up to twenty-fold energy amplification of an ultrashort laser pulse in a plasma by a counterpropagating long pump pulse at high intensities. This and the observed spectral broadening clearly evidence that the superradiant regime has been entered for the first time. In this regime, the ponderomotive forces due to both pulses exceed the electrostatic forces which fundamentally changes the electron dynamics and enables the amplification of few-cycle pulses without pulse lengthening.

I. INTRODUCTION

In recent years, successful efforts have been made to decrease the duration of powerful laser pulses in order to increase their peak power. This has allowed for the investigation of new regimes of laser plasma physics. If the pulse duration becomes shorter than the duration of the period of a Langmuir wave, the laser pulse can drive large plasma wakefields with huge electrostatic fields. Very efficient acceleration of electrons and also protons by these fields has been predicted and meanwhile observed, too.^{1,2} Today's work horse for the generation of ultra-short powerful light pulses are amplifier chains utilizing the chirped-pulse amplification (CPA) scheme.³ For conventional CPA lasers, the bandwidth of the laser medium usable for amplification sets a lower limit on the duration of the pulses to be amplified. For titanium:sapphire, this is about 20 fs. Larger bandwidths can be obtained by optic parametric amplification of the stretched pulse⁴⁻⁶ in a non-linear crystal, but this technique has yet to prove its potential for high pulse powers and sub-10 fs pulses.

Direct amplification without stretching and recom-

pression requires a laser medium which can withstand the extreme field strengths of the laser pulse without getting damaged. These fields usually exceed the threshold for ionization; therefore, plasmas are to be preferentially considered in this context. Two plasma processes have been identified by means of which a laser pulse is amplified employing the compression of a long counterpropagating pump pulse whereby the signal pulse duration is kept short. These two processes are distinguished by the level of the involved pulse intensities. For low intensities, stimulated Raman backward scattering dominates (SRBS).⁷ It is a resonant three-wave process, where a plasma wave and an electromagnetic wave (signal) counterpropagating the pump wave are amplified at the expense of the latter. For a rather modest pump pulse intensity of ($10^{12} - 10^{14}$ W/cm²) and a relatively high plasma density, a pump depletion regime exists that allows the amplification of short laser pulses.⁸

We report on an experiment carried out at high-intensities. In this so-called superradiant amplification (SRA) regime, laser pulses even shorter than 10 fs can be generated.⁹ The name SRA is derived from the feature that all participating plasma electrons backscatter the pump pulse phase-compatible into the signal pulse. The intensities of the pump and signal pulses are chosen high enough that their common ponderomotive force acting on the plasma electrons becomes larger than the electrostatic forces responsible for collective plasma oscillations. The electron dynamics becomes then relatively simple in that the motion of an individual electron caused by the ponderomotive potential can be considered to be independent of the motions

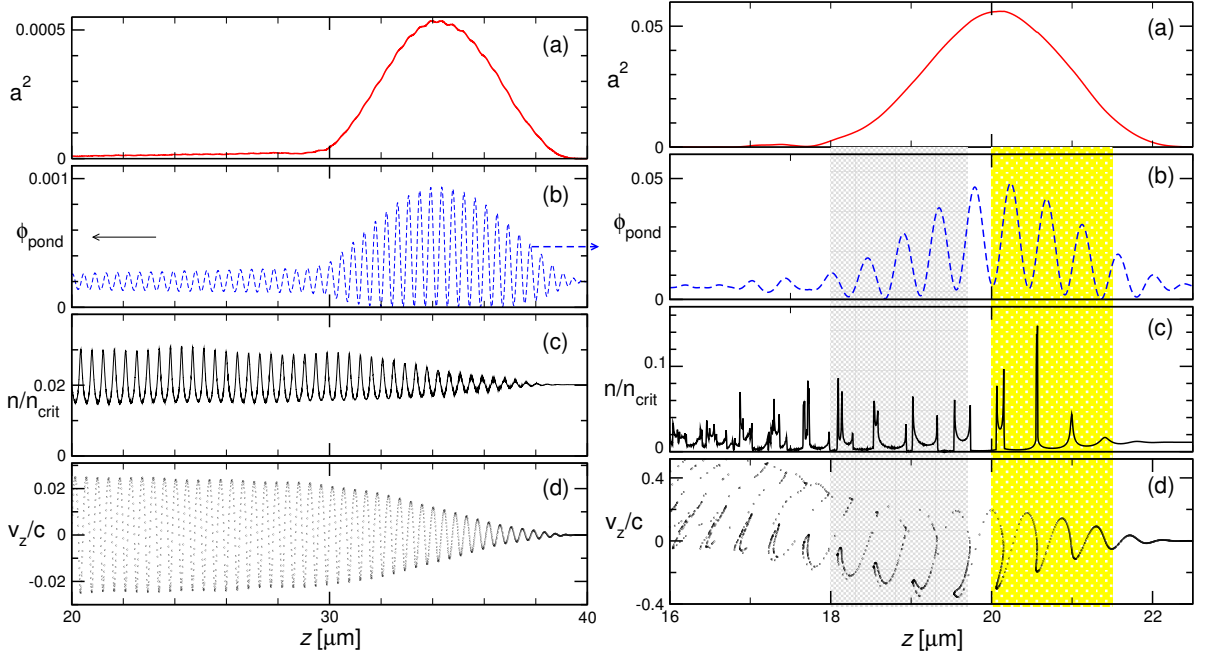


Figure 1: 1D Particle-In-Cell simulations showing the plasma dynamics in the case of SRBS(left) and SRA (right). (a) signal intensity, (b) common ponderomotive potential of the pump and signal pulses, (c) electron plasma density, (d) electron phasespace

of the other electrons (single-electron picture). (Fig.1 right). Since the carrier frequencies of both pulses differ only slightly, the phase velocity $v_{ph} = (\omega_{\text{pump}} - \omega_{\text{sig}})/(k_{\text{pump}} + k_{\text{sig}})$ of the ponderomotive potential is small and most plasma electrons can get trapped in its periodic structure. They start oscillating at the frequency $\omega_b^2 = 4a_{\text{pump}}a_{\text{sig}}\omega_{\text{pump}}\omega_{\text{sig}}$, where $a_{\text{pump/sig}}$ are the normalized vector potentials of the pump and signal pulses, respectively. The initially homogeneously distributed electrons get bunched quickly in space to a layer much thinner than the laser wavelength. The almost perfect bunching of the electrons in combination with the periodicity of the peaks of approximately half a laser wavelength leads to a coherent backscattering of the pump pulse into the signal pulse. The slightly higher frequency of the pump pulse determines the position of the electron density peak relative to the ponderomotive potential (see Fig.1b right column yellow marked area: the electron peak is on the right side of the potential bucket) and the direction of the energy flow which in this case is from the pump to the signal. The ongoing oscillations of the electrons destroy the grating and dis-

tribute them in turn homogeneously in space. Finally, the electrons get bunched once again, but this time the electron peak is located on the left side of the potential bucket which causes the signal pulse to be backscattered into the pump pulse. This strongly attenuates the rear part of the signal pulse and restricts its duration to approximately one half the bouncing period, π/ω_b . Shortening of the signal pulse also takes place in that its intensity and therefore ω_b increase during the amplification. Simulations with a Particle-In-Cell (PIC) code showed that the amplification continues until the amplitude of the signal pulse almost reaches relativistic intensities ($a^2 \approx 0.3$). For higher intensities, the signal pulse breaks up, most likely due to non-linear relativistic effects. For a pump wavelength of $\lambda = 0.8 \mu\text{m}$, a maximally amplified signal pulse reaches an intensity of $\approx 10^{18} \text{ W/cm}^2$, a duration of $< 7 \text{ fs}$, and a flux of 7 kJ/cm^2 .

While the SRBS regime prevails for low laser intensities, the amplification changes to the SRA regime when the signal intensity becomes large enough that the threshold condition $\omega_b > \omega_p^9$ is satisfied. It sets a lower

bound for the product of the laser intensities. The main qualitative differences between the two regimes are the lifetime of the electron density modulation and its phase relation with respect to the ponderomotive potential as shown in Fig. 1. In the case of SRBS, the phase relation between the plasma wave and the interference potential stays the same and therefore the signal will be amplified as long as the pump is not yet depleted. In the case of SRA, the ongoing oscillations of the trapped electrons cause the periodic creation and destruction of the density grating. Each time the electron density grating is shifted with respect to the ponderomotive potential a change in the energy flow occurs from the pump into the signal or vice versa.

II. SETUP

We use the ATLAS (Advanced Titanium:Sapphire Laser) facility at the MPQ, that employs the CPA scheme and delivers 200 mJ/120-fs/790-nm pulses at 10 Hz repetition rate. After the amplification, the pulse is not completely recompressed; its duration is kept between (1-7) ps so that it can serve as the pump pulse in the SRA experiment. The seed pulse is generated from a small fraction split off from the main pulse before compression. The slit-off fraction is compressed in a separate grating compressor to 120 fs and sent through a fused silica capillary filled with argon gas. During the passage through the capillary, self-phase modulation broadens the pulse spectrum to a range from 750 to 830 nm.¹⁰ A dielectric filter blocks the wavelengths below 800 nm. This effectively shifts the central wavelength to the red with respect to the pump pulse as it is required for SRA. The residual chirp obtained from the passage through the fiber is removed by a prism compressor. The input signal pulse when entering the target chamber has a central wavelength of 815 nm, a duration of 70 fs and an energy of 130 μ J.

In the target chamber, the pump and signal pulses are focused into a hydrogen gas jet from opposite directions by two off-axis parabolas with the same f-number such that the two foci overlap. This is achieved by forcing both pulses to pass through a pinhole. Each focus has a diameter of $\approx 28 \mu\text{m}$ and a Rayleigh length of $\approx 600 \mu\text{m}$. To establish the temporal overlap of the pulses in the focal area, their arrival times are synchro-

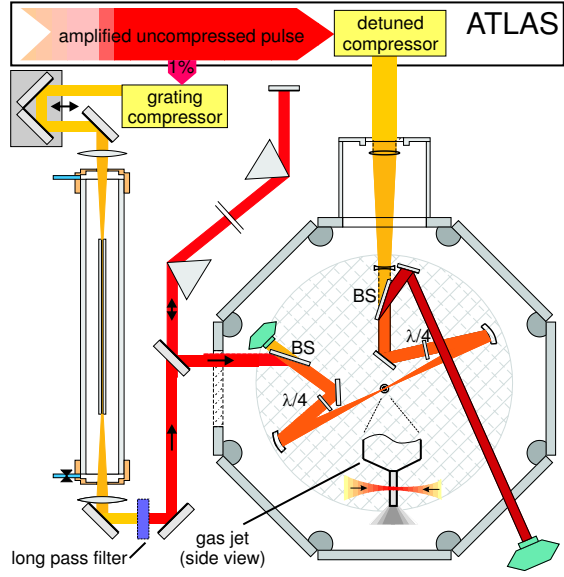


Figure 2: Experimental setup

nized by means of a streak camera. The initial signal intensity reaches $2 \times 10^{14} \text{ W/cm}^2$ and the pump intensity varies from 2 to $5 \times 10^{15} \text{ W/cm}^2$ depending on the pump pulse duration. The length of the gas jet is 1 mm. The gas nozzle is shaped like a chimney to guide the gas and create a more homogenous gas-density profile (see inset in Fig.2). The gas is ionized by the leading edge of the pump pulse so that the interaction of the two pulses takes place in a channel of fully ionized plasma.

SRA works best when both pulses are circularly polarized at opposite helicity. We accomplish this by using a combination of two polarizing beam splitters, BS1 and BS2, and two quarter wave plates, QWP1 and QWP2 (see Fig.2). Our setup ensures that neither the pump pulse enters the signal beam line outside the target chamber nor the signal pulse is fed into the ATLAS amplifier chain. This is important in order to avoid optical damage both in ATLAS as well as in the optical components used for the generation of the signal pulse.

We first consider the signal pulse. Upon entering the target chamber, it is s-polarized with respect to BS2 so that it is reflected from BS2. When passing through QWP2, it gets left-handed circularly polarized. After the interaction with the pump pulse, it passes through QWP1 whereby it recovers its original s-polarization. It is reflected from BS1 and then analysed in terms of

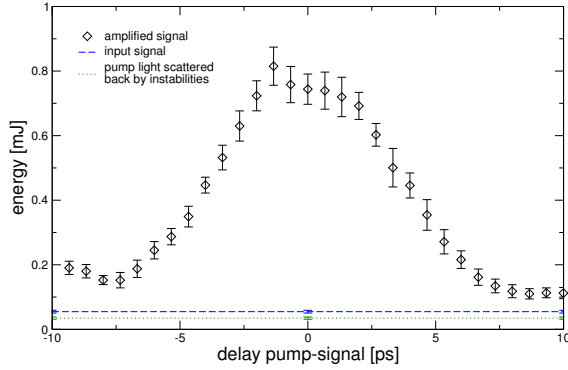


Figure 3: Energy of the amplified signal pulse (diamonds) versus the delay between the pump and signal pulses. The energy of the input signal pulse (dashed-blue) and the level of the pump light backscattered by Raman instabilities (dotted-green) are given for comparison. The values of all measurements are averaged over 20 shots, error bars are given by statistical deviation.

energy, fluence pattern, and spectrum. Upon entering the target chamber, the pump is p-polarized so that it is transmitted through BS1. Behind QWP1, it is right-handed circularly polarized so that both pulses meet in the interaction zone at opposite helicity. After the interaction, QWP2 restores the p-polarization for the pump pulse so that it transmits BS2 and is dumped.

III. RESULTS AND DISCUSSION

For a correct interpretation of the experimental results, it is indispensable to distinguish between the amplified signal and the pump light backscattered by instabilities. For the given parameters, the Raman instability is most likely in the region where the pump has not yet interacted with the signal. The Raman backscattered light has the same polarization as the signal and lies in the same spectral range and cannot be separated from it by BS1. This results in an undesired weak long precursor. During the interaction of the pump and signal pulses, the plasma becomes very turbulent and is heated (see Fig.1) such that instabilities are strongly suppressed in the region which has already passed through by the signal pulse. An upper limit for the backscattered Raman light is hence obtained by blocking the signal pulse and measuring the energy of

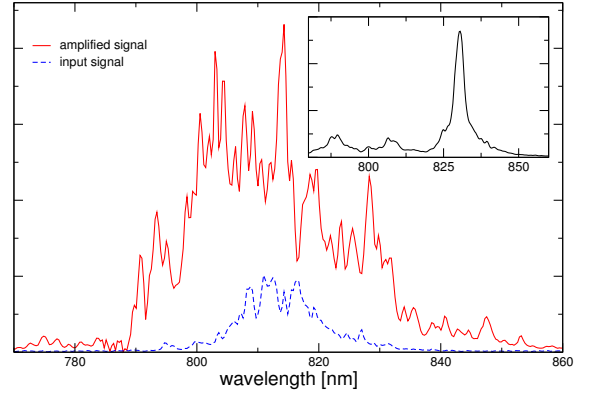


Figure 4: Spectra of the amplified (solid red line) and input pulses (dashed blue line); the delay between the pump and signal pulses is chosen as to maximise the energy gain. The inset shows the sharp spectral line of a pulse amplified in the Raman regime only.

the light backscattered from the plasma. This energy is larger than that occurring in presence of the signal pulse, because the plasma is not heated by the pump-signal interaction and the pump pulse is scattered over the full length of the plasma column. The backscattered Raman light of the pump pulse alone is also used to determine the electron plasma density, $n_e = \omega_p^2 m_e / 4\pi e^2$. The plasma frequency, ω_p , is obtained from the measured spectral shift of the Stokes line. A direct interferometric measurement of the electron density is not possible due to the shape of the nozzle.

Fig.3 shows the energy of the amplified signal as it varies with the delay between the signal and pump pulses, i. e. their arrival times in the plasma. The pump pulse duration is 4 ps and the plasma density, n_e , equals $3 \times 10^{18} \text{ cm}^{-3}$. The output energy of the signal pulse becomes maximal when the pulses completely overlap in the plasma and within the Rayleigh length, where the intensities are highest and the amplification is strongest. The width of the curve depends on the Rayleigh length, the duration of the pump pulse and the length of the plasma column. The maximal energy gain is found to be 14. By increasing the electron density, it could be raised up to 20. Shot-to-shot fluctuations of the output energy can be explained by fluctuations of the intensities of the input signal and pump pulses. For the parameters given, the threshold condition for the SRA

regime is not reached from the very beginning of the interaction. Hence the pulse is first amplified in the SRBS regime. The way we presently generate the input signal pulse does not allow to make it sufficiently short and intense so that the SRBS regime could be overjumped. The reason for this is twofold. First the energy transmission through the hollow fiber is limited and second much of the spectrum is cut by the filtering to establish the wavelength shift which reduces the pulse energy. However, the threshold condition is satisfied for the amplified output signal pulse. This means that the interaction changes from the SRBS type to the SRA type during the interaction. Amplification by SRBS is possible because the resonance condition does not need to be satisfied strictly for very short signal pulses.

The measurements of the spectra shown in Fig.4 confirm a transition from the Raman regime to the SRA regime. A broadening of the spectral width from 15 nm before amplification to 25 nm after amplification is found. The spectral broadening is a characteristic feature of the SRA regime, because signal shortening in time is predicted for growing signal amplitude which requires the spectrum to broaden correspondingly in order to satisfy the time-bandwidth product. No indication of a sharp strong Stokes line is observed, which would be characteristic for Raman amplification demonstrated in the inset. It is observed, when the signal pulse is not filtered after the broadening in the capillary. Its full spectrum is not shifted with respect to that of the pump pulse and can be compressed to ≈ 30 fs. As PIC-simulations show the short signal pulse causes a trailing Raman instability of the pump pulse. It is amplified further in the Raman regime and finally dominates the spectrum as a sharp narrow line.

IV. CONCLUSION

The observed energy amplification of up to the mJ-level and the spectral broadening clearly evidence that the SRA regime has been reached. For further studies aiming at the realization of the full SRA potential, a shorter and stronger input signal pulse is needed that satisfies the threshold condition for SRA from the very beginning on. This is under preparation at our laboratory and should enable us to reach the 10-mJ energy level at pulse durations of less than 15 fs.

References

1. A. PUKHOV, and J. MEYER-TER-VEHN, "Laser Wake Field Acceleration: the Highly Non-Linear Broken-Wave Regime", *Appl. Phys. B* **74**, 355 (2002)
2. V. MALKA *et al.*, "Electron Acceleration by a Wake Field Forced by an Intense Ultrashort Laser Pulse", *Science* **298**, 1596 (2002)
3. D. STRICKLAND and G. MOUROU, "Compression of Amplified Chirped Optical Pulses", *Opt. Comm.*, **55**, 447 (1985)
4. I. N. ROSS, *et al.*, "Generation of Terawatt Pulses by use of Optical Parametric Chirped Pulse Amplification", *Opt. Comm.* **144**, 125 (1997)
5. G. CERULLO, M. NISOLI, S. STAGIRA, and S. DE SILVESTRI, "Sub-8-fs Pulses from an Ultra-broadband Optical Parametric Amplifier in the Visible", *Opt. Lett.* **23**, 1283 (1998)
6. A. SHIRAKAWA, I. SAKANE, and T. KOBAYASHI "Pulse-Front-Matched Optical Parametric Amplification for Sub-10-fs Pulse Generation in the Visible and Near Infrared", *Opt. Lett.* **23**, 1292 (1998)
7. W. L. KRUEER, *The Physics of Laser Plasma Interaction*, Addison-Wesley (1998)
8. V. M. MALKIN, G. SHVETS, and N.J. FISCH, "Fast Compression of Laser Beams to Highly Over-critical Powers", *Phys. Rev. Lett.* **82**, 4448 (1999)
9. G. SHVETS, N.J. FISCH, A. PUKHOV, and J. MEYER-TER-VEHN, "Superradiant Amplification of an Ultrashort Laser Pulse in a by a Counterpropagating Pump", *Phys. Rev. Lett.* **81**, 4879 (1998)
10. M. NISOLI, S. DE SILVESTRI, and O. SVELTO, "Generation of High Energy 10-fs Pulses by a New Pulse Compression Technique", *Appl. Phys. Lett.* **68**, 2793 (1996)

Bibliography

- [1] M. Dreher, E. Takahashi, J. Meyer-ter-Vehn, and K.-J. Witte, Observation of Superradiant Amplification of Ultrashort Laser Pulses in a Plasma, *Physical Review Letters* **93**, 095001 (2004).
- [2] T. H. Maiman, Stimulated Optical Radiation in Ruby Masers, *Nature* **187**, 493 (1960).
- [3] J. A. Armstrong, N. Bloembergen, J. Ducuing, and P. S. Pershan, Interactions between Light Waves in a Nonlinear Dielectric, *Physical Review* **127**, 1918–1939 (1962).
- [4] H. Figger, D. Meschede, and C. Zimmermann, editors, *Laser Physics at the Limits*, Springer, Berlin Heidelberg, 2001.
- [5] H. Rabitz, R. de Vivie-Riedle, M. Motzkus, and K.-L. Kompa, Whither the future of controlling quantum phenomena, *Science* **288**, 824–828 (2000).
- [6] R. W. Hellwarth, *Q Modulation of Lasers*, Columbia University Press, New York, 1961.
- [7] L. E. Hargrove, R. L. Fork, and M. A. Pollack, Locking of He-Ne Laser Modes Induced by Synchronous Intracavity Modulation, *J. Appl. Phys.* **5**, 4 (1964).
- [8] P. Agostini, F. Fabre, G. Mainfray, G. Petite, and N. Rahman, Free-Free Transitions Following Six-Photon Ionization of Xenon Atoms, *Physical Review Letters* **42**, 1127 (1979).
- [9] M. Ferray *et al.*, Multiple-harmonic conversion of 1064 nm radiation in rare gases, *Journal of Physics B* **21**, L31 (1988).
- [10] M. Perry, A. Szöke, O. Landen, and E. Campbell, Nonresonant multiphoton ionization of noble gases: Theory and experiment, *Physical Review Letters* **60**, 1270 (1988).
- [11] M. Perry, O. Landen, A. Szöke, and E. Campbell, Multiphoton Ionization of the noble gases by an intense 10^{14} W/cm² dye laser, *Physical Review A* **37**, 747 (1988).
- [12] J. H. Nuckolls, L. Wood, A. Thiessan, and G. B. Zimmermann, Laser compression of matter to super-high densities: thermonuclear (CTR) applications, *Nature* **239**, 129 (1972).
- [13] H. Daido, Review of soft X-ray laser researches and developments, *Rep. Prog. Phys.* **65**, 1513–1576 (2002).
- [14] F. Krausz, private communication.

-
- [15] S. Bahk, P. Rousseau, T. Planchon, V. Chvykov, G. Kalintchenko, A. Maksimchuk, G. Mourou, and V. Yanovsky, *Opt. Lett.* (to be published), see also.
- [16] D. S. G. Mourou, Compression of amplified chirped optical pulses, *Opt. Commun.* **56**, 219 (1985).
- [17] M. Perry and G. Mourou, Terawatt to Petawatt Subpicosecond Lasers, *Science* **264**, 917 (1994).
- [18] M. D. Perry *et al.*, Petawatt Laser Pulses, *Optics Letters* **24**, 160 (1999).
- [19] H. Baumhacker *et al.*, Advanced Titanium Sapphire Laser ATLAS, MPQ Bericht, MPQ Garching, 2002.
- [20] G. Mourou, C. Barty, and M. Perry, Ultrahigh-Intensity Lasers: Physics of the Extreme on a Tabletop, *Physics Today*, 22 (Januar 1998).
- [21] C. Gahn *et al.*, Multi-MeV Elektron Beam Generation by Direct Laser Acceleration in High-Density Plasma Channels, *Physical Review Letters* **83**, 4772–4775 (1999).
- [22] T. Tajima and J. M. Dawson, Laser Electron Accelerator, *Physical Review Letters* **43**, 267–270 (1979).
- [23] E. Esarey, P. Sprangle, J. Krall, and A. Ting, Overview of Plasma-Based Accelerator Concepts, *IEEE Transactions on Plasma Science* **24**, 252–288 (1996).
- [24] A. Pukhov and J. Meyer-ter-Vehn, Laser wake field acceleration: the highly non-linear broken-wave regime, *Applied Physics B* **74**, 355–361 (2002).
- [25] J. Faure, Y. Glinec, A. Pukhov, S. Kiselev, S. Gordienko, E. Lefebvre, J.-P. Rousseau, F. Burgy, and V. Malka, A laser plasma accelerator producing monoenergetic electron beams, *Nature* **431**, 541–544 (2004).
- [26] R. A. Snavley *et al.*, Intense High-Energy Proton Beams from Petawatt-Laser Irradiation of Solids, *Physical Review Letters* **85**, 2945–2948 (2000).
- [27] U. Andiel, *Isochore Heizung von festem Aluminium mit Femtosekunden-Laserpulsen: eine röntgenspektroskopische Untersuchung der K-Schalenemission*, PhD thesis, TU München, 2000.
- [28] G. Tallents, The physics of soft x-ray lasers pumped by electron collisions in laser plasmas, *J. Phys. D: Appl. Phys.* **36**, R259–R276 (2003).
- [29] T. Brabec and F. Krausz, Intense few-cycle laser fields: Frontiers of nonlinear optics, *Review of Scientific Instruments* **72**, 545–591 (2000).
- [30] P. A. Norreys, M. Zepf, S. Moustazis, A. P. Fews, J. Zhang, . P. Lee, M. Bakarezos, C. N. Danson, A. Dyson, P. Gibbon, P. Loukakos, D. Neely, F. N. Walsh, J. S. Wark, and A. E. Dangor, Efficient Extreme UV Harmonics Generated from Picosecond Laser Pulse Interactions with Solid Targets, *Physical Review Letters* **76**, 1832–1835 (1996).

- [31] N. A. Papadogiannis, B. Witzel, C. Kalpouzos, and D. Charalambidis, Observation of Attosecond Light Localization in Higher Order Harmonic Generation, *Physical Review Letters* **83**, 4289–4292 (1999).
- [32] P. Paul *et al.*, Observation of a train of attosecond pulses from high harmonic generation, *Science* **292**, 1689–1692 (2001).
- [33] M. Hentschel, R. Kienberger, C. Spielmann, G. A. Reider, N. Milosevic, T. Brabec, P. Corkum, U. Heinzmann, M. Drescher, and F. Krausz, Attosecond Metrology, *Nature* **414**, 513–517 (2001).
- [34] J. Schwinger, On Gauge Invariance and Vacuum Polarization, *Physical Review* **82**, 664–679 (1951).
- [35] N. B. Narozhny, S. S. Bulanov, V. D. Mur, and V. S. Popov, $e^{(+)}e^{(-)}$ -pair production by a focused laser pulse in vacuum, *PHYSICS LETTERS A* **330**, 1–6 (2004).
- [36] S. V. Bulanov, T. Espikov, and T. Tajima, Light Intensification towards the Schwinger Limit, *Physical Review Letters* **91**, 085001 (2003).
- [37] S. Gordienko, A. Pukhov, O. Shorokhov, and T. Baeva, Coherent Harmonic Focusing and the Light Extreme, submitted to *Physical Review Letters*, 2004.
- [38] T. J. Kessler, J. Bunkenburg, H. Huang, A. Kozlov, and D. D. Meyerhofer, Demonstration of coherent addition of multiple gratings for high-energy chirped-pulse-amplified lasers, *Optics Letters* **29**, 635–637 (2004).
- [39] T. Tajima and G. Mourou, Zetawatt-exawatt lasers and their applications in ultrastrong-field physics, *Physical Review Special Topics* **5**, 031301 (2002).
- [40] I. N. Ross, J. L. Collier, P. Matousek, C. N. Danson, D. Neely, R. M. Allott, D. A. Pepler, and C. Hernandez-Gomez, Generation of terawatt pulses by use of optical parametric chirped pulse amplification, *Applied Optics* **39**, 2422–2427 (2000).
- [41] G. Cerullo, M. Nisoli, S. Stagira, and S. D. Silvestri, Sub-8-fs pulses from an ultra-broadband optical parametric amplifier in the visible, *Optics Letters* **23**, 1283–1285 (1998).
- [42] A. Shirakawa, I. Sakane, and T. Kobayashi, Pulse-front-matched optical parametric amplification for sub-10-fs pulse generation in the visible and near infrared, *Optics Letters* **23**, 1292–1294 (1998).
- [43] N. Ishii, R. Butkus, V. L. Turi, T. Fuji, G. Veitas, V. Smilgevičius, R. Danielius, A. Piskarskas, F. Krausz, and A. Baltuška, Multimillijoule Chirped Parametric Amplification of Few-Cycle-Pulses, accepted for *Optics Letters*.
- [44] G. Shvets, N. J. Fisch, A. Pukhov, and J. Meyer-ter-Vehn, Superradiant Amplification of an Ultrashort Laser Pulse in a Plasma by a Counterpropagating Pump, *Physical Review Letters* **81**, 4879–4882 (1998).

-
- [45] V. M. Malkin, G. Shvets, and N. J. Fisch, Ultra-Powerful Raman Amplifiers, *Physical Review Letters* **82**, 4448–4451 (1999).
- [46] M. Dreher, Superradiante Verstärkung ultrakurzer Laserpulse in Plasmen, MPQ Bericht 250, MPQ Garching, 2000.
- [47] W. L. Kruer, *The Physics of Laser Plasma Interactions*, Addison-Wesley, California, 1988.
- [48] T. W. B. Kibble, Mutual Refraction of Electrons and Photons, *Physical Review* **150**, 1060–1069 (1966).
- [49] B. Quesnel and P. Mora, Theory and simulation of the interaction of ultraintense laser pulses with electrons in vacuum, *Physical Review E* **58**, 3719–3732 (1998).
- [50] F. F. Chen, *Introduction to Plasma Physics*, Plenum Press, New York and London, 1977.
- [51] S. Atzeni and J. Meyer-ter-Vehn, *The physics of inertial fusion*, Clarendon Press, Oxford, 2004.
- [52] Bergman and Schäfer, *Experimentalphysik*, Bd. 3:Optik, Walter de Gruyter, New York, 9. edition, 1993.
- [53] J. D. Jackson, *Classical Electrodynamics*, John Wiley and Sons, New York, 2. edition, 1974.
- [54] J. Sheffield, *Plasma Scattering of Electromagnetic Radiation*, Academic Press, New York, 1975.
- [55] R. C. Davidson, *Methods in Nonlinear Plasma Theory*, Academic Press, New York and London, 1972.
- [56] A. Yariv, *Quantum Electronics*, John Wiley and Sons, New York, 3. edition, 1988.
- [57] I. Bronstein, K. Semendjajew, G. Musiol, and H. Mühlig, *Taschenbuch der Mathematik*, Harri-Deutsch Verlag, Frankfurt am Main, 2. edition, 1995.
- [58] A. Baltuska *et al.*, Attosecond control of electronic processes by intense laser light fields, *Nature* **421**, 611–616 (2003).
- [59] J. M. J. Madey, Stimulated Emission of Bremsstrahlung in a Periodic Magnetic Field, *J. Appl. Phys.* **42**, 1906 (1971).
- [60] C. A. Brau, *Free-Electron Lasers*, Academic Press, Boston, 1990.
- [61] P. Luchini and H. Motz, *Undulators and Free-Electron Lasers*, Clarendon Press, Oxford, 1990.
- [62] R. Bonifacio, C. Marioli, and N. Piovella, Slippage and Superradiance in the High-Gain FEL: Linear Theory, *Opt. Commun.* **68**, 369 (1988).

- [63] R. Bonifacio, L. D. S. Souza, P. Pierini, and N. Piovell, The Superradiant Regime of an FEL: Analytical and Numerical Results, *Nuclear Instruments and Methods in Physical Research* **296**, 358 (1990).
- [64] C. K. Birdsall and A. B. Langdon, *Plasma Physics Via Computer Simulation*, Adam Hilger, Bristol, Eng., 1991.
- [65] A. Pukhov, Three-dimensional electromagnetic relativistic particle-in-cell code v1pl, *J. Plasma Physics* **61**, 425 (1999).
- [66] A. A. Solodov, V. M. Malkin, and N. J. Fisch, Pump side scattering in ultrapowerful backward Raman amplifiers, *Physical Review E* **69**, 066413 (2004).
- [67] Y. A. Tsidulko, V. M. Malkin, and N. J. Fisch, Suppression of Superluminous Precursors in High-Power Backward Raman Amplifiers, *Physical Review Letters* **88**, 235004 (2002).
- [68] E. S. Dodd and D. Umstadter, Coherent control of stimulated Raman scattering using chirped laser pulses, *Physics of Plasmas* **8**, 3531–3534 (2001).
- [69] M. Maier, W. Kaiser, and J. A. Giordmaine, Intense Light Bursts in the Stimulated Raman Effect, *Physical Review Letters* **17**, 1275–1277 (1966).
- [70] M. Maier, W. Kaiser, and J. A. Giordmaine, Backward Stimulated Raman Scattering, *Physical Review* **177**, 580–599 (1968).
- [71] R. D. Milroy, C. E. Capjack, and C. R. James, A Plasma-Laser in the 11-16 μm Wavelength Range, *Plas. Phys.* **19**, 989–995 (1977).
- [72] R. D. Milroy, C. E. Capjack, and C. R. James, Plasma laser pulse amplifier using induced Raman of Brillouin processes, *Phys. Fluids* **22**, 1922–1931 (1979).
- [73] J. R. Murray, J. Goldhar, D. Eimerl, and A. Szoke, Raman pulse compression of excimer lasers for application to laser fusion, *IEEE Journal of Quantum Electronics* **15**, 342–368 (1979).
- [74] V. M. Malkin, G. Shvets, and N. J. Fisch, Detuned Raman Amplification of Short Laser Pulses in Plasma, *Physical Review Letters* **84**, 1208 (2000).
- [75] V. M. Malkin, G. Shvets, and N. J. Fisch, Ultra-powerful compact amplifiers for short laser pulses, *Physics of Plasmas* **7**, 2232 (2000).
- [76] N. J. Fisch and V. M. Malkin, Generation of ultrahigh intensity laser pulses, *Physics of Plasmas* **10**, 2056–2063 (2003).
- [77] G. M. Fraiman, N. A. Yampolsky, V. M. Malkin, and N. J. Fisch, Robustness of laser phase fronts in backward Raman amplifiers, *Physics of Plasmas* **9**, 3617–3624 (2002).
- [78] V. M. Malkin, Y. A. Tsidulko, and N. J. Fisch, Stimulated Raman Scattering of Rapidly Amplified Short Laser Pulses, *Physical Review Letters* **85**, 4068 (2000).

-
- [79] P. Mardahl, H. J. Lee, G. Penn, J. S. Wurtele, and N. J. Fisch, Intense laser pulse amplification using Raman backscatter in plasma channels, *Phys. Lett. A* **296**, 109–116 (2002).
- [80] D. S. Clark and N. J. Fisch, Particle-in-cell simulations of Raman laser amplification in preformed plasmas, *Physics of Plasmas* **10**, 4848–4855 (2003).
- [81] D. S. Clark and N. J. Fisch, Regime for a self-ionizing Raman laser amplifier, *Physics of Plasmas* **9**, 2772–2780 (2002).
- [82] D. S. Clark and N. J. Fisch, Simulations of Raman amplification in ionizing plasmas, *Physics of Plasmas* **10**, 4837–4847 (2003).
- [83] A. A. Solodov, V. M. Malkin, and N. J. Fisch, Random density inhomogeneities and focusability of the output pulses for plasma-based powerful backward Raman amplifiers, *Physics of Plasmas* **10**, 2540–2544 (2003).
- [84] Y. Ping, I. Geltner, N. J. Fisch, G. Shvets, and S. Sukewer, Demonstration of ultrashort laser pulse amplification in plasmas by a counterpropagating pumping beam, *Physical Review E* **62**, R4532–R4535 (2000).
- [85] Y. Ping, I. Geltner, A. Morozov, N. J. Fisch, and S. Sukewer, Raman amplification of ultrashort laser pulses in microcapillary plasmas, *Physical Review E* **66**, 046401 (2002).
- [86] Y. Ping, I. Geltner, and S. Sukewer, Raman backscattering and amplification in a gas jet plasma, *Physical Review E* **67**, 016401 (2003).
- [87] A. A. Balakin, *et al.*, Laser Pulse Amplification upon Raman Backscattering in Plasma Produced in Dielectric Capillaries, *JETP Letters* **80**, 12–16 (2004).
- [88] Y. Ping, W. Cheng, S. Sukewer, D. S. Clark, and N. J. Fisch, Amplification of Ultrashort Laser Pulses by a Resonant Raman Scheme in a Gas-Jet Plasma, *Physical Review Letters* **92**, 175007 (2004).
- [89] D. W. Forslund, J. M. Kindel, and E. L. Lindman, Theory of stimulated scattering processes in laser-irradiated plasmas, *Phys. Fluids* **18**, 1002–1016 (1975).
- [90] C. B. Darrow, C. Coverdale, M. D. Perry, W. B. Mori, C. Clayton, K. Marsh, and C. Joshi, Strongly coupled stimulated Raman backscatter from subpicosecond laser-plasma interactions, *Physical Review Letters* **69**, 442–445 (1992).
- [91] M. Born and E. Wolf, *Principles of Optics*, Cambridge University Press, Cambridge, 7. edition, 1999.
- [92] E. B. Treacy, Optical Pulse Compression With Diffraction Gratings, *IEEE Journal of Quantum Electronics* **5**, 454–458 (1969).
- [93] T. Wilhelm, J. Piel, and E. Riedle, Sub-20-fs pulses tunable across the visible from a blue-pumped single-pass noncollinear parametric converter, *Optics Letters* **22**, 1494–1496 (1997).

- [94] T. Wilhelm and E. Riedle, 20 Femtosecond Visible Pulses Go Tunable by Noncollinear Parametric Amplification, *Opt. Phot. News* **12**, 50 (1997).
- [95] J. Piel, M. Beutter, and E. Riedle, 20-50-fs pulses tunable across the near infrared from a blue-pumped noncollinear parametric amplifier, *Optics Letters* **25**, 180–182 (2000).
- [96] E. Riedle, M. Beutter, S. Lochbrunner, J. Piel, S. Schenkl, S. Spörlein, and W. Zinth, Generation of 10 to 50 fs pulses tunable through all of the visible and NIR, *Applied Physics B* **71**, 457–465 (2000).
- [97] J. Zhang, Z. Xu, Y. Kong, C. Yu, and Y. Wu, Highly efficient, widely tunable 10-Hz parametric amplifier pumped by frequency-doubled femtosecond Ti:sapphire laser pulses, *Applied Optics* **37**, 3299–3305 (1998).
- [98] Optical properties of BBO necessary for the computation of the angles can be obtained from the manufacturer. Also the program SNLO from the Sandia NL is helpful. It is obtained from <http://www.sandia.gov/imrl/X1118/xxtal.htm>.
- [99] P. D. Trapani, A. Andreoni, P. Foggi, C. Solcia, R. Danielius, and A. Piskarskas, Efficient conversion of femtosecond blue pulses by travelling-wave parametric generation in non-collinear phase matching, *Optics Communications* **199**, 327–332 (1995).
- [100] P. D. Trapani, A. Andreoni, G. P. Banfi, C. Solcia, R. Danielius, A. Piskarskas, P. Foggi, M. Monguzzi, and C. Sozzi, Group-velocity self-matching of femtosecond pulses in noncollinear parametric generation, *Physical Review A* **51**, 3164–3168 (1995).
- [101] V. Krylov, O. Ollikainen, J. Gallus, U. Wild, A. Rebane, and A. Kalintsev, Efficient noncollinear parametric amplification of weak femtosecond pulses in the visible and near-infrared spectral range, *Optics Letters* **23**, 100–102 (1998).
- [102] J. Wang, M. H. Dunn, and C. F. Rae, Polychromatic optical parametric generation by simultaneous phase matching over a large spectral bandwidth, *Optics Letters* **22**, 763–765 (1997).
- [103] G. Cerullo, M. Nisoli, and S. D. Silvestri, Generation of 11 fs pulses tunable across the visible by optical parametric amplification, *Applied Physics Letters* **71**, 3616–3618 (1997).
- [104] A. Shirakawa and T. Kobayashi, Noncollinearly phase-matched femtosecond optical parametric amplification with a 2000 cm^{-1} bandwidth, *Applied Physics Letters* **72**, 147–149 (1997).
- [105] ag-Riedle, *NOPA, Fundamentals and Instructions*, LS für BioMolekulare Optik, Uni München, 11 2001.
- [106] M. K. Reed, M. K. Steiner-Shepard, and D. K. Negus, Widely tunable femtosecond optical parametric amplifier at 250 kHz with a Ti:sapphire regenerative amplifier, *Optics Letters* **19**, 1855–1857 (1995).

- [107] M. K. Reed, M. K. Steiner-Shepard, M. S. Armas, and D. K. Negus, Microjoule-energy ultrafast optical parametric amplifiers, *J. Opt. Soc. Am. B* **12**, 2229–2236 (1995).
- [108] A. Brodeur and S. L. Chin, Ultrafast white-light continuum generation and self-focusing in transparent condensed media, *J. Opt. Soc. Am. B* **16**, 637–350 (1999).
- [109] C. Nagura, A. Suda, H. Kawano, M. Obara, and K. Midorikawa, Generation and Characterization of Ultrafast White-Light Continuum in Condensed Media, *Applied Optics* **41**, 3735–3742 (2002).
- [110] J. Zhang, J. Huang, H. Wang, J. S. Wong, and G. J. Wong, Second-harmonic generation from regeneratively amplified femtosecond laser pulses in BBO and LBO crystals, *J. Opt. Soc. Am. B* **15**, 200–209 (1998).
- [111] Femto Lasers Produktions GmbH, Vienna, Austria, FEMTOSOURCE COMPACT, 2002.
- [112] A. Leitenstorfer, C. Furst, and A. Laubereau, Widely tunable two-color mode-locked Ti:sapphire laser with pulse jitter of less than 2 fs, *Optics Letters* **20**, 916–918 (1995).
- [113] S. J. White, J.-M. Hopkins, W. H. Knox, and A. Miller, Dual-Wavelength, Self-Starting Saturable Bragg Reflector Mode-Locked Ti:Sapphire Laser, *IEEE J. Quant. Elect.* **38**, 246–251 (2002).
- [114] R. K. Shelton, L.-S. Ma, H. C. Kapteyn, M. M. Murnane, J. L. Hall, and J. Ye, Phase-Coherent Optical Pulse Synthesis from Separate Femtosecond Lasers, *Science* **293**, 1286–1289 (2001).
- [115] L. S. Ma, R. K. Shelton, H. C. Kapteyn, M. M. Murnane, and J. Ye, Sub-10-femtosecond active synchronization of two passively mode-locked Ti:sapphire oscillators, *Physical Review A* **64**, 021802 (2001).
- [116] R. K. Shelton, S. M. Foreman, L.-S. Ma, J. L. Hall, H. C. Kapteyn, M. M. Murnane, M. Notcutt, and J. Ye, Subfemtosecond timing jitter between two independent, actively synchronized, mode-locked lasers, *Optics Letters* **27**, 312–314 (2002).
- [117] R. K. Shelton, L.-S. Ma, H. C. Kapteyn, M. M. Murnane, J. L. Hall, and J. Ye, Active synchronization and carrier phase locking of two separate mode-locked femtosecond lasers, *J. Mod. Opt.* **49**, 401–409 (2002).
- [118] J. Ye *et al.*, Phase-coherent synthesis of optical frequencies and waveforms, *Applied Physics B* **74**, S27–S34 (2002).
- [119] M. Nisoli, S. D. Silvestri, and O. Svelto, Generation of high energy 10 fs pulses by a new pulse compression technique, *Applied Physics Letters* **68**, 2793–2795 (1996).
- [120] A. Baltuska, Z. Wei, M. S. Pshenichnikov, and D. A. Wiersma, Optical pulse compression to 5fs at a 1-MHz repetition rate, *Optics Letters* **212**, 483–485 (1997).

- [121] M. Nisoli, S. Stagira, S. D. Silvestri, O. Svelto, S. Sartania, Z. Cheng, M. Lenzner, C. Spielmann, and F. Krausz, Toward a Terawatt-Scale Sub-10-fs Laser Technology, *IEEE Journal of Selected Topics in Quantum Electronics* **4**, 414–419 (1998).
- [122] S. Sartania, M. Lenzner, G. Tampea, C. Spielmann, F. Krausz, and K. Ferencz, Generation of 0.1-TW 5-fs optical pulses at a 1kHz repetition rate, *Optics Letters* **22**, 1562–1564 (1997).
- [123] M. Nisoli, S. D. Silvestri, O. Svelto, R. Szipöcs, K. Ferencz, C. Spielmann, S. Sartania, and F. Krausz, Compression of high-energy laser pulses below 5 fs, *Optics Letters* **22**, 522–524 (1997).
- [124] M. Nisoli, S. Stagira, S. D. Silvestri, O. Svelto, S. Sartania, Z. Cheng, M. Lenzner, C. Spielmann, and F. Krausz, A novel-high energy pulse compression system: generation of multigigawatt sub-5-fs pulses, *Applied Physics B* **65**, 189–196 (1997).
- [125] J.-C. Diels and W. Rudolph, *Ultrashort Laser Pulse Phenomena*, Academic Press, San Diego, 1996.
- [126] C. V. Shank, R. L. Fork, R. Yen, and R. H. Stolen, Compression of femtosecond optical pulses, *Applied Physics Letters* **40**, 761–763 (1982).
- [127] W. J. Tomlinson, R. H. Stolen, and C. V. Shank, Compression of optical pulses chirped by self-phase modulation in fibers, *J. Opt. Soc. Am. B* **1**, 139–149 (1984).
- [128] R. L. Fork, C. H. B. Cruz, P. C. Becker, and C. V. Shank, Compression of optical pulses to six femtoseconds by using cubic phase compensation, *Optics Letters* **12**, 483–485 (87).
- [129] J. A. Stratton, *Electromagnetic Theory*, McGraw-Hill Book Co., New York, 1941.
- [130] E. A. J. Marcatili and R. A. Schmeltzer, Hollow Metallic and Dielectric Waveguides for Long Distance Optical Transmissions and Lasers, *Bell Syst. Tech. J.* **43**, 1783–1809 (1964).
- [131] G. P. Agrawal, *Nonlinear Fiber Optics*, Academic Press, San Diego, 1989.
- [132] A. Dalgarno and A. E. Kingston, The refractive indices and Verdet constants of the inert gases, *Proc. Roy. Soc. London A* **259**, 424–429 (1960).
- [133] B. M. Penetrante, J. N. Bardsley, W. M. Wood, C. W. Siders, and M. C. Downer, Ionization-induced frequency shifts in intense femtosecond laser pulses, *J. Opt. Soc. Am. B* **9**, 2032–2040 (1992).
- [134] S. C. Rae and K. Burnett, Detailed simulations of plasma-induced spectral blueshifting, *Physical Review A* **46**, 1084–1090 (1992).
- [135] S. Augst, D. Strickland, D. D. Meyerhofer, S. L. Chin, and J. H. Eberly, Tunneling ionization of noble gases in a high-intensity laser field, *Physical Review Letters* **63**, 2212–2215 (1989).

-
- [136] H. J. Lehmeier, W. Leupacher, and A. Penzkofer, Nonresonant third order hyperpolarizability of rare gases and N₂ Determined by third harmonic generation, *Opt. Commun.* **56**, 67–72 (1985).
- [137] G. Tempea and T. Brabec, Theory of self-focusing in a hollow waveguide, *Optics Letters* **23**, 768–770 (1998).
- [138] G. Fibich and A. L. Gaeta, Critical power for self-focusing in bulk media and in hollow waveguides, *Optics Letters* **25**, 335–337 (2000).
- [139] G. Pretzler, Lecture Script: Höchstleistungs-Kurzpulslaser, 2000.
- [140] Y. M. Li and R. Fedosejevs, Density measurement of a high-density pulsed gas jet for laser-plasma interaction studies, *Meas. Sci. Technol.* **5**, 1197 (1994).
- [141] S. D. Baton *et al.*, Stimulated Brillouin scattering with a 1 ps pulse in a preformed underdense plasma, *Physical Review E* **49**, R3602–R3605 (1994).
- [142] T. M. Antonsen Jr. and Z. Bian, Ionization Induced Scattering of Short Intense Laser Pulses, *Physical Review Letters* **82**, 3617–3620 (1999).
- [143] J. Faure *et al.*, Dynamics of Raman instabilities using chirped laser pulses, *Physical Review E* **63**, 065401(R) (2001).
- [144] C. G. R. Geddes *et al.*, High-quality electron beams from a laser wakefield accelerator using plasma-channel guiding, *Nature* **431**, 538–541 (2004).
- [145] G. Shvets and A. Pukhov, Nonlinear Focusing of Counter-Propagating Laser Pulses in Plasmas, *Physical Review E* **59**, 1033 (1999).
- [146] S. Yu. Kalmykov, private communication.
- [147] Abehjat, G. J. Tallents, and D. Neely, The characterization of a high-density gas jet, *J. Phys. D* **30**, 2872–2879 (1997).
- [148] R. Benttar, C. Popovics, and R. Sigel, Polarized light interferometer for laser fusion studies, *Review of Scientific Instruments* **50**, 1583 (1979).
- [149] C. M. Jost, *Untersuchung optisch-feldionisierter Wasserstoff und Deuterium Plasmen mittels Thomson gestreuten Laserlichts*, PhD thesis, LMU München, 2001.
- [150] C. Gahn, *Erzeugung relativistischer Elektronen durch Propagation hochintensiver Laserpulse in einem Plasma*, PhD thesis, LMU München, 2000.
- [151] S. Kato, Y. Kishimoto, and J. Koga, Convective amplification of wake field due to self-modulation of a laser pulse by field ionization, *Physics of Plasmas* **5**, 292–299 (1997).
- [152] S. C. Rae, Ionization-induced defocusing of intense laser-pulses in high-pressure gases, *Opt. Commun.* **97**, 25–28 (1993).

-
- [153] A. J. Mackinnon, M. Borghesi, A. Iwase, M. W. Jones, G. J. Pert, S. Rae, K. Burnett, and O. Willi, Quantitative Study of the Ionization-Induced Refraction of Picosecond Laser Pulses in Gas-Jet Targets, *Physical Review Letters* **76**, 1473–1476 (1996).
- [154] M. Lampe, E. Ott, and J. H. Walker, Interaction of electromagnetic waves with a moving ionization front, *Phys. Fluids* **21**, 42 (1978).
- [155] L. Oliveira, D. Silva, and J. T. Mendonca, Photon acceleration in supraluminous and accelerated ionization fronts, *IEEE Trans. Plasma Sci* **24**, 316 (1996).
- [156] M. Ammosov, N. Delone, and V. Krainov, Tunnel ionization of complex atoms and of atomic ions in an alternating electromagnetic field, *Sov. Phys. JETP* **64**, 1191 (1986).
- [157] C. E. Max, J. Arons, and A. B. Langdon, Self-Modulation and Self-Focusing of Electromagnetic Waves in Plasmas, *Physical Review Letters* **33**, 209–212 (1974).
- [158] A. L. Berkhoer and V. E. Zakharov, Self excitation of waves with different polarizations in nonlinear media, *Sov. Phys. JETP* **31**, 486–490 (1970).
- [159] C. J. McKinstrie and R. Bingham, Stimulated Raman forward scattering and the relativistic modulational instability of light waves in rarefied plasma, *Phys. Fluids B* **4**, 2626–2633 (1992).
- [160] G.-Z. Sun, E. Ott, Y. C. Lee, and P. Guzdar, Self-focusing of short intense pulses in plasmas, *Phys. Fluids* **30**, 526–532 (1987).
- [161] W. Walter, *Gewöhnliche Differentialgleichungen*, Springer, Berlin, Heidelberg, 5. edition, 1991.
- [162] C. P. Poole and Jr., *The Physics Handbook*, John Wiley and Sons, New York, 1998.

Danksagung

Mein besonderer Dank gilt Herrn Professor Witte, der mir ermöglicht hat dieses interessante und anspruchsvolle Thema in seiner Arbeitsgruppe anzugehen. Er hat mir auch angesichts vieler Schwierigkeiten und Rückschläge immer den notwendigen Rückhalt gegeben, die Arbeit fortzusetzen und stand mit seinem Rat jederzeit zur Verfügung.

Meinem Doktorvater Herrn Professor Habs danke ich, dass er die Arbeit der LMU München gegenüber vertritt. Er zeigte mir mit seiner großen Begeisterung, dass er von der Bedeutung des Themas immer überzeugt war.

Ich erinnere mich gerne an die Anfangszeit zurück, als mir Horst Baumhacker die ersten Schritte im ATLAS Labor erleichterte und mich beim Aufbau des Experiments unterstützte. Ebenso danke ich Dr. Eiichi Takahashi, der mit seiner Familie für ein Jahr aus Japan zu uns gekommen war, tatkräftig am Aufbau des Experiments mitarbeitete und mit dem ich zusammen die ersten Messungen realisieren konnte.

Vielen Dank an alle Techniker, die ich im Verlauf des Projekts mit eingespannt habe: Herrn Böswald, der aus seinen Schränken viele gute Optiken hergekratzt hat, und Herrn Haas, der mir mit viel nützlicher Elektronik aus seinen Schränken helfen konnte, und das obwohl beide immer Not klagen mussten, weil es nichts gab und wir nichts hatten; Herrn Fischer, Herrn Keller und Herrn Fölsner für die Unterstützung in Belangen der Mechanik, insbesondere Herrn Fischer für das Wissen um Vakuumtechnik. Schließlich sei auch Herrn Horn gedankt, der mir sehr kurzfristig mit Rat und Tat dabei half, die Elektronik für eine Strahlstabilisierung aufzubauen.

Micheal Jost danke ich für seinen Einsatz, einen alternativen Signalpuls zu erzeugen, insbesondere für seine großen Mühen, die er in den Aufbau des neuen Kurzpulssystems gesteckt hat. Dank an Ronald Holzwarth und auch Herrn Brückner für die Hilfe bei der elektronischen Kopplung der Laser-Oszillatoren.

Den Praktikanten Vincent Reboud, Johan Busselez und Jan Krieger sei gedankt für ihre Mitarbeit am Experiment. Insbesondere Jan konnte mit seinen vielseitigen Kenntnissen in Elektronik und bei Computern und nicht zuletzt mit seiner raschen Auffassungsgabe einiges beitragen.

Ich danke Professor Jürgen Meyer-ter-Vehn für die Diskussionen zur Vertiefung des theoretischen Verständnis der superradianten Verstärkung und für seine Bemühungen ihre Bedeutung gegenüber der wissenschaftlichen Gemeinschaft herauszustreichen, auch indem er mich immer wieder motivierte und mir Gelegenheiten gab, das Projekt auf internationalen Konferenzen zu präsentieren. Seinem Gast Sergei Kalmykov danke ich für die Mitarbeit bei der Interpretation der Messergebnisse.

Allen experimentellen wissenschaftlichen Mitarbeitern der Laser-Plasma-Gruppe und der Laser-Plasma Theoriegruppe danke ich für die zahlreichen Gespräche und auch für Rat, der auf bis zu 30-jährige Erfahrung in der Erforschung der Laser-Plasma-Wechselwirkung beruht.

Insbesondere bedanke ich mich bei Dr. Malte Kaluza für die gemeinsame Zeit und die freundschaftlichen Gespräche über viele physikalische und weltliche Beobachtungen.

Schließlich danke ich auch all den weiteren Kolleginnen und Kollegen am MPQ für die angenehme, freundschaftliche Atmosphäre am Institut.

An meine Freunde nah und fern geht Dank dafür, dass sie mich mit ihrem Zuspruch all die Zeit unterstützt haben.

Nicht zuletzt danke ich meinen Eltern dafür, dass sie mir das alles ermöglicht haben.

Lebenslauf

Matthias Dreher

Geboren am 27. August 1973

Werdegang:

- | | |
|---------------|---|
| Seit 2000 | Promotion am MPI für Quantenoptik, Garching, zum Thema “Experimental Demonstration of Superradiant Amplification of Ultra-short Laser Pulses in a Plasma” |
| 12/98 - 11/99 | Diplomarbeit am MPI für Quantenoptik zum Thema “Superradiante Verstärkung ultrakurzer Laserpulse in Plasmen” |
| 10/96 - 12/99 | Studium der Physik an der TU München,
Abschluss: Diplom Physik (mit Auszeichnung) |
| 10/94 - 09/96 | Studium der Physik an der Universität Konstanz |
| 06/93 - 08/94 | Zivildienst am Clemens-Maria-Kinderheim in Putzbrunn |
| 1984 - 93 | Hegau-Gymnasium Singen, Abschluss Abitur |
| 1980 - 84 | Waldeck Grund- und Hauptschule, Singen |

